

**Study of $K^*(892)^0$ resonance production in high
energy pp and Pb–Pb collisions with ALICE
detector at the LHC**

By

Kishora Nayak

PHYS11201204009

National Institute of Science Education and Research

Jatni, Odisha - 752050, India

A thesis submitted to the

Board of Studies in Physical Sciences

In partial fulfillment of requirements

for the Degree of

DOCTOR OF PHILOSOPHY

of

HOMI BHABHA NATIONAL INSTITUTE

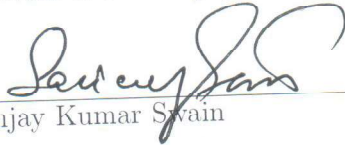


April, 2018

Homi Bhabha National Institute

Recommendations of the Viva Voce Committee


As members of the Viva Voce Committee, we certify that we have read the dissertation prepared by **Kishora Nayak** entitled "**Study of $K^*(892)^0$ resonance production in high energy pp and Pb-Pb collisions with ALICE detector at the LHC**" and recommend that it may be accepted as fulfilling the thesis requirement for the award of Degree of Doctor of Philosophy.


Chairman - Dr. Sanjay Kumar Swain
Date 11/04/2018


Guide / Convener - Prof. Bedangadas Mohanty
Date 11/4/2018

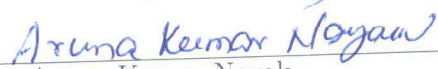
External Examiner - Prof. Hiranmaya Mishra

Date 11th April 2018

Member 1 - Dr. Prolay Kumar Mal

Date April 11, 2018

Member 2 - Dr. Victor Roy

Date 11.04.2018


External Member - Dr. Aruna Kumar Nayak
Date 11/04/2018

Final approval and acceptance of this thesis is contingent upon the candidate's submission of the final copies of the thesis to IIBNI.

I hereby certify that I have read this thesis prepared under my direction and recommend that it may be accepted as fulfilling the thesis requirement.

Date: 11/4/2018
Place: NISER, Jatani


Prof. Bedangadas Mohanty

STATEMENT BY AUTHOR

This dissertation has been submitted in partial fulfillment of requirements for an advanced degree at Homi Bhabha National Institute (HBNI) and is deposited in the Library to be made available to borrowers under rules of the HBNI.

Brief quotations from this dissertation are allowable without special permission, provided that accurate acknowledgement of source is made. Requests for permission for extended quotation from or reproduction of this manuscript in whole or in part may be granted by the Competent Authority of HBNI when in his or her judgment the proposed use of the material is in the interests of scholarship. In all other instances, however, permission must be obtained from the author.

Kishora Nayak

Kishora Nayak

DECLARATION

I, Kishora Nayak, hereby declare that the investigation presented in the thesis has been carried out by me. The work is original and has not been submitted earlier as a whole or in part for a degree/diploma at this or any other Institution/University.

Kishora Nayak
Kishora Nayak

*Dedicated
to
My Well Wishers*

Acknowledgements

This doctoral dissertation was completed with the support of several people. I would like to express my sincere gratitude to all of them. First and foremost, I am extremely grateful to my thesis supervisor Prof. Bedangadas Mohanty for giving me the opportunity to work on the research topic which motivates me throughout my Ph.D. journey. I would like to express my sincere thanks for his valuable guidance, scholarly inputs with logical thinking and consistent encouragement I received throughout the research work. His way of thinking, approach with farsighted action will be a constant source of encouragement to which I will cherish for rest of my career. I am also thankful for the excellent example he has provided as a good person and successful physicist.

The members of the high-energy heavy-ion group of NISER have contributed immensely to my research work. The group has been a source of constant encouragement, collaboration and friendship. I would like to thank Dr. Lokesh Kumar for his guidance during the beginning of my Ph.D. His advice to be systematic during the research work helped in shaping different aspect of my Ph.D. activities. I am thankful to my senior cum friend Dr. Subhash Singha who guided and shed first light on my research work which helped me throughout the research journey. I am especially grateful to have Dr. Ajay Kumar Dash and Dr. Ranbir Singh as my seniors cum collaborators. Their guidance in this doctoral journey was very co-operative and makes me more understandable to my research work. I acknowledge the benefits I have received from the research expertise possessed by Ajay Kumar Dash, which makes my research life more fruitful. With appreciation, I would like to thank Ranbir Singh for his support throughout my doctoral work. The optimistic gesture to handle any situation is amazingly remarkable and I am thankful to have his suggestions during the low tide days of my doctoral career. I am also thankful to have the enthusiastic

discussion with Dr. Chitrasen Jena which leads a better understanding of the research problem. I would like to thank and deeply appreciate Dr. Sandeep Chatterjee with whom I have discussed a lot regarding my research work and philosophy in general.

I would like to acknowledge my senior Dr. Md. Nasim with whom I have collaborated for my doctoral research. I am also thankful to have discussed with my senior Dr. Rihan Haque, Dr. Sabita Das, Dr. Meghna K. K, Dr. Varchaswi Kashyap, Dr. Ananata Mishra, Dr. Rama Chandra Baral and Dr. Subhasis Samanta during my doctoral research work. I would like to thank all my lab mates Vipul Bairathi, Debadeepti Mishra, Sourav Kundu, Dukhishyam Mallick, Debasish Mallick, Samir Banik, Vijay Iyer, Ashutosh Dash and Sandeep Dudi. I acknowledge all of them who have read and given valuable suggestions and also helped me during thesis compilation.

I would like to thank all of my Ph.D. friends from NISER with whom I have spend enormous amount of memorable time. Especial thanks to Rita Maji, Koushik Mandal, Samir Kumar, Mukesh Kumar Shukla, Vantari Siva, Avanendra Singh, Protick Mohanta, Sougata Mallick, Srijani Mallick, Arup Bhowmick for their affection and friendship I have received. I appreciate all my friends who have cared and shared their feeling whose reach is beyond the professional space. I would also like to thank and appreciate my junior Dushmanta Kara's help with whom I have shared so much of precious time since my college days and especially taking care the fooding part during my last years were really an advantagous for me to remain healthy and peaceful. Other juniors like Sushree Subhedarshinee Sahoo and many other juiors who have made my campus life more fun and fruitful.

I was very much privileged to have a great friend circle beyond my research collaboration. My close friends and associates like Shibanaanda Sahoo, Kasinath Das, Sudhanshu Sekhar Dhal, Mihir Ranjan Sahoo, Bibhudatta Sahu, Brundabana Meher,

Ranjan Dora, Ratnamanjari Naik, Anupama Patel, Pragati Sahoo, Sudipta Mahana, Parayana Barik, Rakesh Kumar Sahu helped a lot by ensuring a balance and perfect life in all respect beyond my research life. The good memories shared with them has made my life more pleasant and memorable.

I would like to thank Dr. Federico Antinori (Spokesperson, ALICE), Dr. Tapan Kumar Nayak (Deputy spokesperson, ALICE), Dr. Subhasis Chattopadhyay (ALICE-India spokesperson) and Dr. Paolo Giubellino (Ex-spokesperson, ALICE) for their support in various matters in spite of their busy schedule. I would like to thank Dr. Jurgen Schukraft and Dr. Helmut Oeschler for giving many helpful suggestions for my analysis. I would like to thank the physics analysis group members and conveners in ALICE, specially Dr. Angela Badala, Dr. Christina Markert, Dr. Francesca Bellini, Dr. Alexander Philipp Kalweit, Dr. David Dobrigkeit Chinellato, Dr. Roberto Preghenella, Dr. Viktor Riabov and Dr. Anders Garritt Knospe for their support. Their valuable suggestions and constructive criticism helped me in understanding the analysis in great detail.

I gratefully thank and appreciate ALICE software team and Dr. Latchezar Betev for helping me in computation matters and providing the resources for computation. I would like to thank the LEGO train operator team in ALICE for their help in computation. I would like to thank Dr. Viktor Riabov, Dr. Anders Knospe, Dr. Francesca Bellini and Dr. Martin Vala for their help in resonance analysis. I would like to thank Dr. Angela Badala for inviting me to INFN, Catania and introducing me to the interesting analysis of charged K^{*0} reconstruction which we did for the first time in ALICE.

I would like to express my thanks to Dr. Sudhakar Panda (Director, NISER), Dr. V. Chandrashekhar (Ex-director, NISER) and Dr. T. Chandrashekhar (Ex-director, NISER) for their support. The support from NISER library during my pre-doctoral

study and computer centre while pursuing my research was very supportive, so I acknowledge their help. The academic and physics office staffs of NISER were very supportive towards me primarily during the visits and settling various issues, so I would like to appreciate their kind help for which I have saved my precious time and made my life more smoother. I would like to thank all the members of my doctoral committee. I express my gratitude to the SPS faculty members of NISER who taught me during the pre-doctoral course work. They have been very kind enough to extend their help at various phases of this research whenever I approached them, and I do hereby acknowledge all of them. I would like to take the opportunity to thank all the members of physics group at NISER, IOP and all members of PMD collaboration. I would also like to thank the VECC physics group especially remembering my M.Sc. summer project days. Many people including Dr. Nihar Ranjan Sahoo, Dr. Victor Roy and all other members who had introduced me about the QGP and the research life for the first time during the VECC, Kolkata visit.

My school and university teachers have supported me a lot with their valuable guidance as a result of which I have reached to this stage. I am indebted to all of them. I would like to thank my teacher Binod Chandra Sahu, Sushil Kumar Dash, Prof. Swapna Mahapatra and Prof. Karmadev Maharana whose farsighted vision and wisdom had always an advantage for my career.

I owe a lot to my parents, who encouraged and helped me at every stage of my personal and academic life. My in depth appreciation and respect to them as they have waited long to see my achievement and the dream come true moment. My father has been a role model for my life and his constant support and encouragement is always a blessing for my personal and professional life. I owe to my beloved sister's

love and affection because of which I have always felt a peaceful family life. I would like to thank all other family members and relatives who have supported my family and my study during the low phase of my life. My apologies, if I missed someone who deserved to be in this list of appreciation.

Kishora Nayak

SYNOPSIS

According to quantum chromodynamics (QCD), the theory of strong interaction, at high temperature and/or density, quarks and gluons are no longer confined inside the hadrons. This de-confined state of matter is called Quark-Gluon-Plasma (QGP) [1]. Such a matter is believed to have been formed in the early universe just after the Big-Bang. The Large Hadron Collider (LHC) at CERN provides an opportunity to study such a strongly interacting QCD matter at extreme energy densities by colliding heavy-ions at very high energy. There are clear signatures of the QGP medium formation in Pb–Pb collisions at $\sqrt{s_{NN}} = 2.76$ TeV [2, 3, 4]. Extensive study is ongoing to understand the properties of the QCD matter formed in the ultra-relativistic heavy-ion collisions.

Resonances by definition are short lived ($\sim \text{fm}/c$) particles. Hence they are very useful to study the in-medium dynamics of the strongly interacting matter produced in heavy-ion collisions. The $K^*(892)^0$ is one of the most suitable resonance particle as it has a life time of $\sim 4 \text{ fm}/c$, which is comparable to the time scale of the hot and dense matter produced. As K^{*0} contains strange (s) quark, it may also give information about the mechanism of strange particle energy loss in the medium through the measurement of the nuclear modification factor (R_{AA}). The measured transverse momentum spectra and azimuthal anisotropy (v_2) of K^{*0} are sensitive to in-medium dynamics and various particle production mechanisms.

Due to the short life time of K^{*0} it decays inside the medium and its decay daughters (kaon and pion) undergoes in-medium interaction. The decay daughters may re-scatter with other in-medium hadrons and exchange momentum. As a result, these K^{*0} resonance can not be reconstructed using the invariant mass technique. This phenomena will reduced the measured K^{*0} yields. There is another scenario, where the

pion and kaon in the medium can regenerate K^{*0} via pseudo-elastic interaction ($\pi K \rightarrow K^{*0} \rightarrow \pi K$) between the chemical freeze-out (in-elastic collisions ends) and kinetic freeze-out (elastic collisions ends). These two competitive processes i.e re-scattering and regeneration decide the measured yield of K^{*0} in an experiment. It may be noted that the $\pi\pi$ interaction cross section (mostly responsible for re-scattering) is almost five times larger than the πK interaction cross section (responsible for regeneration). The information as to which of the two processes dominates can be extracted by measuring the resonance to stable particle ratios. The ratio studied in this thesis is K^{*0}/K . The K^{*0} and K have identical quark content but different mass and spin. This ratio will help to disentangle the re-scattering and regeneration effects. There are evidences from the previous ALICE and lower energy STAR measurements that re-scattering is more dominant than the regeneration effect in high energy heavy-ion collisions [5, 6].

In this thesis, a comprehensive study of the K^{*0} resonance production in Pb–Pb collisions at $\sqrt{s_{NN}} = 2.76$ TeV using the high statistics data set collected in 2011 with the ALICE detector in the LHC is performed. The measurement of invariant yield spectra have been done via its hadronic decay channel [$K^{*0} (\bar{K}^{*0}) \rightarrow \pi^- K^+ (\pi^+ K^-)$] with branching ratio of 66.6 %. The invariant yield spectra are measured in finer centrality classes with high- p_T reach up to 20 GeV/ c . The pion and kaon tracks are identified using the specific ionization energy loss in the Time Projection Chamber and the time of flight measurement in ALICE. The dN/dy and $\langle p_T \rangle$ are calculated at mid-rapidity ($|y| < 0.5$) and compared with the corresponding values from lower energies to understand the particle production mechanism at the LHC energies. The p_T -integrated K^{*0}/K^- ratio in various centralities have been obtained. The centrality selection is performed by using the information from V0 detectors in ALICE. This K^{*0}/K^- ratio is compared with the corresponding ϕ/K^- ratio. The life time of ϕ

meson is almost ten times longer than K^{*0} , so it is expected that the ϕ meson yields will not be affected by re-scattering effects. The measurements are compared to the Thermal Model and EPOS3 calculations to confirm the in-medium effects. In order to see the p_T -dependent effect of re-scattering and to understand the particle production mechanism in different p_T regions, various particle ratios such as K^{*0}/K , K^{*0}/π , ϕ/K and ϕ/π as a function of p_T are studied. The data on K^{*0}/K^- in Pb–Pb collisions at $\sqrt{s_{NN}} = 2.76$ TeV presented in this thesis demonstrates that the re-scattering effect is the dominant process and this effect increases with increase in centrality.

The nuclear modification factor (R_{AA}) is defined as the yield of particles in heavy-ion collisions relative to pp collisions, scaled with the average nuclear overlap function.

$$R_{AA} = \frac{1}{\langle T_{AA} \rangle} \times \frac{[d^2N/(dydp_T)]_{AA}}{[d^2\sigma/(dydp_T)]_{pp}}$$

where $\langle T_{AA} \rangle = \langle N_{coll} \rangle / \sigma_{inel}$ is the average nuclear overlap function, $\langle N_{coll} \rangle$ is the average number of binary nucleon-nucleon collisions and σ_{inel} is the inelastic pp cross section. The R_{AA} is used to understand the formation of QGP in heavy-ion collisions. The R_{AA} measurement is sensitive to the dynamics of particle production, in-medium effects, medium density and the energy loss mechanism of partons in the medium. If a nuclear collision were simply a superposition of nucleon-nucleon collisions, the R_{AA} at high- p_T would be equal to unity. Any deviation of the R_{AA} from unity may indicate the presence of in-medium effects. The R_{AA} of K^{*0} are compared to other identified particles such as inclusive charged hadrons, π , K , p and ϕ in order to understand the re-scattering effect (low- p_T), baryon-meson effect (intermediate- p_T) and light flavoured dependence of parton energy loss (high- p_T) in the medium. The R_{AA} values at high- p_T are similar in π , K , K^{*0} , p and ϕ suggesting the light flavour independence of parton energy loss for Pb–Pb collisions at $\sqrt{s_{NN}} = 2.76$ TeV.

In recent measurements from LHC experiments, several collective features similar to Pb–Pb collisions have been observed in high multiplicity pp and p–Pb collisions. The two particle correlation study shows a double ridge structures on the near and away side in p–Pb [7] and in high multiplicity pp collisions [8], analogous to Pb–Pb collisions. Non-vanishing elliptic flow coefficient (v_2) is found in multi-particle cumulant study in pp and p–Pb collisions [9]. The strangeness enhancement in high multiplicity pp collisions at $\sqrt{s} = 7$ TeV [10] is observed and this enhancement in Pb–Pb collisions is a signature of QGP formation. In this thesis, a detailed study of multiplicity dependence K^{*0} production in pp collisions at $\sqrt{s} = 7$ TeV is presented. The K^{*0} p_T -spectra in various multiplicity event classes are measured. The dN/dy and $\langle p_T \rangle$ of K^{*0} at mid-rapidity are extracted. These findings are compared with the corresponding measurement from other identified particles such as π , K , K_s^0 , p , ϕ , Λ , Ξ , Ω to understand the particle production mechanism in high multiplicity pp collisions. The particle ratios like K^{*0}/K are compared with the ϕ/K ratio to see in-medium effects like re-scattering or regeneration effect in high multiplicity pp collisions at $\sqrt{s} = 7$ TeV. This observation might give some idea about the onset of medium formation in high multiplicity pp collisions at LHC energies. The data on p_T -spectra of K^{*0} presented in this thesis are observed to become harder with progressively larger multiplicity event classes. The K^{*0}/K^- in high multiplicity pp collisions shows similar trend as in p–Pb and Pb–Pb collisions suggesting the presence of hadronic re-scattering effect in high-multiplicity pp collisions at $\sqrt{s} = 7$ TeV.

The v_2 of K^{*0} is sensitive to the QGP medium formation and give information about the collective dynamics of the medium created in heavy-ion collisions. The number of constituent quark (NCQ) scaling is a signature of collectivity developed in the partonic level. The NCQ scaling has been observed at RHIC energies, but it seems to be violated at LHC energies [3]. The v_2 of K^{*0} might helps us to understand the

violation of NCQ scaling at LHC energies. In this thesis, the K^{*0} v_2 measurement in Pb–Pb collisions at $\sqrt{s_{\text{NN}}} = 2.76$ TeV are presented. The results have been compared with the corresponding measurement from other identified particles to see the mass ordering at low- p_{T} and baryon-meson effect at intermediate- p_{T} . The effect of hadronic re-scattering on K^{*0} v_2 are discussed. The data on the v_2 of K^{*0} in Pb–Pb collisions at $\sqrt{s_{\text{NN}}} = 2.76$ TeV presented in this thesis shows that the v_2 values decreases with increase in centrality.

References

1. (STAR Collaboration) J. Adams *et al.*, “Experimental and theoretical challenges in the search for the quark gluon plasma: The STAR Collaboration’s critical assessment of the evidence from RHIC collisions”, Nucl. Phys. A 757, 102-183 (2005).
2. (ALICE Collaboration) B. B. Abelev *et al.*, “Centrality, rapidity and transverse momentum dependence of J/ψ suppression in Pb–Pb collisions at $\sqrt{s_{\text{NN}}}=2.76$ TeV”, Phys. Lett. B 734 314 (2014).
3. (ALICE Collaboration) B. B. Abelev *et al.*, “Elliptic flow of identified hadrons in Pb–Pb collisions at $\sqrt{s_{\text{NN}}} = 2.76$ TeV”, JHEP 1506, 190 (2015).
4. (ALICE Collaboration) J. Adam *et al.*, “Centrality dependence of the nuclear modification factor of charged pions, kaons, and protons in Pb–Pb collisions at $\sqrt{s_{\text{NN}}} = 2.76$ TeV”, Phys. Rev. C 93, 034913 (2016).
5. (ALICE Collaboration) B. Abelev *et al.*, “ $K^*(892)^0$ and $\phi(1020)$ production in Pb–Pb collisions at $\sqrt{s_{\text{NN}}} = 2.76$ TeV”, Phys. Rev. C 91, 024609 (2015).

6. (STAR Collaboration) J. Adams *et al.*, “K(892)* resonance production in Au+Au and p+p collisions at $\sqrt{s_{\text{NN}}} = 200$ GeV at STAR”, Phys. Rev. C 71, 064902 (2005).
7. (ALICE Collaboration) B. Abelev *et al.*, “Long-range angular correlations on the near and away side in p–Pb collisions at $\sqrt{s_{\text{NN}}} = 5.02$ TeV”, Phys. Lett. B 719, 29-41 (2013).
8. (ATLAS Collaboration), G. Aad *et al.*, “Observation of long-range elliptic anisotropies in $\sqrt{s} = 13$ TeV and 2.76 TeV pp collisions with the ATLAS detector”, arXiv:1509.04776 [hep-ex].
9. (CMS Collaboration) V. Khachatryan *et al.*, “Evidence for Collective Multiparticle Correlations in p–Pb Collisions”, Phys. Rev. Lett. 115, 012301 (2015).
10. (ALICE Collaboration) J. Adam *et al.*, “Enhanced production of multi-strange hadrons in high-multiplicity proton-proton collisions”, Nature Physics, 4111 (2017).

Publications in Refereed Journal

List of publication related to Thesis

Published

1. **$K^*(892)^0$ and $\phi(1020)$ meson production at high transverse momentum in pp and Pb–Pb collisions at $\sqrt{s_{NN}} = 2.76$ TeV***
ALICE Collaboration (J. Adam *et al.*), Phys. Rev. C **95**, 064606 (2017),
e-Print: arXiv:1702.00555 [nucl-ex].

Communicated

1. **Multiplicity dependence of light flavour hadron production in pp collisions at $\sqrt{s} = 7$ TeV***, ALICE Collaboration (J. Adam *et al.*), the paper draft is in the ALICE Collaboration review and it will be submitted to *Phys. Rev. C*.
2. **A transport model approach to study hadronic phase in heavy-ion collisions using K^{*0} and ϕ resonances***, Kishora Nayak *et al.*, the paper is submitted to *International Journal of Modern Physics E*.

Symposium and conference proceedings

1. **High transverse momentum resonance production in pp, p-Pb, Pb-Pb collisions at LHC***, Kishora Nayak (for the ALICE Collaboration), 7th International Conference on Physics and Astrophysics of Quark Gluon Plasma, VECC, Kolkata, India, February 1-6, 2015, PoS ICPAQGP **2015**, 092 (2017), <http://inspirehep.net/record/1623108>.

2. **Study of re-scattering effect on elliptic flow and production of resonances using AMPT***, Kishora Nayak *et al*, DAE-BRNS Symposium on Nuclear Physics, Thapar University Patiala, India, December 20-24, 2017, <http://sympnp.org/snp2017>.
3. **Multiplicity dependence of identified particle production in pp collisions with ALICE***, Kishora Nayak (for the ALICE Collaboration), 52nd Rencontres de Moriond QCD and High Energy Interaction, La Thule, Italy, 2017. The proceeding is published in web: <http://moriond.in2p3.fr> (2017).
4. **Light hadron production as function of multiplicity in pp collisions at $\sqrt{s} = 7$ TeV measured with ALICE***, Kishora Nayak (for the ALICE Collaboration), XXII DAE-BRNS High Energy Physics Symposium, India, 2016. The proceeding is submitted to *European Physics Journal C*.

List of analysis notes submitted to the ALICE Collaboration

1. **K^{*0} resonance production at high- p_T in Pb–Pb collisions at $\sqrt{s_{NN}} = 2.76$ TeV***, <https://aliceinfo.cern.ch/Notes/node/296>
2. **K^{*(892)}⁰ and $\phi(1020)$ production as a function of charged particle multiplicity in pp collisions at $\sqrt{s} = 7$ TeV***, <https://aliceinfo.cern.ch/Notes/node/426>

List of Publication as a part of the ALICE Collaboration

1. **“ Λ_c^+ production in pp collisions at $\sqrt{s} = 7$ TeV and in p-Pb collisions at $\sqrt{s_{NN}} = 5.02$ TeV”, S. Acharya *et al.*, (ALICE Collaboration), arXiv:1712.09581 [nucl-ex]**

2. **“Relative particle yield fluctuations in Pb-Pb collisions at $\sqrt{s_{\text{NN}}} = 2.76$ TeV”**, S. Acharya *et al.*, (ALICE Collaboration), arXiv:1712.07929 [nucl-ex]
3. **“Constraints on jet quenching in p-Pb collisions at $\sqrt{s_{\text{NN}}} = 5.02$ TeV measured by the event-activity dependence of semi-inclusive hadron-jet distributions”**, S. Acharya *et al.*, (ALICE Collaboration), arXiv:1712.05603 [nucl-ex]
4. **“First measurement of Ξ_c^0 production in pp collisions at $\sqrt{s} = 7$ TeV”**, S. Acharya *et al.*, (ALICE Collaboration), arXiv:1712.04242 [hep-ex],
5. **“Measurement of Z^0 -boson production at large rapidities in Pb-Pb collisions at $\sqrt{s_{\text{NN}}} = 5.02$ TeV”**, S. Acharya *et al.*, (ALICE Collaboration), arXiv:1711.10753 [nucl-ex]
6. **“Longitudinal asymmetry and its effect on pseudorapidity distributions in Pb-Pb collisions at $\sqrt{s_{\text{NN}}} = 2.76$ TeV”**, S. Acharya *et al.*, (ALICE Collaboration), arXiv:1710.07975 [nucl-ex]
7. **“Production of ^4He and $^4\overline{\text{He}}$ in Pb-Pb collisions at $\sqrt{s_{\text{NN}}} = 2.76$ TeV at the LHC”**, S. Acharya *et al.*, (ALICE Collaboration), arXiv:1710.07531 [nucl-ex]
8. **“Production of deuterons, tritons, ^3He nuclei and their anti-nuclei in pp collisions at $\sqrt{s} = 0.9, 2.76$ and 7 TeV”**, S. Acharya *et al.*, (ALICE Collaboration), arXiv:1709.08522 [nucl-ex]
9. **“Search for collectivity with azimuthal J/ψ -hadron correlations in high multiplicity p-Pb collisions at $\sqrt{s_{\text{NN}}} = 5.02$ and 8.16 TeV”**, S. Acharya *et al.*, (ALICE Collaboration), arXiv:1709.06807 [nucl-ex]

10. **“J/ψ elliptic flow in Pb-Pb collisions at $\sqrt{s_{\text{NN}}} = 5.02 \text{ TeV}$ ”**, S. Acharya *et al.*, (ALICE Collaboration), arXiv:1709.05260 [nucl-ex], Phys. Rev. Lett. **119**, no. 24, 242301 (2017)
11. **“Constraining the magnitude of the Chiral Magnetic Effect with Event Shape Engineering in Pb-Pb collisions at $\sqrt{s_{\text{NN}}} = 2.76 \text{ TeV}$ ”**, S. Acharya *et al.*, (ALICE Collaboration), arXiv:1709.04723 [nucl-ex],
12. **“The ALICE Transition Radiation Detector: construction, operation, and performance”**, S. Acharya *et al.*, (ALICE Collaboration), arXiv:1709.02743 [physics.ins-det], Nucl. Instrum. Meth. A **881**, 88 (2018)
13. **“Kaon femtoscopy in Pb-Pb collisions at $\sqrt{s_{\text{NN}}} = 2.76 \text{ TeV}$ ”**, S. Acharya *et al.*, (ALICE Collaboration), arXiv:1709.01731 [nucl-ex], Phys. Rev. C **96**, no. 6, 064613 (2017)
14. **“Systematic studies of correlations between different order flow harmonics in Pb-Pb collisions at $\sqrt{s_{\text{NN}}} = 2.76 \text{ TeV}$ ”**, S. Acharya *et al.*, (ALICE Collaboration), arXiv:1709.01127 [nucl-ex],
15. **“ π^0 and η meson production in proton-proton collisions at $\sqrt{s} = 8 \text{ TeV}$ ”**, S. Acharya *et al.*, (ALICE Collaboration), arXiv:1708.08745 [hep-ex],
16. **“Charged-particle multiplicity distributions over a wide pseudorapidity range in proton-proton collisions at $\sqrt{s} = 0.9, 7$, and 8 TeV ”**, S. Acharya *et al.*, (ALICE Collaboration), arXiv:1708.01435 [hep-ex], Eur. Phys. J. C **77**, no. 12, 852 (2017)
17. **“Measurement of deuteron spectra and elliptic flow in Pb-Pb collisions at $\sqrt{s_{\text{NN}}} = 2.76 \text{ TeV}$ at the LHC”**, S. Acharya *et al.*, (ALICE

- Collaboration), arXiv:1707.07304 [nucl-ex], Eur. Phys. J. C **77**, no. 10, 658 (2017)
18. **“Searches for transverse momentum dependent flow vector fluctuations in Pb-Pb and p-Pb collisions at the LHC”**, S. Acharya *et al.*, (ALICE Collaboration), arXiv:1707.05690 [nucl-ex], JHEP **1709**, 032 (2017)
 19. **“D-meson azimuthal anisotropy in mid-central Pb-Pb collisions at $\sqrt{s_{\text{NN}}} = 5.02 \text{ TeV}$ ”**, S. Acharya *et al.*, (ALICE Collaboration), arXiv:1707.01005 [nucl-ex],
 20. **“Measuring $K_S^0 K^\pm$ interactions using Pb-Pb collisions at $\sqrt{s_{\text{NN}}} = 2.76 \text{ TeV}$ ”**, S. Acharya *et al.*, (ALICE Collaboration), arXiv:1705.04929 [nucl-ex], Phys. Lett. B **774**, 64 (2017)
 21. **“Linear and non-linear flow modes in Pb-Pb collisions at $\sqrt{s_{\text{NN}}} = 2.76 \text{ TeV}$ ”**, S. Acharya *et al.*, (ALICE Collaboration), arXiv:1705.04377 [nucl-ex], Phys. Lett. B **773**, 68 (2017)
 22. **“J/ ψ production as a function of charged-particle pseudorapidity density in p-Pb collisions at $\sqrt{s_{\text{NN}}} = 5.02 \text{ TeV}$ ”**, D. Adamov *et al.*, (ALICE Collaboration), arXiv:1704.00274 [nucl-ex], Phys. Lett. B **776**, 91 (2018)
 23. **“Flow dominance and factorization of transverse momentum correlations in Pb-Pb collisions at the LHC”**, J. Adam *et al.*, (ALICE Collaboration), arXiv:1702.02665 [nucl-ex], Phys. Rev. Lett. **118**, no. 16, 162302 (2017)
 24. **“Azimuthally differential pion femtoscopy in Pb-Pb collisions at $\sqrt{s_{\text{NN}}} = 2.76 \text{ TeV}$ ”**, D. Adamova *et al.*, (ALICE Collaboration), arXiv:1702.01612 [nucl-ex], Phys. Rev. Lett. **118**, no. 22, 222301 (2017)

25. **“Production of muons from heavy-flavour hadron decays in p-Pb collisions at $\sqrt{s_{\text{NN}}} = 5.02$ TeV”**, S. Acharya *et al.*, (ALICE Collaboration), arXiv:1702.01479 [nucl-ex], Phys. Lett. B **770**, 459 (2017)
26. **“Production of π^0 and η mesons up to high transverse momentum in pp collisions at 2.76 TeV”**, S. Acharya *et al.*, (ALICE Collaboration), arXiv:1702.00917 [hep-ex], Eur. Phys. J. C **77**, no. 5, 339 (2017), [Eur. Phys. J. C **77**, no. 9, 586 (2017)]
27. **“First measurement of jet mass in Pb-Pb and p-Pb collisions at the LHC”**, S. Acharya *et al.*, (ALICE Collaboration), arXiv:1702.00804 [nucl-ex], Phys. Lett. B **776**, 249 (2018)
28. **“Measurement of D-meson production at mid-rapidity in pp collisions at $\sqrt{s} = 7$ TeV”**, S. Acharya *et al.*, (ALICE Collaboration), arXiv:1702.00766 [hep-ex], Eur. Phys. J. C **77**, no. 8, 550 (2017)
29. **“Energy dependence of forward-rapidity J/ψ and $\psi(2S)$ production in pp collisions at the LHC”**, S. Acharya *et al.*, (ALICE Collaboration), arXiv:1702.00557 [hep-ex], Eur. Phys. J. C **77**, no. 6, 392 (2017)
30. **“ $K^*(892)^0$ and $\phi(1020)$ meson production at high transverse momentum in pp and Pb-Pb collisions at $\sqrt{s_{\text{NN}}} = 2.76$ TeV”**, J. Adam *et al.*, (ALICE Collaboration), arXiv:1702.00555 [nucl-ex], Phys. Rev. C **95**, no. 6, 064606 (2017)
31. **“Production of $\Sigma(1385)^\pm$ and $\Xi(1530)^0$ in p-Pb collisions at $\sqrt{s_{\text{NN}}} = 5.02$ TeV”**, D. Adamova *et al.*, (ALICE Collaboration), arXiv:1701.07797 [nucl-ex], Eur. Phys. J. C **77**, no. 6, 389 (2017)

32. **“Insight into particle production mechanisms via angular correlations of identified particles in pp collisions at $\sqrt{s} = 7$ TeV”**, J. Adam *et al.*, (ALICE Collaboration), arXiv:1612.08975 [nucl-ex], Eur. Phys. J. C **77**, no. 8, 569 (2017)
33. **“Centrality dependence of the pseudorapidity density distribution for charged particles in Pb-Pb collisions at $\sqrt{s_{NN}} = 5.02$ TeV”**, J. Adam *et al.*, (ALICE Collaboration), arXiv:1612.08966 [nucl-ex], Phys. Lett. B **772**, 567 (2017)
34. **“W and Z boson production in p-Pb collisions at $\sqrt{s_{NN}} = 5.02$ TeV”**, J. Adam *et al.*, (ALICE Collaboration), arXiv:1611.03002 [nucl-ex], JHEP **1702**, 077 (2017)
35. **“Determination of the event collision time with the ALICE detector at the LHC”**, J. Adam *et al.*, (ALICE Collaboration), arXiv:1610.03055 [physics.ins-det], Eur. Phys. J. Plus **132**, no. 2, 99 (2017)
36. **“Measurement of the production of high- p_T electrons from heavy-flavour hadron decays in Pb-Pb collisions at $\sqrt{s_{NN}} = 2.76$ TeV”**, J. Adam *et al.*, (ALICE Collaboration), arXiv:1609.07104 [nucl-ex], Phys. Lett. B **771**, 467 (2017)
37. **“Evolution of the longitudinal and azimuthal structure of the near-side jet peak in Pb-Pb collisions at $\sqrt{s_{NN}} = 2.76$ TeV”**, J. Adam *et al.*, (ALICE Collaboration), arXiv:1609.06667 [nucl-ex], Phys. Rev. C **96**, no. 3, 034904 (2017)
38. **“Anomalous evolution of the near-side jet peak shape in Pb-Pb collisions at $\sqrt{s_{NN}} = 2.76$ TeV”**, J. Adam *et al.*, (ALICE Collaboration),

- arXiv:1609.06643 [nucl-ex], Phys. Rev. Lett. **119**, no. 10, 102301 (2017)
39. **“Measurement of electrons from beauty-hadron decays in p-Pb collisions at $\sqrt{s_{\text{NN}}} = 5.02$ TeV and Pb-Pb collisions at $\sqrt{s_{\text{NN}}} = 2.76$ TeV”**, J. Adam *et al.*, (ALICE Collaboration), arXiv:1609.03898 [nucl-ex], JHEP **1707**, 052 (2017)
 40. **“Jet-like correlations with neutral pion triggers in pp and central Pb-Pb collisions at 2.76 TeV”**, J. Adam *et al.*, (ALICE Collaboration), arXiv:1608.07201 [nucl-ex], Phys. Lett. B **763**, 238 (2016)
 41. **“ J/ψ suppression at forward rapidity in Pb-Pb collisions at $\sqrt{s_{\text{NN}}} = 5.02$ TeV”**, J. Adam *et al.*, (ALICE Collaboration), arXiv:1606.08197 [nucl-ex], Phys. Lett. B **766**, 212 (2017)
 42. **“Enhanced production of multi-strange hadrons in high-multiplicity proton-proton collisions”**, J. Adam *et al.*, (ALICE Collaboration), arXiv:1606.07424 [nucl-ex], Nature Phys. **13**, 535 (2017)
 43. **“Higher harmonic flow coefficients of identified hadrons in Pb-Pb collisions at $\sqrt{s_{\text{NN}}} = 2.76$ TeV”**, J. Adam *et al.*, (ALICE Collaboration), arXiv:1606.06057 [nucl-ex], JHEP **1609**, 164 (2016)
 44. **“Elliptic flow of electrons from heavy-flavour hadron decays at mid-rapidity in Pb-Pb collisions at $\sqrt{s_{\text{NN}}} = 2.76$ TeV”**, J. Adam *et al.*, (ALICE Collaboration), arXiv:1606.00321 [nucl-ex], JHEP **1609**, 028 (2016)
 45. **“ D -meson production in p-Pb collisions at $\sqrt{s_{\text{NN}}} = 5.02$ TeV and in pp collisions at $\sqrt{s} = 7$ TeV”**, J. Adam *et al.*, (ALICE Collaboration), arXiv:1605.07569 [nucl-ex], Phys. Rev. C **94**, no. 5, 054908 (2016)

46. **“Measurement of azimuthal correlations of D mesons and charged particles in pp collisions at $\sqrt{s} = 7$ TeV and p-Pb collisions at $\sqrt{s_{\text{NN}}} = 5.02$ TeV”**, J. Adam *et al.*, (ALICE Collaboration), arXiv:1605.06963 [nucl-ex], Eur. Phys. J. C **77**, no. 4, 245 (2017)
47. **“Pseudorapidity dependence of the anisotropic flow of charged particles in Pb-Pb collisions at $\sqrt{s_{\text{NN}}} = 2.76$ TeV”**, J. Adam *et al.*, (ALICE Collaboration), arXiv:1605.02035 [nucl-ex], Phys. Lett. B **762**, 376 (2016)
48. **“Correlated event-by-event fluctuations of flow harmonics in Pb-Pb collisions at $\sqrt{s_{\text{NN}}} = 2.76$ TeV”**, J. Adam *et al.*, (ALICE Collaboration), arXiv:1604.07663 [nucl-ex], Phys. Rev. Lett. **117**, 182301 (2016)
49. **“Measurement of transverse energy at midrapidity in Pb-Pb collisions at $\sqrt{s_{\text{NN}}} = 2.76$ TeV”**, J. Adam *et al.*, (ALICE Collaboration), arXiv:1603.04775 [nucl-ex], Phys. Rev. C **94**, no. 3, 034903 (2016)
50. **“Centrality dependence of charged jet production in p-Pb collisions at $\sqrt{s_{\text{NN}}} = 5.02$ TeV”**, J. Adam *et al.*, (ALICE Collaboration), arXiv:1603.03402 [nucl-ex], Eur. Phys. J. C **76**, no. 5, 271 (2016)
51. **“Centrality dependence of $\psi(2S)$ suppression in p-Pb collisions at $\sqrt{s_{\text{NN}}} = 5.02$ TeV”**, J. Adam *et al.*, (ALICE Collaboration), arXiv:1603.02816 [nucl-ex], JHEP **1606**, 050 (2016)
52. **“Measurement of D-meson production versus multiplicity in p-Pb collisions at $\sqrt{s_{\text{NN}}} = 5.02$ TeV”**, J. Adam *et al.*, (ALICE Collaboration), arXiv:1602.07240 [nucl-ex], JHEP **1608**, 078 (2016)
53. **“Particle identification in ALICE: a Bayesian approach”**, J. Adam *et*

- al.*, (ALICE Collaboration), arXiv:1602.01392 [physics.data-an], Eur. Phys. J. Plus **131**, no. 5, 168 (2016)
54. **“Anisotropic flow of charged particles in Pb-Pb collisions at $\sqrt{s_{\text{NN}}} = 5.02 \text{ TeV}$ ”**, J. Adam *et al.*, (ALICE Collaboration), arXiv:1602.01119 [nucl-ex], Phys. Rev. Lett. **116**, no. 13, 132302 (2016)
 55. **“Production of $K^* (892)^0$ and $\phi (1020)$ in p-Pb collisions at $\sqrt{s_{\text{NN}}} = 5.02 \text{ TeV}$ ”**, J. Adam *et al.*, (ALICE Collaboration), arXiv:1601.07868 [nucl-ex], Eur. Phys. J. C **76**, no. 5, 245 (2016)
 56. **“Multiplicity dependence of charged pion, kaon, and (anti)proton production at large transverse momentum in p-Pb collisions at $\sqrt{s_{\text{NN}}} = 5.02 \text{ TeV}$ ”**, J. Adam *et al.*, (ALICE Collaboration), arXiv:1601.03658 [nucl-ex], Phys. Lett. B **760**, 720 (2016)
 57. **“Multipion Bose-Einstein correlations in pp,p -Pb, and Pb-Pb collisions at energies available at the CERN Large Hadron Collider”**, J. Adam *et al.*, (ALICE Collaboration), arXiv:1512.08902 [nucl-ex], Phys. Rev. C **93**, no. 5, 054908 (2016)
 58. **“Multi-strange baryon production in p-Pb collisions at $\sqrt{s_{\text{NN}}} = 5.02 \text{ TeV}$ ”**, J. Adam *et al.*, (ALICE Collaboration), arXiv:1512.07227 [nucl-ex], Phys. Lett. B **758**, 389 (2016)
 59. **“Centrality dependence of the charged-particle multiplicity density at midrapidity in Pb-Pb collisions at $\sqrt{s_{\text{NN}}} = 5.02 \text{ TeV}$ ”**, J. Adam *et al.*, (ALICE Collaboration), arXiv:1512.06104 [nucl-ex], Phys. Rev. Lett. **116**, no. 22, 222302 (2016)

60. **“Charge-dependent flow and the search for the chiral magnetic wave in Pb-Pb collisions at $\sqrt{s_{\text{NN}}} = 2.76 \text{ TeV}$ ”**, J. Adam *et al.*, (ALICE Collaboration), arXiv:1512.05739 [nucl-ex], Phys. Rev. C **93**, no. 4, 044903 (2016)
61. **“High transverse momentum resonance production in Pb-Pb, pp and p-Pb collisions at LHC*”**, K. Nayak (ALICE Collaboration), PoS ICPAQGP **2015**, 092 (2017).
62. **“Measurement of an excess in the yield of J/ψ at very low p_{T} in Pb-Pb collisions at $\sqrt{s_{\text{NN}}} = 2.76 \text{ TeV}$ ”**, J. Adam *et al.*, (ALICE Collaboration), arXiv:1509.08802 [nucl-ex], Phys. Rev. Lett. **116**, no. 22, 222301 (2016)
63. **“Pseudorapidity and transverse-momentum distributions of charged particles in proton-proton collisions at $\sqrt{s} = 13 \text{ TeV}$ ”**, J. Adam *et al.*, (ALICE Collaboration), arXiv:1509.08734 [nucl-ex], Phys. Lett. B **753**, 319 (2016)
64. **“Inclusive quarkonium production at forward rapidity in pp collisions at $\sqrt{s} = 8 \text{ TeV}$ ”**, J. Adam *et al.*, (ALICE Collaboration), arXiv:1509.08258 [hep-ex], Eur. Phys. J. C **76**, no. 4, 184 (2016)
65. **“Charged-particle multiplicities in proton-proton collisions at $\sqrt{s} = 0.9 \text{ to } 8 \text{ TeV}$ ”**, J. Adam *et al.*, (ALICE Collaboration), arXiv:1509.07541 [nucl-ex], Eur. Phys. J. C **77**, no. 1, 33 (2017)
66. **“Measurement of electrons from heavy-flavour hadron decays in p-Pb collisions at $\sqrt{s_{\text{NN}}} = 5.02 \text{ TeV}$ ”**, J. Adam *et al.*, (ALICE Collaboration), arXiv:1509.07491 [nucl-ex], Phys. Lett. B **754**, 81 (2016)
67. **“Azimuthal anisotropy of charged jet production in $\sqrt{s_{\text{NN}}} = 2.76 \text{ TeV}$ ”**

- Pb-Pb collisions**", J. Adam *et al.*, (ALICE Collaboration), arXiv:1509.07334 [nucl-ex], Phys. Lett. B **753**, 511 (2016)
68. **"Direct photon production in Pb-Pb collisions at $\sqrt{s_{\text{NN}}} = 2.76$ TeV"**, J. Adam *et al.*, (ALICE Collaboration), arXiv:1509.07324 [nucl-ex], Phys. Lett. B **754**, 235 (2016)
69. **"Centrality evolution of the charged-particle pseudorapidity density over a broad pseudorapidity range in Pb-Pb collisions at $\sqrt{s_{\text{NN}}} = 2.76$ TeV"**, J. Adam *et al.*, (ALICE Collaboration), arXiv:1509.07299 [nucl-ex], Phys. Lett. B **754**, 373 (2016)
70. **"Measurement of D_s^+ production and nuclear modification factor in Pb-Pb collisions at $\sqrt{s_{\text{NN}}} = 2.76$ TeV"**, J. Adam *et al.*, (ALICE Collaboration), arXiv:1509.07287 [nucl-ex], JHEP **1603**, 082 (2016)
71. **"Multiplicity and transverse momentum evolution of charge-dependent correlations in pp, p-Pb, and Pb-Pb collisions at the LHC"**, J. Adam *et al.*, (ALICE Collaboration), arXiv:1509.07255 [nucl-ex], Eur. Phys. J. C **76**, no. 2, 86 (2016)
72. **"Transverse momentum dependence of D-meson production in Pb-Pb collisions at $\sqrt{s_{\text{NN}}} = 2.76$ TeV"**, J. Adam *et al.*, (ALICE Collaboration), arXiv:1509.06888 [nucl-ex], JHEP **1603**, 081 (2016)
73. **"Coherent $\psi(2S)$ photo-production in ultra-peripheral Pb Pb collisions at $\sqrt{s_{\text{NN}}} = 2.76$ TeV"**, J. Adam *et al.*, (ALICE Collaboration), arXiv:1508.05076 [nucl-ex], Phys. Lett. B **751**, 358 (2015)
74. **"Precision measurement of the mass difference between light nuclei**

- and anti-nuclei**", J. Adam *et al.*, (ALICE Collaboration), arXiv:1508.03986 [nucl-ex], Nature Phys. **11**, no. 10, 811 (2015)
75. **"Study of cosmic ray events with high muon multiplicity using the ALICE detector at the CERN Large Hadron Collider"**, J. Adam *et al.*, (ALICE Collaboration), arXiv:1507.07577 [astro-ph.HE], JCAP **1601**, no. 01, 032 (2016)
 76. **"Centrality dependence of pion freeze-out radii in Pb-Pb collisions at $\sqrt{s_{NN}} = 2.76$ TeV"**, J. Adam *et al.*, (ALICE Collaboration), arXiv:1507.06842 [nucl-ex], Phys. Rev. C **93**, no. 2, 024905 (2016)
 77. **"Event shape engineering for inclusive spectra and elliptic flow in Pb-Pb collisions at $\sqrt{s_{NN}} = 2.76$ TeV"**, J. Adam *et al.*, (ALICE Collaboration), arXiv:1507.06194 [nucl-ex], Phys. Rev. C **93**, no. 3, 034916 (2016)
 78. **"Elliptic flow of muons from heavy-flavour hadron decays at forward rapidity in Pb-Pb collisions at $\sqrt{s_{NN}} = 2.76$ TeV"**, J. Adam *et al.*, (ALICE Collaboration), arXiv:1507.03134 [nucl-ex], Phys. Lett. B **753**, 41 (2016)
 79. **"Production of light nuclei and anti-nuclei in pp and Pb-Pb collisions at energies available at the CERN Large Hadron Collider"**, J. Adam *et al.*, (ALICE Collaboration), arXiv:1506.08951 [nucl-ex], Phys. Rev. C **93**, no. 2, 024917 (2016)
 80. **" ϕ -meson production at forward rapidity in p-Pb collisions at $\sqrt{s_{NN}} = 5.02$ TeV and in pp collisions at $\sqrt{s} = 2.76$ TeV"**, J. Adam *et al.*, (ALICE Collaboration), arXiv:1506.09206 [nucl-ex], Phys. Lett. B **768**, 203 (2017)
 81. **"Centrality dependence of inclusive J/ψ production in p-Pb collisions**

- at $\sqrt{s_{\text{NN}}} = 5.02 \text{ TeV}$ ", J. Adam *et al.*, (ALICE Collaboration), arXiv:1506.08808 [nucl-ex], JHEP **1511**, 127 (2015)
82. **"Differential studies of inclusive J/ψ and $\psi(2S)$ production at forward rapidity in Pb-Pb collisions at $\sqrt{s_{\text{NN}}} = 2.76 \text{ TeV}$ ", J. Adam *et al.*, (ALICE Collaboration), arXiv:1506.08804 [nucl-ex], JHEP **1605**, 179 (2016)**
 83. **" ${}^3_{\Lambda}\text{H}$ and ${}^3_{\Lambda}\overline{\text{H}}$ production in Pb-Pb collisions at $\sqrt{s_{\text{NN}}} = 2.76 \text{ TeV}$ ", J. Adam *et al.*, (ALICE Collaboration), arXiv:1506.08453 [nucl-ex], Phys. Lett. B **754**, 360 (2016)**
 84. **"Forward-central two-particle correlations in p-Pb collisions at $\sqrt{s_{\text{NN}}} = 5.02 \text{ TeV}$ ", J. Adam *et al.*, (ALICE Collaboration), arXiv:1506.08032 [nucl-ex], Phys. Lett. B **753**, 126 (2016)**
 85. **"One-dimensional pion, kaon, and proton femtoscopy in Pb-Pb collisions at $\sqrt{s_{\text{NN}}} = 2.76 \text{ TeV}$ ", J. Adam *et al.*, (ALICE Collaboration), arXiv:1506.07884 [nucl-ex], Phys. Rev. C **92**, no. 5, 054908 (2015)**
 86. **"Search for weakly decaying $\overline{\Lambda n}$ and $\Lambda\Lambda$ exotic bound states in central Pb-Pb collisions at $\sqrt{s_{\text{NN}}} = 2.76 \text{ TeV}$ ", J. Adam *et al.*, (ALICE Collaboration), arXiv:1506.07499 [nucl-ex], Phys. Lett. B **752**, 267 (2016)**
 87. **"Centrality dependence of the nuclear modification factor of charged pions, kaons, and protons in Pb-Pb collisions at $\sqrt{s_{\text{NN}}} = 2.76 \text{ TeV}$ ", J. Adam *et al.*, (ALICE Collaboration), arXiv:1506.07287 [nucl-ex], Phys. Rev. C **93**, no. 3, 034913 (2016)**
 88. **"Centrality dependence of high- p_T D meson suppression in Pb-Pb collisions at $\sqrt{s_{\text{NN}}} = 2.76 \text{ TeV}$ ", J. Adam *et al.*, (ALICE Collaboration),**

- arXiv:1506.06604 [nucl-ex], JHEP **1511**, 205 (2015), Addendum: [JHEP **1706**, 032 (2017)]
89. **“Measurement of jet quenching with semi-inclusive hadron-jet distributions in central Pb-Pb collisions at $\sqrt{s_{\text{NN}}} = 2.76 \text{ TeV}$ ”, J. Adam *et al.*, (ALICE Collaboration), arXiv:1506.03984 [nucl-ex], JHEP **1509**, 170 (2015)**
 90. **“Measurement of charm and beauty production at central rapidity versus charged-particle multiplicity in proton-proton collisions at $\sqrt{s} = 7 \text{ TeV}$ ”, J. Adam *et al.*, (ALICE Collaboration), arXiv:1505.00664 [nucl-ex], JHEP **1509**, 148 (2015)**
 91. **“Inclusive, prompt and non-prompt J/ψ production at mid-rapidity in Pb-Pb collisions at $\sqrt{s_{\text{NN}}} = 2.76 \text{ TeV}$ ”, J. Adam *et al.*, (ALICE Collaboration), arXiv:1504.07151 [nucl-ex], JHEP **1507**, 051 (2015)**
 92. **“Measurement of pion, kaon and proton production in proton-proton collisions at $\sqrt{s} = 7 \text{ TeV}$ ”, J. Adam *et al.*, (ALICE Collaboration), arXiv:1504.00024 [nucl-ex], Eur. Phys. J. C **75**, no. 5, 226 (2015)**
 93. **“Coherent ρ^0 photoproduction in ultra-peripheral Pb-Pb collisions at $\sqrt{s_{\text{NN}}} = 2.76 \text{ TeV}$ ”, J. Adam *et al.*, (ALICE Collaboration), arXiv:1503.09177 [nucl-ex], JHEP **1509**, 095 (2015)**
 94. **“Rapidity and transverse-momentum dependence of the inclusive J/ψ nuclear modification factor in p-Pb collisions at $\sqrt{s_{\text{NN}}} = 5.02 \text{ TeV}$ ”, J. Adam *et al.*, (ALICE Collaboration), arXiv:1503.07179 [nucl-ex], JHEP **1506**, 055 (2015)**
 95. **“Measurement of dijet k_T in p-Pb collisions at $\sqrt{s_{\text{NN}}} = 5.02 \text{ TeV}$ ”,**

- J. Adam *et al.*, (ALICE Collaboration), arXiv:1503.03050 [nucl-ex], Phys. Lett. B **746**, 385 (2015)
96. **“Measurement of charged jet production cross sections and nuclear modification in p-Pb collisions at $\sqrt{s_{\text{NN}}} = 5.02 \text{ TeV}$ ”**, J. Adam *et al.*, (ALICE Collaboration), arXiv:1503.00681 [nucl-ex], Phys. Lett. B **749**, 68 (2015)
 97. **“Measurement of jet suppression in central Pb-Pb collisions at $\sqrt{s_{\text{NN}}} = 2.76 \text{ TeV}$ ”**, J. Adam *et al.*, (ALICE Collaboration), arXiv:1502.01689 [nucl-ex], Phys. Lett. B **746**, 1 (2015)
 98. **“Two-pion femtoscopy in p-Pb collisions at $\sqrt{s_{\text{NN}}} = 5.02 \text{ TeV}$ ”**, J. Adam *et al.*, (ALICE Collaboration), arXiv:1502.00559 [nucl-ex], Phys. Rev. C **91**, 034906 (2015)
 99. **“Forward-backward multiplicity correlations in pp collisions at $\sqrt{s} = 0.9, 2.76 \text{ and } 7 \text{ TeV}$ ”**, J. Adam *et al.*, (ALICE Collaboration), arXiv:1502.00230 [nucl-ex], JHEP **1505**, 097 (2015)
 100. **“Centrality dependence of particle production in p-Pb collisions at $\sqrt{s_{\text{NN}}} = 5.02 \text{ TeV}$ ”**, J. Adam *et al.*, (ALICE Collaboration), arXiv:1412.6828 [nucl-ex], Phys. Rev. C **91**, no. 6, 064905 (2015)
 101. **“Inclusive photon production at forward rapidities in proton-proton collisions at $\sqrt{s} = 0.9, 2.76 \text{ and } 7 \text{ TeV}$ ”**, B. B. Abelev *et al.*, (ALICE Collaboration), arXiv:1411.4981 [nucl-ex], Eur. Phys. J. C **75**, no. 4, 146 (2015)
 102. **“Charged jet cross sections and properties in proton-proton collisions at $\sqrt{s} = 7 \text{ TeV}$ ”**, B. B. Abelev *et al.*, (ALICE Collaboration), arXiv:1411.4969 [nucl-ex], Phys. Rev. D **91**, no. 11, 112012 (2015)

103. **“Production of inclusive $\Upsilon(1S)$ and $\Upsilon(2S)$ in p-Pb collisions at $\sqrt{s_{NN}} = 5.02$ TeV”**, B. B. Abelev *et al.*, (ALICE Collaboration), arXiv:1410.2234 [nucl-ex], Phys. Lett. B **740**, 105 (2015)
104. **“Event-by-event mean p_T fluctuations in pp and Pb-Pb collisions at the LHC”**, B. B. Abelev *et al.*, (ALICE Collaboration), arXiv:1407.5530 [nucl-ex], Eur. Phys. J. C **74**, no. 10, 3077 (2014)
105. **“Technical Design Report for the Upgrade of the ALICE Inner Tracking System”**, B. Abelev *et al.*, (ALICE Collaboration), J. Phys. G **41**, 087002 (2014).
106. **“Upgrade of the ALICE Experiment: Letter Of Intent”**, B. Abelev *et al.*, (ALICE Collaboration), J. Phys. G **41**, 087001 (2014).
107. **“Exclusive J/ψ photoproduction off protons in ultra-peripheral p-Pb collisions at $\sqrt{s_{NN}} = 5.02$ TeV”**, B. B. Abelev *et al.*, (ALICE Collaboration), arXiv:1406.7819 [nucl-ex], Phys. Rev. Lett. **113**, no. 23, 232504 (2014)
108. **“Multiplicity dependence of jet-like two-particle correlation structures in p-Pb collisions at $\sqrt{s_{NN}}=5.02$ TeV”**, B. B. Abelev *et al.*, (ALICE Collaboration), arXiv:1406.5463 [nucl-ex], Phys. Lett. B **741**, 38 (2015)
109. **“Production of $\Sigma(1385)^\pm$ and $\Xi(1530)^0$ in proton-proton collisions at $\sqrt{s} = 7$ TeV”**, B. B. Abelev *et al.*, (ALICE Collaboration), arXiv:1406.3206 [nucl-ex], Eur. Phys. J. C **75**, no. 1, 1 (2015)
110. **“Multiparticle azimuthal correlations in p -Pb and Pb-Pb collisions at the CERN Large Hadron Collider”**, B. B. Abelev *et al.*, (ALICE Collaboration), arXiv:1406.2474 [nucl-ex], Phys. Rev. C **90**, no. 5, 054901 (2014)

111. **“Elliptic flow of identified hadrons in Pb-Pb collisions at $\sqrt{s_{\text{NN}}} = 2.76$ TeV”**, B. B. Abelev *et al.*, (ALICE Collaboration), arXiv:1405.4632 [nucl-ex], JHEP **1506**, 190 (2015)
112. **“Suppression of $\Upsilon(1S)$ at forward rapidity in Pb-Pb collisions at $\sqrt{s_{\text{NN}}} = 2.76$ TeV”**, B. B. Abelev *et al.*, (ALICE Collaboration), arXiv:1405.4493 [nucl-ex], Phys. Lett. B **738**, 361 (2014)
113. **“Beauty production in pp collisions at $\sqrt{s} = 2.76$ TeV measured via semi-electronic decays”**, B. B. Abelev *et al.*, (ALICE Collaboration), arXiv:1405.4144 [nucl-ex], Phys. Lett. B **738**, 97 (2014)
114. **“Measurement of electrons from semileptonic heavy-flavor hadron decays in pp collisions at $\sqrt{s} = 2.76$ TeV”**, B. B. Abelev *et al.*, (ALICE Collaboration), arXiv:1405.4117 [nucl-ex], Phys. Rev. D **91**, no. 1, 012001 (2015)
115. **“Suppression of $\psi(2S)$ production in p-Pb collisions at $\sqrt{s_{\text{NN}}} = 5.02$ TeV”**, B. B. Abelev *et al.*, (ALICE Collaboration), arXiv:1405.3796 [nucl-ex], JHEP **1412**, 073 (2014)
116. **“Neutral pion production at midrapidity in pp and Pb-Pb collisions at $\sqrt{s_{\text{NN}}} = 2.76$ TeV”**, B. B. Abelev *et al.*, (ALICE Collaboration), arXiv:1405.3794 [nucl-ex], Eur. Phys. J. C **74**, no. 10, 3108 (2014)
117. **“Measurement of prompt D -meson production in $p - Pb$ collisions at $\sqrt{s_{\text{NN}}} = 5.02$ TeV”**, B. B. Abelev *et al.*, (ALICE Collaboration), arXiv:1405.3452 [nucl-ex], Phys. Rev. Lett. **113**, no. 23, 232301 (2014)
118. **“Transverse momentum dependence of inclusive primary charged-particle production in p-Pb collisions at $\sqrt{s_{\text{NN}}} = 5.02$ TeV”**, B. B. Abelev

- et al.*, (ALICE Collaboration), arXiv:1405.2737 [nucl-ex], Eur. Phys. J. C **74**, no. 9, 3054 (2014)
119. **“Azimuthal anisotropy of D meson production in Pb-Pb collisions at $\sqrt{s_{\text{NN}}} = 2.76 \text{ TeV}$ ”**, B. B. Abelev *et al.*, (ALICE Collaboration), arXiv:1405.2001 [nucl-ex], Phys. Rev. C **90**, no. 3, 034904 (2014)
120. **“Measurement of visible cross sections in proton-lead collisions at $\sqrt{s_{\text{NN}}} = 5.02 \text{ TeV}$ in van der Meer scans with the ALICE detector”**, B. B. Abelev *et al.*, (ALICE Collaboration), arXiv:1405.1849 [nucl-ex], JINST **9**, no. 11, P11003 (2014)
121. **“Freeze-out radii extracted from three-pion cumulants in pp, p-Pb and Pb-Pb collisions at the LHC”**, B. B. Abelev *et al.*, (ALICE Collaboration), arXiv:1404.1194 [nucl-ex], Phys. Lett. B **739**, 139 (2014)
- (* indicated papers are those on which this thesis is based.)

Contents

1	Introduction	1
1.1	A brief description of standard model	1
1.2	Quantum chromodynamics (QCD)	3
1.3	Quark gluon plasma (QGP)	5
1.3.1	Theoretical predictions of QGP	5
1.3.2	QCD Phase Diagram	7
1.4	Heavy-ion collisions	7
1.4.1	Resemblance to big bang	8
1.4.2	Evolution of fireball	8
1.4.3	Experimental heavy-ion facilities	12
1.5	Evidences of QGP formation	13
1.5.1	J/Ψ suppression	14
1.5.2	Strangness enhancement	15
1.5.3	Jet quenching	17
1.5.4	Elliptic flow and QGP	20
1.6	Thesis motivations	22
1.6.1	Resonance production in Pb-Pb collisions at LHC	22
1.6.2	Multiplicity dependence of resonance production in pp collisions at LHC	24

1.6.3	Elliptic flow of K^{*0} in Pb–Pb collisions at $\sqrt{s_{\text{NN}}} = 2.76$ TeV	25
1.6.4	A transport model study of hadronic phase in heavy-ion collisions using K^{*0} and ϕ	26
2	Experimental Setup and Analysis Framework	33
2.1	The Large Hadron Collider (LHC)	34
2.2	A Large Ion Collider Experiment (ALICE)	36
2.3	Central barrel detectors	37
2.3.1	The Inner Tracking System (ITS)	37
2.3.2	Time Projection Chamber (TPC)	38
2.3.3	Transition Radiation Detector (TRD)	40
2.3.4	Time Of Flight (TOF)	41
2.3.5	High Momentum Particle Identification (HMPID)	42
2.3.6	PHOton Spectrometer (PHOS)	42
2.3.7	Electro Magnetic Calorimeter (EMCAL)	43
2.3.8	ALICE Cosmic Ray Detector (ACORDE)	43
2.3.9	Muon Spectrometer	43
2.4	Forward detectors	44
2.4.1	VZERO (V0)	44
2.4.2	TZERO (T0)	45
2.4.3	Forward Multiplicity Detector (FMD)	45
2.4.4	Zero Degree Calorimeter (ZDC)	46
2.4.5	Photon Multiplicity Detector (PMD)	46
2.5	ALICE Online system	46
2.5.1	Trigger System (TRG)	47
2.5.2	High Level Trigger (HLT)	47

2.5.3	Detector and Experiment Control System	48
2.6	ALICE offline and Grid computing	48
2.7	Aliroot framework	49
3	Measurement of $K^*(892)^0$ resonance production in Pb-Pb collisions	
	at $\sqrt{s_{\text{NN}}} = 2.76$ TeV	57
3.1	Analysis details	58
3.1.1	Data sample	58
3.1.2	Offline event selection	58
3.1.3	Track and PID selection	61
3.1.4	Invariant mass reconstruction	62
3.1.5	Residual background	65
3.1.6	Yield extraction	66
3.1.7	Efficiency correction	67
3.2	Results	68
3.2.1	Invariant yield distribution of K^{*0}	68
3.2.2	dN/dy of K^{*0} -meson	69
3.2.3	$\langle p_T \rangle$ of K^{*0} -meson	71
3.2.4	p_T -integrated particle ratio	73
3.2.5	p_T -dependent particle ratio	74
3.2.6	Nuclear modification factor ($R_{\text{AA}}, R_{\text{CP}}$)	77
3.2.7	Systematic uncertainty study	82
3.2.8	Summary	86
3.3	Appendix	90
4	Multiplicity dependence of $K^*(892)^0$ resonance production in pp collisions at $\sqrt{s} = 7$ TeV	99

4.1	Analysis details	100
4.1.1	Data sets and event selection	100
4.1.2	Track cuts and particle identification	103
4.1.3	K^{*0} signal extraction	104
4.1.4	Reconstruction of combinatorial background	104
4.1.5	Residual background	104
4.1.6	K^{*0} raw yield	105
4.1.7	Acceptance \times Efficiency ($A \times \epsilon_{\text{rec}}$)	106
4.2	Results	107
4.2.1	p_T -spectra	107
4.2.2	dN/dy and $\langle p_T \rangle$	110
4.2.3	Particle ratios	114
4.3	Systematic uncertainty	116
4.3.1	Signal extraction	117
4.3.2	Mis-identification of particles	117
4.3.3	Track selection and analysis track cut variations	118
4.3.4	Material budget and hadronic interaction	118
4.3.5	Total systematic uncertainty	119
4.3.6	Multiplicity uncorrelated systematic uncertainties	121
4.4	Summary	124
4.5	Appendix	127
5	Elliptic flow of $K^{*}(892)^0$ in Pb–Pb collisions at $\sqrt{s_{\text{NN}}} = 2.76$ TeV	133
5.1	Data set and analysis cuts	134
5.2	Significance ($S/\sqrt{S+B}$) of K^{*0} signal	135
5.3	Anisotropic flow	135

5.3.1	Event plane resolution	138
5.4	Elliptic flow extraction method	141
5.4.1	Event plane method	141
5.4.2	Invariant mass fit method	143
5.4.3	Comparison of two methods	145
5.5	$K^{*0} v_2$	145
5.6	Systematic uncertainty study	149
5.7	Summary	154
6	A transport model study of hadronic phase in heavy-ion collisions using K^{*0} and ϕ	157
6.1	A Multi Phase Transport (AMPT) model	158
6.2	Results	160
6.2.1	Transverse Momentum Spectra	160
6.2.2	Elliptic Flow (v_2)	163
6.3	Summary	165
7	Summary	169

List of Tables

3.1	The total number of events analysed in various centralities and their corresponding average number of participant ($\langle N_{\text{part}} \rangle$) and average number of binary collisions ($\langle N_{\text{coll}} \rangle$) values in Pb–Pb collisions at $\sqrt{s_{\text{NN}}} = 2.76$ TeV [12].	59
3.2	The values of dN/dy , ratio to K^- and $\langle p_T \rangle$ for different centrality classes in Pb–Pb collisions at $\sqrt{s_{\text{NN}}} = 2.76$ TeV. In each entry, the first uncertainty is statistical and the second is systematic, excluding the normalization uncertainty. A third uncertainty is also given i.e normalization and uncorrelated uncertainty for dN/dy and K^{*0}/K^-	72
3.3	Systematic uncertainties in the yield of K^{*0} measurement for Pb–Pb collisions at $\sqrt{s_{\text{NN}}} = 2.76$ TeV. Where a constant value is given (global tracking efficiency), it is p_T independent. The values given in ranges are minimum and maximum uncertainties depending on p_T and centrality classes.	84
3.4	The values of $1/N_{\text{evn}} d^2N/(2\pi p_T dy dp_T)$ $(\text{GeV}/c)^{-2}$ with statistical and systematic uncertainties in different p_T bins for 0-5%, 5-10% and 10-20% centrality classes in Pb–Pb collisions at $\sqrt{s_{\text{NN}}} = 2.76$ TeV. . . .	91

3.5	The values of $1/N_{\text{evn}} d^2N/(2\pi p_T dy dp_T)$ (GeV/c) $^{-2}$ with statistical and systematic uncertainties in different p_T bins for 20-30%, 30-40% and 45-50% centrality classes in Pb–Pb collisions at $\sqrt{s_{\text{NN}}} = 2.76$ TeV.	91
4.1	The summary of different V0M multiplicity event classes (%) and their corresponding average number of charged particle multiplicity density with $\eta < 0.5$	102
4.2	The event counter loss correction, ϵ_{events} in different V0M multiplicity event classes for pp collisions at $\sqrt{s} = 7$ TeV.	109
4.3	The dN/dy and $\langle p_T \rangle$ of K^{*0} in different V0M multiplicity event classes (%) at mid-rapidity ($ \eta < 0.8$) for pp collisions at $\sqrt{s} = 7$ TeV. The first, second and third uncertainty represents the statistical, total systematic and uncorrelated systematic uncertainties, respectively.	111
5.1	The range of systematic uncertainties (%) for different centralities.	152
6.1	p_T integrated yield (dN/dy) of K^{*0} and ϕ for different τ_{HC} of hadronic phase.	163
6.2	Fraction of K^{*0} and ϕ re-scattered at different τ_{HC} of the hadronic phase.	163

Chapter 1

Introduction

This thesis deals with resonance production in high energy heavy-ion collisions at the Large Hadron Collider (LHC) facility. In order to understand the philosophy of the work presented in the thesis, we start with a brief description of Standard Model, Quantum Chromodynamics (QCD) and Quark Gluon Plasma (QGP) and its signatures. Subsequently, the motivation for carrying out various measurements related to resonance production in Pb–Pb and pp collisions at LHC are discussed.

1.1 A brief description of standard model

The **Quantum Mechanics** [1, 2] and **Special Theory of Relativity** [3] plays vital role in order to understand the standard model of particle physics as describe below.

The **Quark model** [4] in its modern form was developed by Murray Gell-Mann and he was awarded Nobel Prize in the year 1969. According to this model, hadrons (mesons and baryons) are composed of quarks and gluons. The baryon consists of three valence quarks¹ and mesons are composed of a valence quark and an anti-quark

¹Although, hadrons have sea quarks and gluons; it is the valence quark which determines their main properties.

pair. The ‘colour’ (red, blue, green) quantum number is assigned to both quarks and gluons; and gluons are of 8 different kinds. The gluons are the mediator of the strong interaction. This model also includes 6 flavours of quarks (up, down, charm, strange, top and bottom) which are found in nature.

The **Standard model** of particle physics is a theoretical attempt to explain the fundamental properties of matter and their interaction. A major contribution to the model was made by Glashow, Salam and Wienberg in 1970 [4, 5, 6]. A variety of experimental results has been remarkably explained by this model. According to this model, both the elementary fermions and quarks are classified in three families/generations each, as shown in Fig. 1.1. In the first generation of quark, the up (**u**) and down (**d**); charm (**c**) and strange (**s**) are included in second generation and in the third generation top (**t**) and bottom (**b**) quarks are placed. The leptons are also classified in a similar manner as that of the quarks. The fermions (having half odd integral spin quantum number) such as leptons and quarks have their corresponding anti-particle.

There are four fundamental forces in nature such as the **(i) Strong (ii) Weak (iii) Electromagnetic and (iv) Gravitational forces**. All the fundamental forces and their mediators, called gauge bosons, except gravitation and its mediator are included in the standard model of particle physics. The mediator of the strong and the electromagnetic forces are gluons (g) and photons (γ), respectively. Similarly, the weak and gravitational forces are mediated by W^\pm , Z^0 and graviton (yet to be discovered), respectively. All the gauge bosons which were discovered have spin 1 (g , γ , W^\pm , Z^0), except graviton (spin 2). In 1973 and 1983 both the gauge bosons Z^0 and W^\pm were discovered at CERN (European Organisation for Nuclear Research²), Geneva. These discoveries are remarkable as they were predicted to exist by the

²the abbreviation of “CERN” is **Conseil Européen pour la Recherche Nucléaire**, which is the old name in French

standard model [7, 8, 9]. In 2012, the ATLAS and the CMS Collaboration announced the discovery of a neutral boson whose mass is measured to be $125\text{--}126\text{ GeV}/c^2$ [10, 11]. This discovery is compatible with the standard model prediction [7, 8, 9] of existence of Higgs boson. Peter Higgs and Francois Englert were awarded Nobel Prize in the year 2013 for the theoretical prediction of the existence of this new boson.

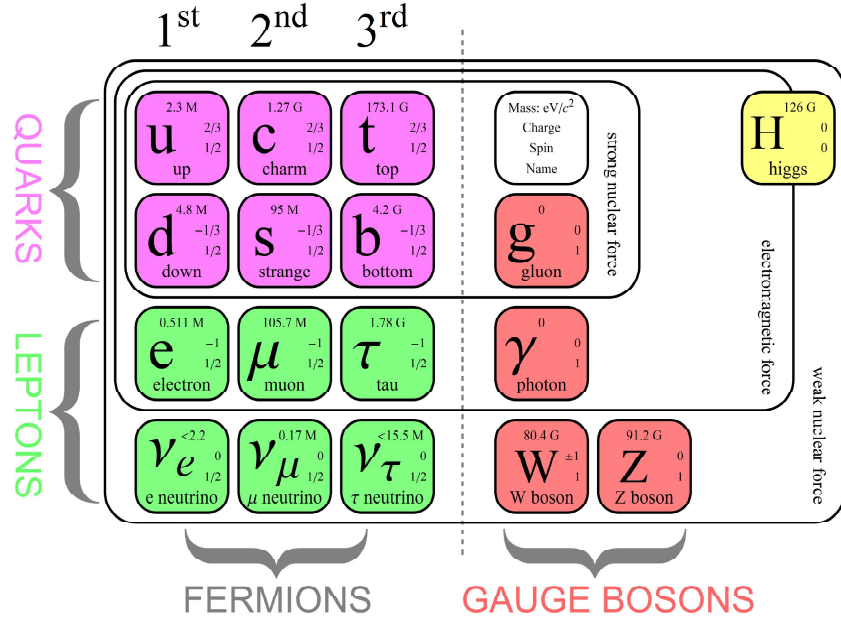


Figure 1.1: The schematic diagram of standard model of particle physics. Image:©Matic Lubej

1.2 Quantum chromodynamics (QCD)

The theory of strong interaction is called Quantum Chromodynamics (QCD) and it is a gauge theory of fields with $\text{SU}(3) \otimes \text{SU}(2) \otimes \text{U}(1)$ symmetry, where SU is the special unitary group. It describes the interaction among quarks and gluons having a colour quantum number, constituting the colourless hadrons. The self-interacting nature of gluon is unique in contrast to photon (whose theory is Quantum Electrodynamics, QED).

The QCD effective potential, well described by the so-called Cornell potential as given by Eq. 1.1,

$$V_{QCD}(r) = -\frac{4}{3} \frac{\alpha_S}{r} + kr \quad (1.1)$$

where α_S is the strong coupling constant and k is a constant called colour string tension. The α_S is also called as QCD running coupling constant as given in Eq. 1.2

$$\alpha_S(Q^2) = \frac{12\pi}{(33 - 2n_f)\ln(Q^2/\Lambda_{QCD}^2)}, \quad (1.2)$$

where, Q^2 is related to momentum transfer, n_f is the number of light flavoured quark having mass (m_q) $\ll Q$ and Λ_{QCD} is the QCD scale parameter corresponding to a α_S value. After the experimental confirmation of Eq. 1.2 which is plotted in Fig. 1.2; D. J. Gross, H. D. Politzer and F. Wilczek were awarded the Nobel Prize in 2004 for their theoretical contribution.

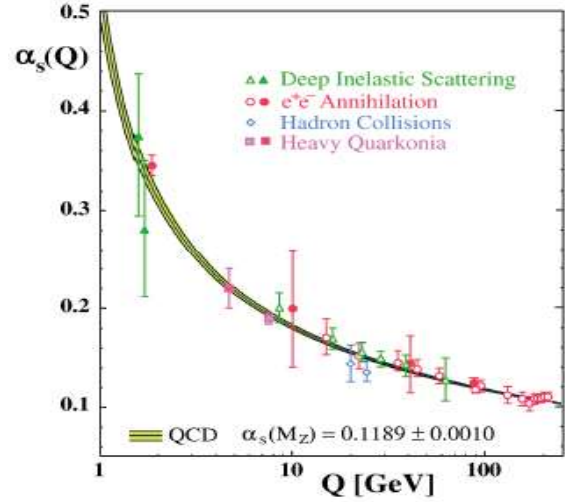


Figure 1.2: QCD running coupling as a function of momentum transfer having $\Lambda_{QCD} \approx 200$ MeV [12].

Eq. 1.2 reveals that when the Q^2 value is very small (in the normal world), the quark and gluon coupling is very strong and hence they are confined inside the hadrons and it is called **quark confinement**. On the other hand, for the process with high momentum transfer (large Q^2 value), the α_S value becomes small and the quarks and gluons behave as free particles in QCD vacuum. This property of QCD is

called **asymptotic freedom** and it leads to deconfinement of partons in high-density form of the matter because of large momentum transfer.

1.3 Quark gluon plasma (QGP)

As discussed in the section 1.2, the strong interaction becomes weaker with large momentum transfer or small distance between quarks and gluons leading to a state of free partons in the vacuum. The state of high momentum transfer and small distance between the partons can be achieved by compressing or heating normal hadronic matter. By the continuous process of heating or compressing, a transition from normal hadronic matter to a novel phase of matter composed of free quarks and gluons can be reached which is generally done in the fixed target or collider experiments [13, 14]. The new phase of matter formed is called **Quark Gluon Plasma (QGP)**.

1.3.1 Theoretical predictions of QGP

The QCD phase transition and equation of state is given by **Lattice-QCD** calculations [15, 16, 17, 18]. Lattice-QCD calculation for baryon chemical potential, (μ_B is the amount of energy required to add or remove a baryon from the system) $\mu_B = 0$ predicts the QCD phase transition from hadronic to partonic phase at $T_c \approx 170$ MeV with corresponding energy density (ε) of ~ 1 GeV/fm³ [17].

The theoretical lattice-QCD prediction of energy density scaled with the fourth power of temperature is given in Eq. 1.3, which is primarily dependent on the number of degrees of freedom. The calculation is done with massless quarks and gluons at zero chemical potential and at high-temperature limit [17].

$$\frac{\varepsilon_{SB}}{T^4} = [(N_c - 1) + \frac{7}{2}N_c N_f] \frac{\pi^4}{30}, \quad (1.3)$$

where ε_{SB} is the Stefan-Boltzmann energy density; N_c and N_f are the number of flavours and colours degrees of freedom, respectively.

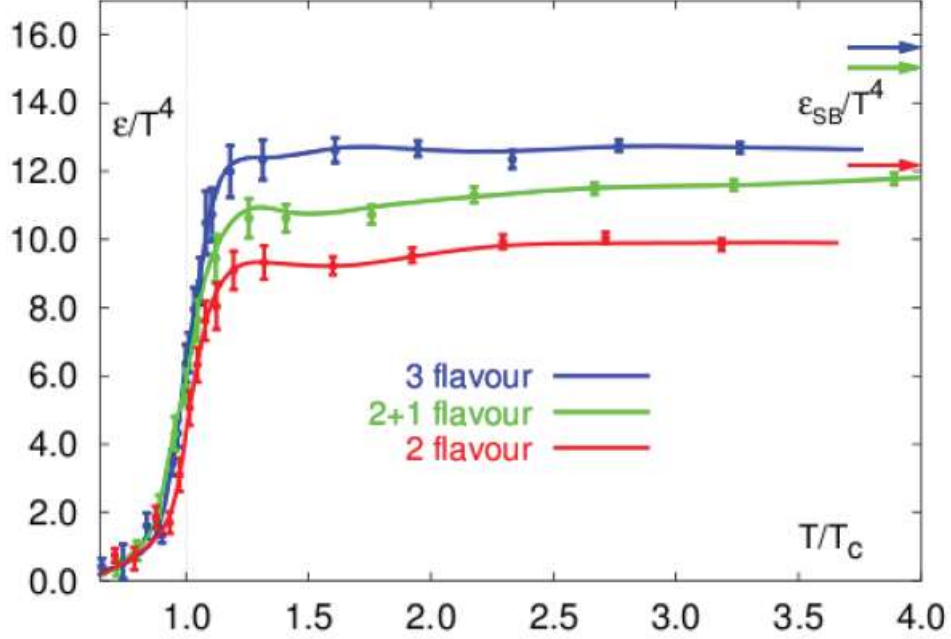


Figure 1.3: The equation of state predicted by lattice QCD for different flavours [15]. The arrows indicate the ideal Stefan-Boltzmann limit (Eq. 1.3).

Figure 1.4 shows the energy density normalised with the fourth power of temperature, which shows the transition from hadronic to partonic degrees of freedom at $T/T_c \sim 1$ with critical temperature, T_c , around 170 MeV. The equation of state shows three different behaviours depending on the temperature:

(i) $T < T_c$: Hadron degree of freedom is prominent and partons are confined inside the hadrons.

(ii) $T \approx T_c$: An abrupt rise is observed. This is an indication of change in the number of degrees of freedom (Eq. 1.3), similar behaviour is seen in phase transition,

(iii) $T > T_c$: Partons are deconfined meaning that the quarks and gluons can travel in a volume larger than the size of hadron. The saturation value depends on

the number of degrees of freedom.

1.3.2 QCD Phase Diagram

As discussed in the section 1.3.1, lattice-QCD predicts a transition from hadronic to partonic medium about the temperature of 170 MeV. At LHC energies the transition is a crossover.

Figure 1.4 shows a schematic diagram of hadronic to phase transition. The solid line indicates the QCD phase boundary with **first order** phase transition and the end point is indicated by the presence of the **critical point** followed by **cross over** at very high temperature and nearly zero baryonic chemical potential (μ_B). The Quark-Gluon-Plasma is believed to be formed in the early stages of the universe, a few microsecond after the **Big Bang** which is discussed below.

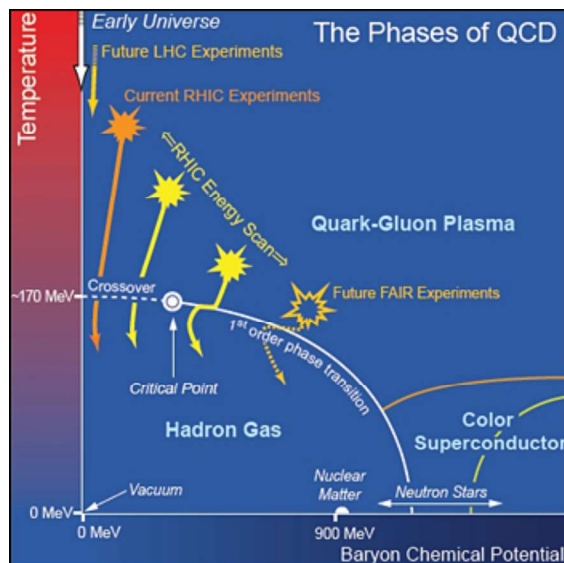


Figure 1.4: Schematic QCD phase diagram of nuclear matter [18, 19]. The phase boundaries for different phases are indicated by solid lines.

1.4 Heavy-ion collisions

The early universe scenario after the Big Bang corresponds to low $\mu_B = 0$ and high-temperature region in the QCD phase diagram as shown in Fig. 1.4.

1.4.1 Resemblance to big bang

According to the Big Bang Model [20], the universe was filled with free quarks and gluons (partons) after the electro-weak transition ($\sim 10^{-11}$ s) after the Big Bang. Due to the expansion, temperature decreases and at $t \approx 10^{-4}$ s after Big Bang, the critical temperature T_c is reached when the transition from deconfined phase to the hadronic phase took place. The present-day Universe was created after a long evolution from hadronic phase. In other words, one could say that today's Universe was determined in $t \leq 10^{-4}$ s after the Big Bang, where quark and gluons constituted the Universe. A comprehensive study of the deconfined phase is a need of present time not only to understand the properties of strongly interacting matter but also to track back the Universe just after the Big Bang. A schematic diagram depicting the evolution of the Universe is given in the Fig. 1.5.

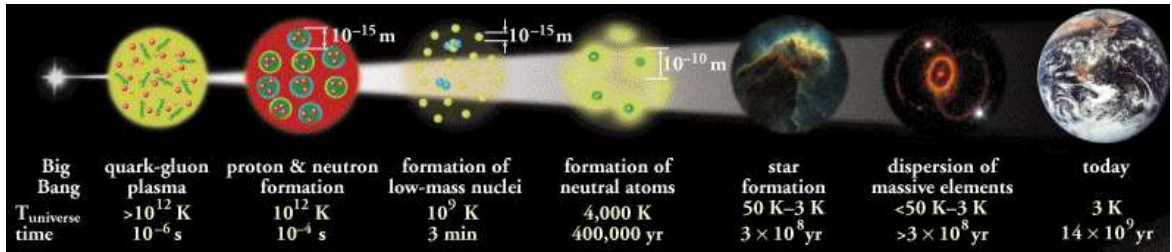


Figure 1.5: Schematic diagram representing the evolution of the Universe [20].

1.4.2 Evolution of fireball

It is possible to find the deconfinement phase of matter with $T > T_c \simeq 170$ MeV in the laboratory by **Ultra-Relativistic Heavy-Ion Collisions**. The final state observables carry the information from each step of the collisions.

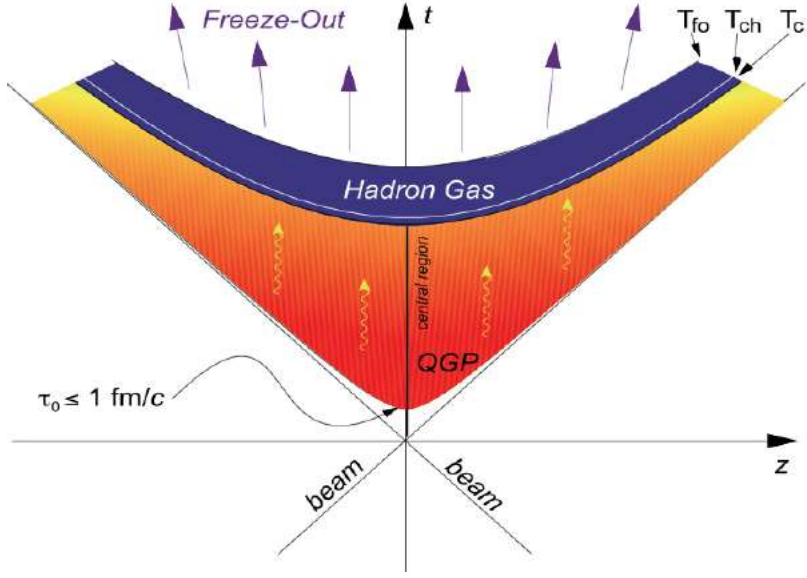


Figure 1.6: Space time evolution of heavy-ion collisions [21].

The heavy-ion nuclei are accelerated in the opposite direction towards each other with ultra-relativistic speed due to which these are Lorentz contracted along the beam direction. At time $t = 0$, the nuclei collide and in the overlap region, the interaction starts developing. As soon as the nuclei collide, inelastic interaction among partons starts by losing the kinetic energy. The loss of kinetic energy comes out in the form of matter, which is created in the vicinity of the collisions and it is commonly known as the **fireball**. The QGP is formed when the fireball is hot and dense enough. The space-time evolution of heavy-ion collision is depicted in Fig. 1.6. Due to the high energy density and pressure gradient, the fireball expands and cools down; at a temperature called critical temperature (T_c), quarks and gluons form hadrons as shown in Fig. 1.6. Subsequently, the hadron gas expands and at a temperature called **chemical freeze-out** (T_{ch}), all the inelastic collision ceases and henceforth the chemical composition of the system (different kinds of particle number) remains the same. Further expansion takes place and at **kinetic freeze-out** (T_{kin}) temperature,

all the elastic collisions stop as the distance among the constituent particles of the system is larger than their mean free path. Finally, the particles come out of the system and fall on the detector which are detected for physics analysis.

1.4.2.1 Collision geometry

Let us consider the collision of two heavy-ions with non-zero impact parameter, \vec{b} , (perpendicular distance between the centre of two nuclei) as shown in the Fig. 1.7. The reaction plane of collision is formed between impact parameter and the beam direction (z-axis in laboratory frame). The angle made by reaction plane with the x-axis is called reaction plane angle (Ψ_R).

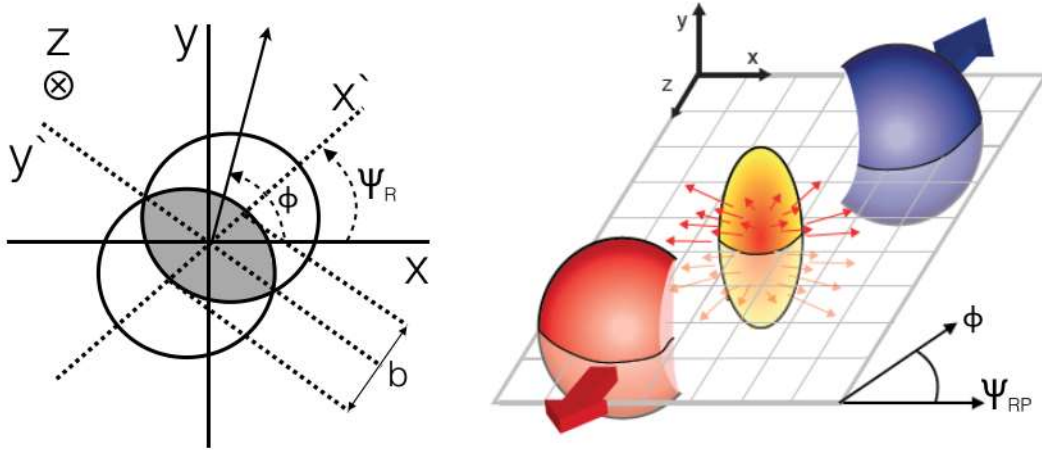


Figure 1.7: Heavy-ion collision geometry in two-dimension (left panel) and three-dimension (right panel).

The nuclear collisions are classified in different centrality classes according to the impact parameter length i.e $|\vec{b}| = 0$ corresponds to central collisions and $|\vec{b}| \simeq R_A + R_B$ (R_A and R_B are the radius of incoming nuclei) are classified as peripheral collisions. The impact parameter of a collision can not be measured directly in an experiment and hence the charged particle multiplicities (number of particles produced in an event) are considered for the centrality selection.

1.4.2.2 Observables and collective flow

One of the fundamental observable in high energy heavy-ion collisions is invariant yield. The invariant yield is defined in Eq. 1.4.

$$E \frac{d^3N}{dp^3} = \frac{1}{N_{\text{event}}} \times \frac{1}{2\pi p_T} \times \frac{d^2N}{dy dp_T} \quad (1.4)$$

where N_{events} is the number of events, $p_T = \sqrt{p_x^2 + p_y^2}$ is the transverse momentum.

$$\text{Rapidity } y = \frac{1}{2} \ln \left(\frac{E + p_z}{E - p_z} \right); \quad \text{Pseudo-rapidity } \eta = -\ln \left[\tan \left(\frac{\theta}{2} \right) \right]; \quad (1.5)$$

where E and θ are the energy and angle made by the particle w.r.t. z-axis (beam direction), respectively.

Let's consider a non-central collision as shown in Fig. 1.7. After the collision, an anisotropic fireball is created and the invariant yield of final state particles can be written in terms of a Fourier expansion (Eq. 1.6) relative to the reaction plane (Ψ_r).

$$E \frac{d^3N}{dp^3} = \frac{1}{2\pi p_T} \frac{d^2N}{dp_T dy} \left[1 + \sum_{n=1}^{\infty} 2v_n \cos[n(\Phi - \Psi_r)] \right] \quad (1.6)$$

where Φ is the azimuthal angle of the particle. Due to the symmetric nature of fireball with respect reaction plane, the sine term vanishes. The n^{th} order Fourier coefficient is given by Eq. 1.7

$$v_n = \langle \cos[n(\Phi - \Psi_r)] \rangle \quad (1.7)$$

The first order co-efficient, v_1 , is called directed flow and it is related to the overall shift of the particle distribution in the transverse plane. The second order coefficient, v_2 , is called elliptic flow and it explains the anisotropic azimuthal distribution of final

state particles.

1.4.3 Experimental heavy-ion facilities

The heavy-ion experimental facility of very first kind had started at the Berkeley Bevalac (USA) in 1971 [22]. After that, several experiments started operating at various facilities around the globe as given below.

- **1987–1994:** The **AGS (Alternating Gradient Synchrotron)** of BNL (Brookhaven National Laboratory) a fixed target heavy-ion collisions facility started with $\sqrt{s_{\text{NN}}} < 14.2$ GeV.
- **1986–2003:** The CERN/**SPS (Super Proton Synchrotron)** heavy-ion collisions facility, which was also a fixed target experiment started with $\sqrt{s_{\text{NN}}} \sim 19$ GeV.
- **1994–2003:** In the **SPS**, fixed target experiments have been operated (Pb nuclei accelerated up to $\sqrt{s_{\text{NN}}} \sim 17$ GeV).
- **2000–now:** The **RHIC (Relativistic Heavy Ion Collider)** at the BNL collides Au–Au, Cu–Cu *etc.* nuclei up to $\sqrt{s_{\text{NN}}} = 200$ GeV. The four experiments: PHENIX, STAR, BRAHMS, PHOBOS were developed at this facility, but now the only one that STAR is operational.
- **2009–now:** The **LHC (Large Hadron Collider)** at CERN starts experimental activity in 2009 and delivered Pb–Pb collisions at $\sqrt{s_{\text{NN}}} = 2.76$ TeV in 2010 (~ 14 times larger energy reached as compared to RHIC). This facility opens a new era for studying the properties of strongly interacting matter under extreme energy and density.

Along with the above mentioned experimental facilities, there are also ongoing lower energy heavy-ion programs. The SIS (SchwerIonen Synchrotron) facility located at GSI (Gesellschaft für Forschung SchwerIonen) which can accelerate heavy-ions at a maximum energy of about 2 AGeV and NICA experiment at Dubna is in preparation. These experiments are primarily dedicated to QCD phase transition study at high baryon chemical potential (μ_B) and low temperature (T) regions.

1.5 Evidences of QGP formation

The biggest QCD factory in the world, the LHC, brought a revolution in heavy-ion physics by colliding Pb–Pb ions at $\sqrt{s_{NN}} = 2.76$ TeV in the year 2010. The very first step to characterise the system produced in the heavy-ion collisions is to measure $\langle dN_{ch}/d\eta \rangle$ to estimate the energy density which is shown in the Fig. 1.8.

The energy density measured at SPS and RHIC are 3 GeV/fm³ and 5 GeV/fm³, respectively [5] and the corresponding value at LHC is 15-60 GeV/fm³ [5, 47]. So, the initial energy density at LHC is significantly higher than the SPS and RHIC.

The $\langle dN_{ch}/d\eta \rangle$ values measured at LHC is more than two times larger as compared to corresponding results from RHIC; the results from other experiments are also shown on the Fig. 1.8 [48]. There are abundant evidence of QGP formation in heavy-ion experiments at SPS, RHIC and LHC.

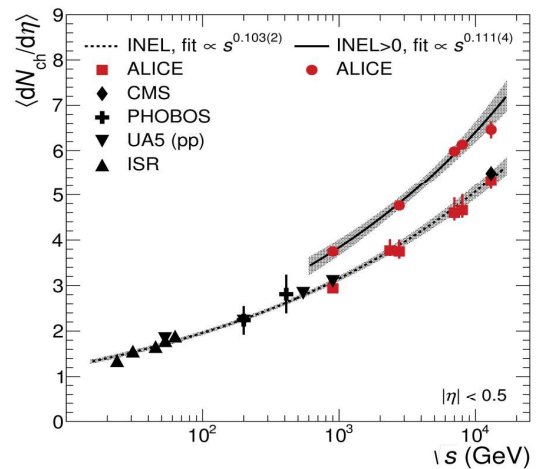


Figure 1.8: The pseudorapidity density of charged-particle measured in $|\eta| < 0.5$ as a function of \sqrt{s} [48].

In the following section, various signatures of QGP formation such as J/Ψ suppression, strangeness enhancement, jet quenching, *etc.* are discussed.

1.5.1 J/Ψ suppression

The bound state of heavy quark and anti-quark such as charmonium, $c\bar{c}$ (J/Ψ) is usually formed at the early stage of the collisions. So, the J/Ψ is an excellent probe to study the early dynamics of the medium formed in heavy-ion collisions. Theoretical calculation suggests that the production of J/Ψ in heavy-ion collisions (expected to have QGP) will be suppressed as compared to pp collisions (no medium formation) [23]. The J/Ψ production will be reduced in heavy-ion collisions if the QGP medium is formed as it will screen the colour charge of the quark. This is called Debye screening which inhibits the formation of $c\bar{c}$ pairs or J/Ψ state. The J/Ψ suppression in heavy-ion collisions is observed in SPS [24] and RHIC [25, 26] energies attributing to the QGP medium formation. Figure 1.9 shows the R_{AA} J/Ψ meson in Pb–Pb collisions at $\sqrt{s_{NN}} = 2.76$ TeV and 5.02 TeV as a function of centrality (represented as $\langle N_{part} \rangle$) measured in ALICE at LHC. The results are also compared with the corresponding measurement of Au–Au collisions at $\sqrt{s_{NN}} = 0.2$ TeV from the PHENIX collaboration at RHIC. The magnitude of J/Ψ R_{AA} measured at $\sqrt{s_{NN}} = 2.76$ TeV and 5.02 TeV is higher than the R_{AA} of 0.2 TeV for central collisions. This increase in the J/Ψ R_{AA} at LHC is attributed to the recombination of $c\bar{c}$ pairs to form the bound state of J/Ψ . As the lifetime of the fireball is longer for central collisions at higher energy ($\sqrt{s_{NN}} = 5.02$ TeV), so there is more $c\bar{c}$ pairs recombination and hence the suppression R_{AA} is less as compared to $\sqrt{s_{NN}} = 2.76$ TeV and 0.2 TeV.

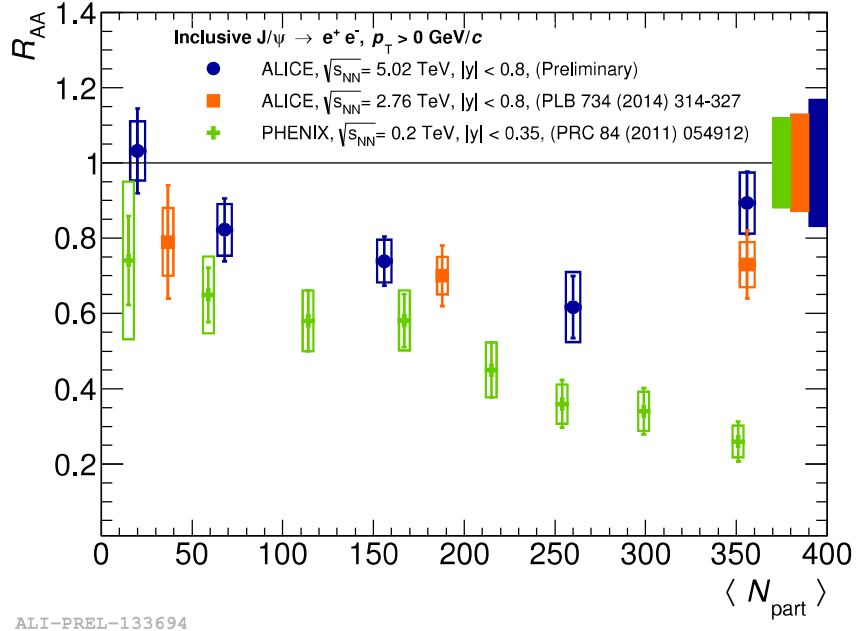


Figure 1.9: The R_{AA} of J/Ψ as function of centrality (represented as $\langle N_{\text{part}} \rangle$) in Pb-Pb collisions at $\sqrt{s_{NN}} = 2.76$ TeV and 5.02 TeV at ALICE and the corresponding measurement is compared with the PHENIX result of Au-Au collisions at $\sqrt{s_{NN}} = 0.2$ TeV.

1.5.2 Strangeness enhancement

The strange particle production is expected to give detail information about the formation and properties of QGP phase of hadronic matter produced in high energy nuclear collisions [29]. The net strangeness is zero before and after the collisions of pp or heavy-ions. So, there would be an abundant production of the strange particle if nucleus-nucleus collisions proceed via a de-confined QGP stage [4]. The formation of $s\bar{s}$ pair from the channel $q\bar{q} \rightarrow s\bar{s}$ and $g g \rightarrow s\bar{s}$ in QGP is more because of high gluon density and annihilation of light $q\bar{q}$ pairs than the pp collisions (where no QGP medium formation is expected [31]).

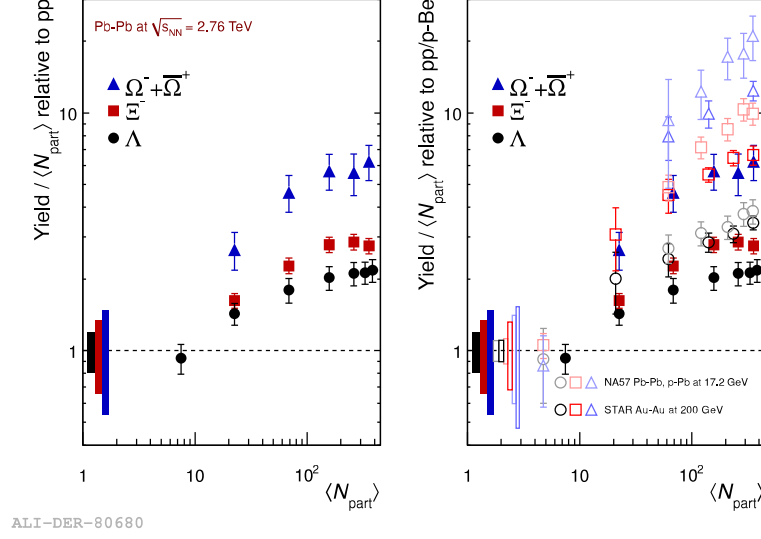


Figure 1.10: The yield of multi-strange hadrons in Pb-Pb relative to pp collisions measured in ALICE (left panel) and NA57, STAR (right panel) as function of centrality (express as average number of participant, $\langle N_{part} \rangle$) [32, 33, 34].

The enhancement factor (ϵ) is defined in the Eq. 1.8.

$$\epsilon = \frac{2}{\langle N_{part} \rangle} \left[\frac{dN(\text{Pb-Pb})}{dy} \Big|_{y=0} \Big/ \frac{dN(\text{pp})}{dy} \Big|_{y=0} \right] \quad (1.8)$$

The results in the Fig. 1.10 shows the yield of hyperons enhancement factor (Eq. 1.8) as a function of centrality (expressed by $\langle N_{part} \rangle$) measured by ALICE [32] and is compared with the corresponding measurement from STAR and NA57 collaboration [33, 34]. The observed abundant production of strange particle in Pb-Pb with respect to pp/p-Be collisions indicates the formation of de-confined state of matter in ALICE and also at RHIC and SPS energies. It is also observed that the enhancement factor is higher for particles containing more strange quark (s) i.e. $\epsilon(\Lambda) < \epsilon(\Xi) < \epsilon(\Omega)$ ³ which further confirms the QGP formation scenario.

³ ϵ is a measure of strangeness enhancement for strange particles.

1.5.3 Jet quenching

High- p_T (hard) partons are created early in the collisions carrying large energy. They lose energy while traversing in the QGP medium via interaction with soft partons in the medium [35]. This is called **quenching effect**. Due to this quenching, most of the parton energy is lost before fragmenting into hadron jets. This leads to decrease in hadron yield at high- p_T with respect to the situation where there is no quenching of energy of the partons. One of the experimental observable to measure the quenching effect is called **nuclear modification factor** (R_{AA}) as defined in Eq. 1.9.

$$R_{AA}(p_T) = \frac{1}{\langle T_{AA} \rangle} \times \frac{(d^2N/dydp_T)_{AA}}{(d^2\sigma/dydp_T)_{pp}}, \quad (1.9)$$

which is the ratio between the invariant yield in nuclear-nuclear collisions to that of pp collisions scaled with the average nuclear overlap function $\langle T_{AA} \rangle$ ($= \langle N_{\text{coll}} \rangle / \sigma_{\text{inel}}$; where $\langle N_{\text{coll}} \rangle$ and σ_{inel} are number of binary collisions and inelastic pp cross section, respectively). The unity value of R_{AA} suggests that the nuclear collisions are simply linear superposition of pp collisions and there is no QGP medium formation. However, any deviation from the unity value at high- p_T is an indication of medium formation.

On the left hand side of Fig. 1.11 shows the π^0 R_{AA} in central Pb–Pb collisions at $\sqrt{s_{NN}} = 2.76$ TeV measured in ALICE. The measurement is compared with the corresponding results from PHENIX and WA98 collaboration at various energies. There is a strong suppression of π^0 R_{AA} at high- p_T with magnitude less than unity in Pb–Pb collisions at $\sqrt{s_{NN}} = 2.76$ TeV. The magnitude of suppression at LHC ($\sqrt{s_{NN}} = 2.76$ TeV) is more as compared to PHENIX ($\sqrt{s_{NN}} = 200, 39, 62.4$ GeV) and WA98 ($\sqrt{s_{NN}} = 17.3$ GeV). This observation suggests that there is a strong parton energy loss and this indicates the presence of strongly interacting QGP matter at LHC and also at RHIC (PHENIX energies). However, with decrease in collisions en-

energy the magnitude of suppression also decreases. The R_{AA} value approaches to unity at high- p_T as observed by WA98 collaboration in Pb–Pb collisions at $\sqrt{s_{NN}} = 17.3$ GeV, where the formation of partonic medium is negligible. The right hand side of Fig. 1.11 shows the charge hadron nuclear modification factor in Pb–Pb (R_{PbPb}) and p–Pb (R_{pPb}) in different centre of mass energies and collisions centralities measured in ALICE. At high- p_T , there is a strong suppression of charge hadron R_{PbPb} for most central (0-5%) collisions as compared to peripheral Pb–Pb collisions at $\sqrt{s_{NN}} = 2.76$ TeV. However, the R_{pPb} value at high- p_T corresponds to unity indicating there is no medium formation in p–Pb collisions at $\sqrt{s_{NN}} = 5.02$ TeV in ALICE at LHC. The R_{AA} of K^{*0} resonance will be discussed in this thesis and also compared with other identified hadrons in Pb–Pb collisions at LHC energy.

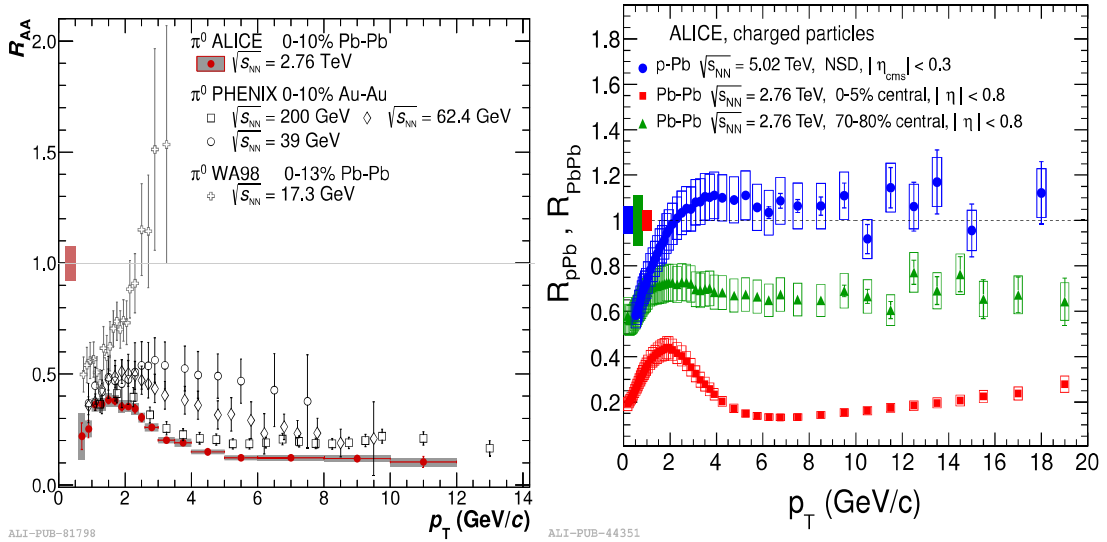


Figure 1.11: The R_{AA} of π^0 for central collisions measured by ALICE, PHENIX and WA98 collaboration in different centre of mass energies [36] (left panel). The charge hadron R_{PbPb} and R_{pPb} measured by ALICE collaboration in various collision centrality at $\sqrt{s_{NN}} = 2.76$ TeV and 5.02 TeV, respectively (right panel).

Figure 1.12 shows a schematic diagram of back to back jets (dijet) in pp (or e^-e^+) collisions where there is no expectation of any medium formation and the quenching of away side jets in A+A collisions (here the medium formation is expected).

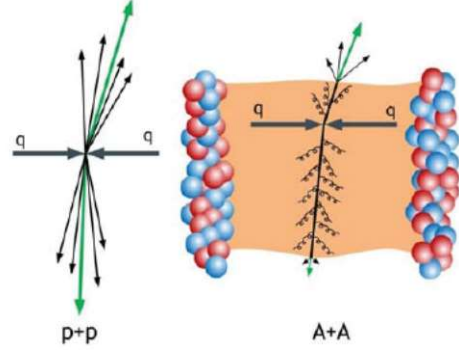


Figure 1.12: Back-to-back jets in pp and jet quenching in A-A [38]

Fig. 1.13 shows two particle azimuthal distribution of identified hadrons in pp, d-Au and Au-Au collisions. When there is no medium formation (pp, d-Au) the hard partons are produced back-to-back (Fig. 1.12) unlike the Au-Au where the medium is formed and away side jets are quenched inside the medium.

One trigger particle (high- p_T) which correspond to high peak side (right side of Fig. 1.13 is selected as the reference. The peak on the opposite side of the trigger particle gets suppress in Au-Au collisions because of the quenching; as partons losses energy while propagating inside the medium unlike in pp or d-Au collisions. It is another evidence of the medium formation in relativistic heavy-ion (Au-Au) collisions.

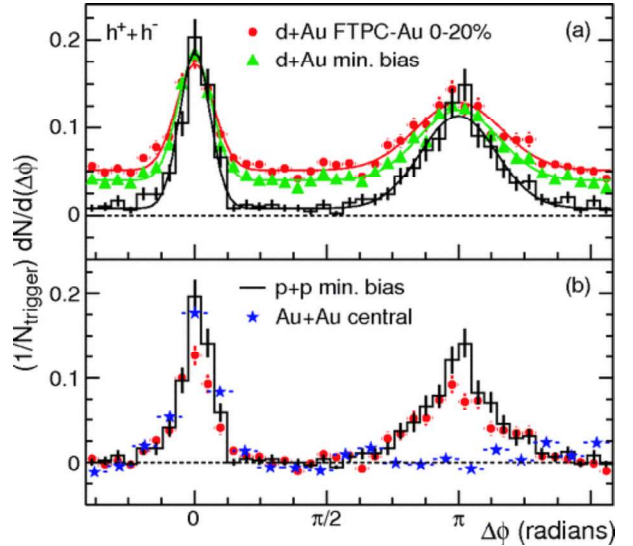


Figure 1.13: Back-to-back jets in pp and jet quenching in A-A [38]

1.5.4 Elliptic flow and QGP

Even though several phenomena shows evidence evident that the QGP is formed at RHIC and LHC energies still the properties of the medium need to be understood.

Elliptic flow is one of the important observable to understand the collective behaviour of the system and also sensitive to initial condition and degrees of freedom in the fireball. Figure 1.14 shows the v_2 scaled with the NCQ as a function of $(m_T - m_0)/n_q$ (where, $m_T = \sqrt{m_0^2 + p_T^2}$, m_0 is the rest mass) for different identified particle in minimum bias Au–Au at $\sqrt{s_{NN}} = 62.4$ GeV measured in STAR [12].

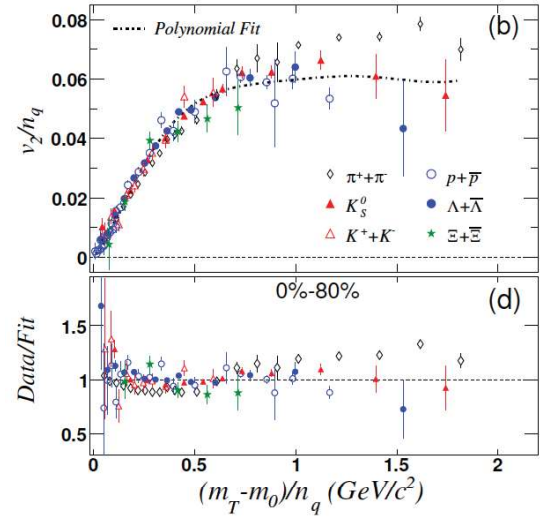
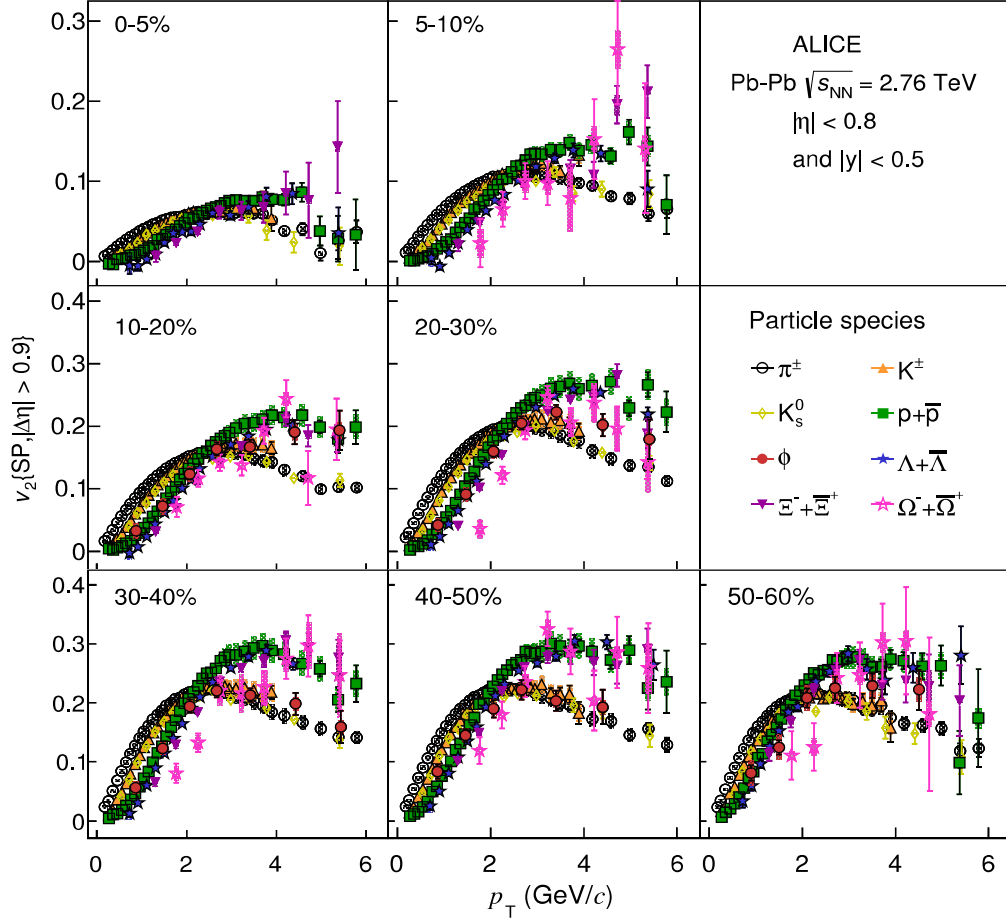


Figure 1.14: v_2/n_q versus $(m_T - m_0)/n_q$ of identified hadrons in Au–Au collisions at $\sqrt{s_{NN}} = 62.4$ GeV.

The polynomial curve is fitted to $v_2(p_T)$ of hadrons excluding pions. The number of constituent quark scaling is observed as the all v_2 ratios to fit function correspond to one suggesting hadron formation via quark coalescence. The NCQ scaling of v_2 is an evidence of the dominance of quark degrees of freedom in the early stage of the collisions when collective flow develops [40, 41, 42].

Figure 1.15 shows the v_2 as a function of p_T for various identified particles in different centralities for Pb–Pb collisions at $\sqrt{s_{NN}} = 2.76$ TeV. A clear mass ordering is observed in the low- p_T (< 3 GeV/ c) for all centralities. This observation is attributed to the interplay between radial and elliptic flow [44, 45]. At high- p_T (> 3 GeV/ c), particles tend to follow according to their type (baryon and meson). The deviation

from NCQ scaling at a level of $\pm 20\%$ is also observed at LHC [43].



ALI-PUB-82451

Figure 1.15: The v_2 as a function of p_T for identified hadrons in different centralities for Pb-Pb collisions at $\sqrt{s_{NN}} = 2.76$ TeV [43]

The properties of the QGP medium created at RHIC and LHC is far from complete understanding. Resonance particles can be used as a powerful tool to understand the QGP medium formed at RHIC and LHC, which will be discussed in the subsequent sections. Specifically, later in the thesis, the measurement of v_2 of the K^{*0} will be presented.

1.6 Thesis motivations

The various motivations of the thesis are described in the following sub-sections.

1.6.1 Resonance production in Pb-Pb collisions at LHC

Resonances by definition are very short-lived particle with lifetime $\tau \sim \text{fm}/c$ (10^{-23} s). The typical lifetime of the resonances which are measurable experimentally in heavy-ion collisions varies from 1 to 47 fm/c. The lifetime of the fireball created in Pb-Pb collisions at LHC is $\mathcal{O} \sim 10 \text{ fm}/c$ (Fig. 1.8).

The resonances can be used as an excellent probe for the study of system evolution in different time scale and to understand various in-medium phenomena. In this thesis, primarily K^{*0} resonance is studied in detail. It is a vector meson (spin 1) containing a strange quark and having lifetime, $\tau_{K^{*0}} = 4.16 \pm 0.05 \text{ fm}/c$ [51], which is comparable to the fireball created in Pb-Pb collisions [49]. Due to this short lifetime of K^{*0} , it decays to pion and kaon daughters inside the hadronic medium separated between chemical and kinetic freeze-out as shown in the Fig. 1.16.

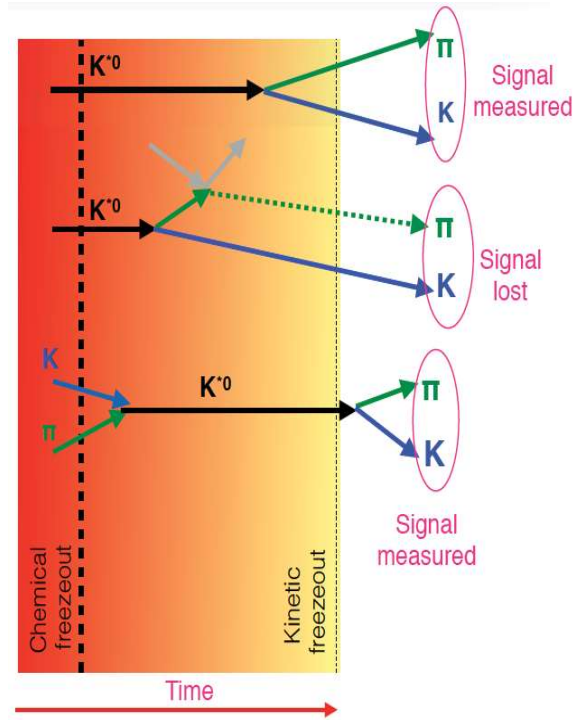


Figure 1.16: Schematic diagram showing chemical and kinetic freeze-out with possible pion and kaon interactions in the hadronic medium.

In this scenario, mainly three possible cases arise (i) K^{*0} decays inside the medium but the decay daughters remain unaffected by the medium particles, (ii) K^{*0} decays in the medium and the decay daughters interact with the medium particles which modified their momentum and (iii) in-medium pions and kaons interact among themselves to form the K^{*0} resonance state.

In the second case, the K^{*0} signal is **lost** from being observed in experiment because of the **re-scattering** of daughter particles which inhibits the parent K^{*0} reconstruction via invariant mass method. In the first and third scenario, the K^{*0} signal is measured. In the later case, the K^{*0} yield **increases** because of the **regeneration** from the in-medium pions and kaons interaction. The interplay of these two competing process (re-scattering and regeneration) interplay which affects the final measured K^{*0} yield. These processes mainly depend on the in-medium hadrons interaction cross sections, chemical and kinetic freeze-out time interval and source size [52, 53].

The re-scattering and regeneration effects can be disentangled and quantified by calculating the resonance to stable particle ratios (K^{*0}/K) in pp and AA collisions. The K^{*0}/K ratios are also compared to ϕ/K ratio because the K^{*0} and ϕ have similar masses and spin but very contrasting lifetimes i.e $\tau_\phi = 46.3 \pm 0.4 \text{ fm}/c$ [51] which is almost ten times larger as compared to K^{*0} . The precise measurement of these ratios reported in this thesis would provide the experimental evidence for the existence of hadronic in-medium (re-scattering, regeneration) phenomenon. There are evidence from the previous STAR experiment at RHIC and ALICE at LHC that re-scattering dominates over regeneration effect [54, 55]. Model calculation suggests that re-scattering effect is more dominant at low- p_T [55]. Hence, in this thesis, the p_T -dependent K^{*0}/K in pp and Pb–Pb collisions are calculated and compared with the corresponding measurement of ϕ/K ratios. The p_T -differential particle ratios like p/K^{*0} and p/ϕ ratios are also measured in order to understand the particle production

mechanism in various p_T -regions.

One of the important measurement to understand the parton energy loss at high- p_T (> 8 GeV/ c) is nuclear modification factor (R_{AA} , R_{CP}). As the K^{*0} contains strange (s) quark, it would be useful to study R_{AA} and R_{CP} to investigate the light flavour hadron energy loss in the medium. It also provides insight into the particle production mechanism, in-medium effects and medium density. The flavour, mass and type (baryon/meson) dependence of parton energy loss is predicted by various model calculation [56, 57, 58]. The measurement presented in this thesis will constrain the models dealing with the particle production mechanism, fragmentation process and parton energy loss in the medium formed in Pb–Pb collisions.

1.6.2 Multiplicity dependence of resonance production in pp collisions at LHC

The importance of small system (pp) study has become more interesting after LHC has taken data in p–Pb and pp collisions at very high energy with high multiplicity event collisions. One of the intriguing question that one must be seeking the answer to the physics mechanism possibility of collectivity in small systems at LHC energies. There are several theoretical predictions and the model calculation which suggests that collective features similar to heavy-ion collisions could be observed in a small system like pp collisions [59, 60, 61, 62]. Recent experimental observation from CMS, ATLAS and ALICE [63, 64, 65, 66, 67] revealed that there are substantial evidence that the small systems like pp and p–Pb collisions shows such features which are attributed to collectivity in Pb–Pb collisions.

In this thesis, a comprehensive study of the event charged particle multiplicity dependence of K^{*0} production by measuring the global observable like p_T -spectra is

performed. The yields of K^{*0} resonance is measured to investigate the presence of a collective phenomenon, hadronic in-medium effects like re-scattering and regeneration. The measurement of $\langle p_T \rangle$ in various multiplicity event classes would also provide information about the hardening of p_T -spectra indicating the dominance of radial flow effect in high multiplicity pp collisions at $\sqrt{s} = 7$ TeV.

1.6.3 Elliptic flow of K^{*0} in Pb–Pb collisions at $\sqrt{s_{NN}} = 2.76$ TeV

The primary focus of the ALICE at the LHC is to study the properties of the medium at an extreme condition of high temperature and density formed in the relativistic heavy-ion collisions. The number of constituent quark scaling (NCQ) scaling of elliptic flow (v_2) is a signature of collectivity developed in the initial stage of collisions. Experimentally measured v_2 in PHENIX at RHIC and ALICE at LHC shows the evidence of NCQ scaling violation [68, 69] of the order of 20%. The K^{*0} v_2 in Au–Au collisions at $\sqrt{s_{NN}} = 200$ GeV in the STAR experiment at RHIC has been measured [70, 71]. However larger uncertainties do not allow firmly to conclude whether NCQ scaling is followed by the K^{*0} v_2 .

The $v_2(p_T)$ measurement at low- p_T compared to hydrodynamic calculations, which shows that the elliptic flow is developed primarily in early partonic stage and then governed by QGP evolution [4]. However, the late hadronic in-medium like re-scattering phenomenon could also contribute to the development of v_2 [5, 6]. As there are experimental evidence which shows that K^{*0} gets affected by hadronic re-scattering, so it would be interesting to measure the K^{*0} $v_2(p_T)$ in order to understand the effect of re-scattering on K^{*0} v_2 . In this study, the measurement of K^{*0} v_2 in Pb–Pb collisions at $\sqrt{s_{NN}} = 2.76$ TeV has been carried out to test the NCQ scaling, understand par-

ticle production mechanism and study the effect of re-scattering and regeneration on $K^{*0} v_2$ at the LHC energies.

1.6.4 A transport model study of hadronic phase in heavy-ion collisions using K^{*0} and ϕ

In this part of the thesis, A Multi-phase Transport Model (AMPT) [74] study is performed to understand the elliptic flow and particle production mechanism of identified particles with a special focus on resonances (K^{*0} and ϕ). To describe the dynamics of heavy-ion collisions, the AMPT model uses HIJING (Heavy-Ion Jet INteraction Generator) for generating the initial conditions, Zhang's Parton Cascade (ZPC) model for partonic scatterings, the Lund string fragmentation or a quark coalescence model for hadronization. The hadronic matter interaction is described by a hadronic cascade based on a relativistic transport (ART) model. The analysis is performed to see the effect of hadronic in-medium effects (re-scattering and regeneration) on the observable presented here by varying hadronic cascade termination time (τ_{HC}) from 0.6 fm/c to 30 fm/c.

One of the primary conclusion of this thesis is the experimental observation of the hadronic re-scattering effect of K^{*0} resonance. Here, a model study is performed to understand the hadronic in-medium effects (re-scattering and regeneration) on K^{*0} and ϕ resonance elliptic flow (v_2) and p_{T} -spectra. The resonance flow result is also compared to corresponding measurements from other identified hadrons. The study is performed by using string-melting version of AMPT in Pb–Pb collisions at $\sqrt{s_{\text{NN}}} = 2.76$ TeV at mid-rapidity ($|y| < 1$) by varying the hadronic cascade time.

Bibliography

- [1] W. Heisenberg, Zeitschrift für Physik, 33 (1), 879–893, 06 (1925).
- [2] M. Born and P. Jordan, Zeitschrift für Physik, 34, 858-888, 09 (1925).
- [3] A. Einstein., Annalen der Physik, 17, 891 (1905).
- [4] S. L. Glashow, Nucl. Phys. 22, 579 (1961).
- [5] A. Salam and J.C. Ward, Phys. Lett. 13, 168 (1964).
- [6] S. Weinberg, Phys. Rev. Lett. 19, 1264 (1967).
- [7] P. W. Higgs, Phys. Lett. 12,132 (1964).
- [8] P. W. Higgs, Phys. Rev. Lett. 13, 508 (1964).
- [9] F. Englert and R. Brout, Phys. Rev. Lett. 13, 321 (1964).
- [10] (ATLAS Collaboration) G. Aad *et al.*, Phys. Lett. B 716, 1 (2012).
- [11] (CMS Collaboration) W. Adam *et al.*, Phys. Lett. B 716, 30 (2012).
- [12] H. D. Politzer, Phys. Rev. Lett. 30, 1346 (1973).
- [13] E. V. Shuryak, Phys. Repo. 61, 71-158 (1980).
- [14] (STAR Collaboration) J. Adam. *et al* Nucl. Phys. A 757, 102-183 (2005).

- [15] F. Karsch, Nucl. Phys. A 698, 199 (2002).
- [16] F. Karsch, Prog. Theor. Phys. Suppl. 153, 106 (2004).
- [17] R. C. Hwa, X. Wang, “Quark-Gluon Plasma”, vol. 3, World Scientific (2004).
- [18] R. V. Gavai and S. Gupta, Phys. Rev. D 71, 114014 (2005).
- [19] B. Mohanty, New Journal of Physics 13, 065031 (2011).
- [20] P. Coles and F. Lucchin, ”Cosmology: The Origin and Evolution of Cosmic Structure”, John Wiley And Sons Ltd. (2002).
- [21] J. D. Bjorken, Phys. Rev. D 27, 140-151 (1983).
- [22] H. A. Grunder *et al.*, <https://inspirehep.net/record/939281/files/HEACC77.I.324-341.pdf>.
- [23] T. Matsui and H. Satz, Phys. Lett. B 178, 416 (1986).
- [24] (NA60 Collaboration) R. Arnaldi *et al.*, Nucl. Phys., A 783, 261-268 (2007).
- [25] (PHENIX Collaboration) A. Adare *et al.*, Phys. Rev. Lett. 98, 232301 (2007).
- [26] (PHENIX Collaboration) A. Adare *et al.*, Phys. Rev. C 84, 054912 (2011).
- [27] (NA50 Collaboration) M. C. Abreu *et al.*, Phys. Lett., B 477, 28-36 (2000).
- [28] C. Spieles *et al.*, Phys. Rev. C 60, 054901 (1999).
- [29] P. Koch *et al.*, Phys. Rep. 142, 167-262 (1986).
- [30] J. Rafelski and B. Müller, Phys. Rev. Lett. 48, 1066 (1982).
- [31] P. Koch, B. Muller and J. Rafelski, Phys. Rept. 142, 167 (1986).

- [32] (ALICE Collaboration) B. Abelev *et al.*, Phys. Lett. B 728, 216 (2013), Erratum-
ibid. 734, 409-410 (2014); (ALICE Collaboration) B. Abelev *et al.*, Phys. Rev.
Lett. 111, 222301 (2013).
- [33] (STAR Collaboration) G. Agakishiev *et al.*, Phys. Rev. Lett. 108, 072301 (2012).
- [34] (NA57 Collaboration) K. F. Hetland *et al.*, J. Phys. G 28, 1607-1614 (2002).
- [35] J. D. Bjorken, FERMILABPUB-82-059-THY (1982).
- [36] S. S. Adler *et al.*, Phys. Rev. Lett. 91, 072301 (2003).
- [37] (STAR Collaboration) J. Adams *et al.*, Phys. Rev. Lett., 91, 072304 (2003).
- [38] [web link] <http://www.ellipsix.net/blog/tagged/heavy%20ion%20physics.html>
- [39] (STAR Collaboration) B. I. Abelev *et al.*, Phys. Rev. C 75, 054906 (2007).
- [40] Dénes Molnár and Sergei A. Voloshin, Phys. Rev. Lett. 91, 092301 (2003).
- [41] R.J Fries *et al.*, Phys. Rev. C 68, 044902 (2003).
- [42] R. C. Hwa and C. B. Yang, Phys. Rev. C 70, 024904 (2004).
- [43] (ALICE Collaboration) B. Abelev *et al.*, JHEP 06, 190 (2015).
- [44] S. A. Voloshin, Phys. Rev. C 55, R1630 (1996).
- [45] P. F Kolb *et al.*, Phys. Lett. B 503, 58 (2001).
- [46] (PHENIX Collaboration) K. Adcox *et al.*, Nucl. Phys. A 757, 184 (2005); J.
Schukraft, Pramana 57, 345-354 (2001); X. Zhang, [https://tel.archives-
ouvertes.fr/tel-00786269](https://tel.archives-ouvertes.fr/tel-00786269) (Ph.D Thesis).
- [47] Berndt Müller *et al.*, arXiv:1202.3233.

- [48] (ALICE Collaboration) J. Adam *et al.*, Phys. Lett. B 753, 319-329 (2016).
- [49] (ALICE Collaboration) K. Aamodt *et al.*, Phys. Lett. B 696, 328-337 (2011).
- [50] (ALICE Collaboration) K. Aamodt *et al.*, Phys. Lett. B 696, 328-337 (2011).
- [51] (Particle Data Group) Olive, K. A. and others, Chin. Phys. C 38, 090001 (2014).
- [52] G. Torrieri, J. Rafelski, Phys. Lett. B 509, 239-245 (2001).
- [53] C. M Ko, Phys. Rev. C 23, 2387 (1981).
- [54] (STAR Collaboration) J. Adams *et al.*, Phys. Rev. C 71, 064902 (2005).
- [55] (ALICE Collaboration) B. Abelev *et al.*, Phys. Rev. C 91, 024609 (2015).
- [56] R. Bellwied and C. Markert, Phys. Lett. B 691, 208 (2010).
- [57] W. Liu and R. J. Fries, Phys. Rev. C 77, 054902 (2008).
- [58] W. Liu, C. M. Ko, and B. W. Zhang, Phys. Rev. C 75, 051901 (2007).
- [59] S. K. Prasad *et al.*, Phys. Rev. C 82, 024909 (2010).
- [60] E. Avsar *et al.*, Nucl. Part. Phys. 38, 124053 (2011).
- [61] B. Schenke *et al.*, Phys. Rev. Lett. 117, 162301 (2016).
- [62] S. Schlichting *et al.*, arXiv:1611.00329 (2017).
- [63] (ALICE Collaboration) B. Abelev *et al.*, Phys. Lett. B 719, 29-41 (2013)
- [64] (ATLAS Collaboration) G. Aad *et al.*, Phys. Rev. Lett. 116, 172301 (2016).
- [65] (CMS Collaboration) V. Khachatryan *et al.*, Phys. Rev. Lett. 115, 012301 (2015).
- [66] (ALICE Collaboration) B. B. Abelev *et al.*, Phys. Lett. B 726, 164-177 (2013).

- [67] (ALICE Collaboration) B. B. Abelev *et al.*, Phys. Lett. B 728, 25-38 (2014).
- [68] (PHENIX Collaboration) A. Adare *et al.*, Phys. Rev. C 85, 064914 (2012).
- [69] (ALICE Collaboration) B. B. Abelev *et al.*, JHEP 1506, 190 (2015).
- [70] (STAR Collaboration) J. Adams *et al.*, Phys. Rev. C 71, 064902 (2005).
- [71] (STAR Collaboration) M. M. Aggarwal *et al.*, Phys. Rev. C 84, 034909 (2011).
- [72] (STAR Collaboration) J. Adams *et al.*, Nucl. Phys. A 757, 102 (2005).
- [73] T. Hirano *et al.*, Phys. Lett. B 636, 299-304(2006).
- [74] Zi-Wei Lin *et al.*, Phys. Rev. C 72, 064901 (2005).

Chapter 2

Experimental Setup and Analysis Framework

In the ultra-relativistic hadronic and heavy-ion collisions, sophisticated experimental apparatus are required not only to create high-energy collisions but also to reconstruct and identify the particles produced. The complex technology has been used for building the accelerator and detectors. The detectors present in the Large Hadron Collider (LHC) at CERN are the scientific-technological wonders of the 21st century.

In this chapter, different aspects of the ALICE detector system which are used for the data analysis presented in this thesis are described. In the Section 2.1, the LHC is introduced. A brief description of the ALICE sub-detectors are given in the Section 2.2, 2.3 and 2.4. The online and offline computing system of ALICE detector is described in the Section 2.5 and Section 2.6, respectively. The AliRoot framework is given in the Section 2.7.

2.1 The Large Hadron Collider (LHC)

The Large Hadron Collider (LHC) [1] is the world's largest particle accelerator. It is based at CERN (the CERN acronym represents in French as “Conseil Européen pour la Recherche Nucléaire or European Council for Nuclear Research”). It is an accelerator composed of two rings installed in an underground tunnel having a circumference of 26.7 km at a depth of about 100 m across Switzerland and France border.

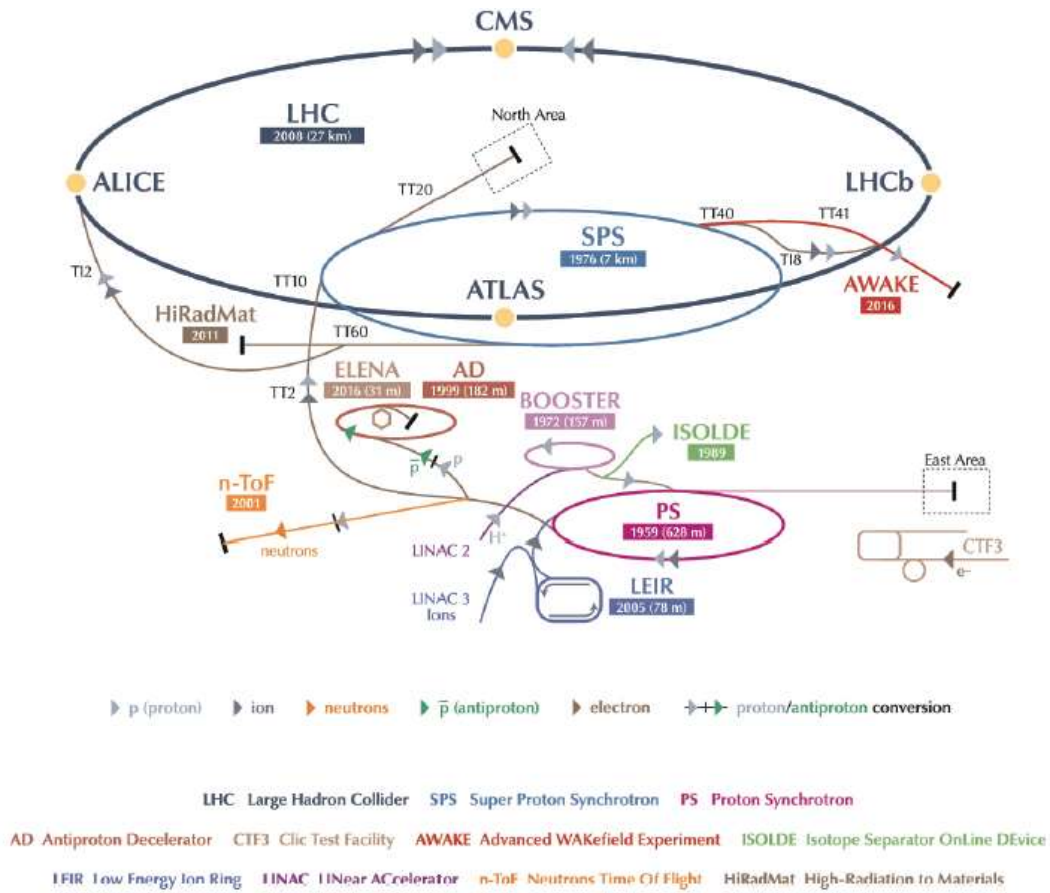


Figure 2.1: CERN accelerator complex showing the locations of the four main LHC experiments (ALICE, ATLAS, CMS and LHCb) around the LHC ring [2]

The schematic diagram of the LHC (CERN accelerator complex) is shown in

Fig. 2.1 [2]. The LHC facility consists of both nuclear and particle physics experiments having four main detectors named as ATLAS, CMS, LHCb and ALICE. ATLAS (A Toroidal LHC Apparatus) [3] and CMS (Compact Muon Solenoid) [4] are general purpose detectors. In the present scenario, the main purpose of these detectors are to search for Super Symmetric particles (SUSY), evidence of extra dimensions and characterisation of the recently discovered Higgs boson [5, 6], resonances, etc. LHCb (LHC beauty) [7] is a forward detector placed very close to the beam direction and is used for the study of CP violation in the b-quark sector. ALICE (A Large Ion Collider Experiment) [8, 9] is the only detector which is specifically designed to study evolution dynamics and characterisation of Quark Gluon Plasma (QGP).

As shown in Fig 2.1, the complex CERN accelerator system consists of various detectors and accelerators. Initially, the protons are accelerated in a linear accelerator (LINAC 2) which provides energy up to 50 MeV. From the LINAC 2, protons are injected into Proton Synchrotron Booster (PSB), then further acceleration takes place in Proton Synchrotron (PS). Before injecting to LHC ring, protons are accelerated in Super Proton Synchrotron (SPS) where the reach of energy is 450 GeV. Like protons, lead ions also follow the similar path, but these are accelerated through LINAC 3 and Low-Energy Ion Ring (LEIR) before being accelerated into PS. The energy reach is 177 GeV per nucleon before injecting them to LHC ring. The maximum centre of mass energy that can be reached in the LHC for proton beam is 14 TeV and heavy-ion up to 5.5 TeV per nucleon. More details about the ALICE detector is presented in the following sections.

2.2 A Large Ion Collider Experiment (ALICE)

ALICE is the only experiment at LHC which is optimised for the study of heavy-ion (Pb–Pb) collisions, in order to understand formation and evolution dynamics of the nuclear matter at high energy density and temperature. The dimension of ALICE detector is $16 \times 16 \times 26 \text{ m}^3$ and approximate weight is 10,000 t. The schematic diagram of ALICE detector is shown in Fig. 2.2.

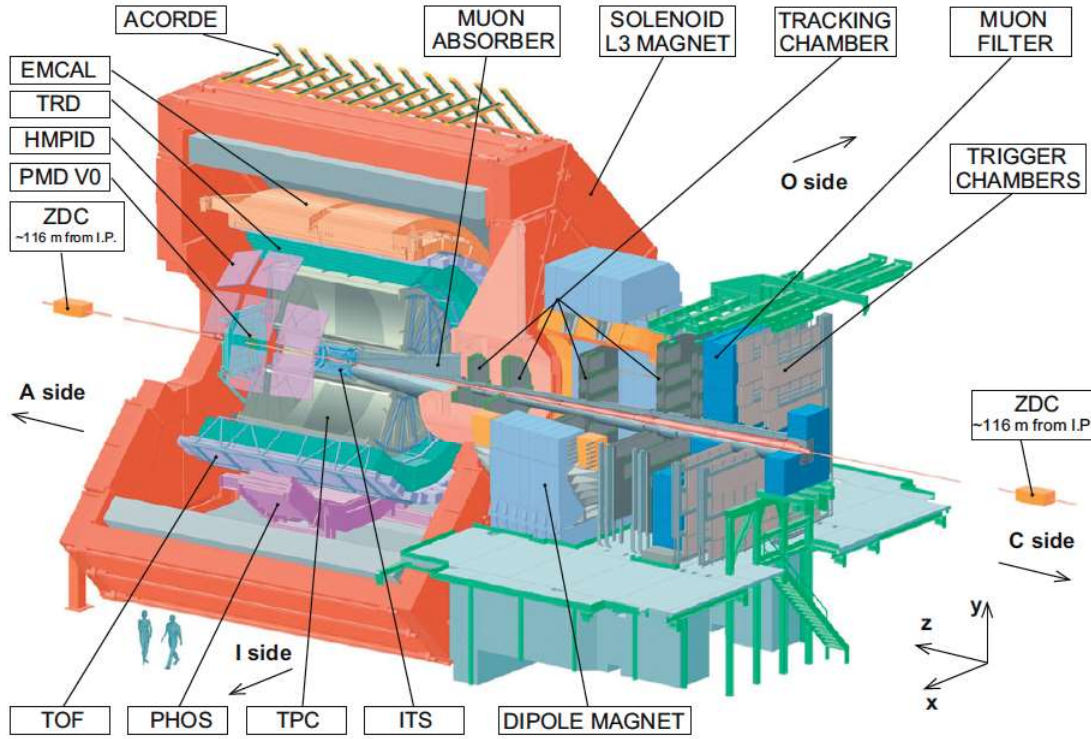


Figure 2.2: The schematic diagram of ALICE detector [10].

The coordinate system of ALICE is right-handed Cartesian system with origin $(x, y, z) = (0, 0, 0)$ at interaction point which is the nominally at centre of the detector. The three axes are orthogonal to each other where the horizontal x-axis is pointing towards the LHC centre, y-axis is vertically upward and z-axis is along the beam direction away from the muon arm (pointing left in Fig. 2.2). The polar angle,

θ , increases from +z to -z direction and the azimuthal angle, ϕ , is 0 along the +x direction and increases counter-clockwise passing through y-axis ($\pi/2$) and then back to x-axis.

A schematic diagram with most important sub-detector systems are given in Fig. 2.2. In the following section, a brief description of some of these detectors are given.

2.3 Central barrel detectors

2.3.1 The Inner Tracking System (ITS)

The Inner Tracking System (ITS) [11] is placed very close to interaction point around the beam pipe. The main purpose of ITS is to determine the primary, secondary vertices, particle identification and tracking of low-momentum particles. It is composed of six layers of silicon detector placed radially outward between 3.9 and 43 cm from the beam line. The first two layers are Silicon Pixel Detectors (SPD) followed by Silicon Drift Detectors (SDD) and Silicon Strip Detectors (SSD) [11] and each of these detectors are having two layers.

The SPD consists of two layers of silicon detector, placed very close to beam pipe in the pseudo-rapidity range $|\eta| < 2.0$. This is the inner most detector and the basic function is to determine primary and secondary vertices. It is also used as level-2 (L2) trigger [11]. It operates in the region where the radiation level is very high and the track density exceeds 50 tracks/cm². The SPD is basically two-dimensional reverse-biased silicon based p-n junction diode. Each cell on the detector matrix is connected via a solder ball to a cell of the same size on a front-end CMOS chip, which contains most of the readout electronics. The information provided is a digital pulse,

a threshold is applied to the pre-amplified and each cell gives a logical output if the threshold is exceeded.

The SDD and SPD are also two layered silicon detectors placed just after the SPD, covers pseudo-rapidity range $|\eta| < 2.0$. The inner radius of SDD is 15 cm and hence the track density is relatively less as compared to SPD. The SDD gives good tracking and PID performance at low- p_T by measuring the transport time of the electrons and holes which are created in the process of ionisation while the particle passes through the 300 mm thick p-n junction.

The two SSD layers start at a radius of 39 cm and it is the outer most layer of ITS. It consists of 300 mm thick, 40 mm long, double sided silicon strip sensor with p^- on one side, and n^- on the other side with a separation of 95 mm. It provides a two-dimensional measurement of track matching between the ITS and TPC.

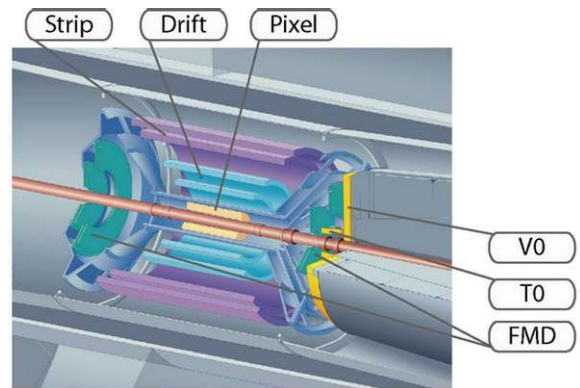


Figure 2.3: The schematic diagram of ITS [12]

The SDD and SSD provides analogue output, so the particle identification information is extracted via specific energy loss information (dE/dx) in the silicon detector.

2.3.2 Time Projection Chamber (TPC)

The ALICE TPC [10] is a large cylindrical gaseous detector placed around the ITS, aligning the axis with the beams from the LHC. The TPC is mainly used for tracking, particle identification purpose and also helps in vertex determination. The active

volume of TPC is close to 90 m^3 with an overall length along the beam direction of 500 cm. The inner and outer radius is about 85 cm and 250 cm, respectively. The detector is filled with gas mixture of Ne-CO₂-N₂ (90%-10%-5%) at atmospheric pressure. A cylindrical conducting electrode is placed at the centre to maintain a uniform axial electrostatic field of 400 V/cm along the beam direction. A charged particle passing the detector ionizes the gas, then the free electron drift towards the endplates of the cylinder under the influence of electric field. The readout chambers are installed at the two endplates which is based on the Multi-Wire Proportional Chamber (MWPC) technique with a gain factor of 10^4 . Figure 2.4 shows some parts of the ALICE TPC.

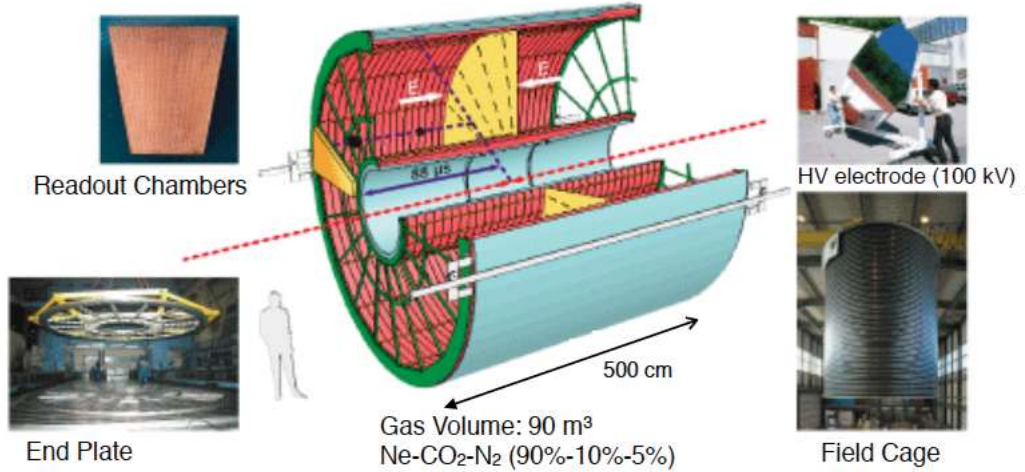


Figure 2.4: An artistic picture of ALICE Time Projection Chamber. Photo © Francis Demange

The TPC has the capability to reconstruct a primary track having momentum from 100 MeV/ c to 100 GeV/ c . In addition to tracking capability, the TPC can also provide particle identification (PID) information via measuring momentum, charge, and specific energy loss (dE/dx) of the particle. The energy loss, described by the Bethe-Bloch formula is parametrised for each particle species by a function originally

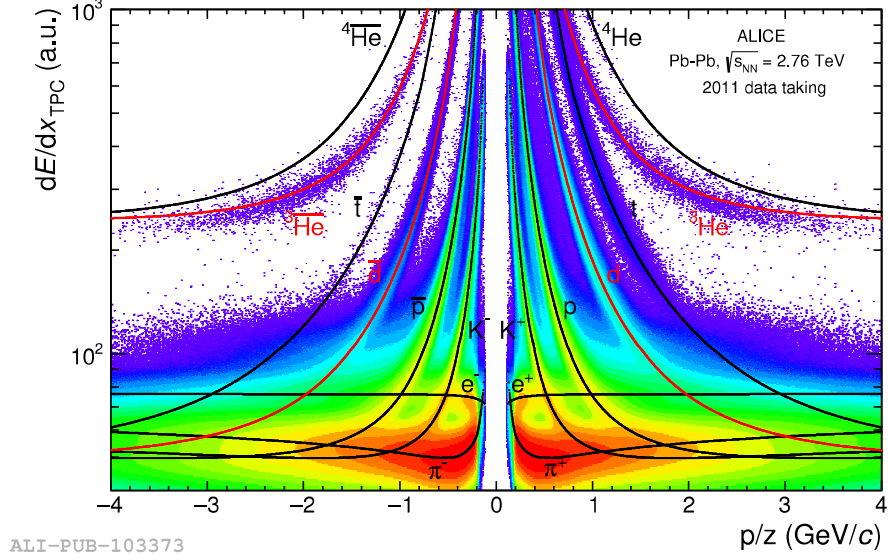


Figure 2.5: Specific energy loss (dE/dx) signal as a function of rigidity (p/z) for different particle and anti-particles in Pb–Pb collisions at $\sqrt{s_{NN}} = 2.76$ TeV. The solid line represents the theoretical modified Bethe-Bloch line.

proposed by the ALEPH collaboration [13].

$$f(\beta\gamma) = \frac{P_1}{\beta^{P_4}} \left(P_2 - \beta^{P_4} - \ln \left(P_3 + \frac{1}{(\beta\gamma)^{P_5}} \right) \right), \quad (2.1)$$

where β and γ are the relativistic velocity and Lorentz factor and P_{1-5} are the fit parameters. The energy loss distribution for various mass particles are shown in Fig. 2.5.

2.3.3 Transition Radiation Detector (TRD)

The ALICE TRD [14] is placed outside the TPC within the radial distance of 2.9 to 3.7 m in the pseudo-rapidity range $|\eta| < 0.84$. The TRD module consists of Multi-Wire Proportional Chambers (MWPC) filled with a Xe-CO₂ gas mixture and a fibre radiator is placed in front of each MWPC. The radiator is used for electron

identification via transition radiation and energy deposition. The TRD can separate electrons from pions very accurately with almost 100% efficiency. The TRD is also used for triggering and tracking of electrons and jets.

2.3.4 Time Of Flight (TOF)

The TOF [15] is placed around the TRD and having the inner radius of 3.7 m in the pseudo-rapidity range of $|\eta| < 0.9$. This is a gaseous detector formed of an array Multi-gap Resistive Plate Chamber (MRPC). Any charged particle passes by, it ionizes the gas and the avalanche electrons move towards the electrode. The avalanche is stopped by the resistive plates in each gap. The induced charge gives very fast signal with overall time resolution for charged particle being about 80 ps. The TOF is mainly used for particle identification at intermediate momenta where the separation between pions and kaons with momenta up to 2.5 GeV/ c , and pions and protons up to 4 GeV/ c is good.

The measure of flight times of charged particle between the collision point and TOF is measured as a difference between the reconstructed times of the hits in the TOF and T0 detectors [16]. The estimation of mass is made from the relationship between the particle momentum and its velocity. The velocity is inversely proportional to the time of flight (t_{TOF}), which is related to rest mass (m_0) as

$$m_0 = \frac{p}{\gamma\beta c} \quad (2.2)$$

where p is the momentum of the particle, γ and c are the Lorentz factor and is the speed of light respectively. The TOF detector performance is shown in Fig. 2.6 for Pb–Pb collisions. The measured β of each particle is plotted against its momentum (as measured in the TPC).

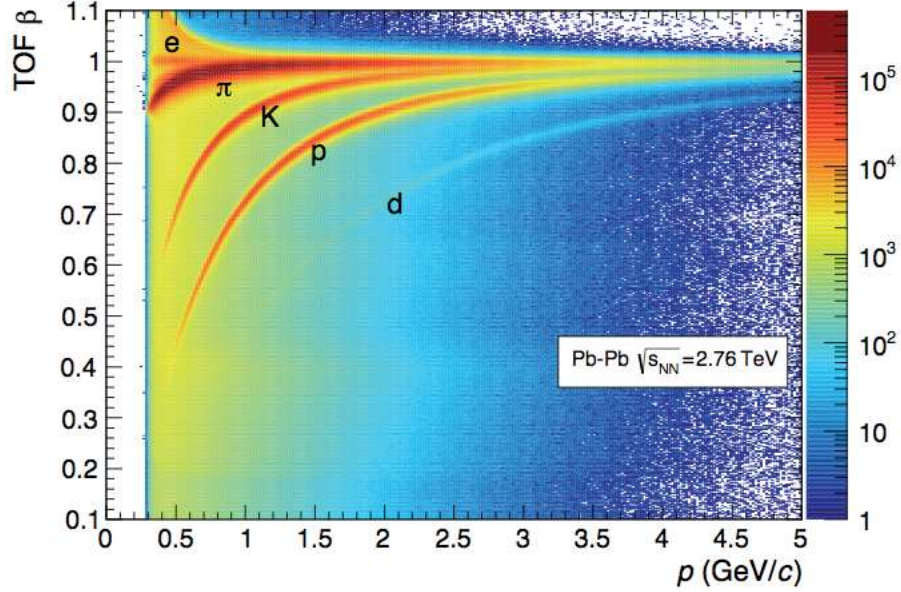


Figure 2.6: Distribution of β as measured by the TOF detector as a function of momentum for particles reaching the TOF in Pb-Pb collisions at $\sqrt{s_{NN}} = 2.76$ TeV [8].

2.3.5 High Momentum Particle Identification (HMPID)

The HMPID [17] consists of 7 identical RICH (ring-imaging Cherenkov) modules with a liquid C_6F_{14} radiator coupled to MWPC based photon detectors with CsI photocathode and covering 11 m^2 . The HMPID detector extends charged hadron identification in ALICE to higher momentum. The identification is based on the Cherenkov angle measurement produced by charged tracks which emit electromagnetic radiation in form of a cone. Using HMPID, the charged pions and kaons can be identified up to $3 \text{ GeV}/c$ and $5 \text{ GeV}/c$ respectively.

2.3.6 PHOton Spectrometer (PHOS)

The PHOS [18] is an electromagnetic calorimeter of high granularity. It is positioned at a radial distance of 4.6 m , within pseudo-rapidity of $|\eta| < 0.12$ and azimuthal

acceptance of 220° to 320° . It consists of 17280 detection channels of lead-tungstate crystals, PbWO_4 . The PHOS is optimised to measure photons (in p_T range ~ 0.5 -10 GeV/c), π^0 (in p_T range ~ 1 -10 GeV/c) and η meson (in p_T range ~ 2 -10 GeV/c).

2.3.7 Electro Magnetic Calorimeter (EMCAL)

The EMCAL [19] is placed at a radial distance of 4.5 m, opposite to PHOS. It contains 10 supermodules of 48×24 cells and 2 supermodules of 48×8 cells within $|\eta| < 0.7$ and azimuthal angle of $80^\circ < \phi < 187^\circ$. It identifies electrons by measuring their energy deposition and comparing it to track momentum (E/p method). The EMCAL enables triggering and full reconstruction of high energy jets and to measure high momentum photons and electrons in ALICE.

2.3.8 ALICE Cosmic Ray Detector (ACORDE)

The ALICE Cosmic Ray Detector [20] is positioned on top of the magnet at a radial distance of 8.5 m, within $|\eta| < 1.3$ and azimuthal angle of $30^\circ < \phi < 150^\circ$. It is a plastic scintillation detector. ACORDE is mainly used for cosmic-ray studies, alignment and calibration of different ALICE detectors.

2.3.9 Muon Spectrometer

The ALICE Muon Spectrometer [21] has the pseudo-rapidity coverage of $-4 < \eta < -2.5$ with full azimuthal coverage. The primary purpose of ALICE Muon Spectrometer is to measure spectrum of heavy-quark vector-meson resonances like J/Ψ , Ψ' , Υ , Υ' , along with some low mass resonance like ϕ ; as these particles decay to $\mu^+ \mu^-$. It is also used as trigger detector. The highly energetic particles are stopped by the absorber made of carbon, concrete and steel.

2.4 Forward detectors

2.4.1 VZERO (V0)

The ALICE VZERO (V0) [16] is a small-angle plastic scintillator detector installed on both sides of the ALICE collision vertex. The detector covers pseudo-rapidity ranges $2.8 < \eta < 5.1$ (V0A) and $-3.7 < \eta < -1.7$ (V0C); V0A and V0C are placed opposite to each other at a distance 328 cm and 88 cm from interaction point (IP), respectively.

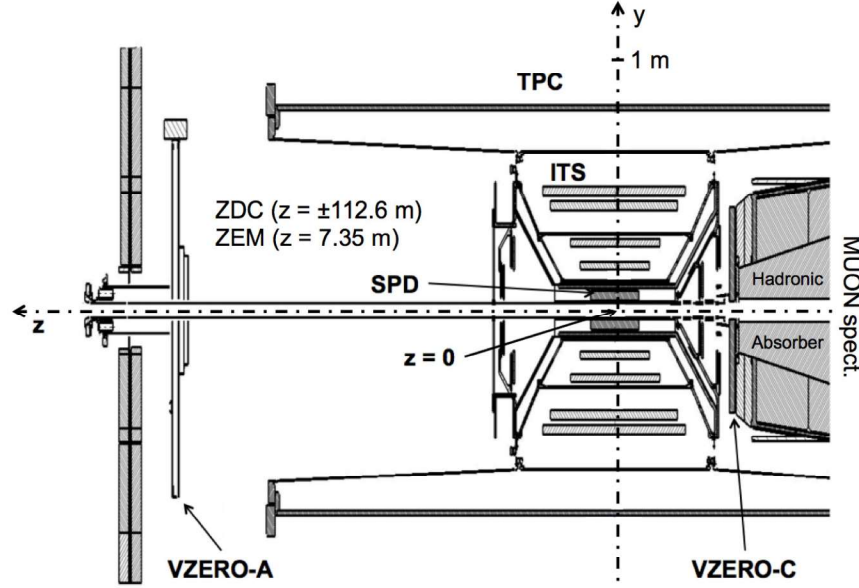


Figure 2.7: Position of the two VZERO arrays, within the general layout of the ALICE experiment [22].

This detector is mainly used for triggering and centrality determination for Pb–Pb collisions. It is also used for multiplicity determination in pp collisions, rejection of beam gas events from the actual event via its timing information. It has a time resolution of about 1 ns. The location of two V0 arrays inside ALICE is shown in Fig. 2.7.

2.4.2 TZERO (T0)

The TZERO (T0) [16] consists of two arrays of Cherenkov counters with the IP in between. The distance from the IP to T0-C is 70 cm and T0-A to the IP is about 360 cm. The pseudo-rapidity range coverage of T0-C is $2.9 < \eta < 3.3$ and T0-A is $4.5 < \eta < 5$. The T0 detector is used for ALICE level-0 (L0) trigger [16] and provide an earlier trigger to the TRD. It is also used to give a start signal with good time resolution for the Time of Flight (TOF) for particle identification. The location of the two T0 arrays inside ALICE is shown schematically in Fig. 2.8.



Figure 2.8: Position of the T0 detector inside ALICE experiment [16].

2.4.3 Forward Multiplicity Detector (FMD)

The FMD [16] consists of silicon strip with five ring counters. It is of two types placed in the rapidity region $-3.4 < \eta < -1.7$ and $1.7 < \eta < 5.0$, which have 20 and 40 sectors each with full azimuthal coverage, respectively. The main purpose of the FMD system is to provide (offline) precise charged particle multiplicity as well as event-by-event determination of the reaction plane.

2.4.4 Zero Degree Calorimeter (ZDC)

The Zero Degree Calorimeter (ZDC) [23] of ALICE is used to detect spectator nucleons that leaves the IP along the beam direction. The ZDC are placed on both sides of the IP at a distance of 116 m from IP. Typically the beams are deflected by dipole magnets, it also deflects the spectator protons, separating them from the spectator neutrons which basically fly away at 0° with beam axis. The main function of ZDC is to determine the centrality and reaction plane of an event in heavy-ion collisions and it is also used for level-1 (L1) trigger [23].

2.4.5 Photon Multiplicity Detector (PMD)

The PMD [24, 25] is pre-shower detector to measure photons multiplicity on event-by-event basis in the forward rapidity region ($2.9 < \eta < 3.9$). It is also used for estimation of reaction plane. The PMD is placed at about 3.6 m from IP. It consists of two identical planes of detectors, separated by a $3X_0$ thick lead converter which is 1.5 cm lead and 0.5 cm stainless steel. It is made up of gas proportional counters having a honeycomb structure with wire readout in it.

2.5 ALICE Online system

The detector online control system in ALICE constitute Trigger system (TRG), Data AcQuisition (DAQ), High Level Trigger (HLT), Detector Control System (DCS), Experiment Control System (ECS) [26, 27].

2.5.1 Trigger System (TRG)

The ALICE Central Trigger Processor (CPT) [28, 29] is design to select all those events which suits the physics requirements. There are three different levels of trigger such as level-0 (L0), level-1 (L1), and level-2 (L2), which have different latencies and depending upon different arrival times of the trigger inputs and the precise timing requirements of the detectors. The Low level trigger (L0) combines the information from the V0 (centrality), TOF, T0 (event vertex), SPD, EMCal, PHOS (photon), MTR (muons) and ACORDE (cosmic rays) all combinedly deliver signal for each bunch crossing after $1.2 \mu\text{s}$. The L1 trigger takes a decision after $6.5 \mu\text{s}$ based on ZDC (MB interaction), EMCal (photons, neutral jets) and TRD (electrons, high- p_T particles, charged jets) information. The third level (L2) trigger takes the decision after 100 ms which comes after the end of the the TPC drift time. After the final trigger decision, the data is recorded via Data AcQuisition (DAQ) system. The data transfer takes place from the detector to DAQ via Detector Data Links (DDL) with the help of Front-End Read-Out (FERO).

2.5.2 High Level Trigger (HLT)

The ALICE High Level Trigger (HLT) [30] collects information from all major detectors and processes it. The HLT decides whether the event needs to be accepted or rejected. It also reduces the size of the event without losing physics information via compression algorithms (e.g in 2011 the HLT was used to reconstruct the TPC clusters) on the accepted and selected data.

2.5.3 Detector and Experiment Control System

The main function of the ALICE Detector Control System (DCS) is to ensure correct safe operation of the ALICE experiment. The DCS is always operational including during the shutdown periods. It provides remote control and monitoring facilities of the experiment. The ALICE Experiment Control System (ECS) is a central control system where all operations are initiated.

2.6 ALICE offline and Grid computing

The purpose of ALICE Offline project is to develop and make an operational framework for data processing. The task includes simulation, reconstruction, calibration, alignment, visualisation and analysis.

The Tier computing centers hierarchy and data processing strategy is derived from Monarch model [31]. During the proton-proton collisions, four activities proceed in parallel on the RAW data which are given below:

- (i) It copies to the CASTOR tapes [32].
- (ii) In order to have a second copy on reliable storage media, it exports to Tier-1 centers for preparing the successive reconstruction passes which will be in Tier-1 centers.
- (iii) The processes like reconstruction, production of calibration, alignment constants and scheduled analysis are processed at Tier-0 centres.
- (iv) Fast processing of data sets which are selected are done, which mainly includes calibration, alignment, reconstruction and analysis on the CERN Analysis Facility (CAF) [33].

As the rate of data acquisition is high for nucleus-nucleus runs, so an excessive

amount of computing resources and network bandwidth would be necessary. Hence, during nucleus-nucleus runs, raw data process follows the steps are given below:

- (i) Registration of raw data in CASTOR.
- (ii) To allow remote users to examine the data locally, these are exported to Tier-1 centers.
- (iii) First processed partially at Tier-0 centre in order to provide rapid feedback on the offline chain.
- (iv) The calibration, alignment, reconstruction and analysis on the CAF are done in a fast processing way.

The service of data processing of the ALICE experiment is coordinated by Worldwide LHC Computing Grid (WLCG). The infrastructure of WLCG is highly hierarchical by nature. The very first phase of the real data obtain from the experiment get processed by CERN computing centre called Tier-0. In order to have a safe storage of the data, large regional computing centres call Tier-1 shares the CERN data. Around the Tire-1's, smaller centres called Tire-2 are clustered. Tire-1 is different from Tire-2 with respect to the availability of high-reliability mass-storage media at Tire-1. For simulation and end-user analysis, Tire-2 plays the major role.

2.7 Aliroot framework

The Aliroot [35] is based on the Object Oriented framework which is used for simulation, alignment, calibration, reconstruction, visualisation and analysis of the experimental data. The basic design features of the AliRoot framework are re-usability, modularity and reliability. The modularity features of Aliroot allows replacement or changes of well defined parts of the system with minimal or even no impact on the rest analysis framework. The re-usability is the protection of the framework made

programming physicists such that whenever the person wants, he/she can regain the framework at any time. The framework is kept preserved by designing it as a modular system and by ensuring that there is maximum backward compatibility while evolving the Aliroot system. All the features are cross checked and the design feature is universal, so it is more reliable as compared to personal framework.

The schematic diagram of Aliroot flow of control is given in Fig. 2.9. The framework provides an environment for the development of software packages helpful for event generation. The example of typical event generators are PYTHIA [36, 37], PHOJET [38], HIJING [39], etc.

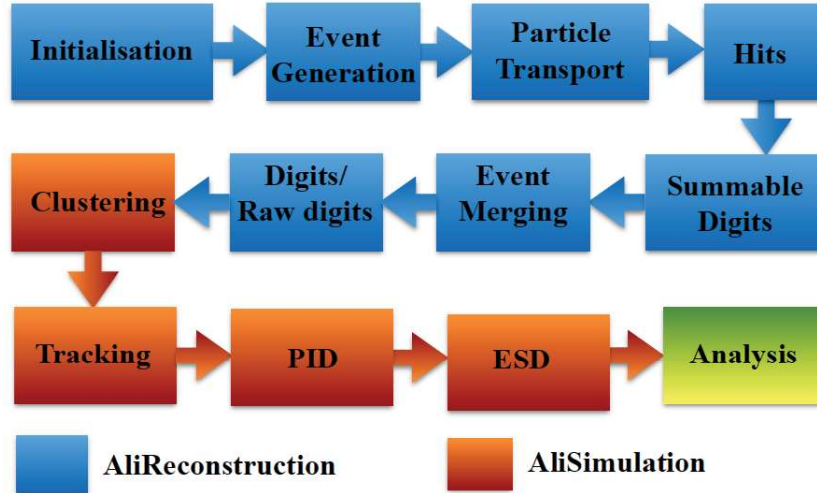


Figure 2.9: Aliroot flow of control [35, 26]

The particles generated from the event generators are propagated through the detector's material. The particles are simulated using the Monte Carlo transport packages GEANT3 [40], GEANT4 [41], FLUKA [42] etc., where the ALICE detector is virtually well described. During the propagation, particle undertakes via all physics interactions like in a real experiment. Each detector stores the hit information, energy deposition at a given point. The hit information is converted into digits by considering

the detector and associated electronic response. At the end of the process, each digits of the corresponding detectors are stored in the specific hardware format as the raw data.

For the track reconstruction of the raw or simulated data, the very first thing is to obtain clusters information from the digits. Then from the cluster information, tracking is performed by combining the most probable path for the particle in the detector. The basic method of track reconstruction is Kalman filter algorithm [43]. In this method, for each track, a set of initial seeds value for the track parameters and covariant matrix are required. The seeding is performed twice by using the space points reconstructed in TPC: (i) assuming that the track originated from the primary vertex and (ii) assuming that the track originated from elsewhere such as decay, secondary interaction, etc. In the first pass, the space points are combined which starts from outermost pad rows using the primary vertex position as a constraint. This procedure is repeated several times choosing a set of pad rows closer and closer to the centre of the TPC. In brief, the Kalman filter essentially consists of the following steps:

- (i) It transfers the track parameters and their corresponding covariance matrix from one pad to next pad rows.

- (ii) The above information adds to the inverted covariance matrix. This information matrix represents the track parameters at that point and also a noise term which takes care loss of information via multiple scattering and fluctuations due to energy loss.

- (iii) Then the track information is updated when the filter finds in the new pad row a space point compatible with the track prolongation.

Then the process of seeding is repeated for the second time without vertex constraint. After completing the TPC, the tracks are propagated to the outer layer of

ITS. Here also similar to TPC refit, two independent passes are done, first constraining the primary vertex position, and then without this condition. Both ITS and TPC are fitted simultaneously for each track and the algorithm uses the seeds from the already reconstructed tracks and then reversed and proceed outwards. In order to remove the improperly assigned points, the tracks are re-calculated. After TPC and ITS tracking, the space points are also extended in different other detectors like TRD, TOF, HMPID, EMCAL, PHOS, etc. Finally with considering all these detectors simultaneously track parameters for track reconstruction using Kalman filter algorithm are extracted with and without primary vertex.

After the reconstruction, the first version of the data is kept as an Event Summary Data (ESD), where complete information for each event is stored. A reduced version of ESD data with relevant information for the analysis called Analysis Object Data (AOD) is extracted. So, these ESD and AOD data are used for the real physics analysis purposes.

Out all these detectors, the main detectors which are used for the analysis presented in this thesis are ITS, TPC, V0. The Inner Tracking System (ITS) is used for tracking, finding primary vertex and particle identification purpose via average energy loss (dE/dx). The Time Projection Chamber (TPC) is also used for tracking the particle, finding the vertex position and for the identification of particle via dE/dx . In Pb–Pb collisions, finding the centrality of an event is important and is performed by the V0 detector which is basically consist of two sub-detectors V0-A and V0-C.

Bibliography

- [1] L. Evans and P. Bryant, JINST 3, S08001 (2008).
- [2] C. De Melis, “The CERN accelerator complex. Complexe des accélérateurs du CERN”, <http://cds.cern.ch/record/2119882>.
- [3] (ATLAS Collaboration) G. Aad *et al.*, JINST 3, S08003 (2008).
- [4] (CMS Collaboration) S. Chatrchyan *et al.*, JINST 3, S08004 (2008).
- [5] (ATLAS Collaboration) G. Aad *et al.*, Phys. Lett. B 716, 1-29 (2012).
- [6] (CMS Collaboration), S. Chatrchyan *et al.*, Phys. Lett. B 716, 30-61 (2012).
- [7] (LHCb Collaboration) Alves *et al.*, JINST 3, S08005 (2008).
- [8] (ALICE Collaboration) B. Abelev *et al.*, Int. J. Mod. Phys. A 29, 1430044 (2014).
- [9] (ALICE Collaboration), JINST 3, S08002 (2008).
- [10] “ALICE Time Projection Chamber: Technical Design Report, CERN-LHCC-2000-001”, <http://cdsweb.cern.ch/record/451098> (2000).
- [11] (ALICE Collaboration), “ALICE Inner Tracking System (ITS): Technical Design Report”, <https://cds.cern.ch/record/391175>.

- [12] (ALICE Collaboration), S. Beolè, "The ALICE Inner Tracking System: performance with proton and lead beams", *Physics Procedia* 37, 1062 (2012).
- [13] W. Blum, W. Riegler, and L. Rolandi, "Particle detection with drift chambers"; Springer, Berlin (2008). <https://cds.cern.ch/record/1105920>.
- [14] (ALICE TRD Collaboration) Andronic *et al*, *Nucl. Instrum. Meth. A* 522, 40 (2004); (ALICE Collaboration) Adler *et al*, *Nucl. Instrum. Meth. A* 552, 364 (2005).
- [15] "ALICE Time-Of-Flight system (TOF): Technical Design Report, CERNLHCC-2000-012"; <http://cdsweb.cern.ch/record/430132>; "ALICE Time-Of-Flight system (TOF): addendum to the technical design report, CERN-LHCC- 2002-016", <http://cdsweb.cern.ch/record/545834>.
- [16] "ALICE forward detectors: FMD, T0 and V0: Technical Design Report", CERNLHCC-2004-025, <http://cdsweb.cern.ch/record/781854>.
- [17] "ALICE electromagnetic calorimeter: addendum to the ALICE technical proposal, CERN-LHCC-2006-014", <http://cdsweb.cern.ch/record/932676>.
- [18] "ALICE Technical Design Report of the Photon Spectrometer (PHOS), CERN/LHCC 99-4 (1999)", <https://edms.cern.ch/document/398934/1>.
- [19] "ALICE electromagnetic calorimeter: addendum to the ALICE technical proposal", CERN-LHCC-2006-014, <http://cdsweb.cern.ch/record/932676>.
- [20] A. Fernandez *et al*. *Czech. J. Phys.* 55, B801-B807 (2005); A. Fernandez *et al*., *Nucl. Instrum. Meth. A* 572, 102 (2007).
- [21] (a) "ALICE dimuon forward spectrometer: Technical Design Report, CERN-LHCC-99-022"; <http://cdsweb.cern.ch/record/401974>; (b) "ALICE dimuon for-

- ward spectrometer: addendum to the Technical Design Report, CERN-LHCC-2000-046”, <http://cdsweb.cern.ch/record/494265>.
- [22] (ALICE Collaboration) E. Abbas *et al.*, JINST 8, P10016 (2013).
 - [23] “ALICE Technical Design Report of the Zero Degree Calorimeter (ZDC)”, CERN LHCC-99-005, <http://cdsweb.cern.ch/record/381433>.
 - [24] “ALICE Photon Multiplicity Detector (PMD): Technical Design Report, CERN/LHCC-99-032”; <http://cdsweb.cern.ch/record/451099>;
 - [25] “ALICE Technical Design Report on Photon Multiplicity Detector, Addendum-1”, CERN/LHCC 2003-038 (2003).
 - [26] J. F. Grosse-Oetringhaus *et al.*, “The ALICE Online-Offline Framework for the Extraction of Conditions Data”, Journal of Physics: Conference Series 219, 022010 (2010).
 - [27] F. Carena *et al.*, Nucl. Inst. and Meth. in Phys. Res. A 741, 130-162 (2014).
 - [28] A Bhasin *et al.* Recent developments on the ALICE central trigger processor, CERN 2007-001 (2007).
 - [29] (ALICE Collaboration), ALICE Technical Design Report of the Trigger, Data Acquisition, High-Level Trigger, Control System, CERN/LHCC 2003/062 (2004), <https://edms.cern.ch/document/456354/2>.
 - [30] (ALICE Collaboration) T. Alt *et al.*, J. Phys., G 30, S1097-S1100 (2004).
 - [31] <http://www.cern.ch/MONARC>.

- [32] J. Durand, O. Barring, S. Ponce and B. Couturier, CASTOR: Operational issues and new developments, in Interlaken, Computing in high-energy physics and nuclear physics, 1221-1226 (2004).
- [33] <http://aliweb.cern.ch/Offline/Activities/Analysis/CAF/index.html>.
- [34] (ALICE Collaboration) B. Abelev *et al.*, Phys. Rev. C 88, 044909 (2013).
- [35] (ALICE Collaboration), ALICE Technical Design Report of the Trigger, Data Acquisition, High-Level Trigger, Control System, CERN/LHCC 2003/062 (2004), <https://cdms.cern.ch/document/456354/2>.
- [36] T. Sjöstrand, S. Mrenna, and P. Skands, J. High Energy Phys. 05, 026 (2006).
- [37] T. Sjöstrand, S. Mrenna *et al.*, Comput. Phys. Commun. 178, 852 (2008).
- [38] R. Engel, Z. Phys. C 66, 203 (1995).
- [39] Xin-Nian Wang and M. Gyulassy, Phys. Rev. D 44, 3501 (1991).
- [40] R. Brun *et al.*, CERN program library long write-up, W5013, GEANT detector description and simulation tool (1994).
- [41] S. Agostinelli *et al.*, Nucl. Instrum. Meth. A 506, 250 (2003), <http://cdsweb.cern.ch/record/602040>.
- [42] A. Fasso *et al.*, Proceedings of the IV International Conference on Calorimeters and their Applications, World Scientific, Singapore (1994).
- [43] P. Billoir, “Progressive track recognition with a Kalman like fitting procedure”, Comput. Phys. Commun. 57, 390 (1989).

Chapter 3

Measurement of $K^*(892)^0$ resonance production in Pb-Pb collisions at $\sqrt{s_{\text{NN}}} = 2.76 \text{ TeV}$

In this chapter, the production of K^{*0} meson in Pb–Pb collisions at $\sqrt{s_{\text{NN}}} = 2.76 \text{ TeV}$ using the high statistic data sets collected in 2011 by ALICE detector at the LHC is presented.

Resonances by definition are very short lived ($\sim \text{fm}/c$) particles, so they are used as a thermometer for the study of properties and dynamics of the QCD medium formed due to the ultra-relativistic heavy-ion collisions. The QCD medium formed is called Quark-Gluon-Plasma (QGP) [1, 2]. In order to understanding the hadronic in-medium phenomenon, various resonance particles yield are measured. In this thesis the K^{*0} resonance is considered because of its lifetime ($\tau_{K^{*0}} = 4.16 \pm 0.05 \text{ fm}/c$ [8]) which is comparable to the lifetime of the fireball. Furthermore, the K^{*0} contains strange quark, so it can also give information about strangeness enhancement which is a signature of QGP formation [4]. The transverse momentum (p_{T}) dependence of

K^{*0} production can also be used to study flavour dependence of the energy loss of the partons in the QGP medium formed in high energy heavy-ion collisions.

The p_T -spectra of K^{*0} meson has been measured via their hadronic decay channel $K^{*0} (\bar{K}^{*0}) \rightarrow \pi^- K^+ (\pi^+ K^-)$ with branching ratio of 66.6% [8]. The p_T -spectra reach of K^{*0} mesons has been measured up to $p_T = 20$ GeV/ c for finer collisions centrality classes which enables us to calculate nuclear modification factor (R_{AA}). Measurement of R_{AA} tells us about the parton energy loss in the medium. The p_T -integrated particle ratios are measured for understanding the hadronic in-medium effects like re-scattering and regeneration processes in the medium [5, 6, 7, 8, 26].

3.1 Analysis details

3.1.1 Data sample

Summary of event statistics: The high luminosity Pb–Pb collisions data was taken in 2011. The dataset have V0 online triggers with enhanced central 0-10%, semi central 10-50% and minimum bias (0-80%) events. The summary of different centrality event classes with corresponding average number of participant ($\langle N_{\text{part}} \rangle$) and average number of binary collision ($\langle N_{\text{coll}} \rangle$) values in Pb–Pb collisions at $\sqrt{s_{\text{NN}}} = 2.76$ TeV are given in the Table 3.1.

3.1.2 Offline event selection

The events used for this analysis are selected using V0 online triggers. There were two triggers named kCentral for 0-10% centrality events and kSemiCentral for 10-50% centrality class. The number of events distribution for these two trigger classes are shown in Fig. 3.1. The trigger was 100% efficient for the 0-8% most central Pb–Pb

collisions and 80% efficient for 8-10% centrality [10]. The inefficiency for the 8-10% centrality range has a negligible ($<1\%$) effect on the results presented in this thesis. In order to remove any centrality bias for 5-10% and 10-20% centrality, a procedure was used which removed events randomly using a suitable function that described the centrality distribution properly (right panel of Fig. 3.1).

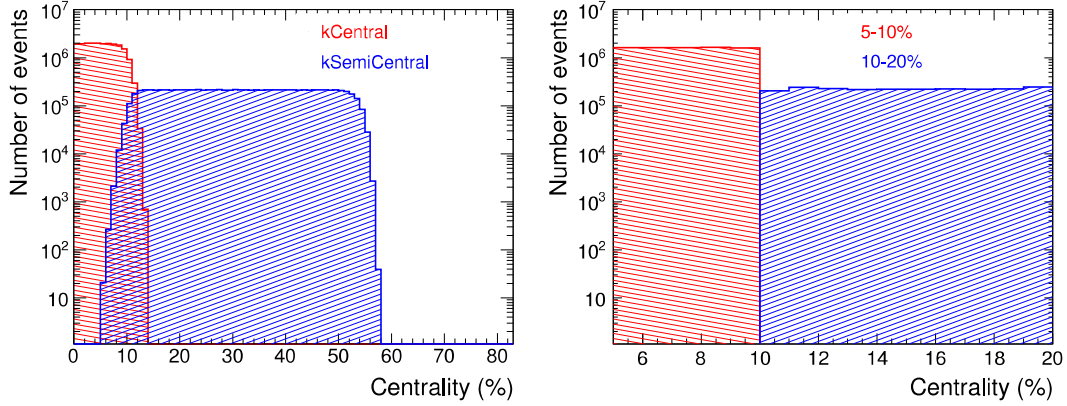


Figure 3.1: Number of events as function of centrality (kCentral and kSemiCentral trigger) is shown in the left panel. Right panel shows the 5-10% and 10-20% flat centrality distribution of events in Pb–Pb collisions at $\sqrt{s_{\text{NN}}} = 2.76$ TeV.

Centrality (%)	Events	$\langle N_{\text{part}} \rangle$	$\langle N_{\text{coll}} \rangle$
0–5	5.12×10^6	382.7	1685
5–10	5.80×10^6	329.4	1316
10–20	2.04×10^6	260.1	921.2
20–30	2.35×10^6	185.8	556.6
30–40	2.35×10^6	128.5	320.0
40–50	2.34×10^6	847.0	171.2

Table 3.1: The total number of events analysed in various centralities and their corresponding average number of participant ($\langle N_{\text{part}} \rangle$) and average number of binary collisions ($\langle N_{\text{coll}} \rangle$) values in Pb–Pb collisions at $\sqrt{s_{\text{NN}}} = 2.76$ TeV [12].

In order to ensure uniform detector acceptance, the primary vertex coordinate along the beam axis, V_z of ± 10 cm from the nominal interaction point is applied for the event selection. The V_z distribution in Pb–Pb collisions at $\sqrt{s_{NN}} = 2.76$ TeV is shown in Fig. 3.2. The full width at half maximum (FWHM) of the z-position of vertex distribution is 14.6 cm.

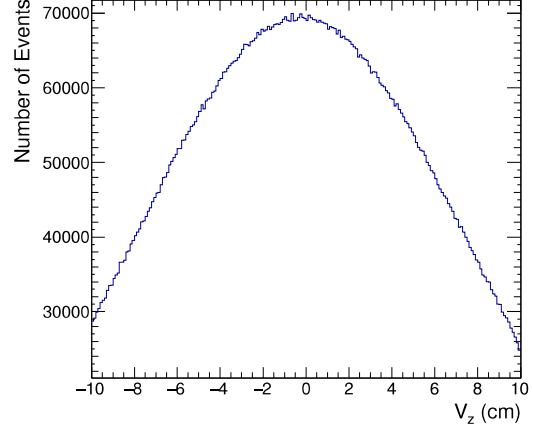


Figure 3.2: The z-position of vertex (V_z) distribution in Pb–Pb collisions at $\sqrt{s_{NN}} = 2.76$ TeV.

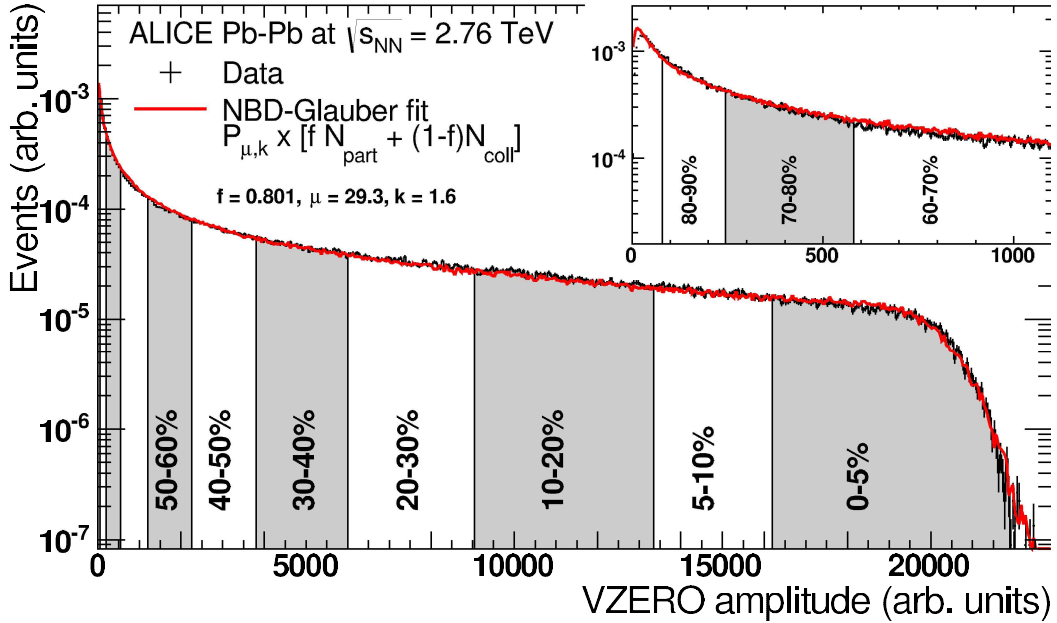


Figure 3.3: The sum of VZERO amplitude distribution of different events. The distribution is fitted with the NBD-Glauber model shown in red line. The inset shows a zoom of the most peripheral region [12].

One of the important part of offline Pb–Pb data analysis is centrality determination. Figure 3.3 shows the VZERO amplitude distribution of different centrality

event classes in Pb–Pb collisions at $\sqrt{s_{\text{NN}}} = 2.76$ TeV. The distribution is fitted with Glauber-Monte-Carlo model [11], by using this the impact parameter of a collision is extracted. The method of selecting the centrality is described in Ref. [12]. The analysis presented in this thesis is performed in various centrality classes such as 0-5%, 5-10%, 10-20%, 20-30%, 30-40%, 40-50%.

3.1.3 Track and PID selection

The maximum TPC coverage for tracking is $|\eta| < 0.9$ with full azimuthal acceptance. For uniform acceptance of TPC, tracks are selected within $|\eta| < 0.8$. The reconstruction primary particles require to have at least 70 pad rows measured along the track out of a maximum possible 159 with a minimum χ^2 of the fit per crossed rows less than equal to 4. The contamination from beam-background events and secondary particles coming from weak decays are reduced by applying distance of closest approach to the primary vertex in the xy plane (DCA_{xy}) and z direction (DCA_z). The standard values of DCA_{xy} is required to be less than 7 times its resolution: ($DCA_{xy}(p_T) < 0.0105 + 0.035p_T^{-1.1}$) cm (p_T in GeV/ c) and DCA_z needs to be less than 2 cm. The p_T of each track is restricted to be greater than 0.15 GeV/ c to have higher efficiency in the reconstruction of the track.

The charged particles are identified using TPC by measuring the specific ionisation energy loss (dE/dx). In the TPC, kaons are distinguished from pions below momentum (p) < 0.7 GeV/ c , and protons are separated from pions and kaons below $p < 1$ GeV/ c . The decay daughter of K^{*0} i.e. pion and kaon candidates are required to have mean values of the specific energy loss in the TPC ($\langle dE/dx \rangle$) within two standard deviations ($2\sigma_{\text{TPC}}$) of the expected dE/dx values for each particle species throughout the momentum range. The energy resolution of the TPC is the deviation of measure dE/dx from expected dE/dx values which is 6.5% for central collisions.

Figure 3.4 shows the specific energy loss (dE/dx) of different identified particles.

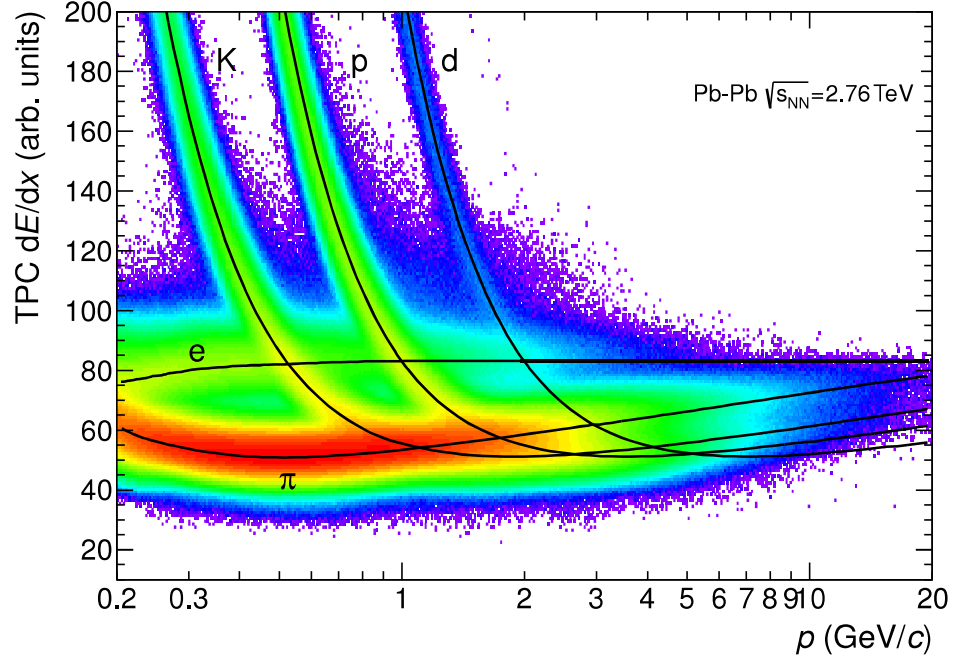


Figure 3.4: Specific energy loss (dE/dx) in the TPC vs. particle momentum in Pb–Pb collisions at $\sqrt{s_{NN}} = 2.76$ TeV. The lines show the parameterisation of the expected mean energy loss [13].

3.1.4 Invariant mass reconstruction

The primary pions and kaons are indistinguishable from decay daughters of K^{*0} . So, the K^{*0} signal is reconstructed via the invariant mass of opposite sign pion and kaon pairs in the same event as given in Eq. 3.1.

$$M_{\pi K} = \sqrt{(E_{\pi} + E_K)^2 - (|\vec{p}_{\pi}| + |\vec{p}_K|)^2} \quad (3.1)$$

where, $E_{\pi} = \sqrt{m_{\pi}^2 + |\vec{p}_{\pi}|^2}$ and $E_K = \sqrt{m_K^2 + |\vec{p}_K|^2}$

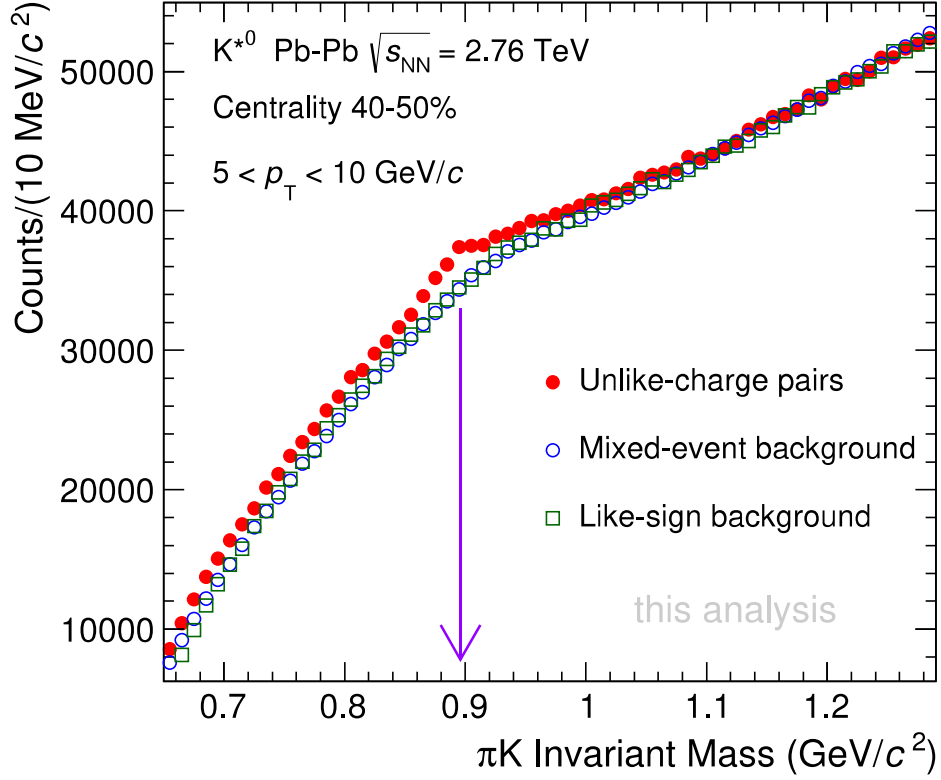


Figure 3.5: Same event unlike charge πK invariant mass distribution using like sign and mixed event distribution for 40-50% centrality in Pb-Pb collisions at $\sqrt{s_{NN}} = 2.76$ TeV.

Figure 3.5 shows the πK invariant mass distribution for 40-50% centrality in Pb-Pb collisions at $\sqrt{s_{NN}} = 2.76$ TeV. The K^{*0} signal is not clearly visible because of huge uncorrelated background which are not originating from K^{*0} . The signal is extracted after subtracting the combinatorial background via event mixing or like sign technique as described below. The arrow line indicates K^{*0} invariant mass peak position as per PDG.

Event mixing method well reproduces the shape of the background. In this method, a pool of events are collected which are having similar characteristics. The event samples are divided into different centrality percentile, event plane angle and

z-vertex bins. In this analysis, the z-vertex is divided in 20 bins (-10 to $+10$ cm), similarly the centrality is also divided in 10 bins (0 to 100 %) and event plane angle (0 to 2π) is divided in 12 bins. The continuous event mixing method has been used where it always ensures the event which are getting mixed are as similar as possible. The pion and kaon pairs of five different events are mixed. The mixing events have z-vertex difference less than 1 cm, difference in event plane angle and centrality are 20° and 10%, respectively. As the mixed event statistics is five times higher than the signal, the former is normalised in the invariant mass region 1.1 to 1.3 GeV/c², more than 5Γ (where Γ is full width at half maxima of the Breit-Wigner function as shown in Eq. 3.5) away from the signal where πK pairs are very much uncorrelated. The K^{*0} signal is obtained after subtracting the normalised mixed event invariant mass distribution from the same event as given in Eq. 3.2.

$$M_{K^{*0}} = N_{\pi_1^+ K_1^-} + N_{\pi_1^- K_1^+} - B \times \sum_{l=2}^6 (N_{\pi_l^+ K_1^-} + N_{\pi_l^- K_1^+} + N_{\pi_1^- K_l^+} + N_{\pi_1^+ K_l^-}) \quad (3.2)$$

where, B is the normalization constant and the summation is over the total number of events mixed.

Like sign method is another technique to subtract the combinatorial background. In this method, like sign invariant mass pair $\pi^+ K^+$ and $\pi^- K^-$ are sampled in the same event. As the number of reconstructed like sign pair may not be the same as the unlike sign $\pi^- K^+$ and $\pi^+ K^-$ pairs, so to correctly subtract the uncorrelated pairs, the like sign πK invariant mass distribution is estimated as in Eq. 3.3,

$$N_{like \ sign} = 2 \times \sqrt{N_{\pi_1^+ K_1^+} \times N_{\pi_1^- K_1^-}}. \quad (3.3)$$

The like sign invariant mass spectrum is subtracted from the unlike sign pair:

$$N_{K^{*0}} = N_{\pi_1^- K_1^+} + N_{\pi_1^+ K_1^-} - N_{like\ sign}. \quad (3.4)$$

3.1.5 Residual background

Although the combinatorial background is subtracted from the signal (unlike charged kaon and pion distribution) with uncorrelated background distribution, some amount of residual background still remains along with the K^{*0} signal. The sources of residual background are,

- (i) correlated πK pairs emitted within jets.
- (ii) mis-reconstructed πK pairs.
- (iii) effect of elliptic flow.

There are several particles which decay to kaon and pion pairs such as $\rho^0 \rightarrow \pi\pi$, $K_1 \rightarrow K\rho \rightarrow K\pi\pi$, $K^*(1410) \rightarrow K\rho \rightarrow K\pi\pi$, etc and contribute to residual background. Mis-identification of daughter particles, for example pion with momentum larger than 0.7 GeV/ c may be mis-identified as a kaon and vice-versa, can also contribute to the invariant mass and this can't be subtracted, hence it remains as a residual background.

Figure 3.6 shows a typical example of πK invariant-mass distributions for 0–5% centrality in Pb–Pb collisions at $\sqrt{s_{NN}} = 2.76$ TeV for $10 < p_T < 15$ GeV/ c . The K^{*0} signals in different p_T bins for various centrality classes which has been analysed here are shown in the Appendix 3.3. In this thesis chapter, the K^{*0} and \bar{K}^{*0} are averaged i.e $(K^{*0} + \bar{K}^{*0})/2$ and denoted as K^{*0} .

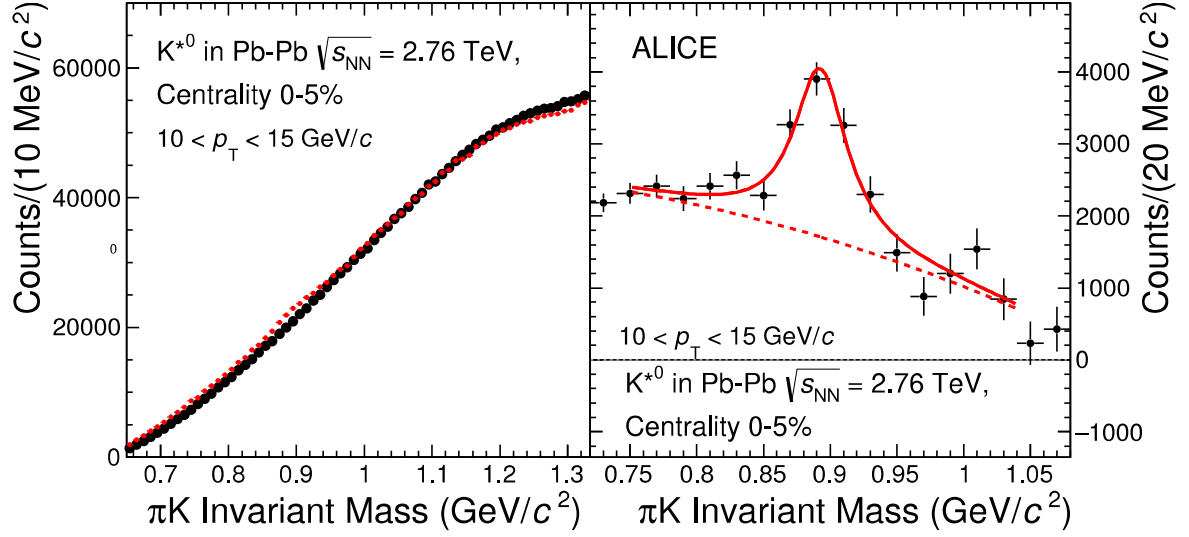


Figure 3.6: Invariant-mass distributions of πK pairs for 0-5% centrality in Pb-Pb collisions at $\sqrt{s_{NN}} = 2.76$ TeV for $10 < p_T < 15$ GeV/c. Left panel shows the unlike charge πK invariant-mass distribution from the same event (red open marker) and normalised mixed event background (solid black marker) are shown. Right panel shows the invariant-mass distribution of πK pair after subtraction of the combinatorial background. The solid curves represent fits to the distributions and the red dashed curves are the components of those fits that describe the residual background.

3.1.6 Yield extraction

The K^{*0} signal is reconstructed via hadronic decay channel $K^{*0} \rightarrow \pi^\pm K^\mp$ with branching ratio of 66.6%. The invariant-mass distribution of the daughter pairs are constructed using unlike-charged kaon and pion pairs. The πK invariant-mass distribution is fitted with a peak fit function (Breit-Wigner) and a polynomial function (second order in invariant mass) to account for the residual background. The K^{*0} M_{inv} fit function is

$$\frac{dN}{dm_{\pi K}} = \frac{Y}{2\pi} \times \frac{\Gamma_0}{(m_{\pi K} - M_0)^2 + \frac{\Gamma_0^2}{4}} + (Am_{\pi K}^2 + Bm_{\pi K} + C), \quad (3.5)$$

where M_0 , Γ_0 are the rest mass and width of K^{*0} invariant mass distribution,

respectively. The width is fixed to the PDG value 47.4 ± 0.6 MeV/ c^2 [8] and Y is yield of the K^{*0} meson. A , B and C are the polynomial fit parameters. The difference in the yield due to keeping the width fix to PDG value and free is considered in the systematic uncertainty.

While fitting the πK invariant-mass distribution with a peak fit function (Eq. 3.5), the mass parameter was kept free. The mass extracted for each p_T and centralities classes are shown in the Fig. 3.7. The measured K^{*0} mass is found to be consistent with PDG value 0.89594 GeV/ c^2 [8]. The K^{*0} yield and mass is measured in different p_T (GeV/ c) bins (0.3, 0.7, 1.2, 1.6, 2.0, 2.5, 3.0, 3.5, 4.0, 5.0, 7.0, 10.0, 15.0, 20.0) for each centrality class.

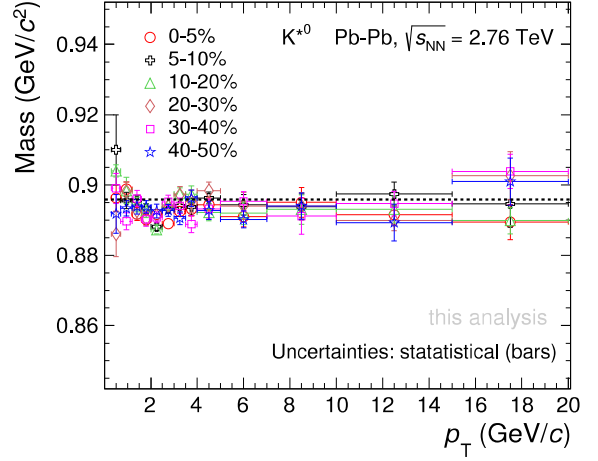


Figure 3.7: K^{*0} mass as a function of p_T for different centralities in Pb-Pb collisions at $\sqrt{s_{NN}} = 2.76$ TeV. The black dotted line represents the vacuum value of K^{*0} mass [8]. The bar represents the statistical uncertainties.

3.1.7 Efficiency correction

The raw yield is normalized to number of accepted events and corrected for the branching ratio (BR) of 66.6% [8], detector acceptance (A) and reconstruction efficiency (ϵ_{rec}). A Monte Carlo event generator HIJING and GEANT 4 (to take care detector geometry) are used for the estimation of the acceptance \times efficiency ($A \times \epsilon_{\text{rec}}$). Figure 3.8 shows $A \times \epsilon_{\text{rec}}$ for various centrality in Pb-Pb collisions at $\sqrt{s_{NN}} = 2.76$ TeV. The decay products of the generated K^{*0} are propagated in GEANT3 [14] (a MC that simulates the ALICE detector material). The $A \times \epsilon_{\text{rec}}$ is the ratio of

generated to reconstructed K^{*0} after passing through the detector simulation. The tracks used are subjected to the PID, pair rapidity and track quality cuts as used in the analysis of real data. The $A \times \epsilon_{\text{rec}}$ has a very mild centrality dependence as shown in Fig. 3.8.

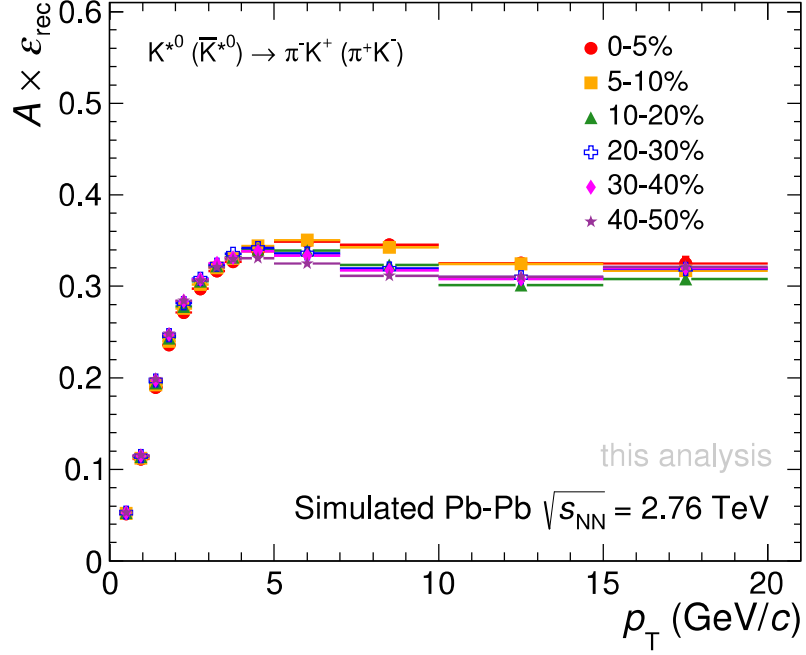


Figure 3.8: The p_T -dependent of acceptance and efficiency of K^{*0} for various centralities in Pb-Pb collisions at $\sqrt{s_{\text{NN}}} = 2.76$ TeV.

3.2 Results

3.2.1 Invariant yield distribution of K^{*0}

The K^{*0} raw yield is extracted by fitting the πK invariant mass signal by Breit-Wigner fit function to each p_T bin and the process is performed in various centralities. Each raw spectrum is corrected for the reconstruction efficiency, detector acceptance and branching ratio as given in Eq. 3.6.

$$\frac{1}{2\pi p_T} \frac{d^2 N}{dy dp_T} = \frac{1}{N_{\text{ev}}} \times \frac{1}{2\pi p_T} \times \frac{dN^{\text{raw}}}{dy dp_T} \times \frac{1}{A \times \epsilon_{\text{rec}} \times BR} \quad (3.6)$$

where N_{ev} is the number of events used and N^{raw} is the raw K^{*0} count.

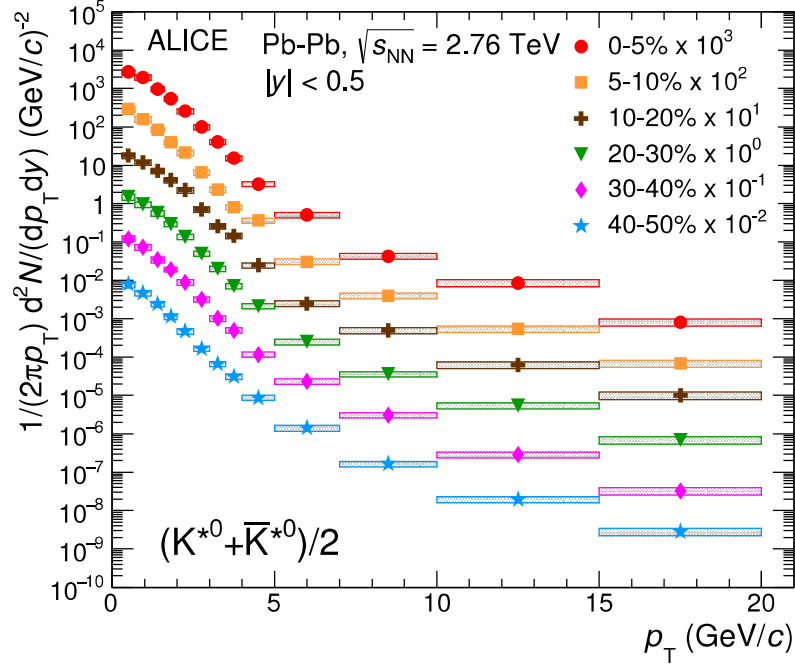


Figure 3.9: K^{*0} invariant yield in different centralities in Pb–Pb collisions at $\sqrt{s_{\text{NN}}} = 2.76$ TeV. Invariant yield is calculated by taking the value of p_T at the corresponding bin centre. The bars and boxes are statistical and systematic uncertainties, respectively [24].

The corrected invariant yield distribution of K^{*0} as a function of p_T in various centralities are showed in Fig. 3.9. The spectra are multiplied by different scale factor for clear visibility.

3.2.2 dN/dy of K^{*0} -meson

The dN/dy value of K^{*0} is calculated by integrating over p_T in the measured region of the spectra and in the unmeasured region, the integral of the extrapolated Blast-

Wave [15] fit function is used. The Blast-Wave function has the form given in Eq. 3.7.

$$\frac{1}{p_T} \frac{d^2 N}{dy dp_T} = \int_0^R r dr m_T I_0\left(\frac{p_T \sinh \rho}{T_{kin}}\right) K_1\left(\frac{m_T \cosh \rho}{T_{kin}}\right), \quad (3.7)$$

where T_{kin} is the kinetic freeze-out temperature, ρ is the velocity profile as given in Eq. 3.8,

$$\rho = \tanh^{-1}(\beta_T) = \tanh^{-1}\left[\left(\frac{r}{R}\right)^n \beta_s\right] \quad (3.8)$$

and $m_T = \sqrt{m^2 + p_T^2}$ is the transverse mass and β_T is the radial flow velocity. K_1 , I_0 are the modified Bessel functions, R is the fireball radius, and r is the radial distance in the transverse plane.

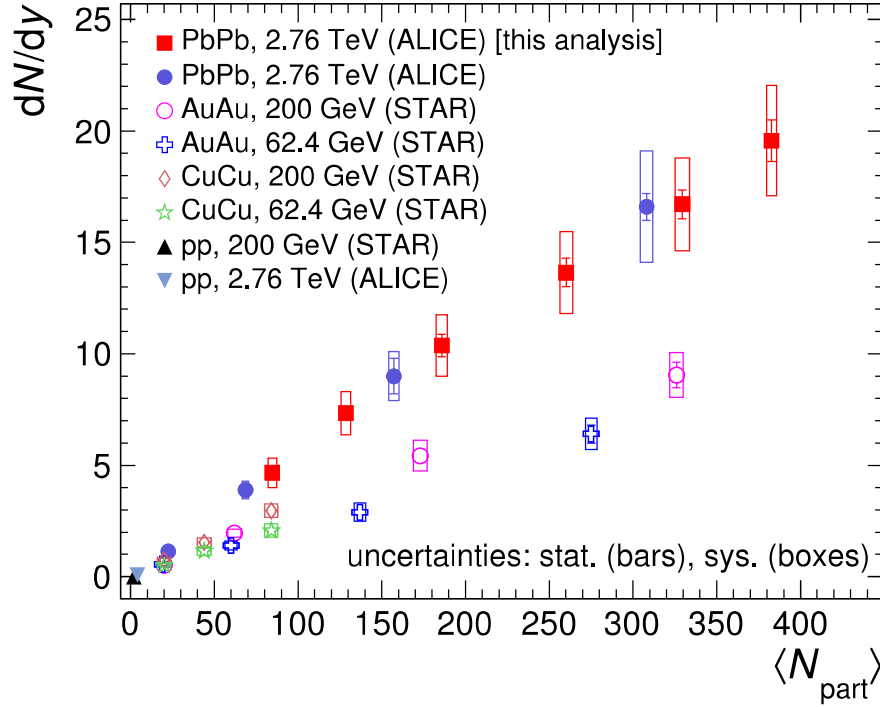


Figure 3.10: dN/dy of K^{*0} meson as function of $\langle N_{part} \rangle$ [24] is compared with the corresponding measurement done by STAR at lower centre of mass energies [5, 6]. Bars represent statistical uncertainties and total systematic uncertainties are represented by empty boxes.

The low- $p_T < 0.3 \text{ GeV}/c$ extrapolation integral from Blast-Wave is about 5% and negligible at high- $p_T (> 20 \text{ GeV}/c)$. The dN/dy values of K^{*0} as a function of $\langle N_{part} \rangle$ is shown in the Fig. 3.10 and also compared with the corresponding measurement from the STAR experiment at lower centre of mass energies [5, 6]. Figure 3.10 also shows the system size dependence (including the pp collisions) of K^{*0} p_T -integrated yield. The dN/dy values increases from peripheral to central collisions and also increases with increase in centre of mass energies.

3.2.3 $\langle p_T \rangle$ of K^{*0} -meson

The average transverse momentum ($\langle p_T \rangle$) of K^{*0} is calculated using Eq. 3.9,

$$\langle p_T \rangle = \frac{\int p_T f(p_T) dp_T}{\int f(p_T) dp_T} \quad (3.9)$$

For the measured region in p_T , $f(p_T)$ is given by the data and for the extrapolated region, the $f(p_T)$ is the Blast-Wave function in the calculation of the $\langle p_T \rangle$ value. The $\langle p_T \rangle$ is also calculated using Lévy-Tsallis function [25] and the difference in the $\langle p_T \rangle$ values have been considered in the systematic uncertainty. The $\langle p_T \rangle$ of K^{*0} is shown in Fig. 3.11, and compared with the corresponding values from the STAR experiment [5, 6]. The $\langle p_T \rangle$ values increases with the increase in number of participant nucleons and then saturates. The $\langle p_T \rangle$ also increases with increase in centre of mass energies.

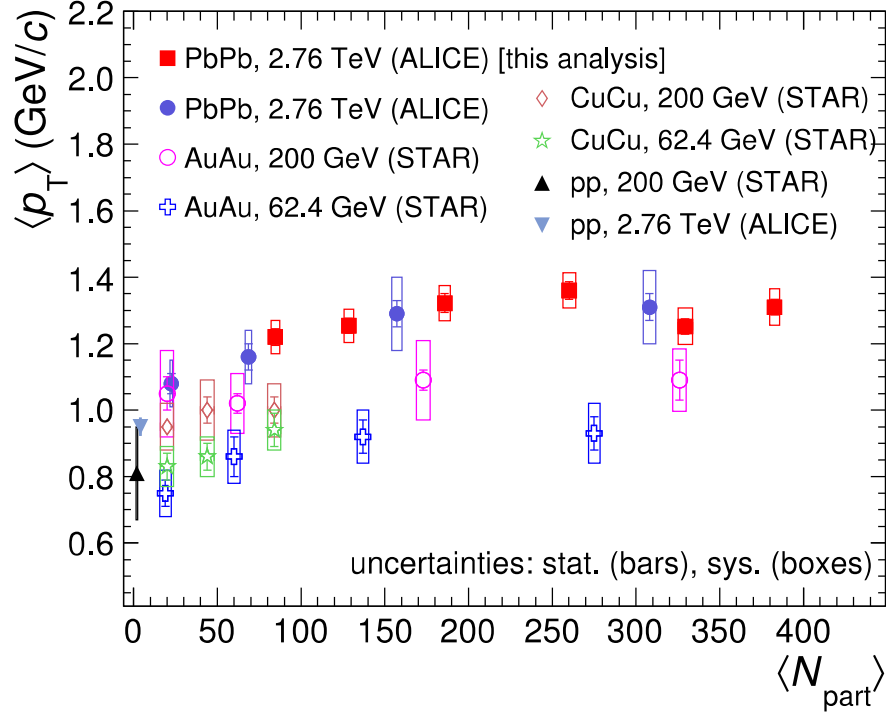


Figure 3.11: $\langle p_T \rangle$ of K^{*0} -meson as function of $\langle N_{part} \rangle$ is compared with the corresponding measurement of STAR experiment at lower centre of mass energies [5, 6]. Bars and empty boxes represents statistical and total systematic uncertainties, respectively.

Centrality	dN/dy	K^{*0}/K^-	$\langle p_T \rangle$ (GeV/c)
0–5%	$19.56 \pm 0.93 \pm 2.48 \pm 0.097$	$0.180 \pm 0.008 \pm 0.026 \pm 0.023$	$1.310 \pm 0.023 \pm 0.055$
5–10%	$16.71 \pm 0.65 \pm 2.08 \pm 0.083$	$0.186 \pm 0.007 \pm 0.026 \pm 0.024$	$1.252 \pm 0.023 \pm 0.055$
10–20%	$13.65 \pm 0.63 \pm 1.84 \pm 0.009$	$0.200 \pm 0.009 \pm 0.026 \pm 0.023$	$1.360 \pm 0.026 \pm 0.053$
20–30%	$10.37 \pm 0.50 \pm 1.38 \pm 0.010$	$0.225 \pm 0.011 \pm 0.025 \pm 0.023$	$1.322 \pm 0.028 \pm 0.053$
30–40%	$7.35 \pm 0.28 \pm 0.97 \pm 0.146$	$0.245 \pm 0.009 \pm 0.025 \pm 0.021$	$1.254 \pm 0.023 \pm 0.050$
40–50%	$4.66 \pm 0.20 \pm 0.65 \pm 0.111$	$0.258 \pm 0.011 \pm 0.025 \pm 0.022$	$1.220 \pm 0.025 \pm 0.050$

Table 3.2: The values of dN/dy , ratio to K^- and $\langle p_T \rangle$ for different centrality classes in Pb–Pb collisions at $\sqrt{s_{NN}} = 2.76$ TeV. In each entry, the first uncertainty is statistical and the second is systematic, excluding the normalization uncertainty. A third uncertainty is also given i.e normalization and uncorrelated uncertainty for dN/dy and K^{*0}/K^- .

3.2.4 p_T -integrated particle ratio

The dN/dy value of K^{*0} for different centrality in Pb–Pb collisions at $\sqrt{s_{NN}} = 2.76$ TeV is given in the Table 3.2 and this is used for the calculation p_T -integrated K^{*0}/K^- ratio. The K^{*0}/K^- ratio as function of proxy of system size $\langle dN_{ch}/d\eta \rangle^{1/3}$ [16] is shown in the Fig. 3.12. For the calculation of $\langle dN_{ch}/d\eta \rangle$ value, the combined information from ITS and TPC are used [12]. The K^{*0}/K^- ratio in Pb–Pb collisions at $\sqrt{s_{NN}} = 2.76$ TeV is compared with ϕ/K^- ratio along with the corresponding ratios in pp collisions at $\sqrt{s} = 2.76$ TeV and 7 TeV. The K^{*0}/K^- ratio measured in this analysis is consistent with the trend observed previously [26] (also shown in Fig. 3.12). In the most central Pb–Pb collisions, the K^{*0}/K^- ratio is suppressed as compared to pp and peripheral Pb–Pb collisions unlike ϕ/K^- ratio. This suppression suggests that K^{*0} decays inside the hadronic medium due to short lifetime (~ 4.2 fm/c) and the decay daughters have re-scattered in the hadronic medium which reduces the measurable K^{*0} yield. This aspect is confirmed by thermal model calculations [17], which over predict the K^{*0}/K^- ratio but well predicts ϕ/K^- ratio. Thermal model does not have re-scattering effect included in the calculations. The hadronic cascade model EPOS3 [18] includes UrQMD to take care re-scattering and regeneration effects. EPOS3 reproduces the K^{*0}/K and ϕ/K ratios trend in Pb–Pb collisions, which suggests that the observed suppression of K^{*0}/K ratio is due to the re-scattering of K^{*0} decay daughters inside the hadronic medium. However, the model quantitatively fails to reproduce the data. So, this observation suggests that re-scattering effect is more dominant over the regeneration in the hadronic medium formed in Pb–Pb collisions at $\sqrt{s_{NN}} = 2.76$ TeV, which is consistent with the previous observations [5, 6, 7, 26, 8].

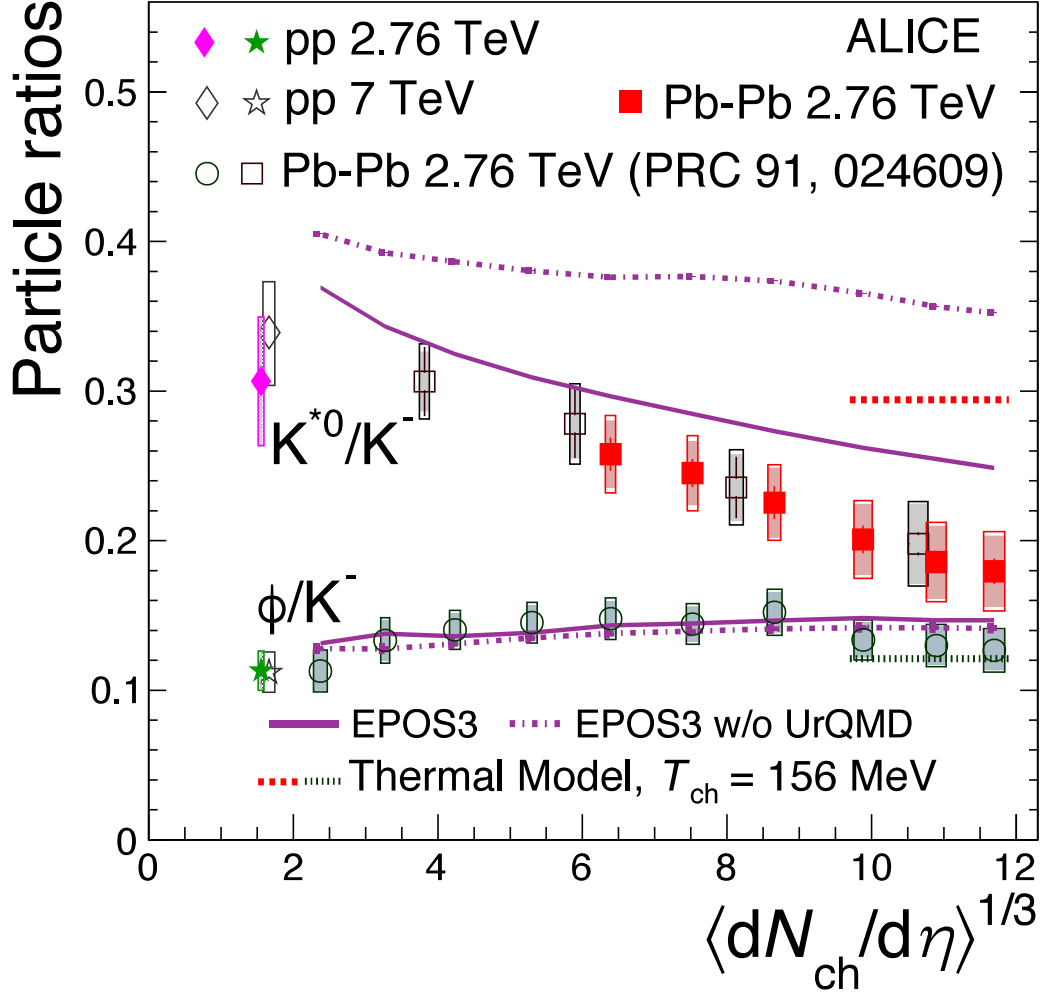


Figure 3.12: K^{*0}/K^- ratio as a function of $\langle dN_{ch}/d\eta \rangle^{1/3}$ measured at mid-rapidity [19] in pp collisions at $\sqrt{s} = 2.76$ TeV and 7 TeV [20], and Pb–Pb collisions at $\sqrt{s_{NN}} = 2.76$ TeV. Bars represent statistical uncertainties, shaded and empty boxes represent the uncorrelated and total systematic uncertainties, respectively. The thermal model prediction at chemical freeze-out temperature of 156 MeV for the central collisions [17] are shown. The EPOS3 model calculations are shown as violet band for various centralities [18].

3.2.5 p_T -dependent particle ratio

In order to investigate the hadronic re-scattering effect in various p_T regions, the p_T -differential resonance to stable particle ratios such as K^{*0}/K and ϕ/K ratios are

studied. The K^{*0} and ϕ ratios with respect to kaon are shown in the Fig. 3.13a for pp and most central (0–5%) Pb–Pb collisions at $\sqrt{s_{\text{NN}}} = 2.76$ TeV. In the low- p_{T} (< 2 GeV/ c) region, the K^{*0}/K ratio for central Pb–Pb collisions is less than the pp collisions unlike the case for the ϕ/K ratio. The suppression of K^{*0}/K is consistent with the K^{*0} re-scattering scenario in the hadronic phase due to which the signal gets lost and K^{*0} yield is reduced whereas ϕ meson yields remain unaffected due to longer lifetime (10 times larger) than K^{*0} .

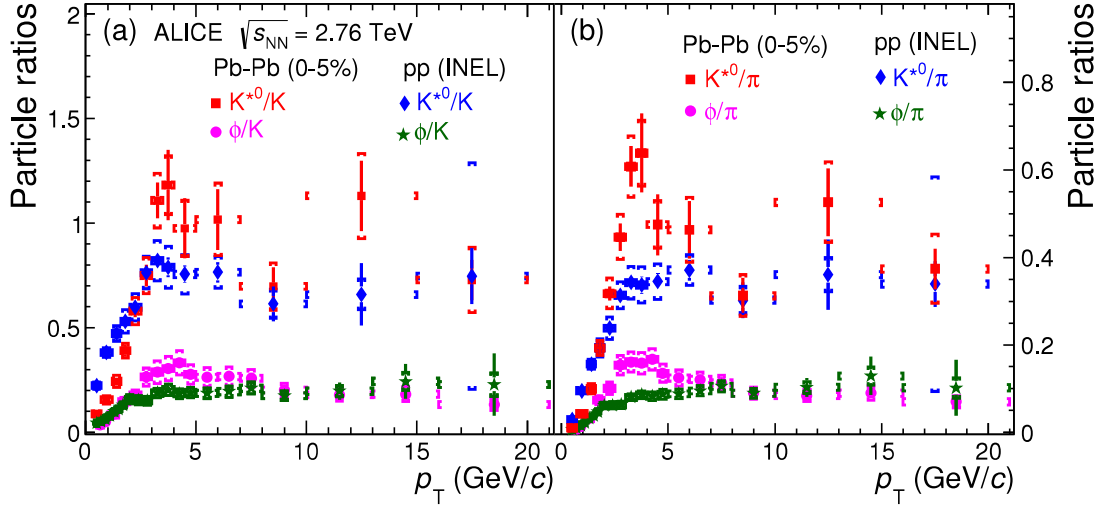


Figure 3.13: p_{T} -dependent particle yield ratios of K^{*0}/K and ϕ/K in the panel (a) and K^{*0}/π and ϕ/π in panel (b) for pp and Pb–Pb collisions at $\sqrt{s_{\text{NN}}} = 2.76$ TeV. The $(K^{*0} + \bar{K}^{*0})$, $(K^+ + K^-)$ and $(\pi^+ + \pi^-)$ are denoted as K^{*0} , K , π , respectively. The bar and cap on the represents the statistical and systematic uncertainties, respectively.

Similarly, Fig. 3.13b shows the p_{T} -dependent of K^{*0}/π and ϕ/π ratios for pp and most central (0–5%) Pb–Pb collisions at $\sqrt{s_{\text{NN}}} = 2.76$ TeV. These K^{*0}/π and ϕ/π ratios saturate at $p_{\text{T}} \sim 4$ GeV/ c for pp collisions unlike Pb–Pb collisions where the ratios increases up to 4 GeV/ c followed by a decreasing trend up to 8 GeV/ c and then it saturates. An enhancement in K^{*0}/π for central Pb–Pb with respect to pp collisions at intermediate- p_{T} (~ 3 GeV/ c) has been observed. Similar observation

(meson-to-meson enhancement) has been reported in the reference [21] for K/π ratio and is attributed to radial flow. In both pp and central Pb–Pb collisions, all these ratios K^{*0}/K , ϕ/K , K^{*0}/π and ϕ/π are similar at high p_T (> 8 GeV/ c), which suggests fragmentation as the dominant hadron production mechanism in this p_T range. These observations for particle ratios measurement presented here are consistent with the previously reported p/π and K/π ratios [21].

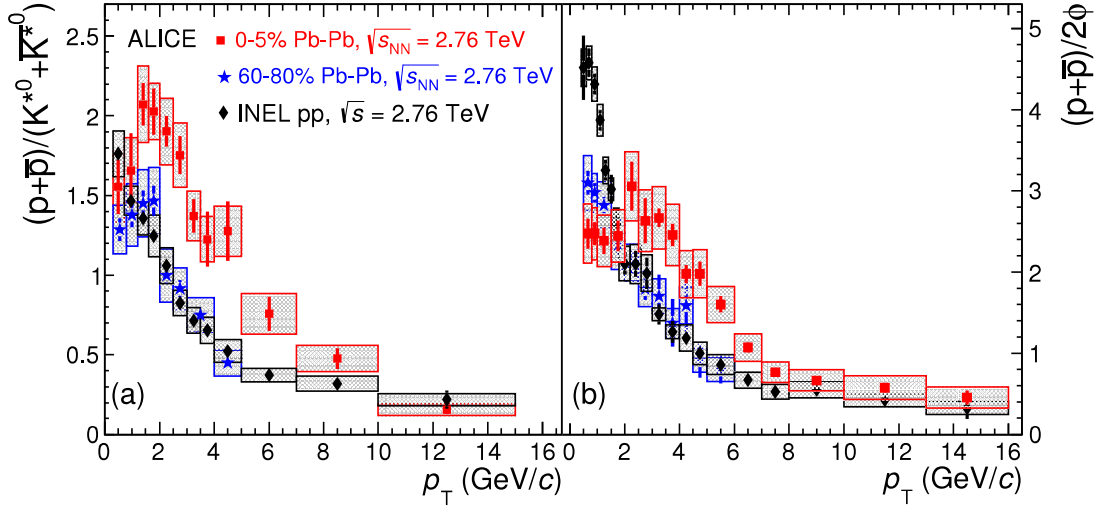


Figure 3.14: p_T -dependent particle yield ratios of p/K^{*0} and p/ϕ in the panel are shown in panel (a) and (b), respectively for pp and Pb–Pb collisions at $\sqrt{s_{NN}} = 2.76$ TeV [26, 24]. The bar and box on the data point represents the statistical and systematic uncertainties, respectively.

The p/K^{*0} and p/ϕ ratios as a function of p_T in pp and Pb–Pb collisions are shown in the (a) and (b) panel of Fig. 3.14, respectively. The spectral evolution from pp to Pb–Pb ratios as a function of p_T for particles having similar masses (p , K^{*0} and ϕ) are shown. The p/ϕ ratio shows a weak p_T dependence ($p_T < 4$ GeV/ c). The similarity in spectral shape of similar masses particle having different valence quarks suggest that the shapes are mostly driven by masses as per the hydrodynamic model expectation [23]. At high- p_T (> 8 GeV/ c), p/K^{*0} and p/ϕ ratios are similar in pp

and Pb–Pb collisions within uncertainties which indicate the parton fragmentation dominance in this p_T region.

3.2.6 Nuclear modification factor (R_{AA} , R_{CP})

The nuclear modification factor (R_{AA}) is defined in Eq. 3.10 which is the ratio between the yield of particles in heavy-ion collisions to that of pp collisions and scaled with average nuclear overlap function. Another representation of nuclear modification factor is also defined as R_{CP} ; C and P stand for central and peripheral collisions, respectively.

$$R_{AA} = \frac{1}{\langle T_{AA} \rangle} \times \frac{(d^2N/dydp_T)_{AA}}{(d^2\sigma/dydp_T)_{pp}}; \quad R_{CP} = \frac{\langle N_{coll}^P \rangle (d^2N/dydp_T)_{AA}^C}{\langle N_{coll}^C \rangle (d^2N/dydp_T)_{AA}^P} \quad (3.10)$$

where $\langle T_{AA} \rangle = \langle N_{coll} \rangle / \sigma_{inel}$ is the average nuclear overlap function. The average number of binary nucleon-nucleon collisions ($\langle N_{coll} \rangle$) is calculated using Glauber MC [26] simulations and the inelastic pp cross section ($\sigma_{inel} = 62.8$ mb) is from [27].

The R_{AA} is used to study the medium formed in ultra-relativistic heavy-ion collisions. It is sensitive to the density and size of the system formed. The R_{AA} is also sensitive to the particle production dynamics and the partons energy loss mechanism in the medium. The nuclear modification factor would correspond to unity at high p_T , if the nuclear collision were a simple superposition of nucleon-nucleon collisions. Any deviation of R_{AA} from unity indicates the presence of in-medium effects. The centrality evolution of K^{*0} R_{AA} suggests formation of a dense partonic medium in central Pb-Pb collisions at $\sqrt{s_{NN}} = 2.76$ TeV. In Fig. 3.15, nuclear modification factor of K^{*0} in three different centrality classes as function of p_T is shown. The suppression is maximum for most central (0-5%) collisions as compared to semi central collisions

(40-50%). A centrality evolution of K^{*0} R_{AA} is observed.

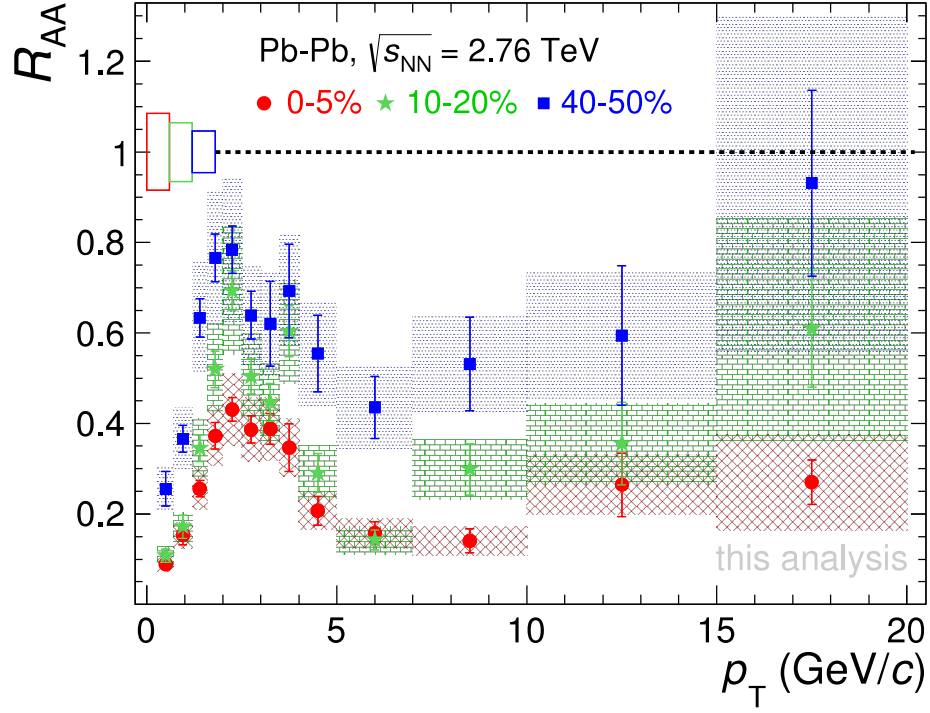


Figure 3.15: Transverse momentum (p_T) dependent of K^{*0} R_{AA} is shown for three different centrality classes in Pb–Pb collisions at $\sqrt{s_{NN}} = 2.76$ TeV. The bars and grid boxes represents the statistical and systematic uncertainties, respectively. The boxes around unity is the uncertainty on the R_{AA} normalization (see Tab. 3.2) including the $\langle T_{AA} \rangle$ uncertainty.

The K^{*0} R_{AA} in various centralities from most central 0–5% to 40–50% in Pb–Pb collisions at $\sqrt{s_{NN}} = 2.76$ TeV is shown in Fig. 3.16 and are compared with the charged hadrons and ϕ R_{AA} . The R_{AA} of K^{*0} is found to be lower than unity for $p_T > 8$ GeV/ c in most central and semicentral Pb–Pb collisions. For $p_T < 2$ GeV/ c , the R_{AA} of K^{*0} is found to be less than ϕ and the charged hadron R_{AA} and the magnitude of this additional suppression reduces as one goes from central to peripheral collisions. This change is consistent with re-scattering scenario in Pb–Pb collisions which is maximum for central Pb–Pb collisions [26]. The R_{AA} of all the identified particles such as K^{*0} ,

ϕ and charged hadrons are observed to be similar at high- p_T (> 8 GeV/ c) and the magnitude of R_{AA} increases from most central to peripheral collisions.

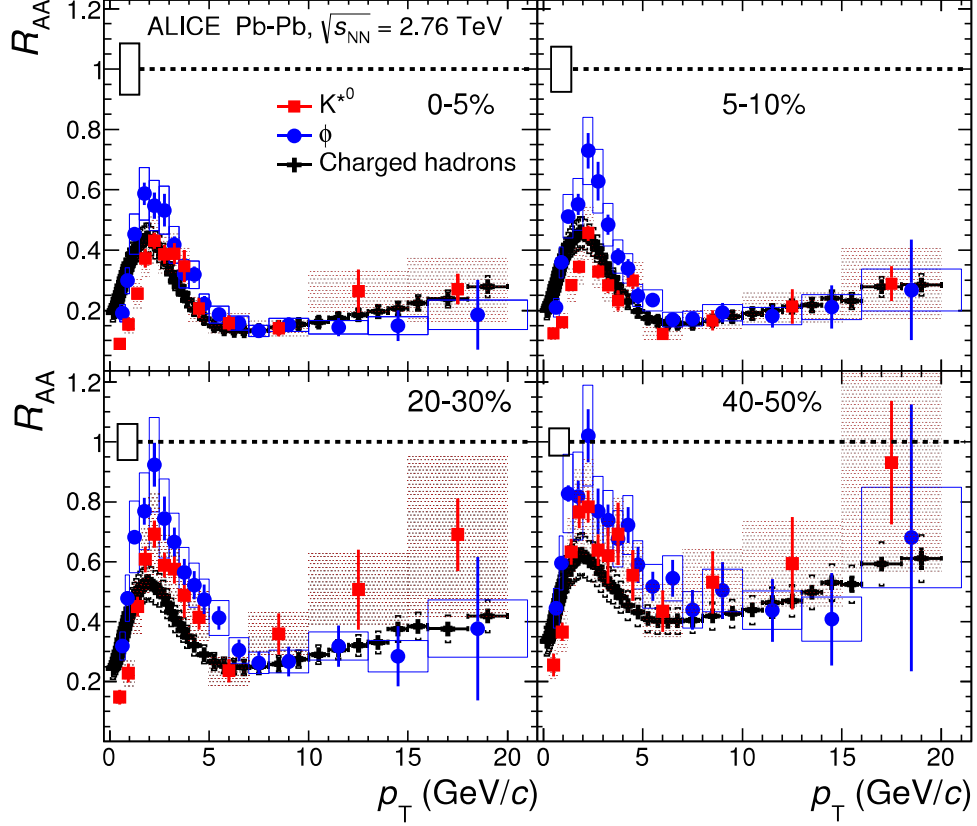


Figure 3.16: p_T -dependent of K^{*0} meson R_{AA} for various centrality classes in Pb–Pb collisions at $\sqrt{s_{NN}} = 2.76$ TeV. The R_{AA} is also compared with ϕ and charged hadrons R_{AA} [28]. The bars and boxes represents the statistical and systematic uncertainties, respectively. The boxes around unity is the uncertainty on the R_{AA} normalization (see Tab. 3.2) including the $\langle T_{AA} \rangle$ uncertainty.

The comparison of K^{*0} R_{AA} with other identified particles like ϕ , π , K and p [21] for 0-5% is shown in Fig. 3.17. For p_T range of 2–6 GeV/ c , the K^{*0} R_{AA} is found to be similar to kaon. Although ϕ and proton have similar masses, they have different R_{AA} trend. The difference in R_{AA} of proton and ϕ at RHIC was thought to be the effect of hadronisation via parton recombination [29, 30, 31]. But, in central Pb–Pb collisions at LHC, the p/ϕ ratio is observed to be flat for $p_T < 4$ GeV/ c (see also

Fig. 3.14b). This suggests that shape of the p_T spectra is determined by mass, so may not be necessary to invoke recombination model. At high- p_T (> 8 GeV/ c), K^{*0} along with pion, kaon, proton [21] and ϕ R_{AA} show similar suppression within the uncertainties. This observation has ruled out all models where suppression of different light flavoured species are considered to be dependent on their mass and it has also applied a stringent constraint on the models which deals with the fragmentation and energy loss mechanisms [32, 33, 34].

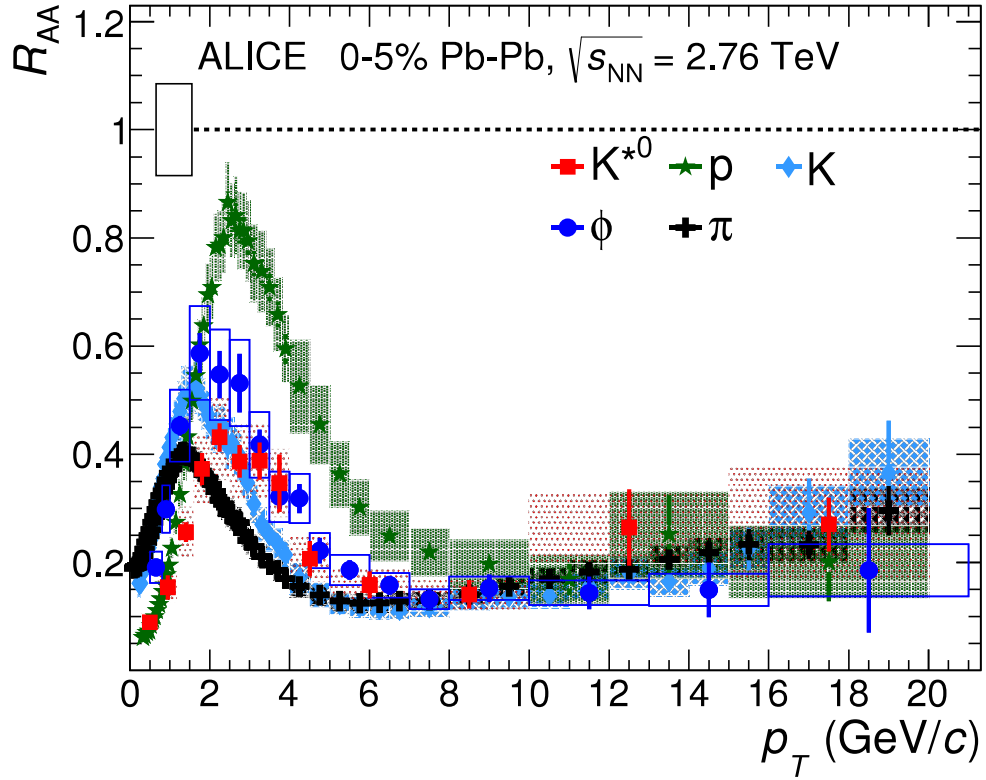


Figure 3.17: The R_{AA} for K^{*0} meson as a function of p_T is compared with ϕ and π , K and p [21] R_{AA} for 0–5% centrality in Pb–Pb collisions at $\sqrt{s_{NN}} = 2.76$ TeV. The bars and boxes represents the statistical and systematic uncertainties, respectively. The boxes around one is the uncertainty on the R_{AA} normalization (see Tab. 3.2) including the $\langle T_{AA} \rangle$ uncertainty.

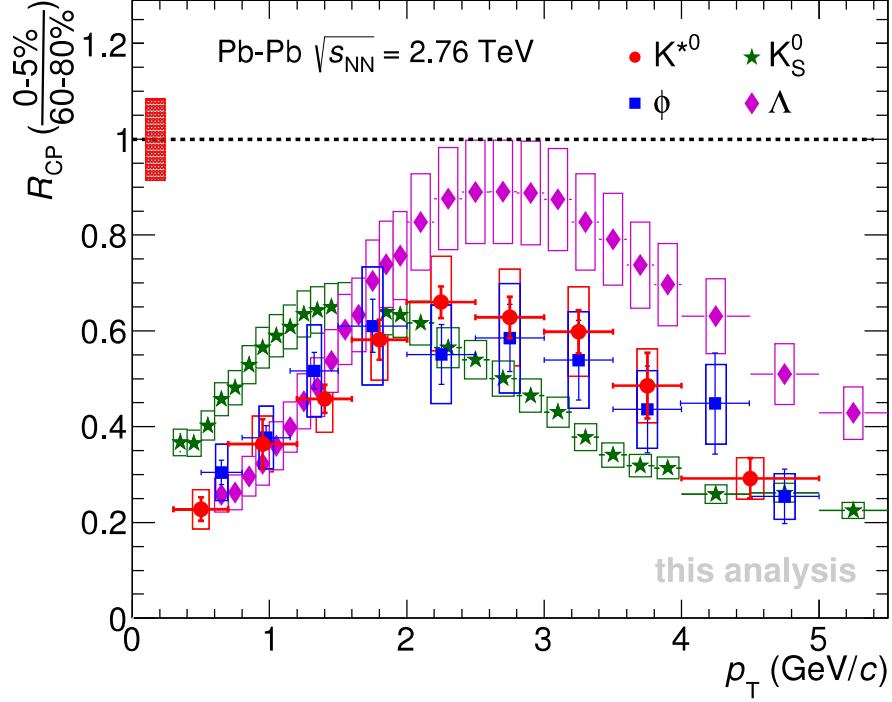


Figure 3.18: The R_{CP} for K^{*0} meson as a function of p_T is compared with the corresponding value of K_S^0 , ϕ and Λ [24] R_{AA} in Pb–Pb collisions at $\sqrt{s_{NN}} = 2.76$ TeV. The bars and boxes represents the statistical and systematic uncertainties, respectively.

For R_{CP} measurement the pp reference is not used unlike the R_{AA} . In the nuclear-nuclear collisions, the R_{CP} is calculated by taking the particle yield ratio between the central and peripheral collisions scaled with the corresponding binary collisions (Eq. 3.10). The R_{CP} of K^{*0} is compared with the R_{CP} of K_S^0 , ϕ and Λ in Pb–Pb collisions at $\sqrt{s_{NN}} = 2.76$ TeV and is shown in the Fig. 3.18 [22]. The suppression of K^{*0} as observed in R_{AA} is approximately 2.5 times more than the corresponding R_{CP} measurement at low- p_T . This significant difference between the K^{*0} R_{AA} and R_{CP} is might be due to pp reference rather than nuclear effects. At low- p_T (< 2 GeV/c), the similar mass particle have similar value of suppression. The peak value in the R_{CP} of Λ is observed at relatively higher p_T as compared to K^{*0} and K_S^0 . The peak shift might be due to the radial flow of the particle which is more for the higher mass

particle.

3.2.7 Systematic uncertainty study

The systematic uncertainty study is performed using the procedure described in Ref. [35] and shown in the Fig 3.19. In this procedure, a test commonly known as “Barlow test” is performed. Let us consider an example, one measurement is performed with default settings and the yield is denoted as Y_{def} and the corresponding statistical uncertainty is σ_{def} . Another measurement with some systematic variation (e.g. signal peak fitting range variation) is performed and the yield and statistical uncertainty are Y_{sys} and σ_{sys} , respectively. A ratio is defined as $R = (Y_{\text{def}} - Y_{\text{sys}}) / \Delta$, where $\Delta = \sqrt{\sigma_{\text{def}}^2 - \sigma_{\text{sys}}^2}$; and when $R \leq 1$, then it is rejected and not considered for systematic error because the measurement is consistent within the statistical uncertainties. For other cases, it is considered as a source of systematic uncertainty. The main sources of systematic uncertainties with a brief description are given below.

3.2.7.1 Uncertainties due to signal and yield extraction method

The invariant mass distribution of pions and kaons are fitted with a Breit-Wigner along with a polynomial function to take care the remaining residual background as describe in the section 3.1.5. The shape of the remaining residual background are different for each p_T bin and centrality classes which affect the raw yield extraction of K^{*0} . Hence, different methods of signal extraction as given below has been studied and used to extract the systematic uncertainty in K^{*0} yield.

- (i) The K^{*0} peak and residual background fit range variations. The default range of fitting the πK invariant mass is 0.77-1.03 GeV/ c^2 and the variation for systematic studies are 0.78-1.06 GeV/ c^2 , 0.76-1.04 GeV/ c^2 and 0.75-1.05 GeV/ c^2 .
- (ii) Normalization of mixed event background range variations. The default normal-

ization range is 1.1-1.3 GeV/ c^2 and for systematic study the variation includes 1.1-1.5 GeV/ c^2 , 1.2-1.3 GeV/ c^2 , 1.0-1.1 GeV/ c^2 and 0.7-0.8 GeV/ c^2

(iii) The second order polynomial is taken as the default function to describe the residual background and polynomial of third order is considered for the systematic study.

(iv) In the default setting, the K^{*0} raw yield is extracted by keeping the width of Breit-Wigner function fixed to K^{*0} PDG value and then the width is freed to consider the changed in yield for the systematic study.

3.2.7.2 Uncertainty due to mis-identification of particles

The pions and kaons are selected using the TPC average energy loss ($\langle dE/dx \rangle$) within two standard deviation (σ). For the systematic variation the σ is varied on both side of the default cut, i.e (i) $|N\sigma| < 1.5$ and (ii) $|N\sigma| < 2.5$.

3.2.7.3 Uncertainty due to track selection and cut variations

The details about the good quality track selection is described in the section 3.1.3. The uncertainty in global tracking is 5% for the single track. As the K^{*0} is reconstructed from it's two decay daughter (pion and kaon) tracks, so the global tracking efficiency of 10% has been used in this analysis. For the systematic checks of different track selection cuts such as minimum number of TPC crossed rows, the minimum crossed rows to findable cluster ratio, the distance of closest approach in z (DCA_z) and xy (DCA_{xy}) directions are varied. The systematic uncertainty varies from 3 to 6% depending on p_T and centralities.

K ^{*0} in Pb–Pb collisions at $\sqrt{s_{\text{NN}}} = 2.76$ TeV	
Systematic variation	Uncertainty in %
Global tracking efficiency	10
Track selection	3-6
Particle identification	4-8
Material budget	<1
Yield extraction	4-15
p_{T} -spectra extrapolation	5
Total	12-21

Table 3.3: Systematic uncertainties in the yield of K^{*0} measurement for Pb–Pb collisions at $\sqrt{s_{\text{NN}}} = 2.76$ TeV. Where a constant value is given (global tracking efficiency), it is p_{T} independent. The values given in ranges are minimum and maximum uncertainties depending on p_{T} and centrality classes.

3.2.7.4 Uncertainty due to material budget

The tracking of the particle is affected by the detector material. As the energy loss of the particles depends on the type of detector material used and hence it needs to be taken into account. The uncertainty associated to ALICE material budget is about 1% for low- p_{T} (< 2 GeV/ c) and negligible at high- p_{T} . The detailed study is performed in the reference [37] and the uncertainty values have been taken from it.

3.2.7.5 Estimation of total systematic uncertainty

In the Fig. 3.19, p_{T} -dependent systematic uncertainty summary details with individual contributions for various centralities are given. The individual contributions of fractional systematic uncertainties are added in quadrature to get the total systematic uncertainties.

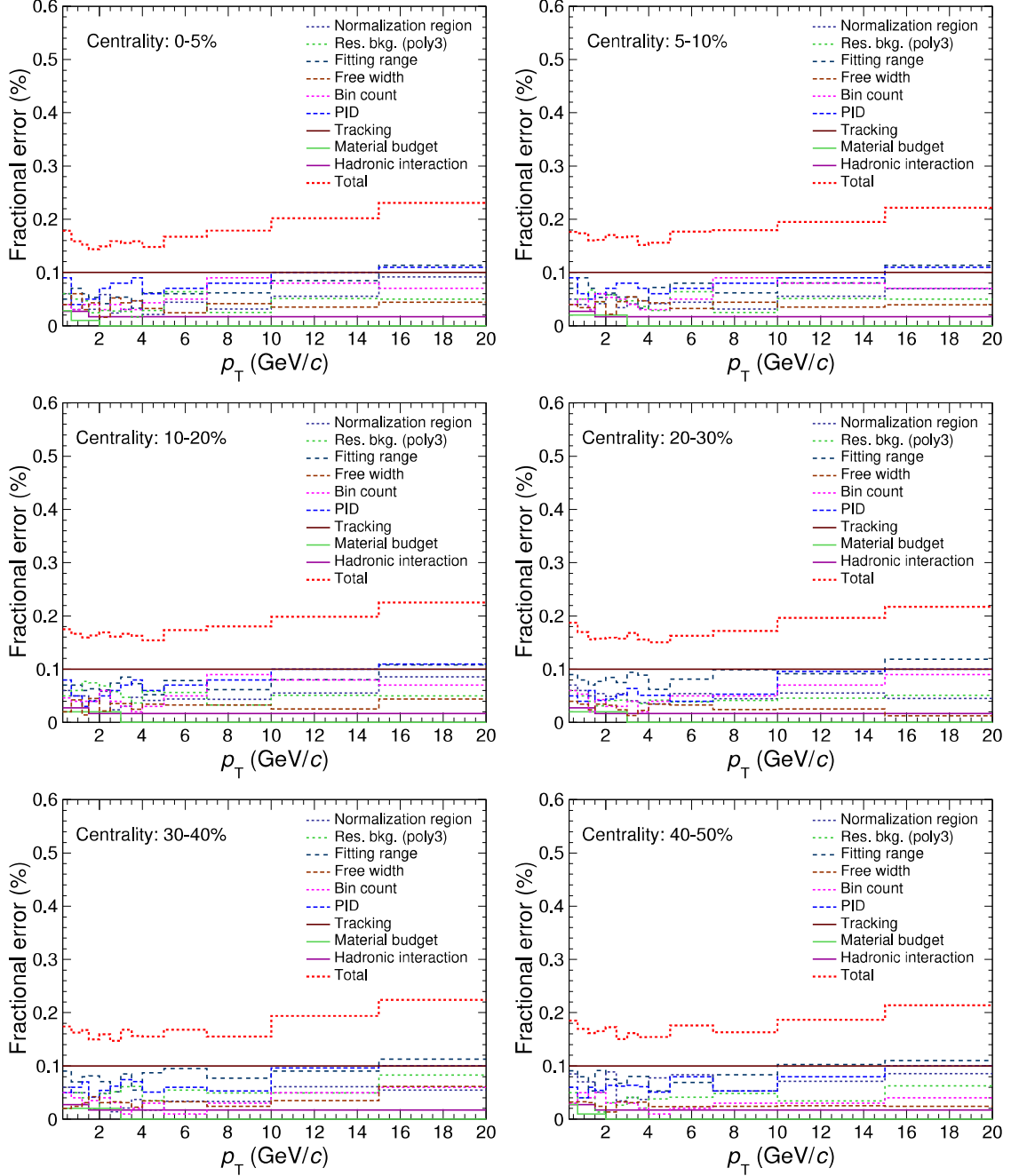


Figure 3.19: Summary of fractional systematic errors (in %) of K^{*0} p_T -spectra in different p_T bins for 0-5%, 5-10%, 10-20%, 20-30%, 30-40% and 40-50% centralities in Pb-Pb collisions at $\sqrt{s_{NN}} = 2.76$ TeV. Various sources of error are represented by different colour lines.

3.2.8 Summary

The K^{*0} resonance production in Pb–Pb collisions at $\sqrt{s_{NN}} = 2.76$ TeV using the high statistics data collected in 2011 by the ALICE detector at LHC has been studied. The spectra are measured in finer centrality classes with a high- p_T reach up to 20 GeV/ c . The p_T -integrated resonance to stable particle ratio K^{*0}/K shows a decreasing trend with the increase in system size, unlike ϕ/K . This observation is understood by considering the lifetime of these resonance particles. The K^{*0} decays inside the medium and hence the decay daughters (pions and kaons) re-scatter with other medium particles by changing their momentum. So, the reconstruct of parent K^{*0} via decay daughters invariant-mass can not be done and hence the K^{*0} signal is lost unlike ϕ which decays outside the medium. When the system size is bigger, i.e. in central collisions, the re-scattering effect is more prominent as compared to peripheral Pb–Pb and pp collisions. The presence of the re-scattering effect is further confirmed the Thermal and EPOS3 model calculations. The Thermal model over predicts the K^{*0}/K ratio and well describes the ϕ/K ratio and this is because of the re-scattering effect is not included in this thermal model. EPOS3 which includes re-scattering effect, well predicts the observed decreasing trend of the K^{*0}/K ratio qualitatively.

For further understanding of particle production mechanism in different p_T regions, p_T -dependent particle ratios has been extracted. In central Pb–Pb collisions, the p_T -dependent K^{*0}/K ratio is suppressed for $p_T < 2$ GeV/ c with respect to pp collisions, indicating the dominance of the re-scattering effect at low- p_T . The p_T -dependent K^{*0}/K and K^{*0}/π ratios in central Pb–Pb collisions show an enhancement at $p_T \sim 3$ GeV/ c as compared to pp collisions, indicating strong radial flow at LHC energies. The nuclear modification factor R_{AA} of K^{*0} is observed to be less than unity at high- p_T (> 8 GeV/ c) for central collisions indicating the partonic medium forma-

tion at LHC energies. The R_{AA} of K^{*0} is also compared to other identified particles such as ϕ , π , K , p and at high- p_T ($p_T > 8 \text{ GeV}/c$) the suppression of all these particles are found to be of the similar order. The particle ratios such as K^{*0}/π , K^{*0}/K , ϕ/π and ϕ/K are found to be of similar order for pp and Pb–Pb collisions in this p_T range. These observations indicate the partonic energy loss is particle species independent for light quark flavors (u, d, s) and particle production mechanism is dominated by fragmentation in vacuum in this kinematic regime. This also rejects all those models where the energy loss mechanism depends on light quark content and hadron masses.

Bibliography

- [1] (STAR Collaboration) J. Adams *et al.*, Nucl. Phys. A 757, 102-183 (2005).
- [2] M. Gyulassy *et al.*, Nucl. Phys. A 750, 30-63 (2005).
- [3] Olive, K. A. and others (Particle Data Group), Chin. Phys. C 38, 090001 (2014).
- [4] J. Rafelski and B. Müller, Phys. Rev. Lett. 48, 1066 (1982).
- [5] (STAR Collaboration) J. Adams *et al.*, Phys. Rev. C 71, 064902 (2005).
- [6] (STAR Collaboration) M. M. Aggarwal *et al.*, Phys. Rev. C 84, 034909 (2011).
- [7] (STAR Collaboration) Sadhana Dash's Ph.D thesis, HBNI (2010).
- [8] (ALICE Collaboration) Subhash Singha's Ph.D thesis, HBNI (2014).
- [9] (ALICE Collaboration) B. Abelev *et al.*, Phys. Rev. C 91, 024609 (2015).
- [10] (ALICE Collaboration) J. Adam *et al.*, Phys. Lett. B 763, 238 (2016).
- [11] M. L. Miller *et al.*, Annu. Rev. Nucl. Part. Sci. 57, 205 (2007).
- [12] (ALICE Collaboration) B. Abelev *et al.*, Phys. Rev. C 88, 044909 (2013).
- [13] (ALICE Collaboration) B. B. Abelev *et al.*, Int. J. Mod. Phys. A 29, 1430044 (2014).

- [14] R. Brun, *et al.*, CERN-W5013, CERN-W-5013, W5013, W-5013 (1994),
- [15] Ekkard Schnedermann *et al.*, Phys. Rev. C 48, 2462 (1993).
- [16] (ALICE Collaboration) K. Aamodt *et al.*, Phys. Lett. B696 328, (2011).
- [17] J. Stachel, *et al.*, J. Phys. Conf. Ser. 509, 012019 (2014).
- [18] A. G. Knospe, *et al.*, Phys. Rev. C 93, 014911 (2016).
- [19] (ALICE Collaboration), K. Aamodt *et al.*, Phys. Lett. B 696, 328-337, (2011).
- [20] (ALICE Collaboration) B. Abelev *et al.*, Eur. Phys. J. C 72, 2183 (2012).
- [21] (ALICE Collaboration) B. Abelev *et al.*, Phys. Lett. B 736, 196-207 (2014).
- [22] (ALICE Collaboration) B. Abelev *et al.*, Phys. Rev. Lett. 111, 222301 (2013).
- [23] C. Shen *et al.*, Phys. Rev. C 84 044903 (2011).
- [24] (ALICE Collaboration) J. Adam *et al.*, Phys. Rev. C 95, 064606 (2017).
- [25] C. Tsallis, J. Stat. Phys. 52, 479 (1988).
- [26] M. L. Miller *et al.*, Ann. Rev. Nucl. Part. Sci. 57, 205-243 (2007).
- [27] (ALICE Collaboration) B. Abelev *et al.*, Phys. Rev. C 88, 044909 (2013).
- [28] (ALICE Collaboration) B. Abelev *et al.*, Phys. Lett. B 720, 52-62 (2013).
- [29] (PHENIX Collaboration) A. Adare *et al.*, Phys. Rev. C 83, 024909 (2011).
- [30] J. Ma, J. Phys. G30, S543-S548 (2004).
- [31] (STAR Collaboration) G. Agakishiev *et al.*, Phys. Rev. Lett. 108, 072302 (2012).
- [32] R. Bellwied, and C. Markert, Phys. Lett. B 691, 208-213 (2010).

- [33] W. Liu and R. J Fries, Phys. Rev. C 77, 054902 (2008).
- [34] W. Liu, C. M. Ko and B. W. Zhang, Phys. Rev. C 75, 051901 (2009).
- [35] R. Barlow, arXiv:hep-ex/0207026 (2002).
- [36] (ALICE Collaboration) K. Aamodt *et al.*, Eur. Phys. J. C 71, 1594 (2011).
- [37] (ALICE Collaboration) B. Abelev *et al.*, Phys. Lett. B 720, 52 (2013).

3.3 Appendix

In the Table 3.43.5, the following abbreviation has been used.

$X = p_T$ range in GeV/ c

$$Y = \frac{1}{N_{\text{evn}}} \times \frac{d^2N}{2\pi p_T dy dp_T} \text{ in } (\text{GeV}/c)^{-2}$$

where, N_{evn} is the number of events analysed. The corresponding figure to the data table is Fig. 3.9. In this Tab. 3.43.5, both the statistical and systematic uncertainties of the measured K^{*0} invariant mass spectra for all centralities are given here.

The K^{*0} signal for various p_T bins in different centrality classes in Pb–Pb collisions are shown in the Fig. 3.20 to 3.25. The solid red line is the peak fit function as describe in Eq. 3.5, and blue dotted line represents the remaining residual background function (quadratic function in πK invariant mass).

	0-5% $\times 10^3$			5-10% $\times 10^2$			10-20% $\times 10$		
X	Y	stat	syst	Y	stat	syst	Y	stat	syst
0.3 - 0.7	2698.3	293.23	480.64	292.940	39.903	50.374	17.86500	2.36550	3.14770
0.7 - 1.2	1939.6	274.84	307.47	158.050	10.486	26.812	11.83200	1.74260	1.98080
1.2 - 1.6	970.24	61.684	147.62	84.3570	4.4728	13.192	7.159900	0.57519	1.15170
1.6 - 2.0	543.50	38.989	78.043	39.3220	2.1396	6.1988	4.145300	0.29186	0.68289
2.0 - 2.5	255.71	12.743	38.148	21.1640	0.93412	3.5209	2.249200	0.11936	0.38348
2.5 - 3.0	98.770	6.7795	15.704	6.55920	0.37946	1.0639	0.703700	0.048024	0.11452
3.0 - 3.5	40.790	3.0986	6.3241	2.31830	0.17231	0.37652	0.256750	0.021029	0.042817
3.5 - 4.0	15.303	2.1604	2.4230	0.80289	0.10391	0.1179	0.145700	0.010707	0.023737
4.0 - 5.0	3.2128	0.4695	0.47492	0.36163	0.026458	0.054698	0.024697	0.0033447	0.0038079
5.0 - 7.0	0.50652	0.071982	0.084587	0.030666	0.004475	0.0052474	0.002498	0.00035394	0.00043276
7.0 - 10.0	0.042681	0.0055399	0.0076242	0.0039573	0.00058036	0.00068814	0.0004951	6.8255e-05	8.9332e-05
10.0 - 15.0	0.0085528	0.00125	0.001713	0.00053862	7.95690e-05	0.00010196	6.2846e-05	8.13190e-06	1.24710e-05
15.0 - 20.0	0.00081244	9.61140e-05	0.00017125	6.7849e-05	9.4618e-06	1.45900e-05	1.0008e-05	1.58790e-06	2.32160e-06

Table 3.4: The values of $1/N_{\text{evn}} d^2N/(2\pi p_T dy dp_T)$ (GeV/c) $^{-2}$ with statistical and systematic uncertainties in different p_T bins for 0-5%, 5-10% and 10-20% centrality classes in Pb-Pb collisions at $\sqrt{s_{\text{NN}}} = 2.76$ TeV.

	20-30%			30-40% $\times 10^{-1}$			40-50% $\times 10^{-2}$		
X	Y	stat	syst	Y	stat	syst	Y	stat	syst
0.3 - 0.7	1.478100	0.235240	0.259110	0.1226800000	0.0156920	0.021506	0.0078693	0.0011549	0.001473
0.7 - 1.2	0.952140	0.129260	0.155890	0.0730710000	0.0059182	0.011963	0.0046880	0.00036727	0.00079668
1.2 - 1.6	0.563630	0.037055	0.095009	0.0343360000	0.0024130	0.005788	0.0024397	0.00014948	0.00039591
1.6 - 2.0	0.293130	0.018433	0.044263	0.0191640000	0.0012813	0.0028939	0.0011356	7.0044e-05	0.00018821
2.0 - 2.5	0.135730	0.007522	0.021783	0.0088669000	0.00048586	0.0014230	0.00047266	2.7585e-05	8.17610e-05
2.5 - 3.0	0.049627	0.0029874	0.0073671	0.0032041000	0.00019361	0.00047564	0.00016584	1.2171e-05	2.49100e-05
3.0 - 3.5	0.020007	0.0014179	0.0033616	0.0010153000	8.3756e-05	0.0001706	6.6318e-05	9.5856e-06	1.07090e-05
3.5 - 4.0	0.0071236	0.0010241	0.0011119	0.0005005600	7.0987e-05	7.8129e-05	3.1073e-05	4.27910e-06	4.78320e-06
4.0 - 5.0	0.0021271	0.00017586	0.00032783	0.0001164400	1.6958e-05	1.7946e-05	8.7459e-06	1.2399e-06	1.34860e-06
5.0 - 7.0	0.00024941	3.7029e-05	4.18690e-05	2.33260e-05	3.322e-06	3.9159e-06	1.415e-06	2.05510e-07	2.49200e-07
7.0 - 10.0	3.5941e-05	4.9479e-06	5.57210e-06	3.06320e-06	4.1095e-07	4.7490e-07	1.637e-07	2.324e-08	2.67470e-08
10.0 - 15.0	5.4210e-06	7.5735e-07	9.87960e-07	2.84480e-07	3.6161e-08	5.1846e-08	1.953e-08	2.64940e-09	3.65340e-09
15.0 - 20.0	6.8555e-07	7.2754e-08	1.45590e-07	3.24470e-08	4.460e-09	6.89080e-09	2.843e-09	4.853e-10	6.23060e-10

Table 3.5: The values of $1/N_{\text{evn}} d^2N/(2\pi p_T dy dp_T)$ (GeV/c) $^{-2}$ with statistical and systematic uncertainties in different p_T bins for 20-30%, 30-40% and 45-50% centrality classes in Pb-Pb collisions at $\sqrt{s_{\text{NN}}} = 2.76$ TeV.

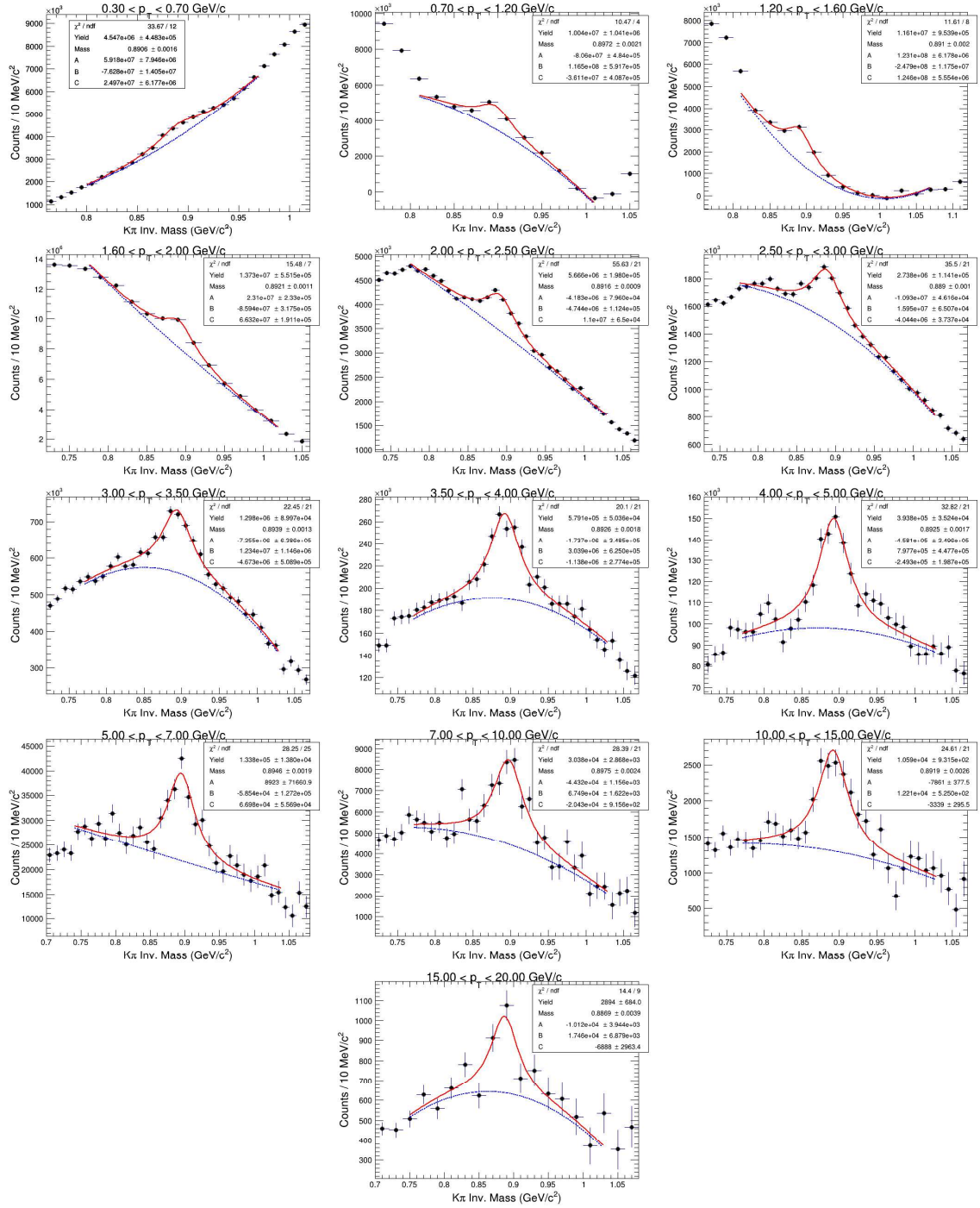


Figure 3.20: The K^*0 signal in different p_T bins for 0-5% centrality in Pb-Pb collisions at $\sqrt{s_{NN}} = 2.76$ TeV.

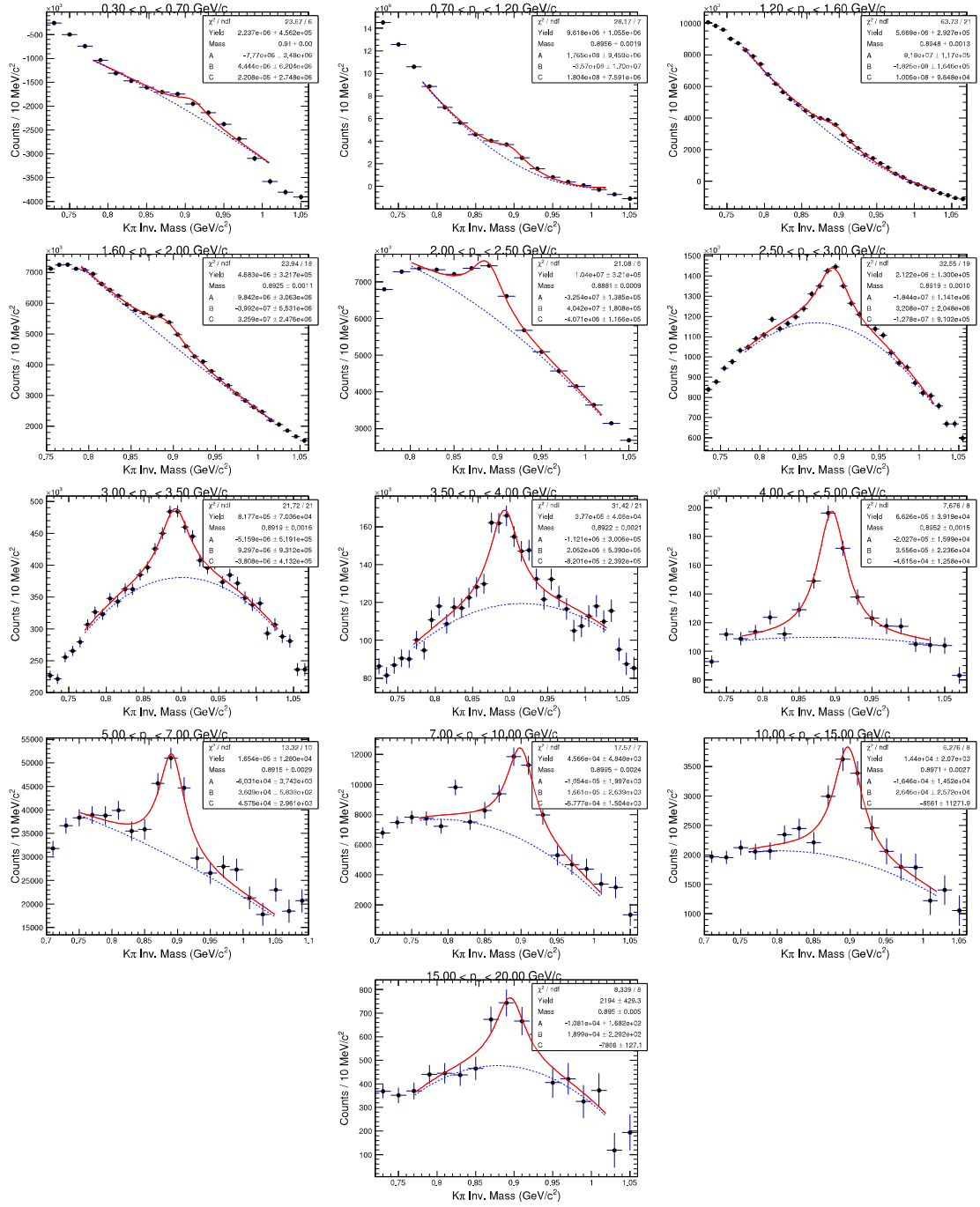


Figure 3.21: The K^*0 signal in different p_T bins for 5-10% centrality in Pb-Pb collisions at $\sqrt{s_{NN}} = 2.76$ TeV.

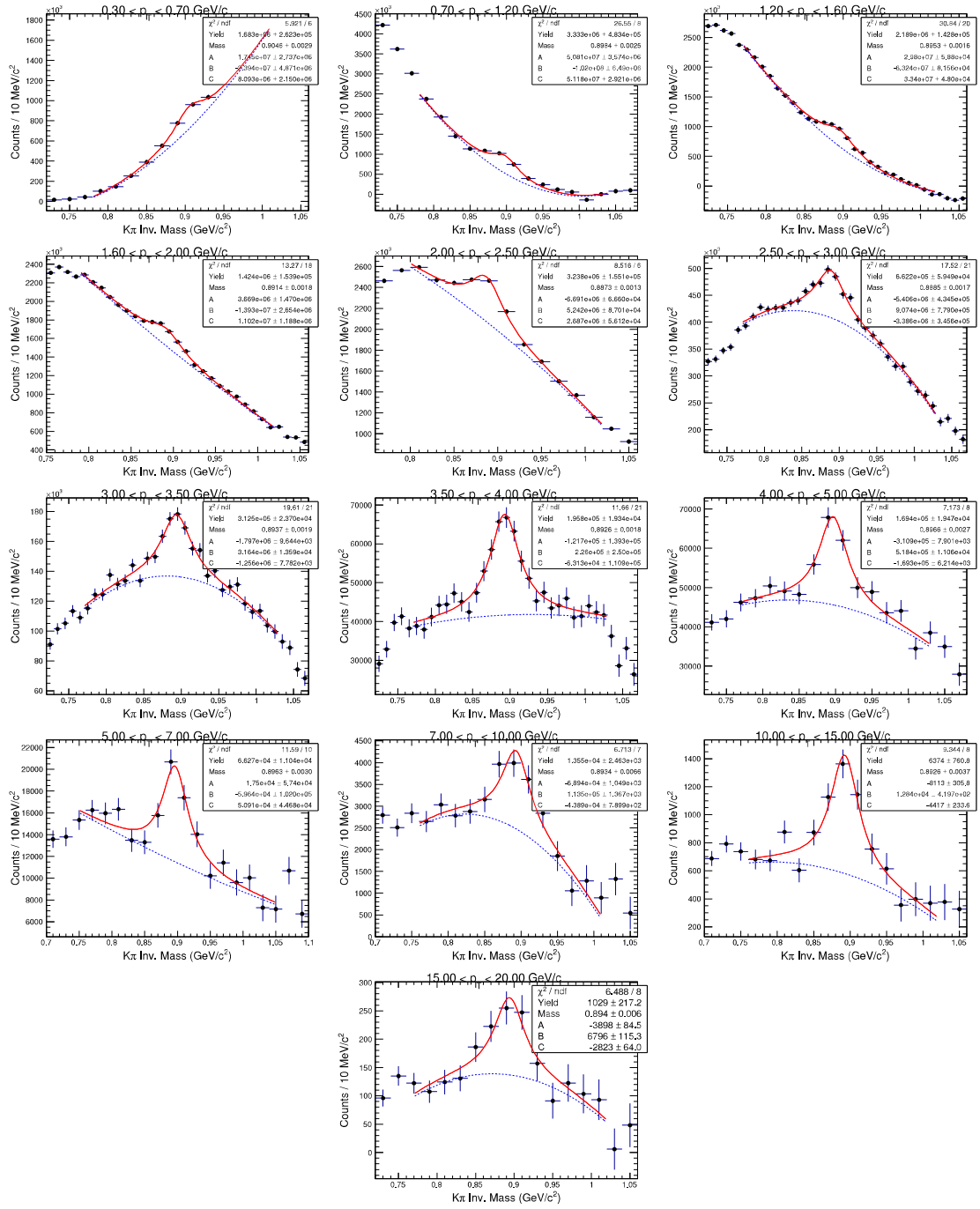


Figure 3.22: The K^*0 signal in different p_T bins for 10-20% centrality in Pb-Pb collisions at $\sqrt{s_{NN}} = 2.76$ TeV.

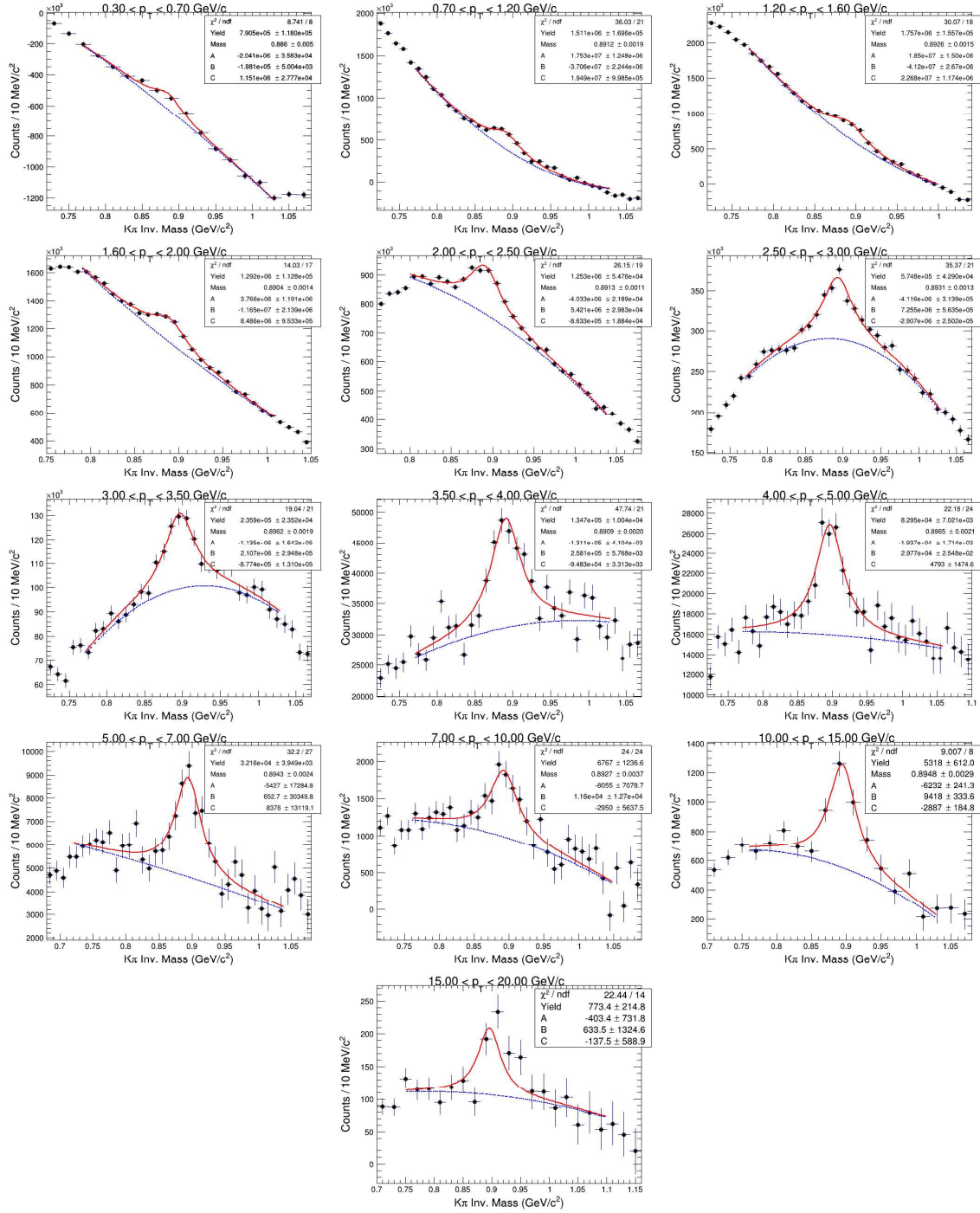


Figure 3.23: The K^*0 signal in different p_T bins for 20-30% centrality in Pb-Pb collisions at $\sqrt{s_{NN}} = 2.76$ TeV.

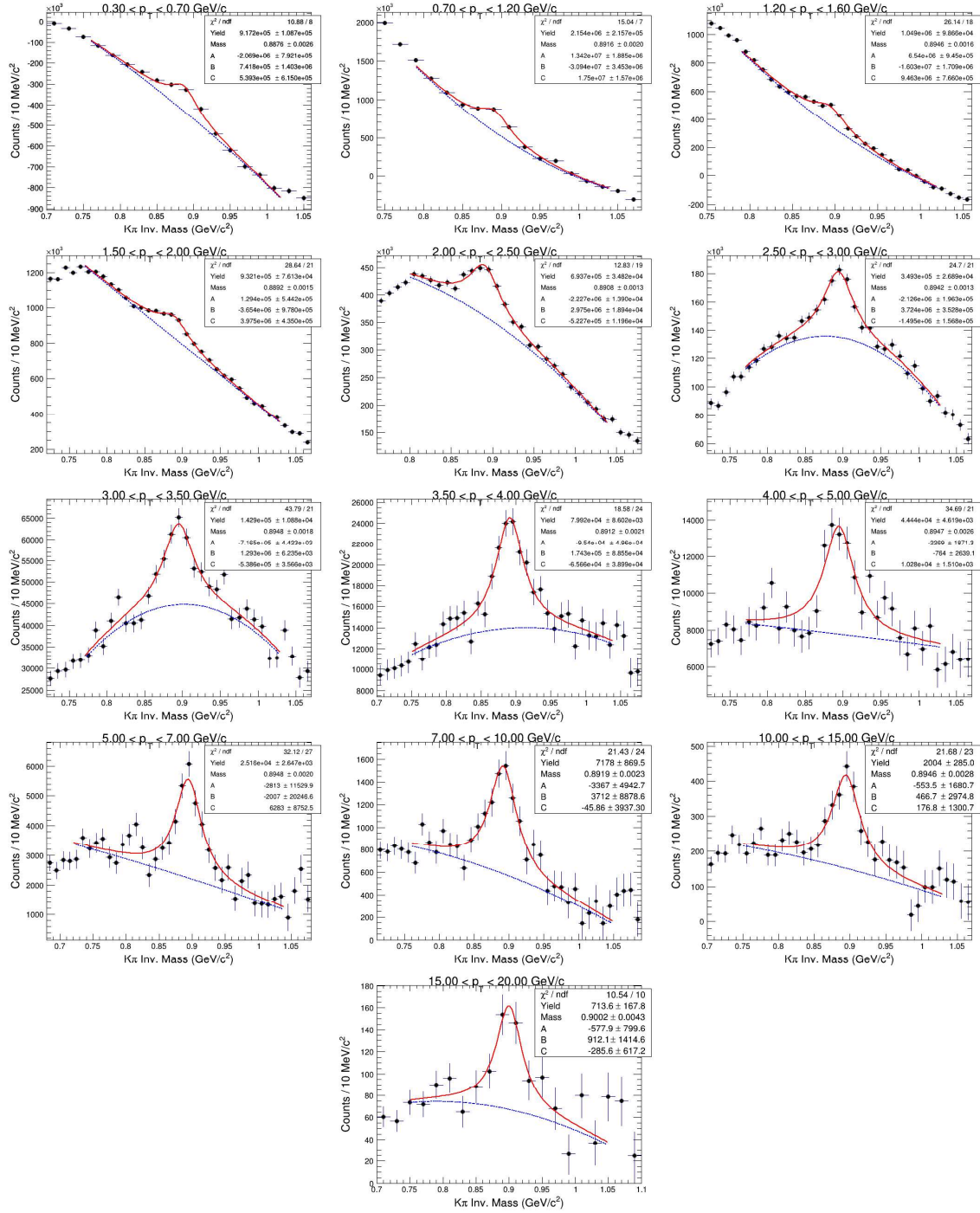


Figure 3.24: The K^*0 signal in different p_T bins for 30-40% centrality in Pb-Pb collisions at $\sqrt{s_{NN}} = 2.76$ TeV.

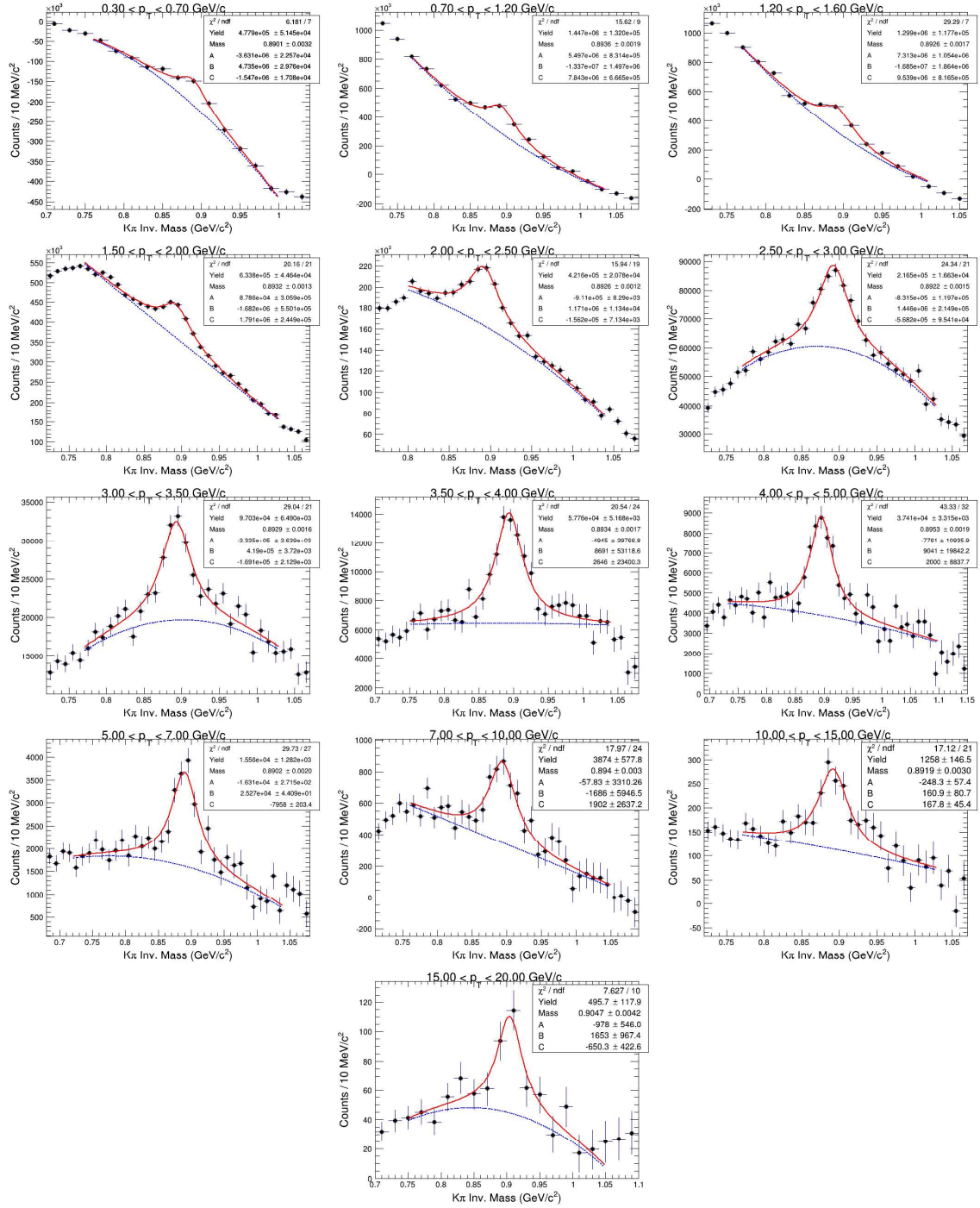


Figure 3.25: The K^*0 signal in different p_T bins for 40-50% centrality in Pb-Pb collisions at $\sqrt{s_{NN}} = 2.76$ TeV.

Chapter 4

Multiplicity dependence of $K^*(892)^0$ resonance production in pp collisions at $\sqrt{s} = 7$ TeV

At the LHC energies, one of the most intriguing questions is to address the possible presence of collective effects in high-multiplicity pp or p-Pb collisions. Recently, several phenomena have been observed in these collision systems which resembles the observation that is attributed to the creation of a medium in Pb–Pb collisions. These includes, the observation of (i) two-particle correlation study: double ridge structures on the near and away side in p-Pb collisions [1] and in high multiplicity pp collisions [2], (ii) multi-particle cumulant study: a non-vanishing elliptic flow (v_2) coefficients [3], (iii) identified particle p_T -spectra study: mass dependent hardening of identified particle p_T -spectra [4, 5] and the consistency of the integrated particle yield ratios with the thermal model expectations at high multiplicities [6] and (iv) multiplicity dependence study: strangeness enhancement in high multiplicity pp collisions at $\sqrt{s} = 7$ TeV [7].

In this chapter, a comprehensive study of event multiplicity dependence of K^{*0} resonance production in pp collisions at $\sqrt{s} = 7$ TeV is presented. The p_T -spectra of K^{*0} resonance are measured via its hadronic decay channel $K^{*0} (\bar{K}^{*0}) \rightarrow \pi^- K^+ (\pi^+ K^-)$. The p_T -spectra are measured in various multiplicity event classes. The K^{*0} dN/dy and $\langle p_T \rangle$ values are extracted and compared with different identified particles to understand the particle production mechanism. The p_T -integrated K^{*0}/K ratio in various multiplicity event classes are also obtained and compared with ϕ/K ratios to understand the possible hadronic in-medium effects like re-scattering and regeneration in high multiplicity pp collisions at $\sqrt{s} = 7$ TeV.

4.1 Analysis details

The K^{*0} production in high multiplicity pp collisions at $\sqrt{s} = 7$ TeV analysis details are given in the following sub-sections.

4.1.1 Data sets and event selection

In this analysis, the data used are collected by ALICE in the LHC pp run of 2010. In total, about 93 million good events have been used for this analysis. This minimum bias trigger requiring a hit either in the VZERO (V0) or in the SPD, in coincidence with the arrival of proton bunches from both directions are collected. By using the V0 timing information (time resolution better than 1 ns), contamination from background events are removed offline. The background events are also rejected by studying the correlation between the number of pixel hits and the number of SPD tracklets (short tracks with a hit in each of the SPD layers pointing to the primary vertex). Furthermore, the events used for the data analysis are required to have a reconstructed primary vertex within $|V_z| < 10$ cm as shown in Fig. 4.1 (left panel).

The events containing more than one vertex are tagged as pileup events and those events are rejected in this analysis.

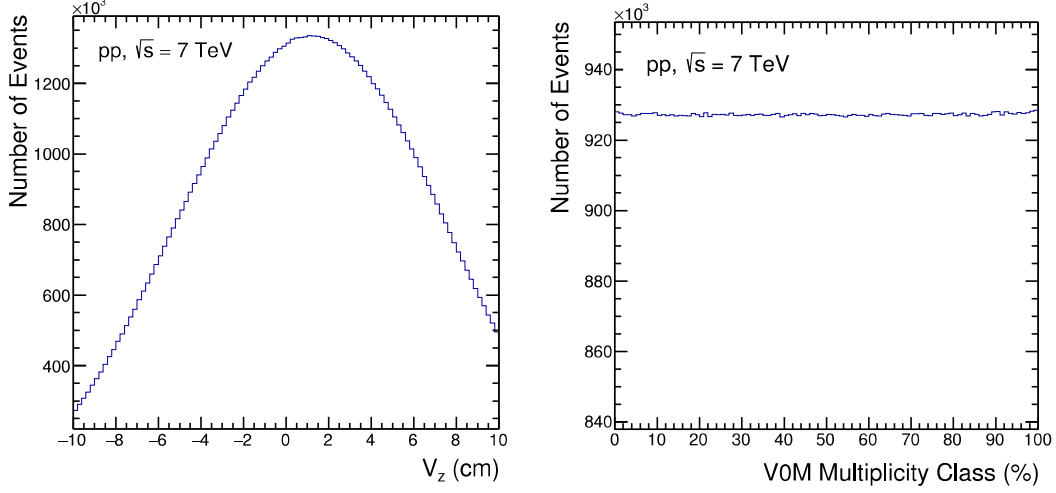


Figure 4.1: The z -position (V_z) vertex distribution of events in pp collisions at $\sqrt{s} = 7$ TeV (Left panel). V0M multiplicity event class distribution percentile for pp collisions at $\sqrt{s} = 7$ TeV (Right panel).

The V0 estimators are used for event classification according to hadronic activity based on V0 amplitudes, similar to what is done in Pb–Pb collisions [8]. The V0 amplitude has been estimated using the signals from both V0A and V0C denoted by V0M. The right panel of Fig. 4.1 shows the V0M multiplicity event class distribution in percentile for pp collisions at $\sqrt{s} = 7$ TeV.

Figure 4.2 shows the charged particle multiplicity distribution in different V0M event classes as a function of number of tracks within $|\eta| < 0.5$. The average number of charged particle multiplicity corresponding to each multiplicity event classes are also mentioned. A summary table for the corrected averaged charged particle multiplicity density within $|\eta| < 0.5$ in different multiplicity event classes are given in Table 4.1. The second and third value represents the statistical and systematic uncertainties, respectively.

Sr. No.	Event Class (%)	Roman letter	$\langle dN_{ch}/d\eta \rangle_{ \eta <0.5}$ (Corrected)
1	0-1	I	$21.294 \pm 0.038 \pm 0.639$
2	1-5	II	$16.513 \pm 0.010 \pm 0.495$
3	5-10	III	$13.457 \pm 0.010 \pm 0.404$
4	10-20	IV	$10.793 \pm 0.010 \pm 0.324$
5	20-30	V	$8.447 \pm 0.000 \pm 0.254$
6	30-40	VI	$6.724 \pm 0.000 \pm 0.207$
7	40-50	VII	$5.398 \pm 0.000 \pm 0.173$
8	50-70	IX	$3.897 \pm 0.000 \pm 0.143$
9	70-100	X	$2.261 \pm 0.000 \pm 0.117$
10	0-100	-	$5.964 \pm 0.002 \pm 0.230$

Table 4.1: The summary of different V0M multiplicity event classes (%) and their corresponding average number of charged particle multiplicity density with $\eta < 0.5$.

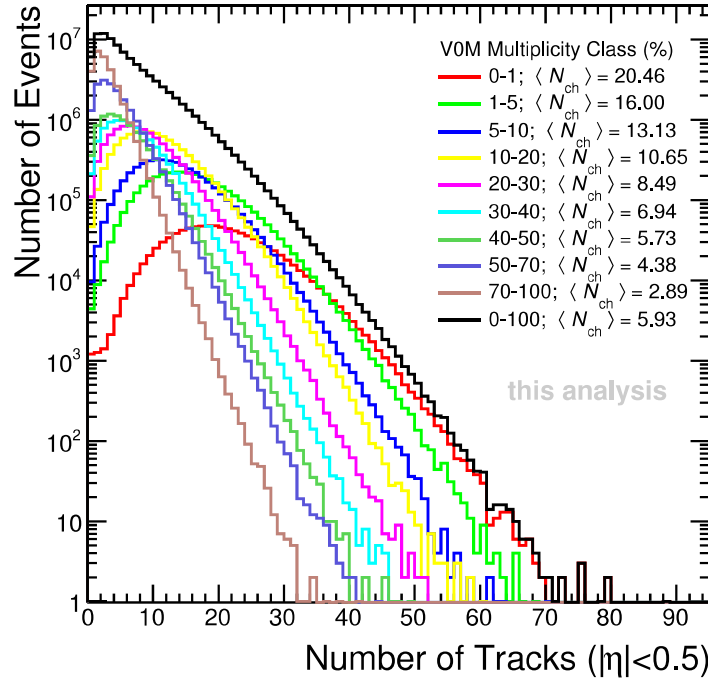


Figure 4.2: The charged particle multiplicity distribution in different V0M multiplicity event classes with corresponding average number of charged particle.

4.1.2 Track cuts and particle identification

The charged particles are identified by using the information from both the TPC and the TOF detector. In order to select the good quality of tracks (within $|\eta| < 0.8$), a set of optimised track cuts are applied. The track must pass at least 70 out of maximum possible 159 rows in the TPC and the ratio between the crossed rows to findable cluster must be larger than 0.8. A p_T -dependent 7σ DCA_{xy} ($< 0.0182 + 0.0350/p_T^{1.01}$; p_T in GeV/ c) and $DCA_z < 2$ cm are applied to reduce the contamination from beam-background events and secondary particle coming from weak decays. Each track is restricted to p_T greater than 0.2 GeV/ c . The decay daughters of K^{*0} (pion and kaon) are identified by measuring the specific ionization energy loss (dE/dx) using the TPC and time-of-flight information from the TOF detector (Fig. 4.3). When the track has both the TPC and TOF information available then $|N_\sigma^{\text{TPC}}| < 2$ and $|N_\sigma^{\text{TOF}}| < 3$ is applied and without the availability of TOF information only $|N_\sigma^{\text{TPC}}| < 2$ is applied.

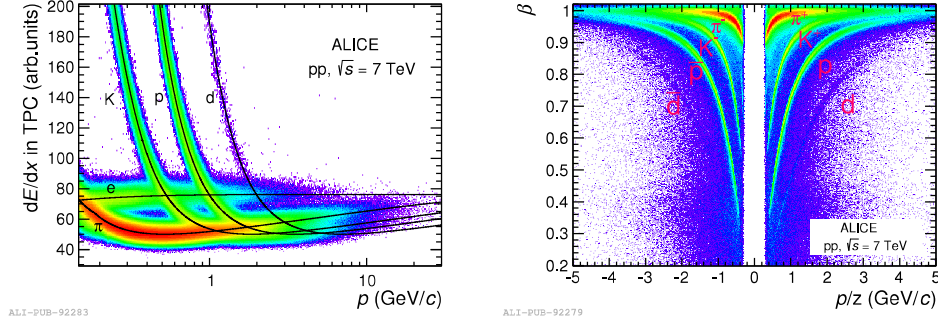


Figure 4.3: Distribution of dE/dx of charged particles as a function of momentum in the TPC (Left panel) and particle velocity β measured by the TOF detector as a function of the rigidity p/z (z is the charge of the particle) in pp collisions at $\sqrt{s} = 7$ TeV (Right panel).

4.1.3 K^{*0} signal extraction

The unlike-sign kaon and pion are paired by using the invariant-mass formula as describe in section 3.1.4 to construct the K^{*0} signal. The πK invariant-mass for 1-5% and 50-70% V0M multiplicity event classes in pp collisions at $\sqrt{s} = 7$ TeV are shown in Fig. 4.4. In the upper panel of Fig. 4.4, the K^{*0} signal is not clearly visible due to the huge combinatorial background.

4.1.4 Reconstruction of combinatorial background

The uncorrelated combinatorial background is subtracted using the event mixing technique. The **event mixing** method used in this analysis is similar to that described in Pb–Pb analysis in section 3.1.4 with the similar event mixing criteria such as the number of event mixed, z-vertex difference between the events. In addition a multiplicity difference between the event mixed should be less than 5 is also applied unlike the centrality difference condition of Pb–Pb collisions. The open marker in the upper panel of Fig. 4.4 represents the normalised mixed event background.

4.1.5 Residual background

The combinatorial background is subtracted from the signal with uncorrelated background distribution. However, due to the correlation of particles, some of residual background still remains with the K^{*0} signal. The main sources of correlation could be due to mis-reconstructed $K\pi$ pairs, effect of elliptic flow, correlated $K\pi$ pairs, correlated $K\pi$ pair emitted within jets.

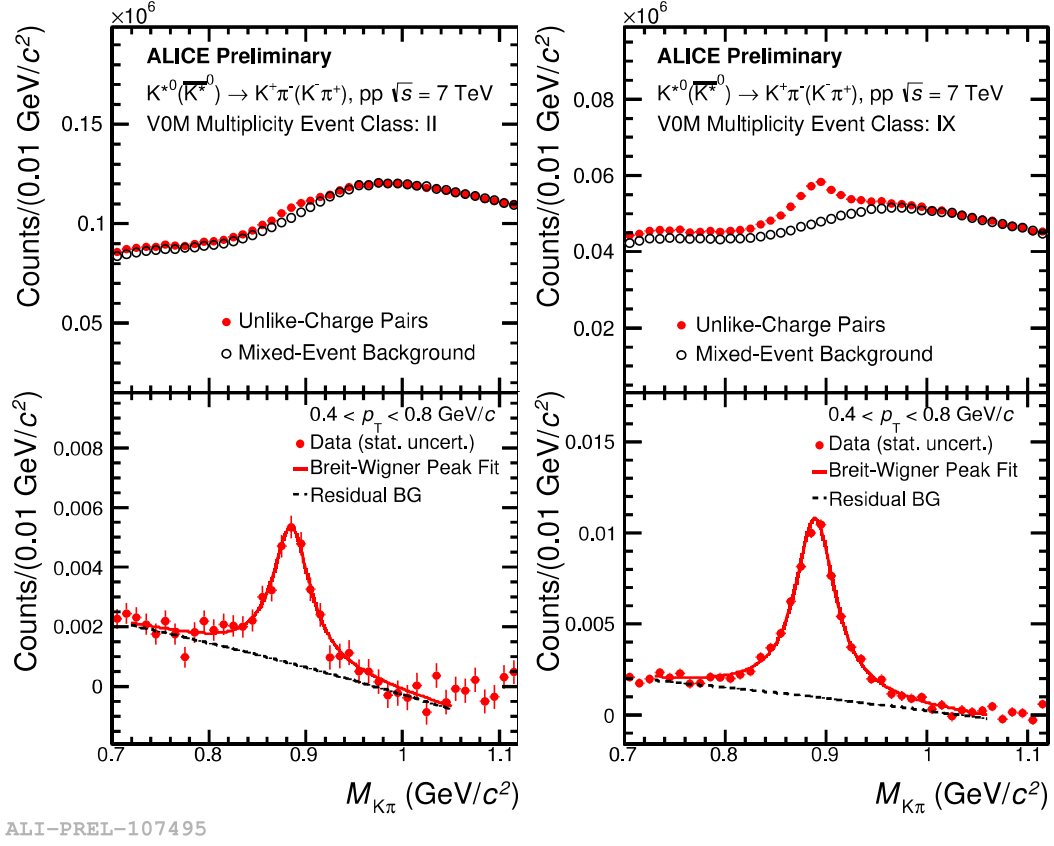


Figure 4.4: $K\pi$ invariant-mass distribution in pp collisions at $\sqrt{s} = 7$ TeV for V0M multiplicity class II (1-5%) and IX (50-70%). The upper (lower) panels are the $K\pi$ invariant mass distribution before (after) mixed event background subtraction.

4.1.6 K^{*0} raw yield

The reconstructed K^{*0} signal is fitted with a Breit-Wigner along with a quadratic function in invariant mass to account for the remaining residual background (Eq. 4.1) as done in Pb-Pb analysis. The residual background function is also varied and the difference in the extracted raw yield of K^{*0} is considered in the systematic uncertainty.

$$\frac{dN}{dM_{K\pi}} = \frac{Y}{2\pi} \times \frac{\Gamma_0}{(M_{K\pi} - M_0)^2 + \frac{\Gamma_0^2}{4}} + (AM_{K\pi}^2 + BM_{K\pi} + C), \quad (4.1)$$

where M_0 and Γ_0 are the reconstructed mass and width, respectively. Y is the yield of K^{*0} ; A , B and C are the polynomial fit parameters. The width of K^{*0} is fixed to vacuum value (47.4 ± 0.6 MeV/ c^2 [8]) while extracting the raw yield. The difference in the yield due to keeping the width fixed and free is considered in the systematic uncertainty.

The K^{*0} invariant mass is also another free parameter of the Eq. 4.1 which is shown in Fig. 4.5 for different p_T bins in various multiplicity event classes for pp collisions at $\sqrt{s} = 7$ TeV. The K^{*0} mass is found to be consistent with the vacuum value 0.8959 GeV/ c^2 [8] (represented by black dotted line) within the statistical uncertainties at high- p_T .

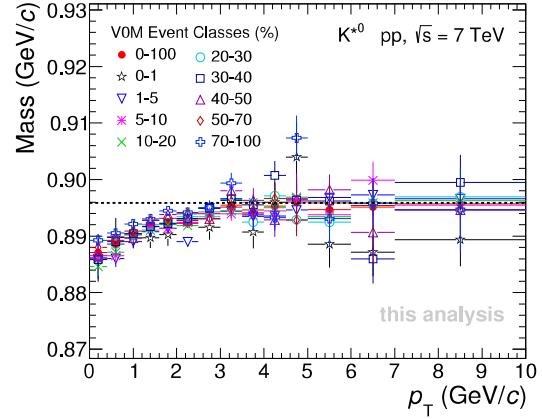


Figure 4.5: K^{*0} mass distribution as a function of p_T for various V0M multiplicity event classes in pp collisions at $\sqrt{s} = 7$ TeV.

4.1.7 Acceptance \times Efficiency ($A \times \epsilon_{\text{rec}}$)

The $A \times \epsilon_{\text{rec}}$ calculation procedure is similar to Pb–Pb analysis discussed in 3.1.7 except that for pp collisions one uses Monte Carlo event generator PYTHIA 6.4 instead of HIJING. Figure 4.6 shows the K^{*0} $A \times \epsilon_{\text{rec}}$ for various V0M multiplicity event classes at mid-rapidity ($|\eta| < 0.8$) in pp collisions at $\sqrt{s} = 7$ TeV.

There is a mild multiplicity dependence in $A \times \epsilon_{\text{rec}}$ as function of p_T . The corrected p_T -spectra are obtained by using the 0-100% $A \times \epsilon_{\text{rec}}$ to correct each V0M multiplicity event class in pp collisions at $\sqrt{s} = 7$ TeV. The raw yield is corrected for detector

$A \times \epsilon_{\text{rec}}$ and also normalised to number of analysed events and branching ratio (BR) 66.6% [8] as given in Eq. 4.2.

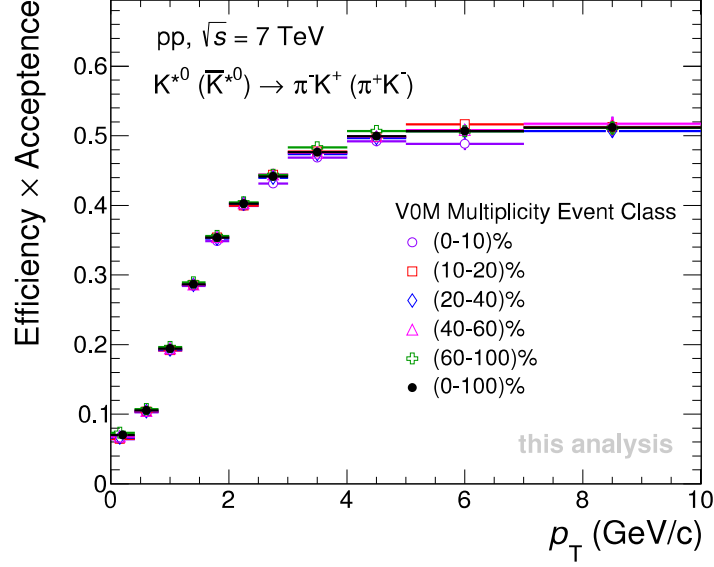


Figure 4.6: Acceptance \times Efficiency ($A \times \epsilon_{\text{rec}}$) calculation for 0-100% multiplicity event classes at mid-rapidity ($|\eta| < 0.8$) in pp collisions at $\sqrt{s} = 7$ TeV.

4.2 Results

4.2.1 p_T -spectra

The K^{*0} raw is yield extracted from πK invariant mass by fitting with the Eq. 4.1 for each p_T bin in various V0M multiplicity event classes. The raw yields are corrected for number of analysed events, reconstruction efficiency, detector acceptance and branching ratio as given in Eq. 4.2 for each multiplicity event classes.

$$\frac{d^2 N}{dy dp_T} = \frac{1}{N_{\text{evt}}} \times \frac{dN^{\text{raw}}}{dy dp_T} \times \frac{1}{A \times \epsilon_{\text{rec}} \times B.R} \quad (4.2)$$

where N_{evt} is the number of events for different multiplicity classes used in the

analysis and N^{raw} is the K^{*0} raw yield counts. The p_T -spectra is further corrected for event counter loss and signal loss as shown in Eq. 4.3. To calculate the event and signal loss correction factor Pythia 6.4 simulation has been used as described in [10]. In this analysis an event class requiring at least one charged particle in the pseudo-rapidity interval $|\eta| < 1$ ($\text{INEL} > 0$) are used and denoted as N_{events} in Eq. 4.5. The accepted events ($N_{\text{events}}^{\text{accepted}}$) were required to have a reconstructed vertex and at least one tracklet with $|\eta| < 1$ and z-vertex range $|V_z| < 10$ cm.

$$\frac{1}{N_{\text{events}}} \times \frac{dN_{\text{particles}}}{dp_T}(p_T) = \frac{1}{N_{\text{events}}^{\text{accepted}}} \times \frac{dN_{\text{particles}}^{\text{accepted}}}{dp_T}(p_T) \frac{\epsilon_{\text{events}}}{\epsilon_{\text{particles}}(p_T)}, \quad (4.3)$$

where, ϵ_{events} accounts for the event counter loss and given as

$$\epsilon_{\text{events}} = \frac{N_{\text{events}}^{\text{accepted}}}{N_{\text{events}}}, \quad (4.4)$$

The event loss correction factors used in different multiplicity classes are listed in Table 4.2. $\epsilon_{\text{particles}}$ accounts for the signal loss and given as

$$\epsilon_{\text{particles}}(p_T) = \frac{\frac{dN_{\text{gen}}}{dp_T} (\text{applied event selection})}{\frac{dN_{\text{gen}}}{dp_T} (\text{INEL} > 0)} \quad (4.5)$$

The numerator and denominator of Eq. 4.5 corresponds to the generated particles after and before the event selection, respectively.

Fig. 4.7 shows the p_T dependent signal loss correction K^{*0} in different V0M multiplicity classes.

The corrected K^{*0} p_T -spectra measured in various multiplicity V0M event classes at mid-rapidity ($|\eta| < 0.8$) in pp collisions at $\sqrt{s} = 7$ TeV are shown in Fig. 4.8. The p_T -spectra are scaled with different numbers for clear visibility. The lower panel of

Fig. 4.8 shows that p_T -spectra ratios with respect to 0-100% multiplicity event class. The p_T -spectra get harder with the increase in multiplicity event class.

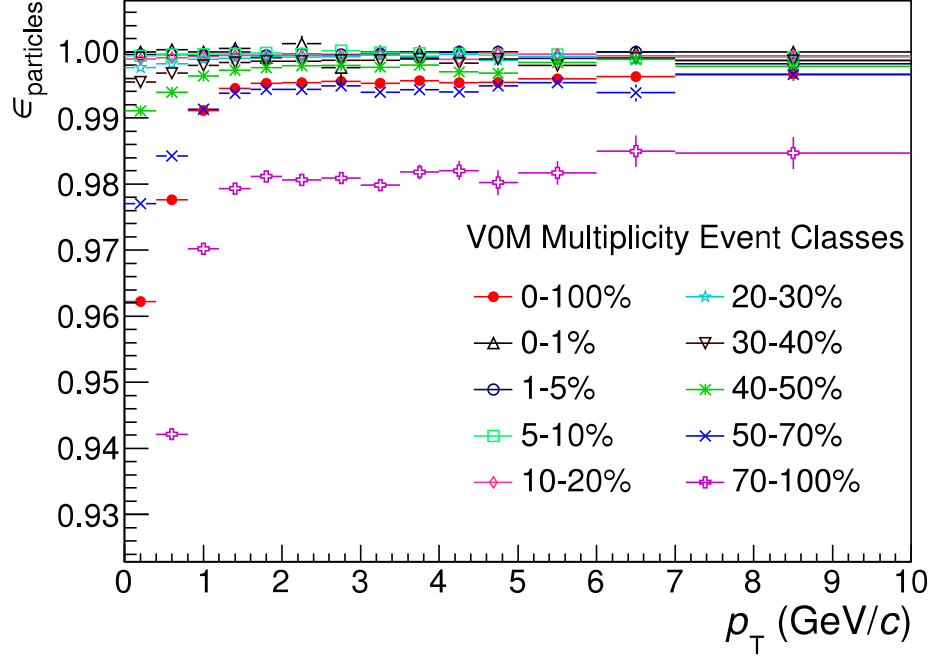


Figure 4.7: The $\epsilon_{particles}$ as function of p_T for K^{*0} in different V0M multiplicity event classes in pp collisions at $\sqrt{s} = 7$ TeV.

Sr. No.	V0M event classes	ϵ_{events}
1	0-1%	0.999
2	1-5%	0.999
3	5-10%	0.999
4	10-20%	0.997
5	20-30%	0.993
6	30-40%	0.984
7	40-50%	0.972
8	50-70%	0.945
9	70-100%	0.877

Table 4.2: The event counter loss correction, ϵ_{events} in different V0M multiplicity event classes for pp collisions at $\sqrt{s} = 7$ TeV.

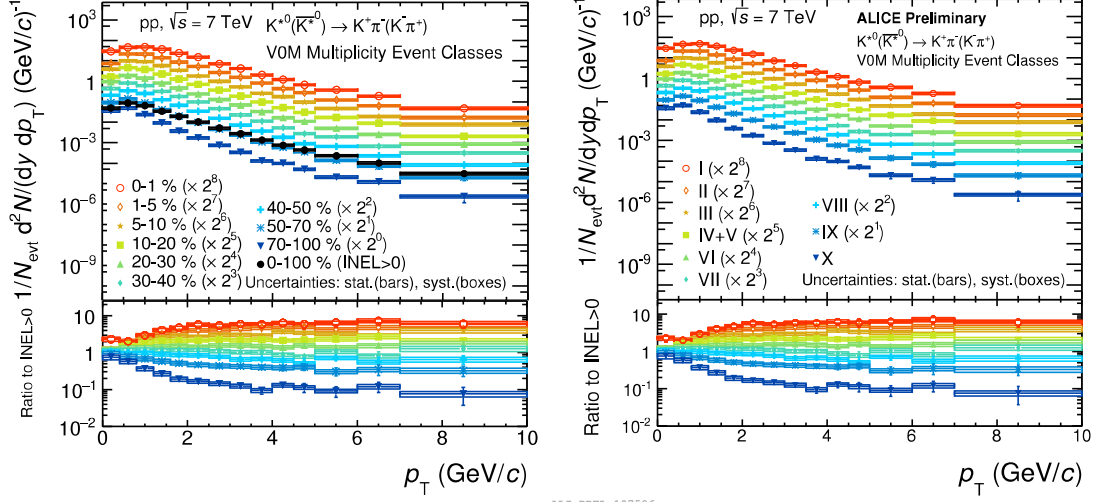


Figure 4.8: The K^{*0} p_T -spectra measured at mid-rapidity ($|\eta| < 0.8$) in various V0M multiplicity event classes (INEL>0) in pp collisions at $\sqrt{s} = 7$ TeV are shown with 0-100% event class (without) in left (right) panel. The line and boxes represent the statistical and systematic uncertainties, respectively.

4.2.2 dN/dy and $\langle p_T \rangle$

The integrated K^{*0} yield (dN/dy) and $\langle p_T \rangle$ are extracted from data by fitting the corrected p_T -spectra with Levy-Tsallis function [11, 12] as given in Eq. 4.6

$$\frac{d^2N}{dp_T dy} = p_T \times \frac{dN}{dy} \times \frac{(n-1)(n-2)}{nT[nT + m(n-2)]} \left[1 + \frac{m_T - m}{nT} \right]^{-n} \quad (4.6)$$

Where m is the mass of the resonance and $m_T = \sqrt{m^2 + p_T^2}$ is the transverse mass and n , T (effective temperature) are the free parameters.

Figure 4.9 shows the K^{*0} dN/dy (left panel) and $\langle p_T \rangle$ (right panel) as function of $\langle dN_{ch}/dy \rangle_{|\eta| < 0.5}$ for different V0M multiplicity event classes at mid-rapidity ($|\eta| < 0.8$) in pp collisions at $\sqrt{s} = 7$ TeV. The dN/dy and $\langle p_T \rangle$ values increases with increase in multiplicity event classes. The $\langle p_T \rangle$ increases with multiplicity indicating the hardening of p_T -spectra in pp collisions at $\sqrt{s} = 7$ TeV.

Event Class (%)	dN/dy	$\langle p_T \rangle$ (GeV/c)
0-1	$0.3478 \pm 0.0185 \pm 0.0404 \pm 0.0230$	$1.3074 \pm 0.0381 \pm 0.0432 \pm 0.0432$
1-5	$0.2730 \pm 0.0078 \pm 0.0328 \pm 0.0183$	$1.2952 \pm 0.0222 \pm 0.0350 \pm 0.0350$
5-10	$0.2348 \pm 0.0058 \pm 0.0293 \pm 0.0190$	$1.2109 \pm 0.0183 \pm 0.0366 \pm 0.0367$
10-20	$0.1950 \pm 0.0045 \pm 0.0230 \pm 0.0125$	$1.1500 \pm 0.0159 \pm 0.0325 \pm 0.0345$
20-30	$0.1568 \pm 0.0027 \pm 0.0197 \pm 0.0110$	$1.0639 \pm 0.0111 \pm 0.0311 \pm 0.0325$
30-40	$0.1313 \pm 0.0032 \pm 0.0157 \pm 0.0093$	$1.0140 \pm 0.0151 \pm 0.0292 \pm 0.0311$
40-50	$0.1080 \pm 0.0025 \pm 0.0129 \pm 0.0070$	$0.9556 \pm 0.0134 \pm 0.0283 \pm 0.0292$
50-70	$0.0809 \pm 0.0013 \pm 0.0107 \pm 0.0053$	$0.8655 \pm 0.0088 \pm 0.0245 \pm 0.0283$
70-100	$0.0510 \pm 0.0007 \pm 0.0074 \pm 0.0039$	$0.7184 \pm 0.0057 \pm 0.0244 \pm 0.0245$
0-100	$0.1127 \pm 0.0007 \pm 0.0136 \pm 0.0128$	$1.0227 \pm 0.0038 \pm 0.0305 \pm 0.0305$

Table 4.3: The dN/dy and $\langle p_T \rangle$ of K^{*0} in different V0M multiplicity event classes (%) at mid-rapidity ($|\eta| < 0.8$) for pp collisions at $\sqrt{s} = 7$ TeV. The first, second and third uncertainty represents the statistical, total systematic and uncorrelated systematic uncertainties, respectively.

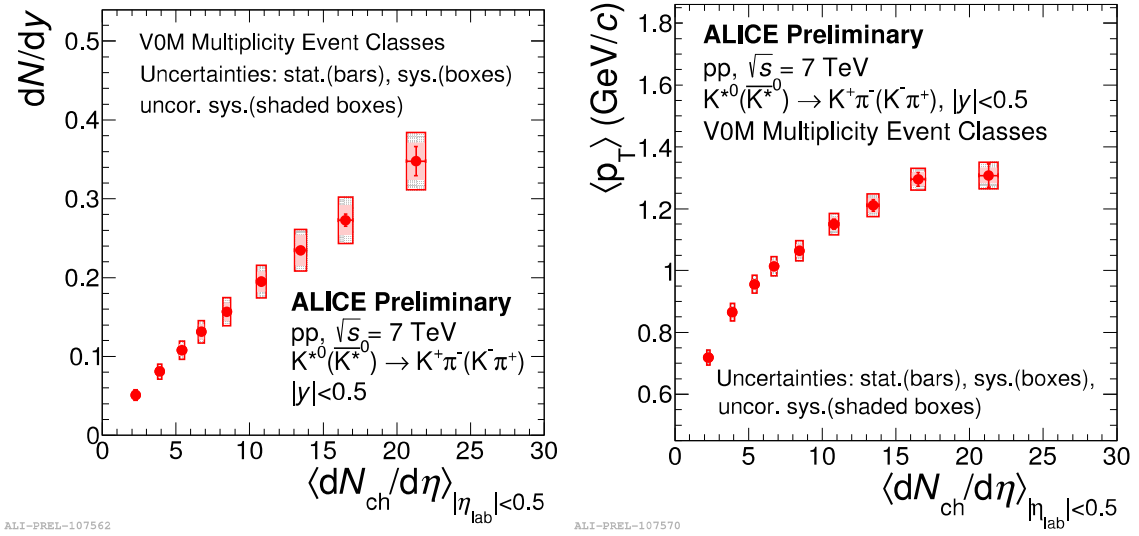


Figure 4.9: p_T -integrated K^{*0} yield (left panel) and $\langle p_T \rangle$ (right panel) as function of average charged particle multiplicity for various V0M multiplicity event classes at mid-rapidity ($|\eta| < 0.8$) in pp collisions at $\sqrt{s} = 7$ TeV.

The dN/dy and $\langle p_T \rangle$ values of K^{*0} for different event classes in pp at $\sqrt{s} = 7$ TeV are given in Table 4.3. The K^{*0} p_T -spectra starts from zero, so the systematic uncertainty due to extrapolation at high- p_T is negligible.

The $\langle p_T \rangle$ of various identified particles (π , K , K_S^0 , K^{*0} , p , ϕ , Λ , Ξ and Ω) in pp collisions at $\sqrt{s} = 7$ TeV are shown in the Fig. 4.10. The Logarithmic fit function (dotted line) are shown to guide the eye. The $\langle p_T \rangle$ of π (small mass hadron) is having a lower value than heavier mass particles like Ω indicating the mass ordering of $\langle p_T \rangle$. However, resonance such as K^{*0} and ϕ violates the mass ordering nature of $\langle p_T \rangle$ in pp collisions which is depicted in Fig. 4.11 more clearly.

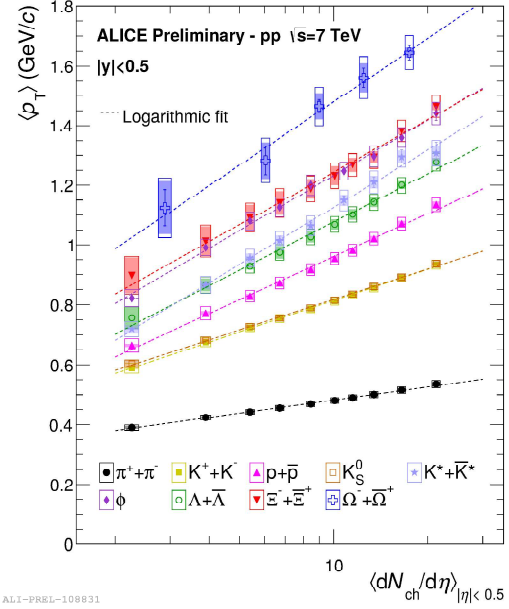


Figure 4.10: The $\langle p_T \rangle$ comparison of various identified particles as a function of change particle multiplicity ($|\eta| < 0.8$) in pp collisions at $\sqrt{s} = 7$ TeV.

The $\langle p_T \rangle$ of similar mass particles (K^{*0} , p , ϕ) are compared for different colliding systems such as pp, p-Pb and Pb-Pb at $\sqrt{s_{NN}} = 7$ TeV, 5.02 TeV and 2.76 TeV, respectively, in Fig. 4.11. On the both side of the Fig. 4.11, proton $\langle p_T \rangle$ is compared with K^{*0} (left panel) and ϕ (right panel). The $\langle p_T \rangle$ of K^{*0} , p and ϕ approaches similar values from mid-central to central Pb-Pb collisions. In small colliding systems (pp, p-Pb), the $\langle p_T \rangle$ of K^{*0} and ϕ are different than the proton $\langle p_T \rangle$ values. The rate of increase of $\langle p_T \rangle$ values with multiplicity in pp and p-Pb is more than Pb-Pb and the $\langle p_T \rangle$ values are also larger for smaller system (pp, p-Pb) than Pb-Pb for similar multiplicity event classes.

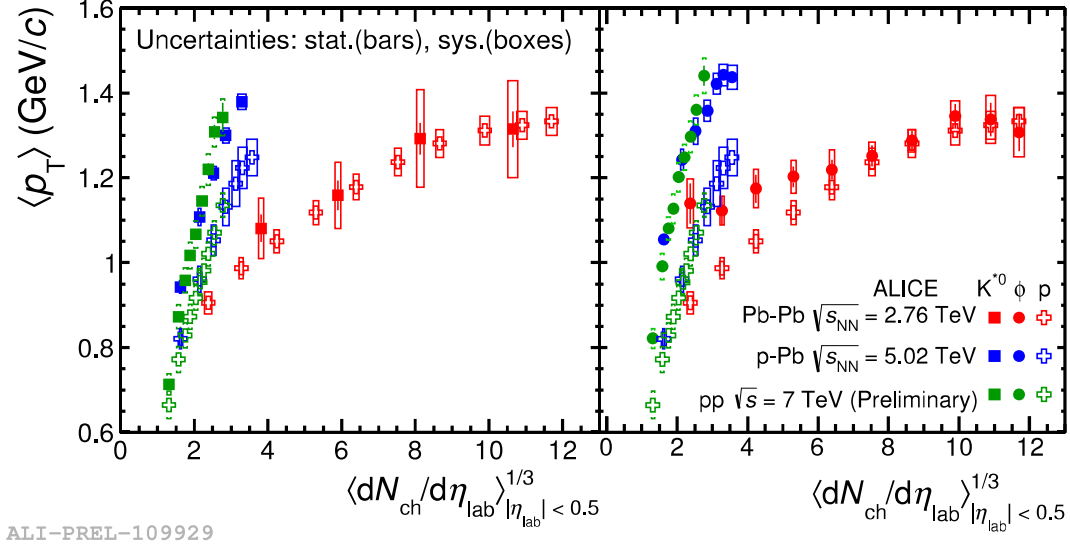


Figure 4.11: $\langle p_T \rangle$ of K^{*0} (left panel) and ϕ (right panel) with proton as a function of proxy of system size [13] at mid-rapidity ($|\eta| < 0.8$) for pp, p-Pb and Pb-Pb collisions at $\sqrt{s_{NN}} = 7$ TeV, 5.02 TeV and 2.76 TeV, respectively [15, 16].

The left panel of Fig. 4.12 shows the $\langle p_T \rangle$ of identified particles as a function of mass scaled with the number of constituent quark (ncq, 3 for baryon and 2 for meson) of the hadrons in various multiplicity event classes for pp collisions at $\sqrt{s} = 7$ TeV. A mass and multiplicity dependent increase of the $\langle p_T \rangle$ values are observed. However, the resonances (K^{*0} and ϕ) $\langle p_T \rangle$ values do not follow the general trend as guided by a dotted line. The right panel of Fig. 4.12 shows the $\langle p_T \rangle$ different identified hadrons scaled with the mass of the particle as a function of multiplicity density for pp, p-Pb and Pb-Pb collisions at $\sqrt{s_{NN}} = 7$ TeV, 5.02 TeV and 2.76 TeV, respectively. At a given multiplicity density, the $\langle p_T \rangle/M$ values of identified particles in pp and p-Pb collisions are found to be similar but the corresponding value in Pb-Pb collisions are different.

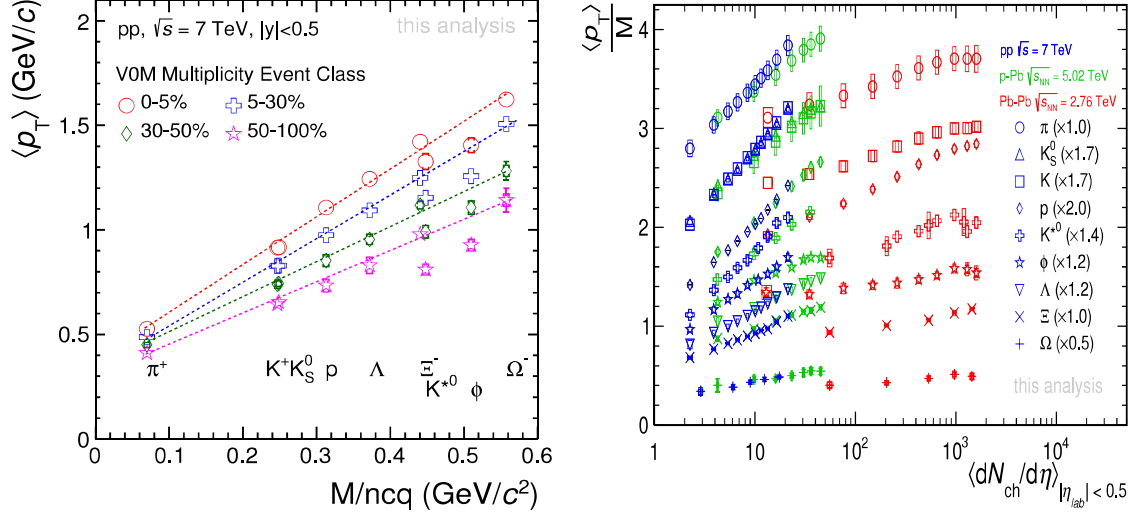
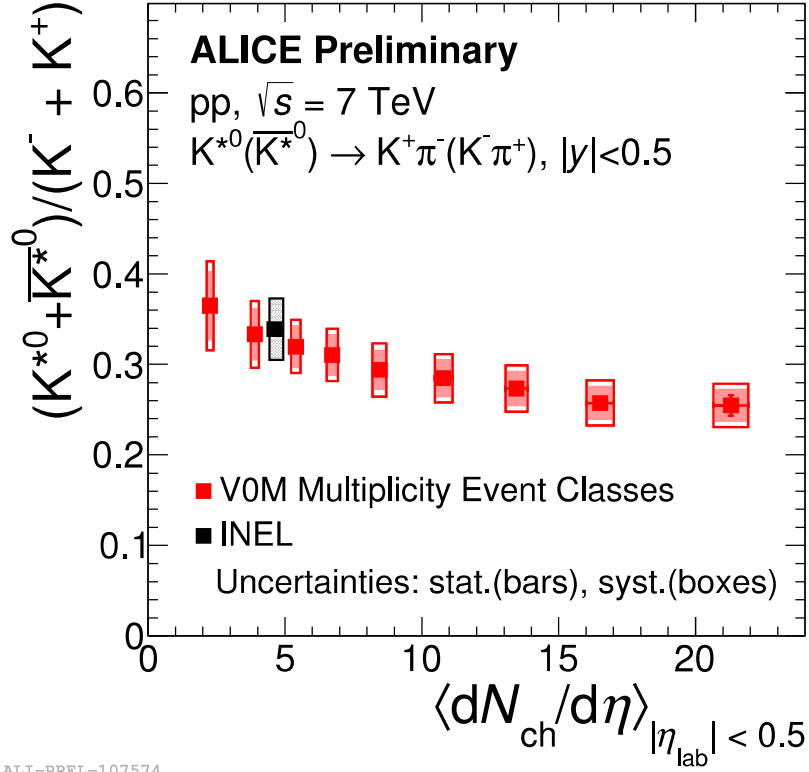


Figure 4.12: Left panel shows the $\langle p_T \rangle$ as function of mass (M) of the particle scaled with number of constituent quark (ncq) for various event classes in pp collisions at $\sqrt{s} = 7$ TeV. The dotted line is drawn to guide the eye. Right panel shows $\langle p_T \rangle/M$ as a function of average number of charged particle for different identified particles in pp, p-Pb and Pb-Pb collisions at $\sqrt{s_{NN}} = 7$ TeV, 5.02 TeV and 2.76 TeV, respectively [15, 16, 17].

4.2.3 Particle ratios

The particle ratio having similar strange quark (s) content like K^{*0}/K (resonance to stable particle) as a function of average charged particle multiplicity measured at mid-rapidity ($|\eta| < 0.8$) in pp collisions at $\sqrt{s} = 7$ TeV is shown in the Fig. 4.13. The multiplicity dependence of K^{*0}/K ratio values are consistent with the corresponding measurement from inelastic (INEL) pp collisions at 7 TeV [14]. The K^{*0}/K ratio shows a decreasing trend with multiplicity with a non-zero slope.



ALI-PREL-107574

Figure 4.13: The p_T -integrated K^{*0}/K ratio as function of average charged particle multiplicity for various V0M multiplicity event classes and the in-elastic (INEL) measurement at mid-rapidity ($|\eta| < 0.8$) in pp collisions at $\sqrt{s} = 7$ TeV [14].

The resonance to stable particle (K^{*0}/K , ϕ/K) in various colliding systems (pp, p-Pb and Pb-Pb) as a function of proxy of system size ($\langle dN_{ch}/d\eta_{lab} \rangle_{|\eta_{lab}| < 0.5}^{1/3}$) [13] measured at mid-rapidity ($|\eta| < 0.8$) are shown in Fig 4.14. The decreasing trend of K^{*0}/K unlike ϕ/K ratio (which remains almost independent with respect to system size) is understood by in-medium re-scattering effect in Pb-Pb collisions. A similar trend is also observed in small colliding systems like p-Pb and pp at $\sqrt{s_{NN}} = 5.02$ and 7 TeV, respectively.

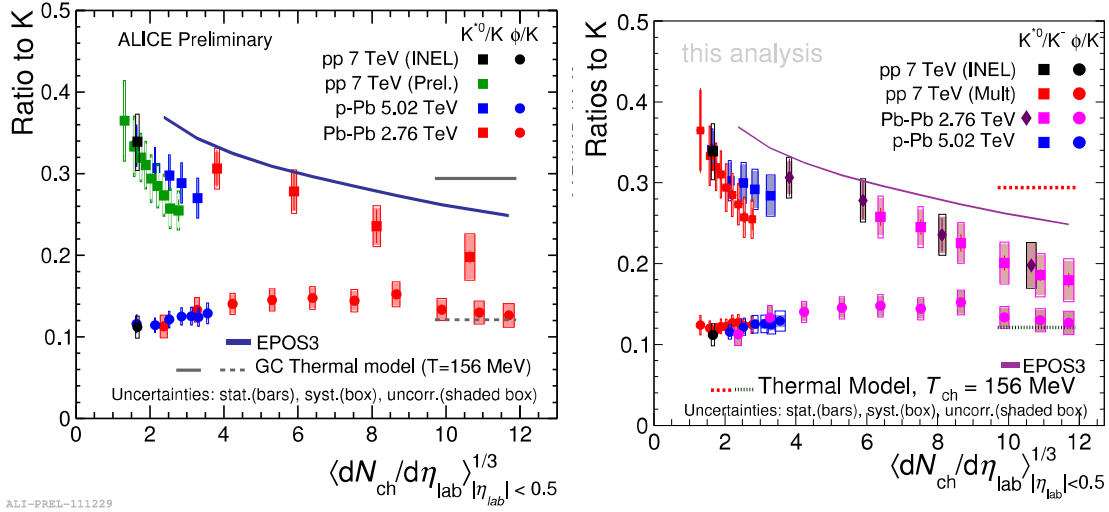


Figure 4.14: The particle ratios to K [without (with) ϕ/K ratio in pp $\sqrt{s} = 7$ TeV as shown in left (right) panel] as a function of proxy of system size ($\langle dN_{ch}/d\eta_{lab} \rangle^{1/3}_{|\eta_{lab}| < 0.5}$) [13] at mid-rapidity ($|\eta| < 0.8$) for pp, p-Pb and Pb-Pb collisions at $\sqrt{s_{NN}} = 7$ TeV, 5.02 TeV and 2.76 TeV, respectively [15, 16, 18]. The thermal model calculation of K^{*0}/K and ϕ/K with chemical freeze-out temperature of 156 MeV for the most central Pb-Pb collisions at $\sqrt{s_{NN}} = 2.76$ TeV are shown [19]. The prediction of EPOS3 model for the K^{*0}/K ratio is shown in violet band for various centrality intervals in Pb-Pb collisions at $\sqrt{s_{NN}} = 2.76$ TeV [20]

4.3 Systematic uncertainty

The study of different sources of systematic uncertainty for the K^{*0} meson in pp collisions at $\sqrt{s} = 7$ TeV is similar to the Pb-Pb analysis as described in the section 3.2.7. The procedure followed is similar to described in the Ref. [21]. A test commonly known as “Barlow test” [21] is performed to separate the statistical effect while estimating the systematic uncertainty. Let Y_{def} be the measured yield of K^{*0} with default setting and the corresponding statistical uncertainty is σ_{def} . Another yield of K^{*0} measured with some systematic cut variation (e.g. signal peak fitting range variation) is performed and the yield and statistical uncertainty are Y_{sys} and σ_{sys} , respectively. A ratio is defined as $R = (Y_{\text{def}} - Y_{\text{sys}}) / \Delta$, where $\Delta = \sqrt{\sigma_{\text{def}}^2 - \sigma_{\text{sys}}^2}$;

and when $R \leq 1$ for a particular systematic variation, then that yield measurement is rejected and not considered for systematic because the measurement is consistent with the statistical uncertainties. For other cases, it is considered for systematic uncertainties. A brief description the main sources of systematic uncertainties are given below.

4.3.1 Signal extraction

The shape of the residual background is different for each p_T bin and centrality classes as describe in the section 4.1.5. It affects the raw yield value of K^{*0} and hence different method have been used to include the changes as systematic uncertainties.

- The fit range variation of K^{*0} invariant mass peak with the corresponding residual background.
- Normalization range variation of the same and mixed event πK distribution.
- The width (Γ) range of K^{*0} invariant mass distribution variation.
- Residual background function of K^{*0} invariant mass variation from quadratic to a cubic function.

4.3.2 Mis-identification of particles

The pion and kaon are selected using the TPC average energy loss ($\langle dE/dx \rangle$) and measurement of the time-of-flight of particle using the TOF. When both the TPC and TOF information are available, $|N_{\sigma}^{\text{TPC}}| < 2$ and $|N_{\sigma}^{\text{TOF}}| < 3$ else only $|N_{\sigma}^{\text{TPC}}| < 2$ is applied for kaon and pion selection. For the systematic variation the N_{σ} is varied from default to $|N_{\sigma}^{\text{TPC}}| < 1$ and $|N_{\sigma}^{\text{TOF}}| < 2$.

4.3.3 Track selection and analysis track cut variations

A detail description for the selection of good quality track can be found in the section 4.1.2. The ITS-TPC matching uncertainty is 3% for a single track, so for the K^{*0} (re-constructed from two pion and kaon tracks) an uncertainty of 6% (an uncertainty of 3% is associated with each decay daughter) is considered. For the estimation of systematic uncertainties, different track selection cuts such as minimum number of TPC crossed rows, the distance of closest approach, TPC χ^2/NDF cuts are varied. The systematic uncertainty variation is about 1-4% depending on the p_T and multiplicity event classes.

4.3.4 Material budget and hadronic interaction

The tracking is performed via the energy loss of the particle while transversing in the detector material. Hence, the kind of detector material used affects the tracking of the particle and it needs to take into account. The p_T -dependent material budget uncertainty of single K and π tracks are estimated using PYTHIA 6.4 simulation. In this simulation, for a given p_T , the material budget uncertainty associated with pion and kaon (decay daughters of K^{*0}) are estimated and their average value is taken as the material budget uncertainty for K^{*0} . The uncertainty due to material budget varies from 1-4% for low- p_T ($< 2 \text{ GeV}/c$) and negligible at high- p_T . The systematic uncertainty associated with the hadronic interactions with detector material is studied by GEANT4 simulation. The uncertainty due hadronic interaction is about 1-2% for $p_T < 2 \text{ GeV}/c$ and negligible at high- p_T .

4.3.5 Total systematic uncertainty

A summary of p_T -dependent systematic uncertainties with individual contributions for various multiplicity event classes are given in the Fig. 4.15 and Fig. 4.16. The individual contributions of fractional systematic uncertainties are added in quadrature to get the total systematic uncertainties.

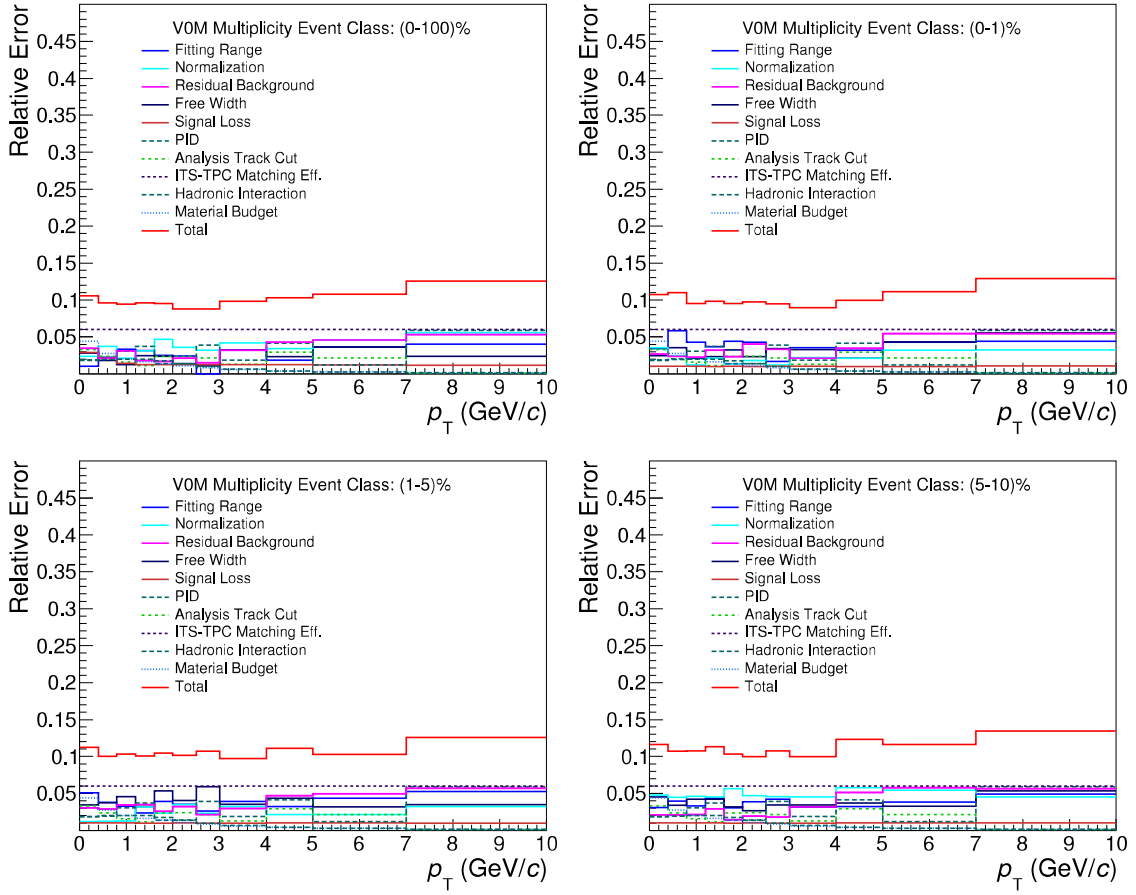


Figure 4.15: Summary of different sources of systematic uncertainties in the K^{*0} yield extraction for 0-100%, 0-1%, 1-5% and 5-10% V0M multiplicity event classes in pp collisions at $\sqrt{s} = 7$ TeV.

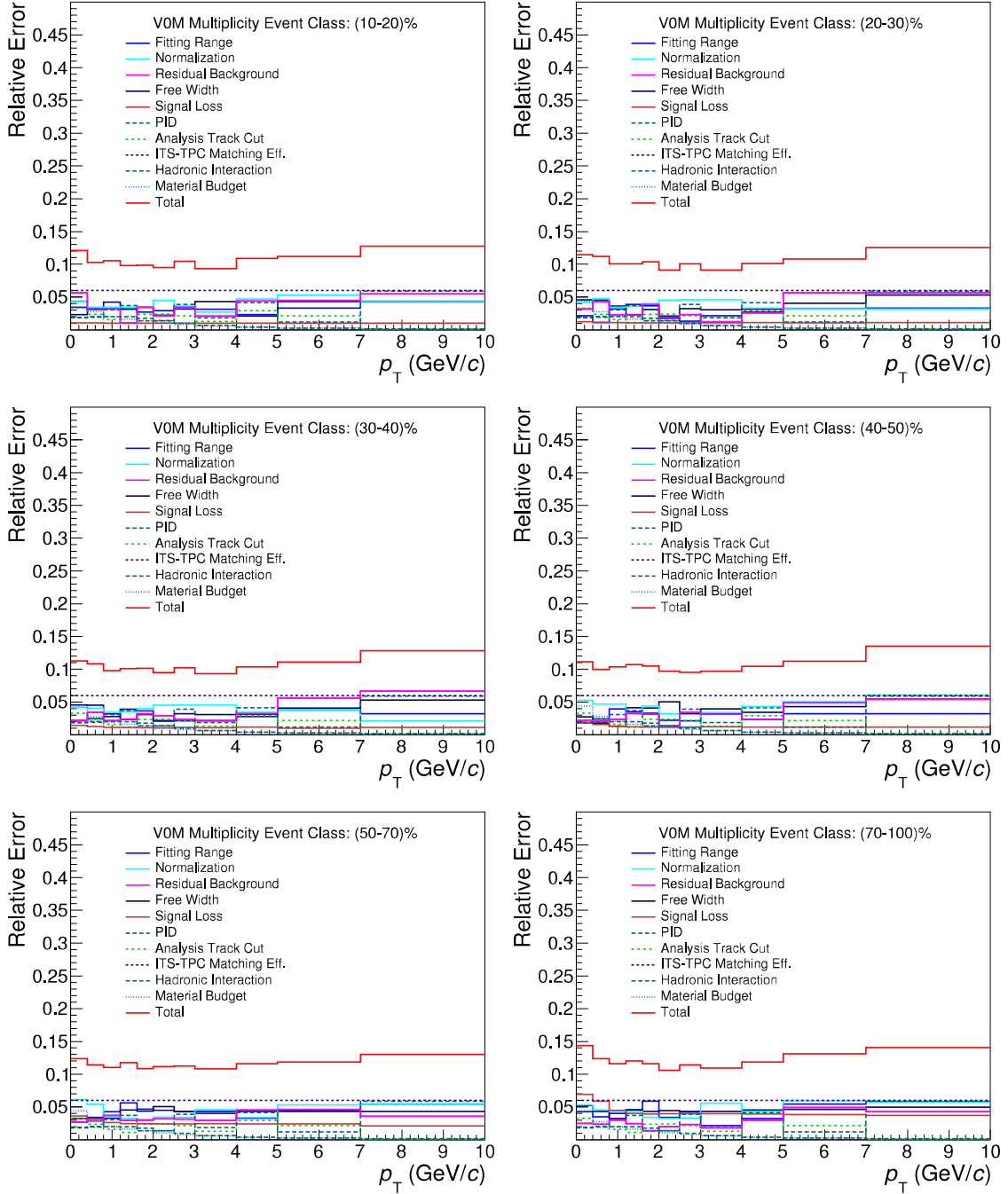


Figure 4.16: Summary of different sources of systematic uncertainties in the K^{*0} yield extraction for 10-20%, 20-30%, 30-40%, 40-50%, 50-70% and 70-100% V0M multiplicity event classes in pp collisions at $\sqrt{s} = 7$ TeV.

4.3.6 Multiplicity uncorrelated systematic uncertainties

A study is performed in order to extract the component of uncorrelated systematic uncertainty of K^{*0} yield across different multiplicity event classes. As systematic uncertainties are largely correlated across multiplicity, so any type of systematic variation will cause a similar amount of deviations from the default value across different multiplicity event classes. However, a fraction of the total error could be dependent on the multiplicities considered. Here the procedure to isolate multiplicity uncorrelated systematic uncertainty is performed. The procedure adopted is similar to the p-Pb [23] and pp [24] analysis. The ratio given in Eq. 4.7 determines the uncorrelated component of the total systematic uncertainty for each selection cut of the corresponding multiplicity event class i :

$$R = \frac{Y_{modified-cut}^{MultBin-i}}{Y_{default-cut}^{MultBin-i}} \bigg/ \frac{Y_{modified-cut}^{INEL>0}}{Y_{default-cut}^{INEL>0}} \quad (4.7)$$

Where $Y_{modified-cut}^{MultBin-i}$ and $Y_{modified-cut}^{INEL>0}$ are the spectra with the modified cut for multiplicity event class i and INEL>0 (0-100% V0M multiplicity event class), respectively. This ratio R sorts out the part of systematic uncertainty which is uncorrelated over p_T . For each source of systematic uncertainty discussed above, the R factor is evaluated and the quadratic sum of all the contributions gives the fraction of systematic uncertainty which is uncorrelated over multiplicity.

The main contribution of multiplicity uncorrelated systematic uncertainties are from yield extraction and the cut variations are (i) fitting range, (ii) normalization range, (iii) free width and (iv) residual background variations. Details variation of multiplicity uncorrelated systematic uncertainty for the K^{*0} yield in different event classes is given in the Fig. 4.17, Fig. 4.18 and left pane of Fig. 4.19.

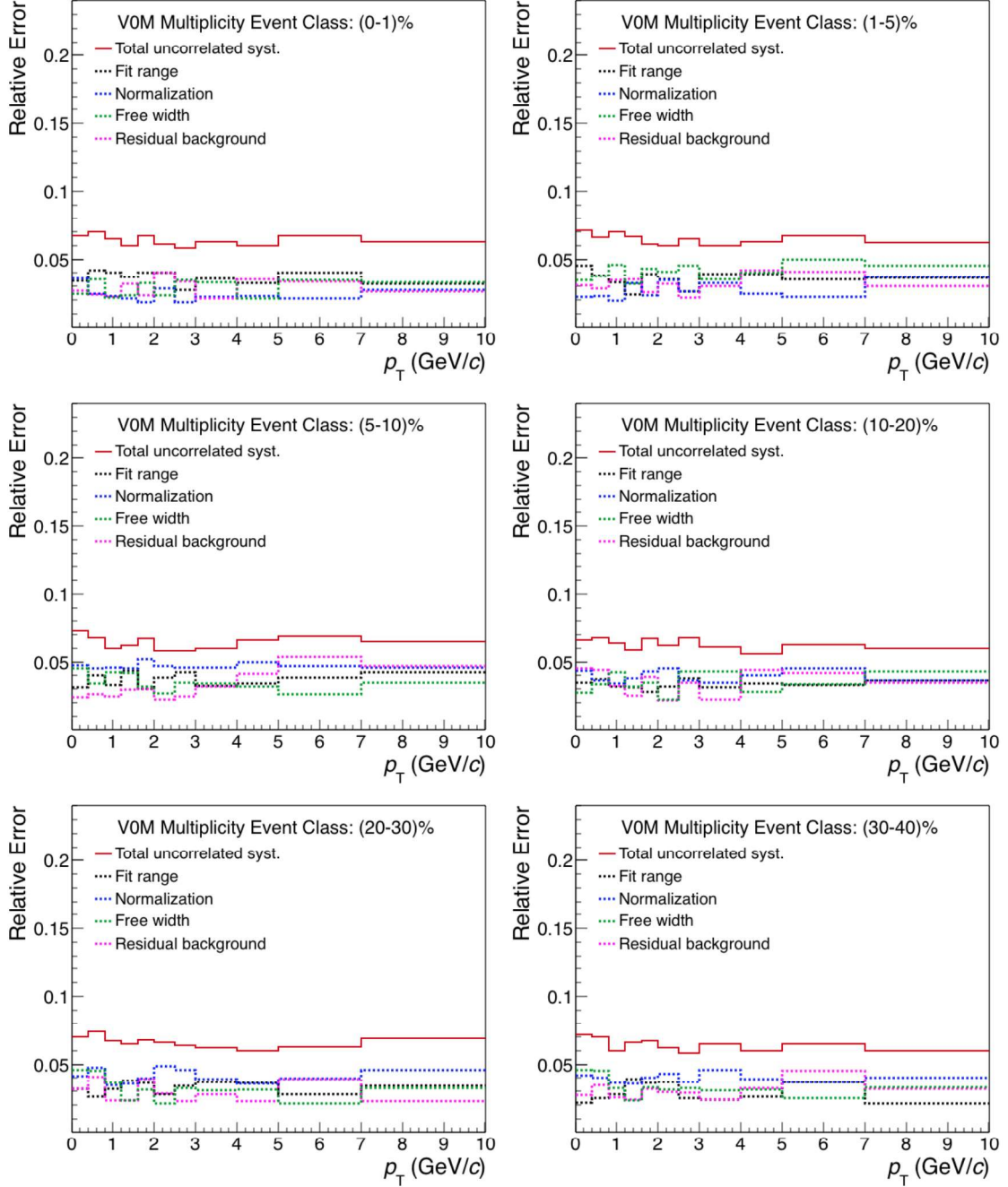


Figure 4.17: Relative error as a function of p_T for different sources of uncorrelated systematic uncertainties for K^{*0} in 0-1%, 1-5%, 5-10%, 10-20%, 20-30% and 30-40% V0M multiplicity event classes in pp collisions at $\sqrt{s} = 7$ TeV.

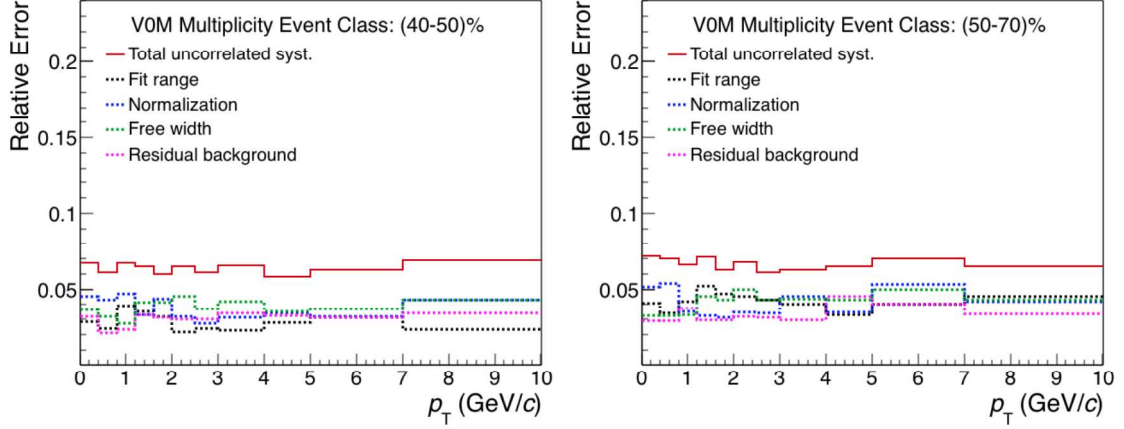


Figure 4.18: Relative error as a function of p_T for different sources of uncorrelated systematic uncertainties for K^{*0} in 40-50% and 50-70% V0M multiplicity event classes in pp collisions at $\sqrt{s} = 7$ TeV.

The fraction of uncorrelated systematic uncertainty in different V0M multiplicity event classes are compared with the total systematic uncertainty for INEL>0 (0-100% event class) as shown on the right panel of Fig. 4.19.

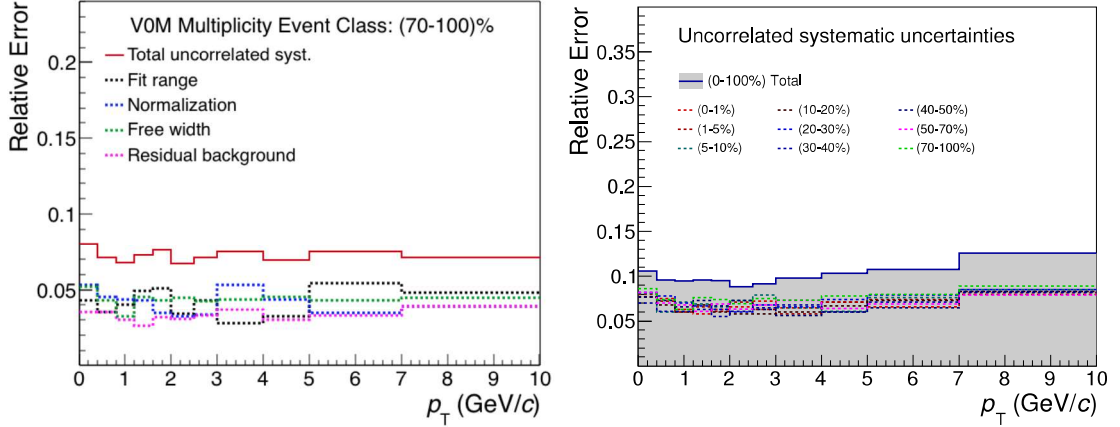


Figure 4.19: Relative error as a function of p_T for different sources of uncorrelated systematic uncertainties for K^{*0} in 70-100% V0M multiplicity event class (left panel). Summary of total multiplicity uncorrelated systematic uncertainties for K^{*0} in pp collisions at $\sqrt{s} = 7$ TeV (right panel).

4.4 Summary

The measurement of charged particle multiplicity dependence of K^{*0} p_T -spectra for various V0M multiplicity event classes in pp collisions at $\sqrt{s} = 7$ TeV has been carried out in this thesis. The hardening of high multiplicity p_T -spectra as compared to low multiplicity event class has been observed. The increase of K^{*0} $\langle p_T \rangle$ with increase in charged particle multiplicity also suggests hardening of p_T -spectra for high multiplicity event classes relative to low multiplicity event classes. The $\langle p_T \rangle$ of K^{*0} and ϕ resonance deviates from the general trend of mass ordering of identified particles in pp collisions at $\sqrt{s} = 7$ TeV. For a similar value of charged particle multiplicity, the $\langle p_T \rangle$ scaled with mass of the identified particle is found to be of similar order for small colliding system pp and p-Pb but have different magnitude for Pb-Pb collisions. The p_T -integrated K^{*0}/K yield ratio in pp collisions shows a decreasing trend with respect to system size and have a non zero slope, unlike ϕ/K ratio which is independent of system size. The observation is similar to p-Pb and Pb-Pb collisions. The decreasing trend in Pb-Pb collision is attributed to re-scattering effect in the hadronic medium.

Bibliography

- [1] (ALICE Collaboration) B. Abelev *et al.*, Phys. Lett. B 719, 29-41 (2013).
- [2] (ATLAS Collaboration) G. Aad *et al.*, Phys. Rev. Lett. 116, 172301 (2016).
- [3] (CMS Collaboration) V. Khachatryan *et al.*, Phys. Rev. Lett. 115, 012301 (2015).
- [4] (ALICE Collaboration) B. B. Abelev *et al.*, Phys. Lett. B 726, 164–177 (2013).
- [5] (ALICE Collaboration) B. B. Abelev *et al.*, Phys. Lett. B 728, 25–38 (2014).
- [6] (ALICE Collaboration) J. Adam *et al.*, Phys. Lett. B 758, 389-401 (2016).
- [7] (ALICE Collaboration) J. Adam *et al.*, Nature Physics, 4111 (2017).
- [8] (ALICE Collaboration) B. Abelev *et al.*, Phys. Rev. C 88, 044909 (2013).
- [9] Olive, K. A. and others (Particle Data Group), Chin. Phys. C 38, 090001 (2014).
- [10] (ALICE Collaboration) Analysis Note: <https://aliceinfo.cern.ch/Notes/node/390>
- [11] C. Tsallis, J. Stat. Phys. 52, 479 (1988).
- [12] (STAR Collaboration) B. I. Abelev *et al.*, Phys. Rev. C 75, 064901 (2007).
- [13] (ALICE Collaboration) K. Aamodt *et al.*, Phys. Lett. B 696, 328-337 (2011).
- [14] (ALICE Collaboration) B. Abelev *et al.*, Eur. Phys. J. C 72, 2183 (2012).

- [15] (ALICE Collaboration) J. Adam *et al.*, Eur. Phys. J. C 76, 245 (2016).
- [16] (ALICE Collaboration) B. B. Abelev *et al.*, Phys.Rev. C 91, 024609 (2015).
- [17] (ALICE Collaboration) B. B. Abelev *et al.*, Phys. Lett. B 728, 25-38 (2014).
- [18] (ALICE Collaboration) J. Adam *et al.*, arXiv:1702.00555v1 (2017).
- [19] J. Stachel *et al.*, J. Phys. Conf. Ser. 509, 012019 (2014).
- [20] A. G. Knospe *et al.*, Phys. Rev. C 93, 014911 (2016).
- [21] R. Barlow, arXiv:hep-ex/0207026 (2002).
- [22] (ALICE Collaboration), B. Abelev *et al.*, Phys. Lett. B 720, 52 (2013).
- [23] (ALICE Collaboration) Analysis Note: <https://aliceinfo.cern.ch/Notes/node/279>.
- [24] (ALICE Collaboration) Analysis Note: <https://aliceinfo.cern.ch/Notes/node/429>.

4.5 Appendix

The πK invariant mass distribution for various V0M multiplicity event classes at mid-rapidity ($|\eta| < 0.8$) in pp collisions at $\sqrt{s} = 7$ TeV are shown in the Fig. 4.20 to Fig. 4.25.

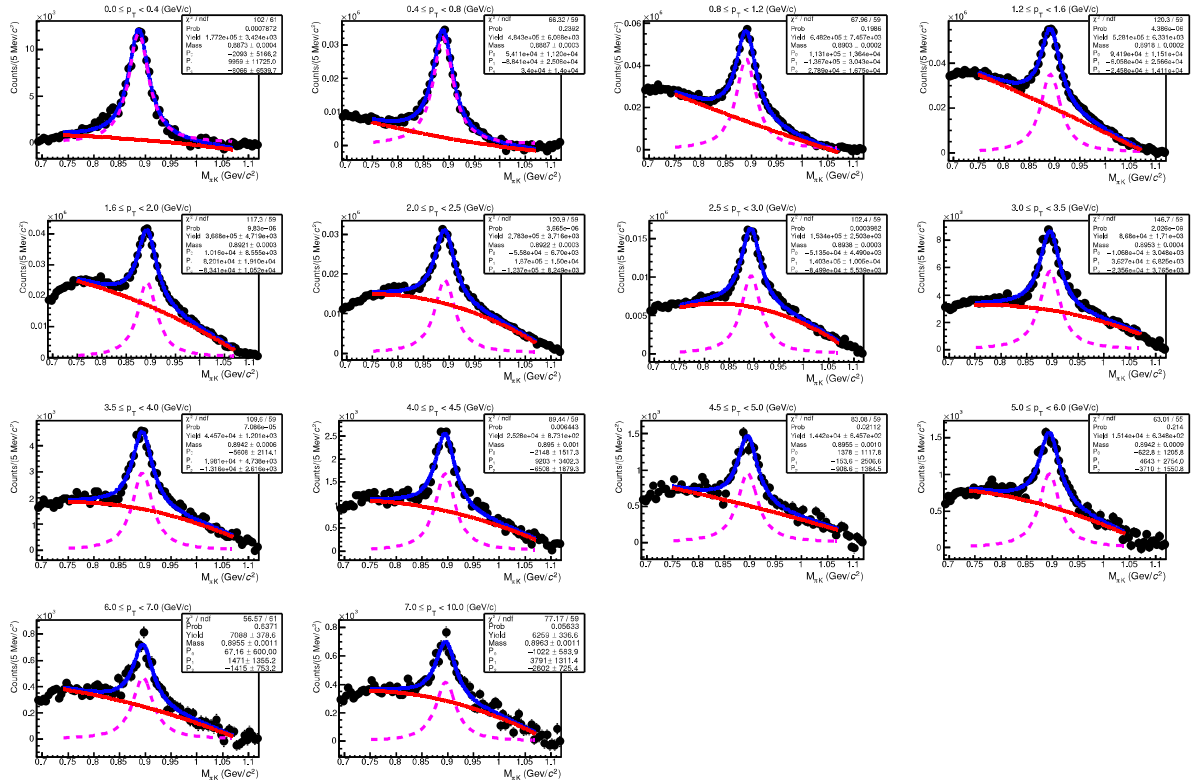


Figure 4.20: The πK invariant mass for 0-100% V0M multiplicity event classes in pp collisions at $\sqrt{s} = 7$ TeV. The blue line is the BW with quadratic function (red line) in invariant mass and magenta line is the only BW function.

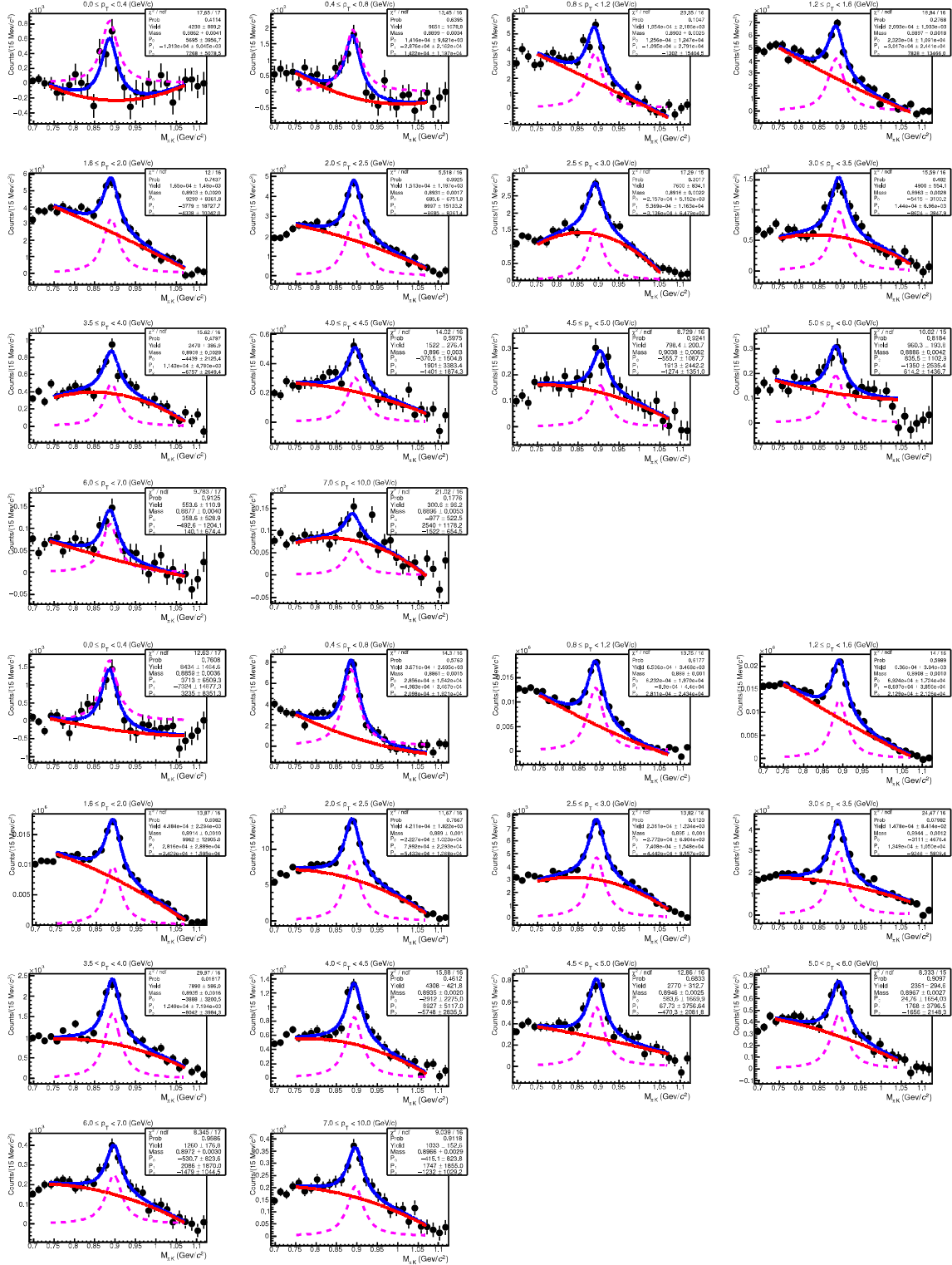


Figure 4.21: The πK invariant mass for 0-1% (upper panel) and 1-5% (lower panel) V0M multiplicity event classes in pp collisions at $\sqrt{s} = 7$ TeV. The blue line is the BW with quadratic function (red line) in invariant mass and magenta line is the only BW function.

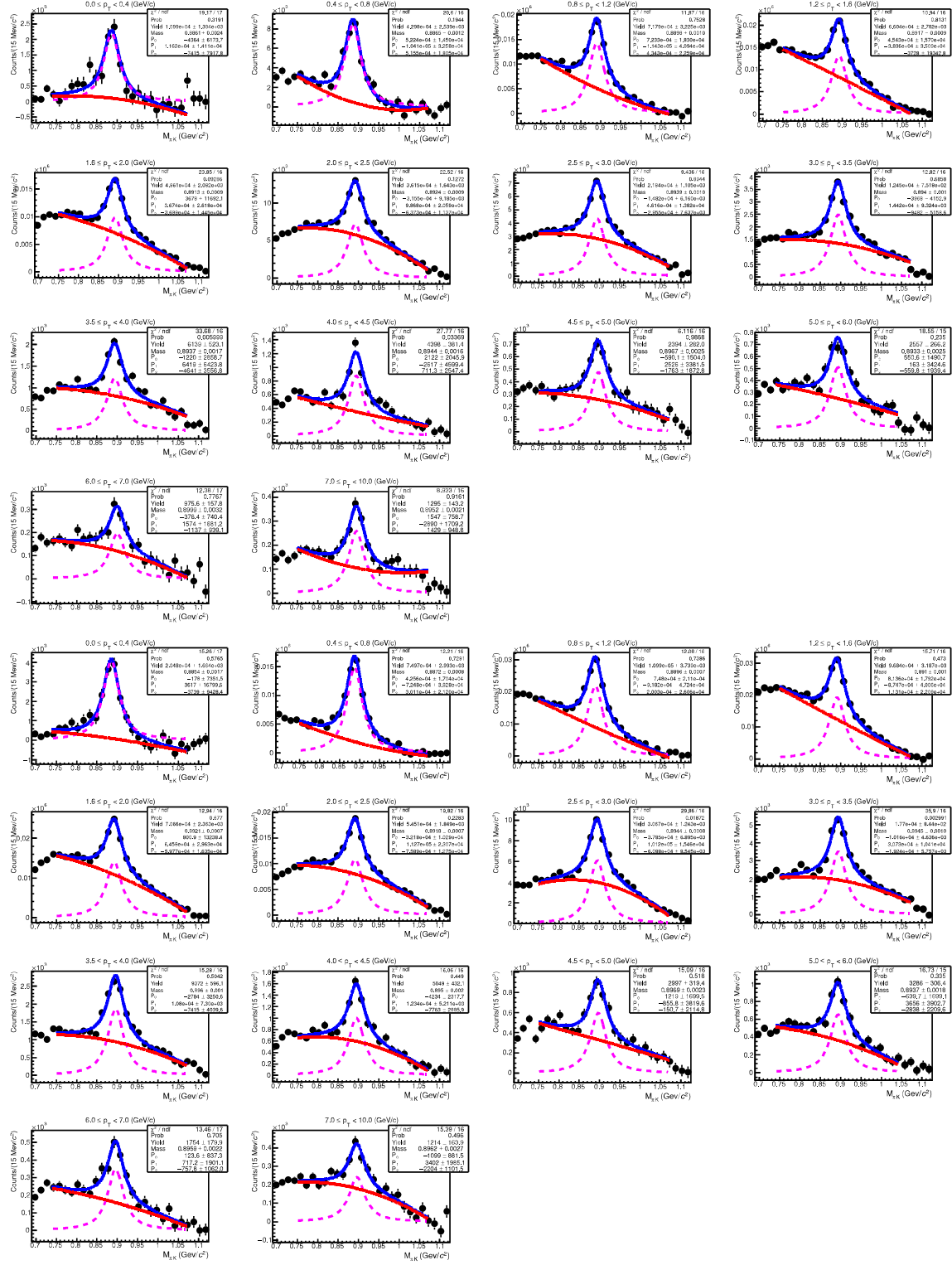


Figure 4.22: The πK invariant mass for 5-10% (upper panel) and 10-20% (lower panel) V0M multiplicity event classes in pp collisions at $\sqrt{s} = 7$ TeV. The blue line is the BW with quadratic function (red line) in invariant mass and magenta line is the only BW function.

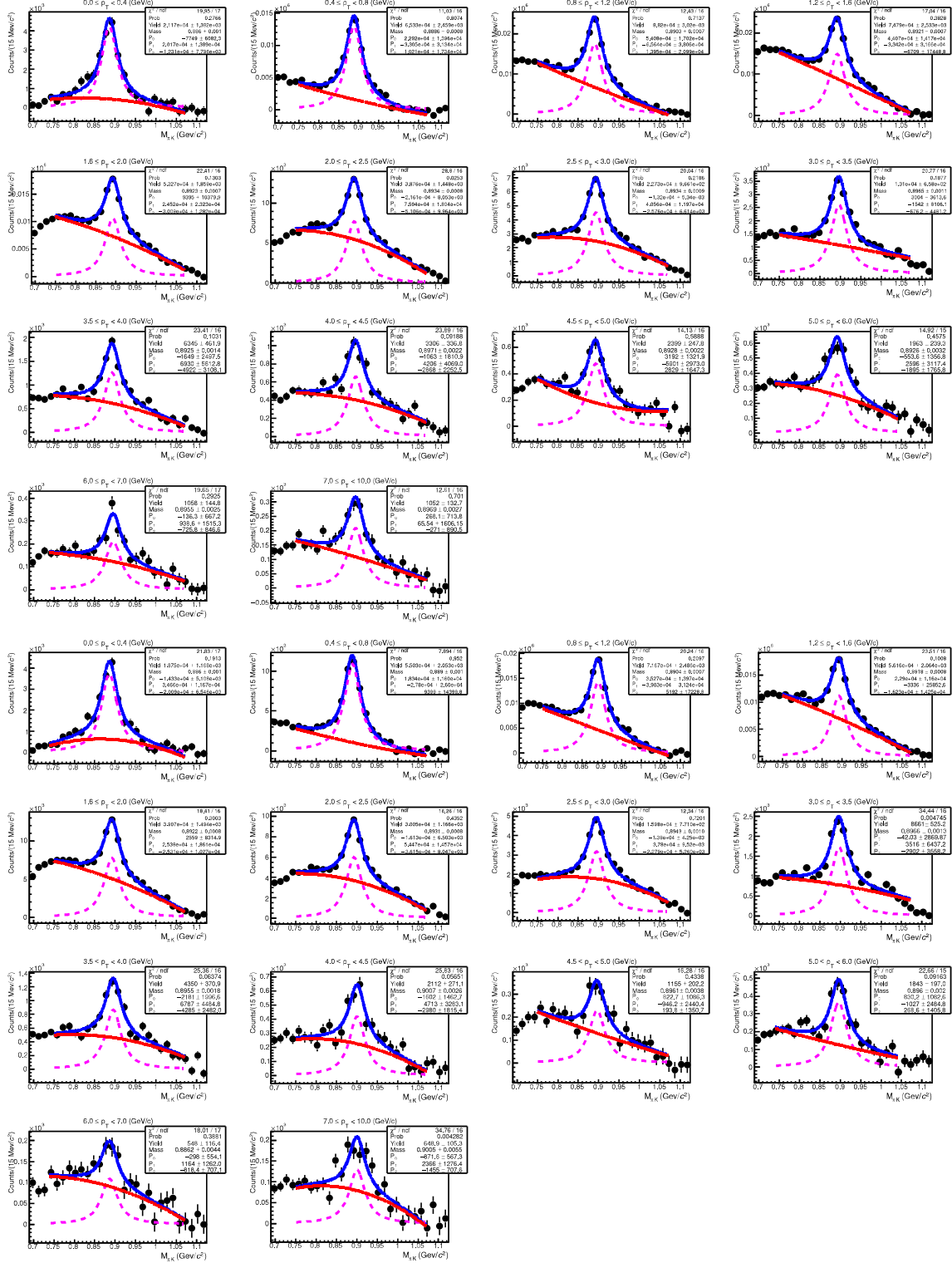


Figure 4.23: The πK invariant mass for 20-30% (upper panel) and 30-40% (lower panel) V0M multiplicity event classes in pp collisions at $\sqrt{s} = 7$ TeV. The blue line is the BW with quadratic function (red line) in invariant mass and magenta line is the only BW function.

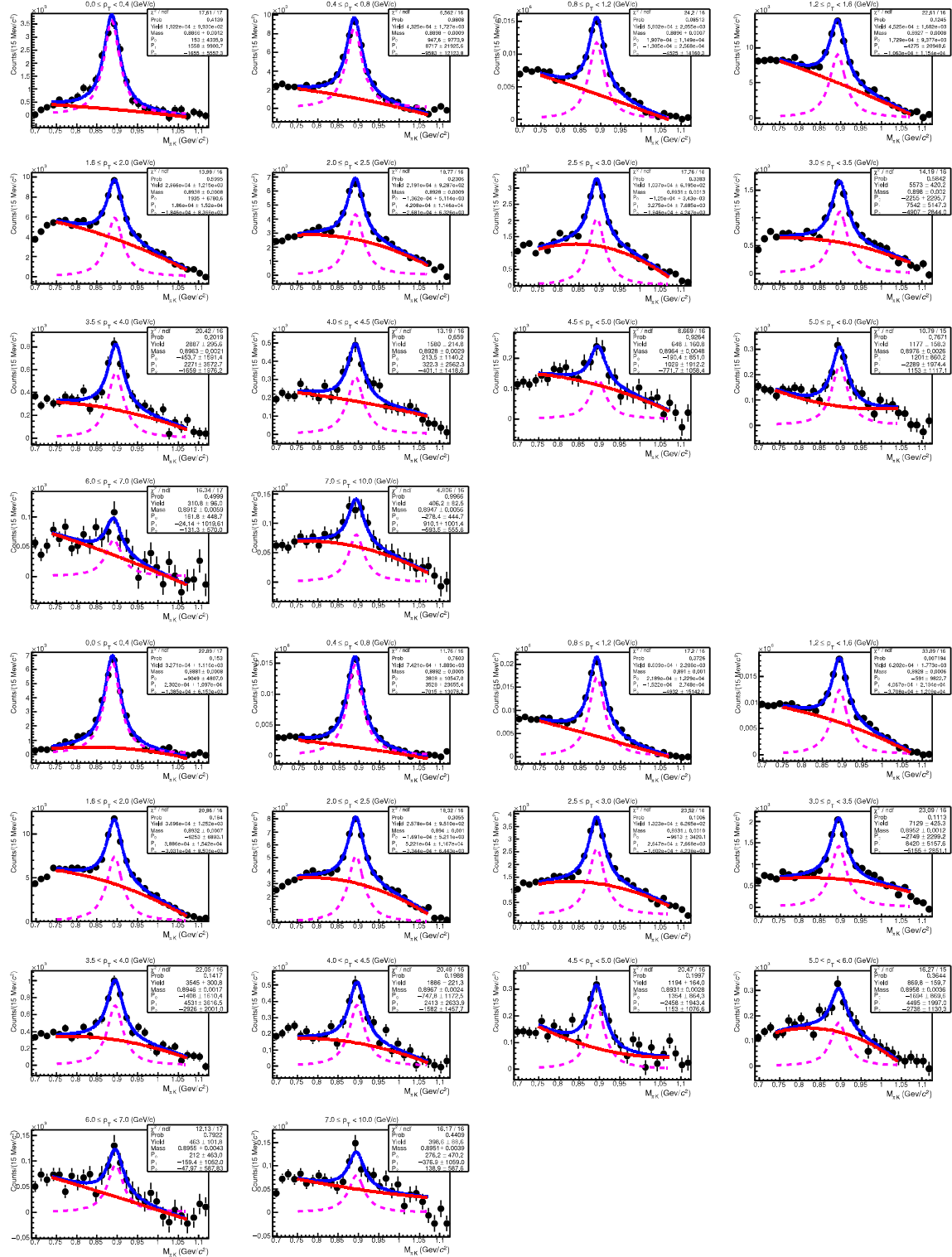


Figure 4.24: The πK invariant mass for 40-50% (upper panel) and 50-70% (lower panel) VOM multiplicity event classes in pp collisions at $\sqrt{s} = 7$ TeV. The blue line is the BW with quadratic function (red line) in invariant mass and magenta line is the only BW function.

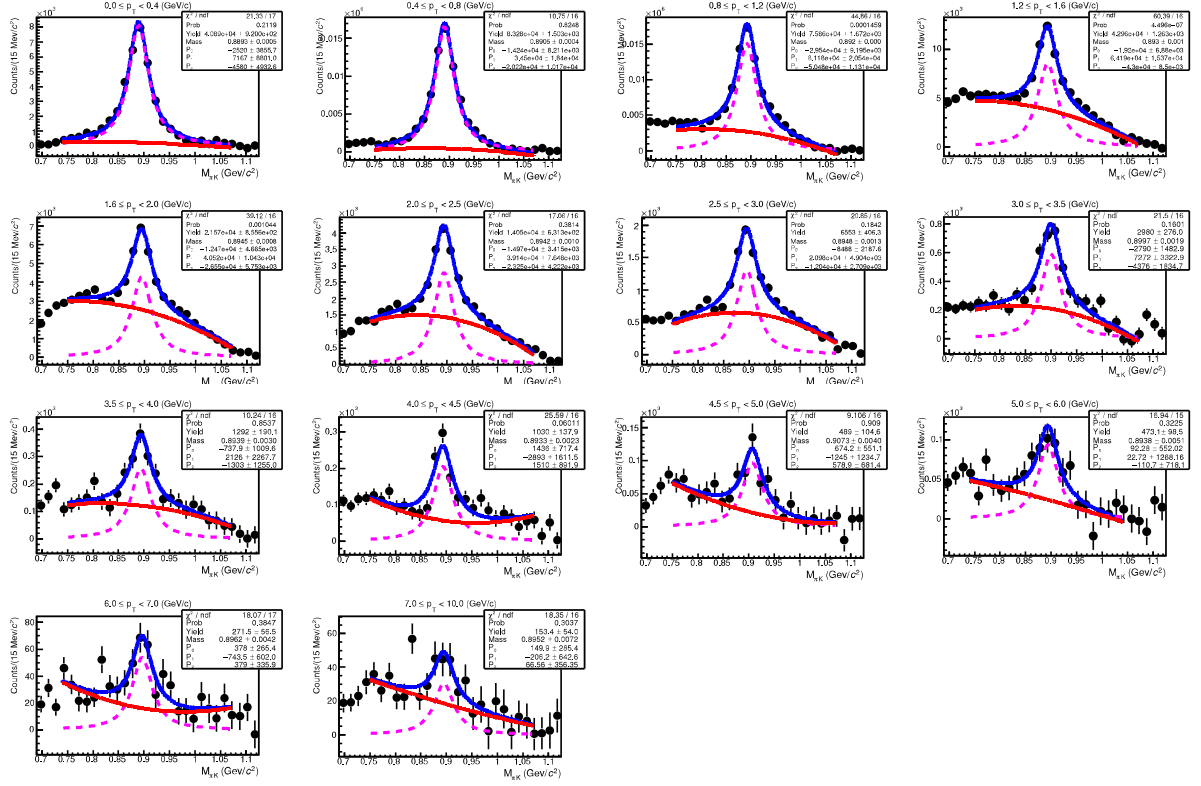


Figure 4.25: The πK invariant mass for 70-100% V0M multiplicity event classes in pp collisions at $\sqrt{s} = 7$ TeV. The blue line is the BW with quadratic function (red line) in invariant mass and magenta line is the only BW function.

Chapter 5

Elliptic flow of $K^*(892)^0$ in Pb–Pb collisions at $\sqrt{s_{\text{NN}}} = 2.76 \text{ TeV}$

Elliptic flow (v_2) measurement provides information about the equation of state and the transport properties of the QGP medium created by relativistic heavy-ion collisions. Anisotropic particle production in the azimuthal direction is the experimental signature of collective flow in heavy-ion collisions [28, 30, 3]. This flow is mainly caused by the asymmetries in the non-central heavy-ion collision geometry.

The $v_2(p_T)$ measurement at low- p_T compared to hydrodynamic calculations shows that the elliptic flow is developed primarily in early partonic stage and then governed by the QGP evolution [4]. However, the late hadronic in-medium effects like re-scattering phenomenon could also contribute to the development of v_2 [5, 6]. As there are experimental evidence which shows that K^{*0} gets affected by hadronic re-scattering, so it would be interesting to measure the $K^{*0} v_2(p_T)$ in order to understand the effect of re-scattering on K^{*0} flow.

The number of constituent quark (NCQ or n_q i.e $n_q = 2$ and 3 for mesons and baryon, respectively) scaling of v_2 is a signature of collectivity developed in the par-

tonic level [4]. There are experimental evidence from recent highest energy RHIC and LHC precision measurements which show that NCQ scaling is not universal [7, 8]. The study of K^{*0} v_2 might give us the idea about the collectivity developed in the partonic level and can help to understand the violation of NCQ scaling at LHC energies. This study includes the measurement of K^{*0} v_2 in Pb–Pb collisions at $\sqrt{s_{NN}} = 2.76$ TeV to test the NCQ scaling to understand particle production mechanism and effect of hadronic re-scattering and regeneration on K^{*0} flow at the LHC energies.

In this chapter, the K^{*0} v_2 measurement in various centrality classes at mid-rapidity ($|\eta| < 0.8$) for Pb–Pb collisions at $\sqrt{s_{NN}} = 2.76$ TeV are presented. A detail of the event plane angle (ψ) calculation is given at the beginning. Then, two different standard methods of extracting v_2 , one using the event plane method with $(\phi - \psi)$ binning procedure and other using the invariant mass fit method is performed. The results have been compared with the corresponding measurements from other identified hadrons (π , K , K_S^0 , p , ϕ , Λ , Ξ , Ω) to test the mass ordering hypothesis of v_2 at low- p_T and baryon-meson effect at intermediate- p_T and number of constituent quark scaling.

5.1 Data set and analysis cuts

The analysis is based on the Pb–Pb data at $\sqrt{s_{NN}} = 2.76$ TeV collected by the ALICE experiment at LHC in the year 2010. The analysis track cuts are the same as described in the section 3.1.3. Furthermore, a minimum transverse momentum (p_T) and pseudo-rapidity (η) cuts of $p_T > 0.15$ GeV/ c and $|\eta| < 0.8$, respectively are applied. A pair rapidity cut of $|y_{pair}| < 0.5$ is applied to select K^{*0} resonance.

The daughter tracks of K^{*0} (pions and kaons) are identified using both TPC and TOF detector. The particle identification in TPC is based on the specific energy loss

(dE/dx) in the gas medium of the TPC and using the time of flight information from TOF detector. When the information from both the TPC and TOF are available, the pion and kaon are selected using a PID cut of $|N_{\sigma}^{\text{TPC}}| < 2.0$ and $|N_{\sigma}^{\text{TOF}}| < 3.0$. For the tracks without the availability of TOF information, a cut of $|N_{\sigma}^{\text{TPC}}| < 2.0$ is applied.

5.2 Significance ($S/\sqrt{S+B}$) of K^{*0} signal

The K^{*0} signal reconstruction and yield extraction procedure is the same as described in the sub-sections 3.1.4 and 3.1.6, respectively. The significance is defined as $S/\sqrt{S+B}$, where S and B are the signal and background calculated in the 5Γ range. Figure 5.1 shows the K^{*0} significance as a function of p_T for various centralities in Pb–Pb collisions at $\sqrt{s_{\text{NN}}} = 2.76$ TeV. The K^{*0} significance value is the highest for minimum bias.

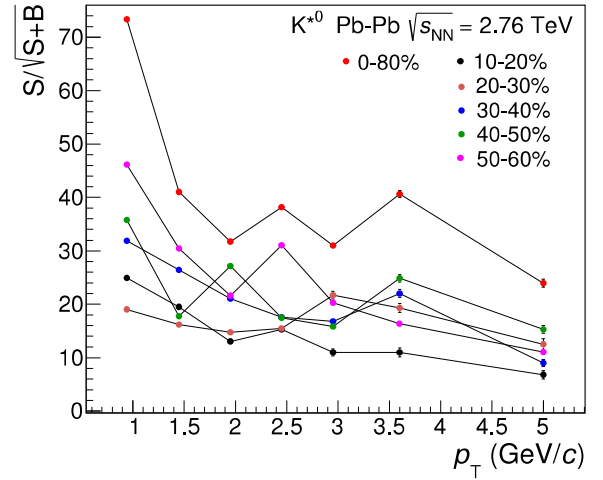


Figure 5.1: Significance of K^{*0} signal in different p_T bins for various centralities in Pb–Pb collisions at $\sqrt{s_{\text{NN}}} = 2.76$ TeV.

5.3 Anisotropic flow

Two nuclei are approaching towards each other in ultra-relativistic speed are Lorentz contracted along the direction of motion (as shown in the introduction section 1.4.2.1, Fig. 1.7). Due to the collision of nuclei, a large number of particles get produced and they are subsequently detected in various sub-detectors. One of the direct experi-

mental evidence of QGP comes from the measurement of flow which is the azimuthal anisotropy in the momentum distributions of particles correlated with reaction plane. The reaction plane is constituted by the impact parameter and beam direction (z) (see Fig. 1.7 of the collision geometry section of the introduction chapter). A convenient way of characterising the different pattern of anisotropic flow is via a Fourier expansion of the invariant yield differential distributions as given in Eq. 5.1.

$$E \frac{d^3 N}{dp^3} = \frac{1}{2\pi p_T} \frac{d^2 N}{dp_T dy} \left[1 + \sum_{n=1}^{\infty} 2v_n \cos[n(\phi - \psi_R)] \right] \quad (5.1)$$

where E is the energy of the particle, ψ_R denotes the reaction plane angle, ϕ is the azimuthal angle. Due to the reflection symmetry with respect to reaction plane, the sine terms vanishes. The Fourier coefficients are p_T and rapidity (y) dependent as given by

$$v_n(p_T, y) = \langle \cos[n(\phi - \psi_R)] \rangle \quad (5.2)$$

The angular bracket represents the average over the particles and summed over all events in a given (p_T, y) . The first harmonic coefficient (v_1) and second harmonic (v_2) are called as directed flow and elliptic flow, respectively. In order to measure the elliptic flow, ψ_R has to be estimated event-by-event. As impact parameter is not an experimentally measurable quantity, so reaction plane can't be determined and hence an estimated reaction plane angle from observed event plane angle is calculated. The event plane angle is calculated using the event flow vector Q_n defined as:

$$Q_{n,x} = Q_n \cos(n\psi_n) = \sum_i w_i \cos(n\phi_i), \quad Q_{n,y} = Q_n \sin(n\psi_n) = \sum_i w_i \sin(n\phi_i) \quad (5.3)$$

where w_i is the weight factor and the summation is over the number of particles

used in the determination of the event plane angle. The event plane angle is calculated using the Eq. 5.4.

$$\psi_n = \frac{1}{n} \left[\tan^{-1} \left(\frac{Q_{n,y}}{Q_{n,x}} \right) \right] \quad (5.4)$$

We have estimated event plane angle using V0 detector. The V0 detector calibration is performed in two steps (i) Gain equalisation and (ii) Recentering of flow vector [9].

(i) Gain equalisation : The gain equalisation is done separately for each ring of the V0 detector to account for the different acceptance using the Eq. 5.5. Figure 5.2 shows the RMS of the multiplicity distribution for each V0 channel before and after gain equalisation. The gain equalisation not only flattens the RMS but also makes the mean multiplicity the same for all channels from one ring.

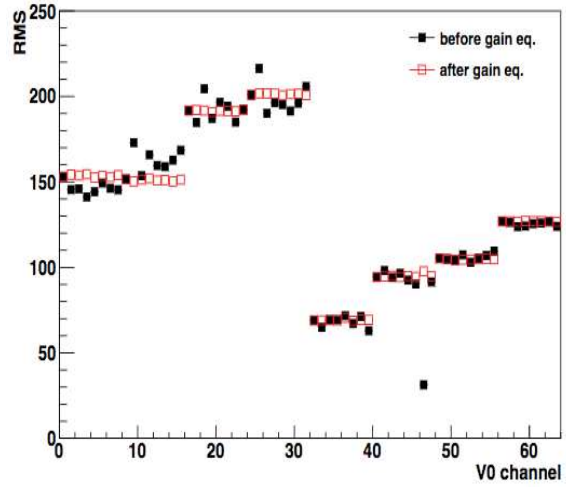


Figure 5.2: RMS of the multiplicity distribution before (black) and after (red) gain equalisation [9].

$$M_i^{cor} = M_i / \langle M_i \rangle \times M, \quad (5.5)$$

where M_i is the multiplicity of the i^{th} channel of the V0 detector in the event analysed, $\langle M_i \rangle$ the mean multiplicity of the i^{th} channel from all good events, M is the gain factor fixed to the multiplicity of the first channel from each ring.

(i) Recentering of flow vector : The recentering is performed in 1% central-

ity bins using the following equations:

$$Q_{n,x}^{cor} = \frac{Q_{n,x} - \langle Q_{n,x} \rangle}{\sigma_{Q_{n,x}}}; \quad Q_{n,y}^{cor} = \frac{Q_{n,y} - \langle Q_{n,y} \rangle}{\sigma_{Q_{n,y}}}, \quad (5.6)$$

where $\langle Q_n \rangle$ and σ_{Q_n} are the mean value and the width of the Q_x (Q_y) distribution from the data sample under study.

After applying the gain equalisation and recentering to the data sample, the V0C event plane angle for various centralities are calculated and shown in the Fig. 5.3. The distributions are fitted to a function $p_0[1 + p_1\cos(2\psi) + p_2\sin(2\psi)]$, where p_0 , p_1 and p_2 are free parameters. The fit is performed in order to understand bias on the v_2 due to event plane angle. The values of p_1 and p_2 are 0.02% and 0.01%, respectively for minimum bias collisions. The value of p_1 and p_2 parameters are suggesting that the bias due to non-flatness of event plane angle, ψ on the final v_2 result is negligible.

5.3.1 Event plane resolution

The finite number of particles in an event (which are available for calculating the event plane) leads to a limited resolution in the measured event plane angle. So to find the flow coefficient, v_n , with respect to the event plane, the measured v_n^{obs} is divided by a resolution correction factor R_n .

$$v_n = v_n^{\text{obs}} / R_n \quad (5.7)$$

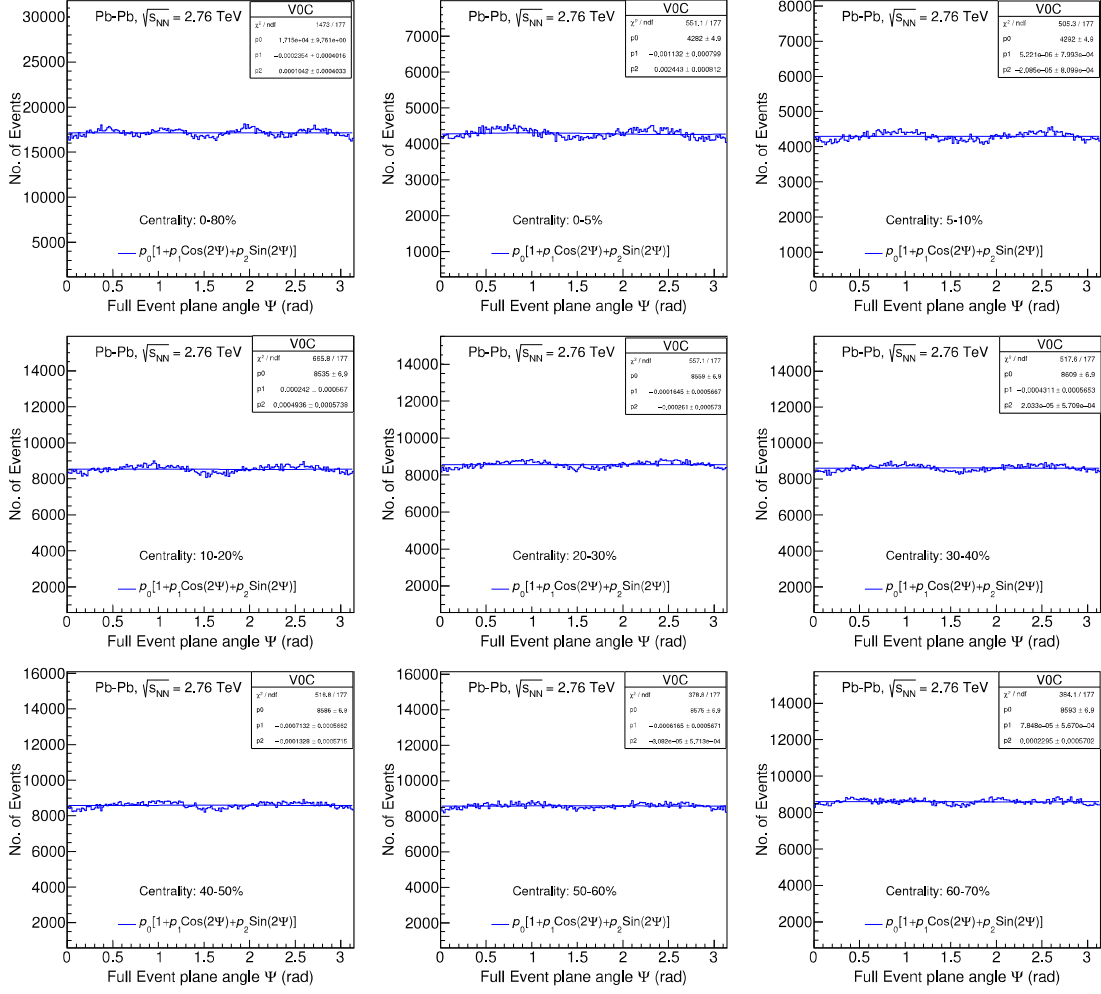


Figure 5.3: Event plane angle (ψ) distribution in different centrality using V0C detector in Pb–Pb collisions at $\sqrt{s_{NN}} = 2.76$ TeV. The blue line is the fit function $\frac{dN}{d\psi} = p_0[1 + p_1 \cos(2\psi) + p_2 \sin(2\psi)]$.

Three sub-event technique is used to calculate the event plane resolution and the detectors used for this purpose are TPC, V0A and V0C. The resolution of a given detector (V0C) is defined from the correlation between each detector pair as given in Eq. 5.8 [14].

$$\text{Resolution, } R_2^A = \sqrt{\frac{\langle \cos 2(\psi_2^A - \psi_2^B) \rangle \langle \cos 2(\psi_2^A - \psi_2^C) \rangle}{\langle \cos 2(\psi_2^B - \psi_2^C) \rangle}} \quad (5.8)$$

where A, B and C represents V0C, V0A and TPC detectors, respectively. ψ_2^A is the event plane angle for which the resolution is calculated i.e for V0C and B, C are for other sub-detectors.

The event plane resolution depends on the number of particles and magnitude of flow, so it varies as a function of centrality and attains a maximum value in mid-central (20-30%) and then degrades with more peripheral collisions as shown in Fig. 5.4. As the event plane is calculated using the anisotropic flow of the event itself, for more central collisions the resolution also becomes poorer since the shape of overlap region becomes less elliptical. The second order event plane resolution obtained using TPC, V0C and V0A detectors are consistent with the published results within 5% [14].

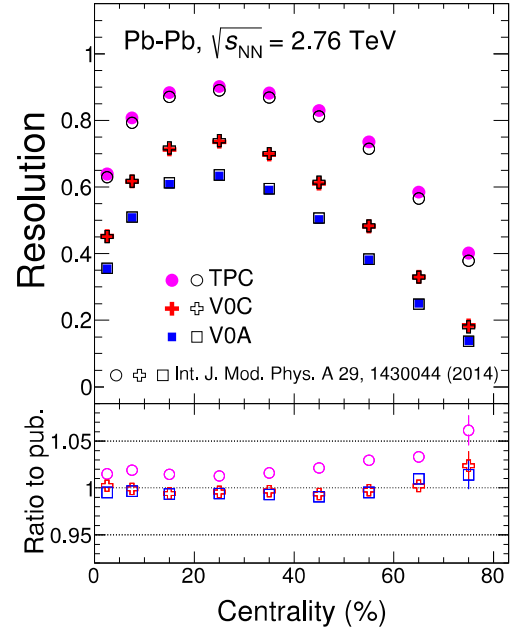


Figure 5.4: The second order event plane resolution as function of centrality in Pb–Pb collisions at $\sqrt{s_{\text{NN}}} = 2.76$ TeV for TPC, V0C and V0A compared with the published results [14].

In this analysis, the event plane resolution is calculated in various centrality classes i.e 0-5%, 5-10%, 10-20%, 20-30%, 30-40%, 40-50%, 50-60%, 60-70%, 70-80%. For minimum bias (0-80%), the combined resolution is calculated using weighted average procedure where the K^*0 raw yield is used as the weight factor for each centrality.

There are various techniques to calculate the flow such as event plane, invariant mass technique, scalar product, two particle cumulant, four particle cumulant *etc.*

For this analysis, the invariant mass method and event plane method with $(\phi - \psi)$ binning are used to estimate the elliptic flow of K^{*0} meson. However, invariant mass method is taken as the default method to calculate $K^{*0} v_2$ in various centralities.

5.4 Elliptic flow extraction method

In this analysis, two different methods are used to extract the K^{*0} -meson elliptic flow namely event plane method with $(\phi - \psi)$ binning [11] and the invariant mass fit method [15]. The details of elliptic flow extraction methods are described in the following sub-sections.

5.4.1 Event plane method

The event plane method [11] needs decomposition of the K^{*0} signals and background in different $(\phi - \psi)$ bins for each p_T bin and centrality classes. The K^{*0} signal extracted in a different $(\phi - \psi)$ bins are fitted to the following function:

$$\frac{dN}{d(\phi - \psi)} = p_0[1 + 2v_2^{obs}\cos(\phi - \psi)] \quad (5.9)$$

where p_0 and v_2^{obs} are the fit parameters. The measured v_2^{obs} values are divided or corrected by appropriate event plane resolution correction factor (Fig. 5.4) to obtain the final v_2 . For a given centrality class, the process is performed for different p_T intervals and then the p_T -dependent K^{*0} flow is obtained as shown in the Fig. 5.5 for 0-80% centrality.

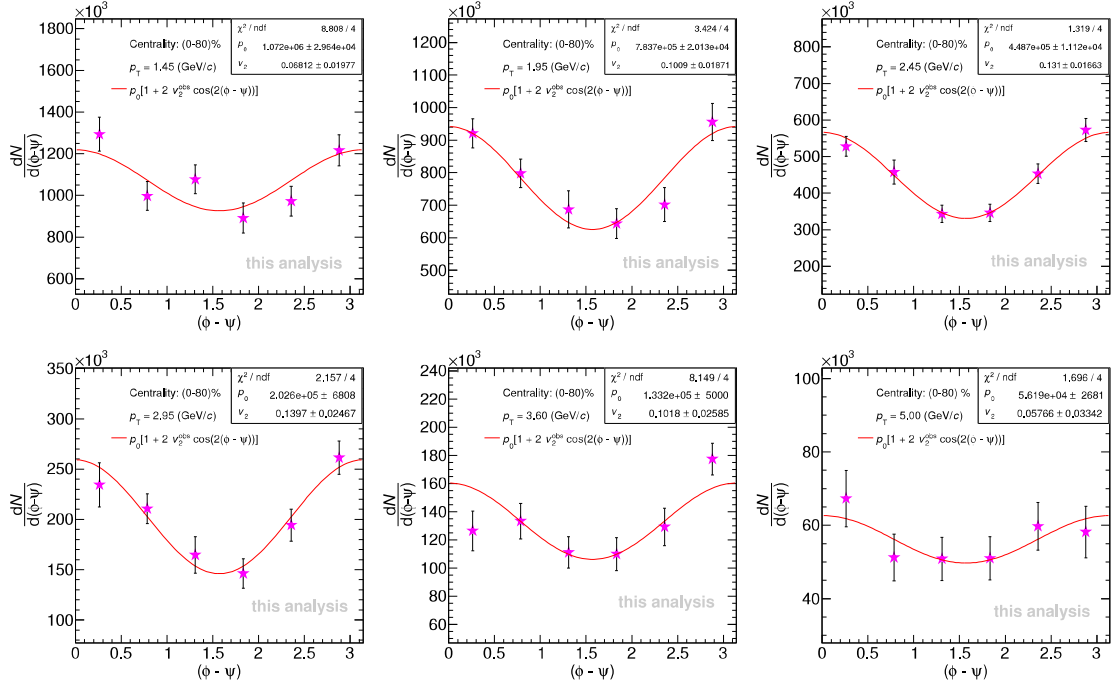


Figure 5.5: $(\phi - \psi)$ distribution of K^{*0} meson in different p_T bins for 0-80% centrality at mid-rapidity ($|\eta| < 0.8$) in Pb-Pb collisions at $\sqrt{s_{NN}} = 2.76$ TeV.

In case of resonances like K^{*0} , typically the signal consists of a resonance peak sitting above the large combinatorial background (i.e. the signal to background ratio is less than unity), so it is a humongous task to extract raw yields in different $(\phi - \psi)$ bins in each p_T -intervals. So when a single p_T bin is decomposed into different $(\phi - \psi)$ bins, the signal quality also decreases and even signal couldn't be extracted in some cases and this stringent process of signal extraction leads to large systematic error as the fits to the invariant mass peak are difficult to constrain. However, the event plane method doesn't need the assumption of a background v_n shape and hence it has some advantage for the case like K^{*0} when the signal to background ratio is poor as compared to invariant mass method as described in the next section.

5.4.2 Invariant mass fit method

This method of calculating v_2 is proposed in Ref. [15]. The invariant mass method is primarily useful for those particles which are reconstructed from their decay daughters (e.g $\phi \rightarrow K^+ K^-$). The additive nature of flow allows us to decompose the anisotropic flow v_n of a short-lived particle from that of all possible daughter pairs as a function of invariant mass. For extracting the v_2 of the K^{*0} meson, it utilises the fact that the v_2 of πK pairs is composed of the v_2 of the K^{*0} meson and the v_2 of the combinatorial background. The invariant mass distribution can be decomposed into:

$$N^{Sig+Bg}(M_{inv}) = N^{Sig}(M_{inv}) + N^{Bg}(M_{inv}) \quad (5.10)$$

Where N^{Sig+Bg} is the total number of pairs, N^{Sig} is the number of signal pairs (number of real particles) and N^{Bg} is the number of combinatorial background pairs.

The invariant mass method involves estimating the event plane angle the same way as before and then measuring the $v_2 = \langle \cos 2(\phi - \psi) \rangle$ of all same-event combinations of πK pairs as a function of invariant mass.

$$v_2^{Sig+Bg}(M_{inv}) = \langle \cos[n(\phi - \psi)]_{inv} \rangle = A(M_{inv})v_2^{Sig} + [1 - A(M_{inv})]v_2^{Bg} \quad (5.11)$$

where $v_2^{Sig+Bg}(M_{inv})$ is the v_2 of same-event πK pairs which includes the signal and background, v_2^{Sig} is the v_2 of the K^{*0} meson, v_2^{Bg} is the effective v_2 of the combinatorial background and $A(M_{inv}) = N^{Sig}(M_{inv})/N^{Sig+Bg}(M_{inv})$ is the ratio of the K^{*0} signal to the sum of the background and K^{*0} signal M_{inv} distribution. The signal count of the ratios are obtained by fitting the mixed-event background subtracted signal with a Breit-Wigner (to describe peak) convoluted with a polynomial function (to parameterise the residual background shape). The background counts are obtained

from mixed event distribution.

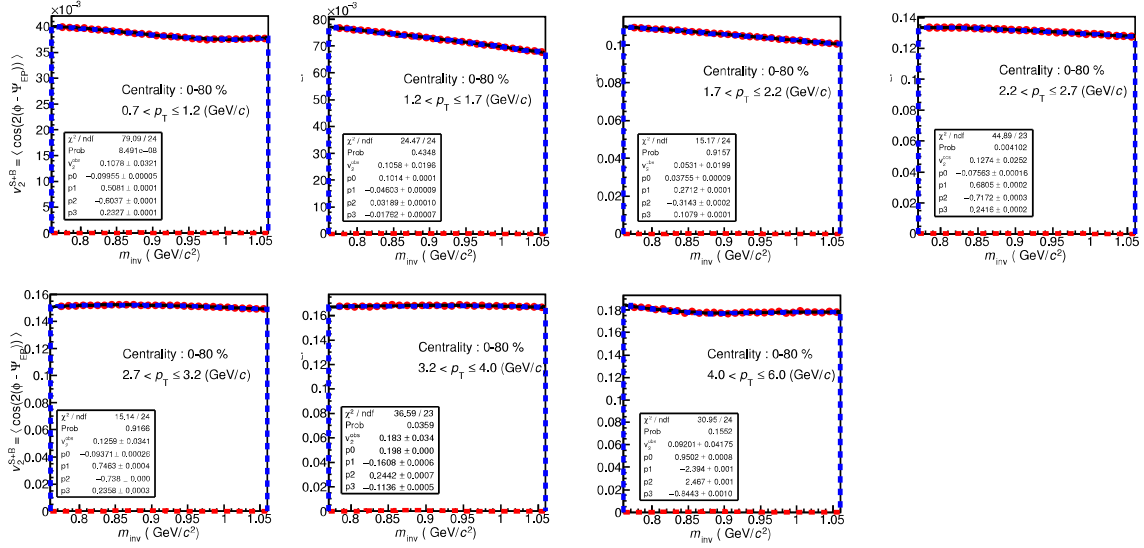


Figure 5.6: The v_2^{S+B} distributions (black line) in different p_T bins for (0-80%) centrality as a function of M_{inv} at mid-rapidity ($|\eta| < 0.8$) in Pb-Pb collisions at $\sqrt{s_{NN}} = 2.76$ TeV. The distributions are fitted with Eq. 5.11. The red and blue line represents the first and second part of Eq. 5.11.

Figure 5.6 shows the v_2^{Sig+Bg} distribution as a function of invariant mass, M_{inv} , in different p_T intervals for 0-80% centrality in Pb-Pb collisions at $\sqrt{s_{NN}} = 2.76$ TeV. Assuming the background contribution to v_2^{Bg} (the second part on the right side of Eq. 5.11) as a smooth function M_{inv} , a polynomial function of 3rd order is used to parameterise the background v_2^{Bg} . The free parameter, v_2^{Sig} , is obtained by fitting v_2^{Sig+Bg} versus M_{inv} by Eq. 5.11 for each p_T bin in a given collision centrality. The v_2^{Sig} value obtained from the fit is then corrected by the event plane resolution to obtain the final K^{*0} v_2 .

5.4.3 Comparison of two methods

Two standard methods of calculating v_2 has been used in this analysis as described in the section 5.4.1 and 5.4.2. The upper panel of Fig. 5.7 shows the $K^{*0} v_2$ obtained using (i) event plane and (ii) invariant mass method for 0-80% centrality in Pb-Pb collisions at $\sqrt{s_{NN}} = 2.76$ TeV and the corresponding ratio is shown in the lower panel. The $K^{*0} v_2$ comparison obtained using two different methods are consistent within 5%. The invariant mass method is used for obtaining $K^{*0} v_2$ in various centralities as discuss below.

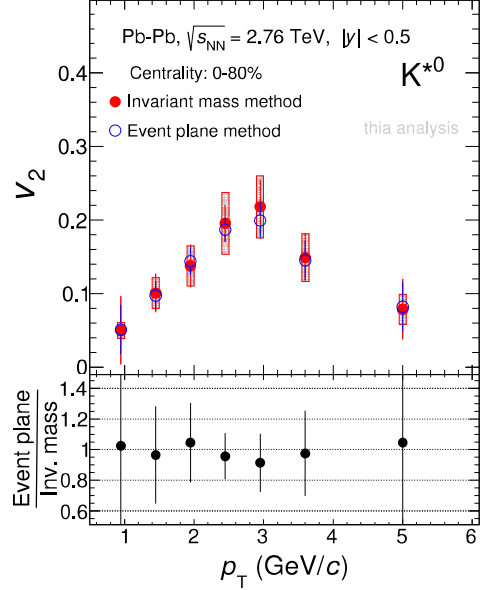


Figure 5.7: p_T dependent $K^{*0} v_2$ for 0-80% centrality in Pb-Pb collisions at $\sqrt{s_{NN}} = 2.76$ TeV. The box (line) represents the systematic (statistical) uncertainty.

5.5 $K^{*0} v_2$

The p_T -dependent (p_T -integrated) $K^{*0} v_2$ measured using the invariant mass method for different centralities are shown on the left (right) panel of Fig. 5.8. The statistical (systematic) uncertainty is represented by bars (box and cap). The value of $K^{*0} v_2$ progressively increases from central (10-20%) to peripheral (40-50%) collisions. So, there is reasonable centrality dependence of $K^{*0} v_2$ even though statistical and systematic uncertainties are larger. This observation is consistent with the notion that initial collision geometry (higher eccentricity for peripheral collisions) is the main driving cause for final state anisotropy. For all centralities, $K^{*0} v_2$ increases

linearly upto $p_T = 3 \text{ GeV}/c^2$ and then decreases.

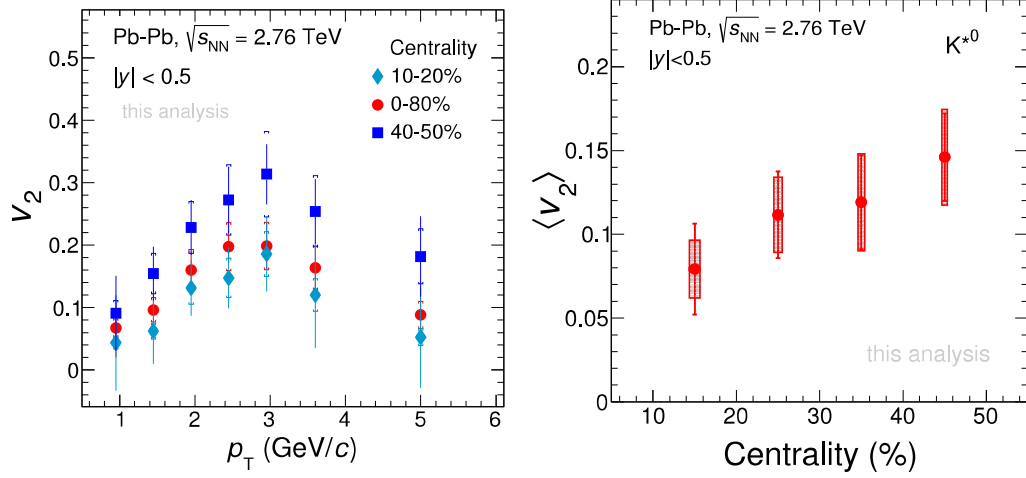


Figure 5.8: The p_T -dependent (left panel) and p_T -integrated (right panel) $K^{*0} v_2$ in various centralities at mid-rapidity ($|\eta| < 0.8$) in Pb-Pb collisions at $\sqrt{s_{NN}} = 2.76 \text{ TeV}$. The vertical line and box (cap for the left figure) represent the statistical and systematic uncertainties, respectively.

The p_T -dependent $K^{*0} v_2$ is also compared with other identified particles (π , K , p , K_S^0 , ϕ , Λ , Ξ , Ω) in various centralities are shown in Fig. 5.9 i.e from top left 10-20% to bottom right 50-60% centralities. The $K^{*0} v_2$ trend seems to follow mass ordering at low- p_T ($\leq 3 \text{ GeV}/c$), similar to other hadrons. However, the v_2 of K^{*0} seems to be high at about $3 \text{ GeV}/c$ although the error bars are large. This increase might be due to hadronic re-scattering effect, which tries to increase the $K^{*0} v_2$. The mass ordering nature of identified hadrons v_2 at low- p_T is an interplay between radial and elliptic flow [16, 17, 18]. Due to radial flow, particles with low- p_T values gets pushed towards the high- p_T values creating a depletion in low- p_T region. This process increases with increase in particle masses and transverse velocity. This radial flow when introduced to a system that exhibits azimuthal anisotropy, the depletion becomes larger in-plane than out-of-plane and it reduces the v_2 . As a result of these, heavier particles flows less as compared to lighter hadrons at a fixed value of p_T .

In the intermediate- p_T , the v_2 values tends to group as per their hadron type i.e baryons and mesons [19, 20]. It was also reported that when both v_2 and p_T are scaled by n_q , the different identified hadron species approximately follow a common trend [19, 20]. The scaling properties is also extended by taking transverse kinetic energy ($KE_T = \sqrt{m_T - m_0}$, where $m_T = \sqrt{p_T^2 + m_0^2}$) instead of p_T . This baryon and meson scaling behaviour is successfully explained by models which invoke quark coalescence as the dominant hadronization mechanism at intermediate- p_T [21, 22, 23]. So, NCQ scaling of v_2 is an evidence that quark degrees of freedom dominate in the early stage of heavy-ion collisions, when collectivity develops [21, 22].

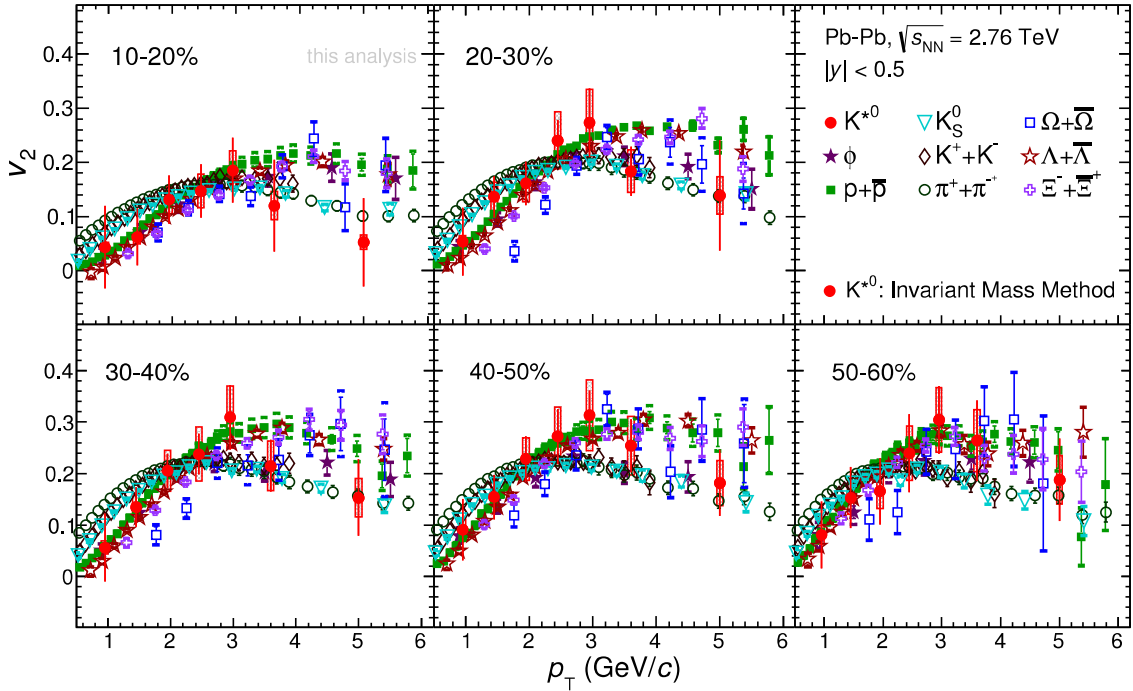


Figure 5.9: K^{*0} v_2 as a function of p_T compared with other identified hadrons in various centralities in Pb-Pb collisions at $\sqrt{s_{NN}} = 2.76$ TeV [8].

Figure 5.10 shows the v_2/n_q as a function of $(m_T - m_0)/n_q$ for different identified hadrons including the K^{*0} in various collision centralities. The scaling is observed

to be approximate at LHC energies [8]. After adding the K^{*0} v_2 , the scaling gets even worsen although the uncertainties are larger. This imply that K^{*0} v_2 in Pb–Pb collisions at $\sqrt{s_{NN}} = 2.76$ TeV is not following the scaling behaviour. However, more statistics is needed to conclude firmly.

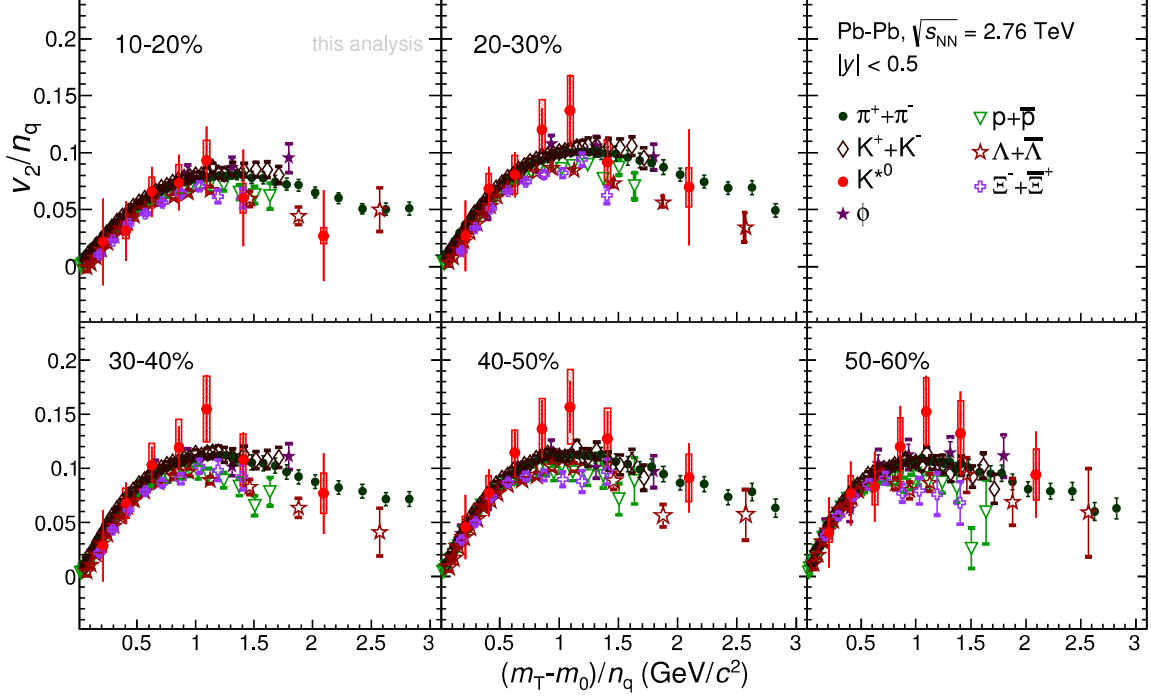


Figure 5.10: v_2/n_q as a function of $(m_T - m_0)/n_q$ of identified hadrons in various centralities in Pb–Pb collisions at $\sqrt{s_{NN}} = 2.76$ TeV [8].

The p_T -integrated K^{*0} v_2 in different centralities are calculated as given in Eq. 5.12.

$$\langle v_2 \rangle = \frac{\int v_2 f(p_T) dp_T}{\int f(p_T) dp_T}. \quad (5.12)$$

Where the $f(p_T)$ is the p_T -spectra [24]. Let $a = \int v_2 f(p_T) dp_T$ and $b = \int f(p_T) dp_T$, then for the uncertainty on $\langle v_2 \rangle$ is calculated as by using error propagation formula $\sigma_{\langle v_2 \rangle} = (a/b) \times \sqrt{(\delta a/a)^2 + (\delta b/b)^2}$

5.6 Systematic uncertainty study

A detail systematic study of K^{*0} signal and v_2 extraction is performed in this analysis. The study of systematic uncertainty calculation due to K^{*0} signal extraction procedure is similar to that described in sub-section 3.2.7.1.

The systematic study is performed by measuring the change in K^{*0} v_2 value by varying one parameter at a time. The main sources of the systematic uncertainties can be combined in four groups such as (i) Signal extraction, (ii) Analysis track cut, (iii) PID selection and (iv) Global Tracking efficiency.

(i) **Signal extractions (E_{sigext}):** To estimate the systematic uncertainties due to signal extractions, we have varied mixed event background normalization range, residual background function, invariant mass fitting range, width of the K^{*0} signal peak. The details of these variations is given below:

- **Mixed event background normalization:** The mixed event background is normalised in the region of invariant mass between 1.1 to 1.15 GeV/ c^2 as a default range which is more than 5σ away from the K^{*0} peak. For the systematic study, the variation in the normalization range is performed on the right side, 1.1-1.5 GeV/ c^2 , and on left hand side 0.7-0.8 GeV/ c^2 of the K^{*0} peak value.
- **Residual background function:** The default function used for the estimation of residual background is 2^{nd} order polynomial function in πK invariant mass. The change in the K^{*0} yield due to consideration of 3^{rd} order polynomial is taken as the systematic uncertainty.
- **Invariant mass fitting range:** The default value of invariant mass fit range is 0.77-1.03 GeV/ c^2 and for systematic study the range variations are 0.72-1.07,

0.78-1.01 GeV/ c^2 .

- **Width of K^{*0} signal peak:** The width of K^{*0} is freed from default fixed valued and the change in yield is considered in systematic uncertainty.

(ii) Global Tracking efficiency (E_{gtrk}): The global tracking efficiency uncertainty shows the difference in TPC-ITS matching probabilities between data and simulation. As a result it should be applied only once, either in reconstruction efficiency or in data. We assign this as an additional systematic uncertainty of 6%.

(iii) Analysis Cuts (E_{anacut}): In this analysis, the tracks are selected which pass a set of standard cuts. For the systematic study, some of the standard cuts are varied. The variation of analysis cuts w.r.t. to default one is shown below:

- Minimum number of crossed rows in TPC: 80 (70 is default)
- DCA_{xy} : 9 sigma (7 sigma is default)
- DCA_z : 3 cm (2 cm is default)
- χ^2/NDF in TPC: 6 (4 is default)

(iv) PID selections (E_{pid}): When the TOF information of a particle is available then $|N\sigma_{TPC}| < 2$ and $|N\sigma_{TOF}| < 3$, but without TOF information only $|N\sigma_{TPC}| < 2$ cut is considered as the default cut. However, for systematic study two other PID cuts are taken: (i) when the TOF information is available then $|N\sigma_{TPC}| < 1$ and $|N\sigma_{TOF}| < 2$; else $|N\sigma_{TPC}| < 1$ and (ii) $|N\sigma_{TPC}| < 2$.

Total Systematic Uncertainty (E_{total}): The total systematic uncertainty is the quadrature sum of all above mention sources.

$$E_{total} = \sqrt{E_{sigext}^2 + E_{anacut}^2 + E_{pid}^2 + E_{gtrk}^2} \quad (5.13)$$

Barlow test [25] has been performed to ensure that the measured systematic

uncertainty is not due to a statistical fluctuation.

Barlow Test: Study of statistical effect on systematic uncertainty

Let a default or central value of a measurement with statistical uncertainty is denoted by $(F_c \pm \sigma_c)$. The measurement for systematic studies are indicated by $(F_i \pm \sigma_i)$, then one can define $\Delta\sigma_i$ (Eq. 5.14).

$$\Delta\sigma_i = \sqrt{|\sigma_i^2 - \sigma_c^2|} \quad (5.14)$$

Then we calculate $R_i = \Delta F_i / \Delta\sigma_i$ (Fig. 5.11), where $\Delta F_i = |F_c - F_i|$. If $R_i \leq 1.0$ then the effects are due to the statistical fluctuation otherwise there is a systematic effect which means that the two measurements are not compatible within the statistical errors.

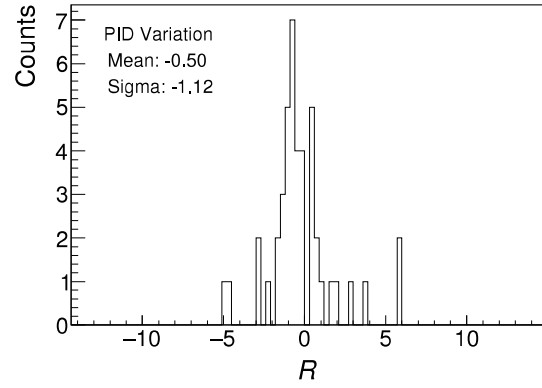


Figure 5.11: The $R = \Delta F / \Delta\sigma$, where ΔF is the v_2 (PID cut) - v_2 (default PID cut) and $\Delta\sigma$ are the corresponding statistical errors distribution for PID cut in 0-80% centrality at mid-rapidity ($|\eta| < 0.8$) in Pb-Pb collisions at $\sqrt{s_{NN}} = 2.76$ TeV.

In ideal case, when two measurements are statistically consistent then R_i distribution should have the criteria: (i) Mean ~ 0 and (ii) RMS ~ 1 . As the number of entries are less, so the criteria for passing the Barlow check we choose any of the 3 conditions out of the 4 criteria : (i) Mean ~ 0 (ii) RMS < 1.1 , (iii) within $|R_i| < 1.0$ there will be ~ 58 to 68 % of counts and (iv) within $|R_i| < 2.0$ there will be ~ 85 to 95 % of counts.

The measurements which passed the Barlow check are not used to determine the systematic uncertainty. When Barlow check fails, then the measurement has been

considered for the systematic.

$$\delta F_{Syst.} = \sqrt{\frac{1}{N} \sum_i (F_i - \bar{F})^2} \quad (5.15)$$

Here N is the total number of available measurements including F_c and \bar{F} is the average value of the measurements. Whenever only two measurements were available and did not pass “Barlow” check, zero systematic uncertainty has been assigned to the value.

Centrality (%)	Syst. uncert. (%)
0-80	19-25
10-20	19-24
20-30	20-23
30-40	19-23
40-50	18-24
50-60	20-25

Table 5.1: The range of systematic uncertainties (%) for different centralities.

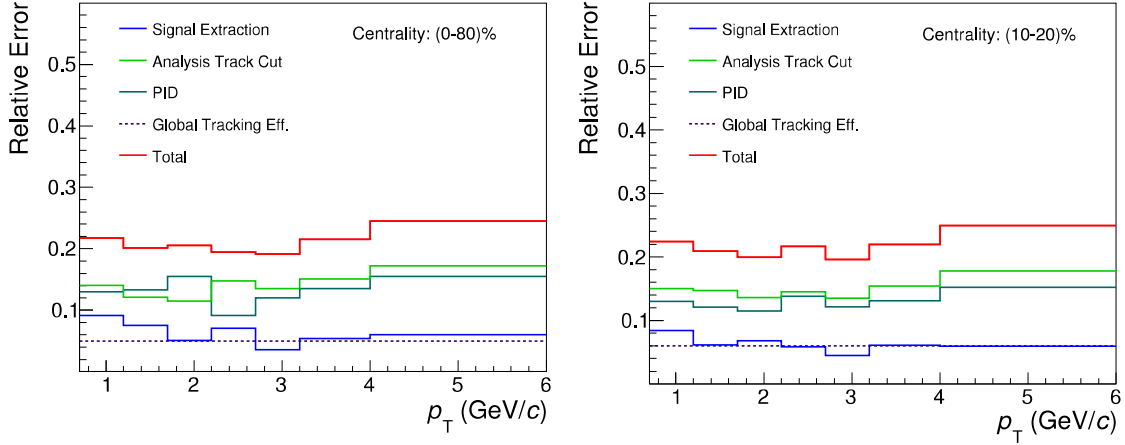


Figure 5.12: Summary of different sources of systematic uncertainties in the measurement of $K^{*0} v_2$ as a function of p_T for 0-80% and 10-20% centralities at mid-rapidity ($|\eta| < 0.8$) in Pb-Pb collisions at $\sqrt{s_{NN}} = 2.76$ TeV.

The summary of systematic uncertainties in various centralities are given in

Fig. 5.12 to Fig. 5.14. The total systematic uncertainties varies from 18-25% depending on the p_T and centrality classes as given in the Table 5.1.

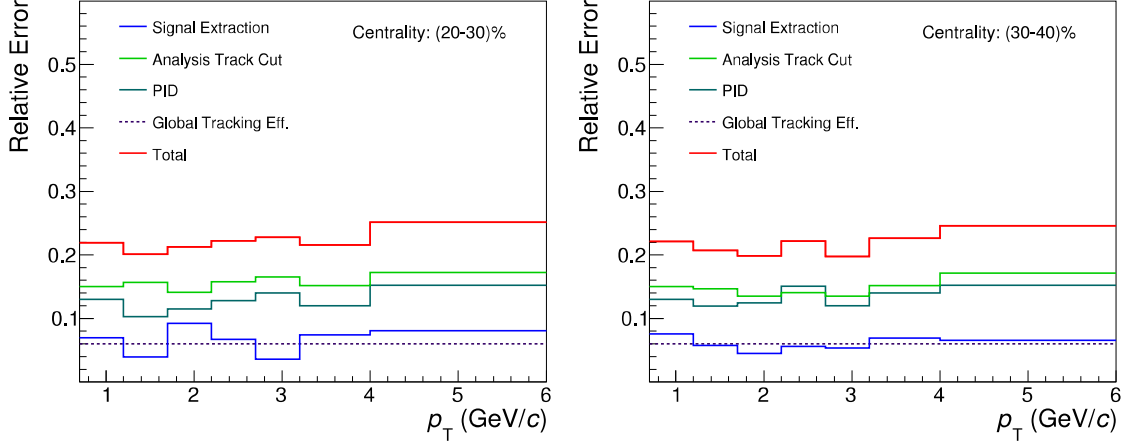


Figure 5.13: Summary of different sources of systematic uncertainties in the measurement of $K^{*0} v_2$ as a function of p_T in 20-30% and 30-40% centralities at mid-rapidity ($|\eta| < 0.8$) in Pb-Pb collisions at $\sqrt{s_{NN}} = 2.76$ TeV.

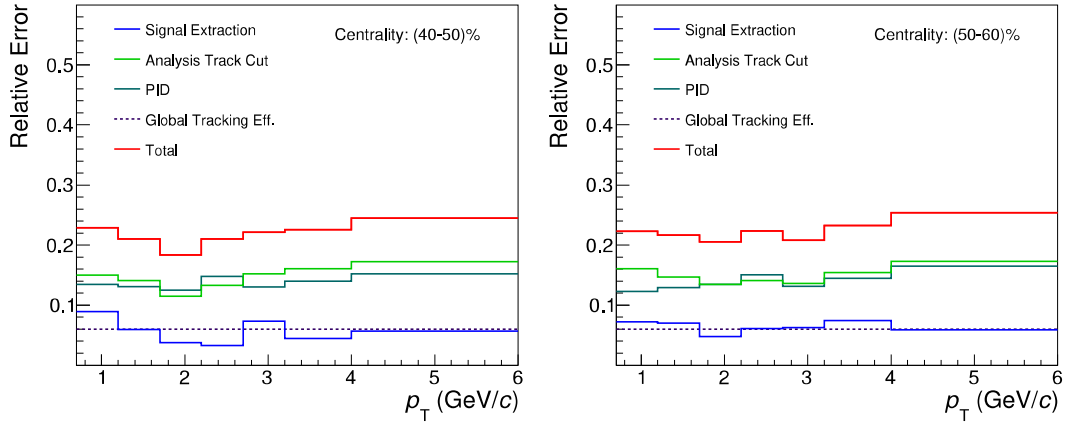


Figure 5.14: Summary of different sources of systematic uncertainties in the measurement of $K^{*0} v_2$ as a function of p_T in 40-50%, 50-60% centralities at mid-rapidity ($|\eta| < 0.8$) in Pb-Pb collisions at $\sqrt{s_{NN}} = 2.76$ TeV.

5.7 Summary

The measurement of $K^{*0} v_2$ at mid-rapidity ($|\eta| < 0.8$) in Pb–Pb collisions at $\sqrt{s_{\text{NN}}} = 2.76$ TeV using ALICE detector has been reported. The $K^{*0} v_2$ for minimum bias (0-80%) is calculated using two different methods (event plane with $(\phi - \psi)$ bin and invariant mass fit) and compared. The results using both the methods are consistent within 5%. The invariant mass method has been used for v_2 calculation in various centralities. A centrality dependence of $K^{*0} v_2$ is observed. The v_2 of K^{*0} is compared with other identified hadrons (π , K, p, K_S^0 , ϕ , Λ , Ξ and Ω) which suggest that mass ordering hypothesis is respected by $K^{*0} v_2$ at low- p_T . For $p_T \geq 3$ GeV/ c , the trend of $K^{*0} v_2$ is observed to be high as compared to other mesons in different centralities even though the uncertainties are larger. This increase of $K^{*0} v_2$ around mid- p_T might be due to the hadronic re-scattering effect which increases the flow value. One observes a violation of NCQ scaling by $K^{*0} v_2$ although error bars are very large. However, more statistics are needed for further confirmation of this effect in future.

Bibliography

- [1] J. Y. Ollitrault, Phys. Rev. D 46, 229 (1992).
- [2] R. Snellings, New J. Phys.13, 055008 (2011).
- [3] P. Huovinen and P. V. Ruuskanen, Ann. Rev. Nucl. Part. Sci. 56, 163 (2006).
- [4] (STAR Collaboration) J. Adams *et al.*, Nucl. Phys. A 757, 102 (2005).
- [5] (PHENIX Collaboration) K. Adcox *et al.*, Nucl. Phys. A 757, 184 (2005).
- [6] T. Hirano *et al.*, Phys. Lett. B 636, 299(2006).
- [7] (PHENIX Collaboration) A. Adare *et al.*, Phys. Rev. C, 85, 064914 (2012).
- [8] (ALICE Collaboration) B. B. Abelev *et al.*, JHEP 1506, 190 (2015).
- [9] (ALICE Collaboration), R. Bertens *et al.*, <https://aliceinfo.cern.ch/Notes/node/586>.
- [10] (CMS Collaboration), S. Chatrchyan *et al.*, Phys. Rev. C 87, 014902 (2013).
- [11] A. M. Poskanzer and S. A. Voloshin, Phys. Rev. C 58 1671 (1998).
- [12] (STAR Collaboration), L. Adamczyk *et al.*, Phys. Rev. C 88, 014902 (2013).
- [13] (STAR Collaboration) J. Adams *et al.*, Phys. Rev. C 84, 034909 (2011).

- [14] (ALICE Collaboration) B. Abelev *et al.*, Int. J. Mod. Phys. A 29, 1430044 (2014).
- [15] N. Borghini and J. Y. Ollitrault, Phys. Rev. C 70, 064905 (2004).
- [16] P. Huovinen *et al.*, Phys. Lett. B 503, 58 (2001).
- [17] D. Teaney *et al.*, Phys. Rev. Lett. 86, 4783 (2001).
- [18] S. A. Voloshin *et al.*, Phys. Rev. C 55, 1630 (1997).
- [19] (STAR Collaboration) J. Adam *et al.*, Phys. Rev. Lett. 92, 052302 (2004).
- [20] (PHENIX Collaboration) S. S. Adler *et al.*, Phys. Rev. Lett. 91, 182301 (2003).
- [21] D. Molnar *et al.*, Phys. Rev. Lett. 91, 092301 (2003).
- [22] V. Greco *et al.*, Phys. Rev. C 68, 034904 (2003).
- [23] R. J. Fries *et al.*, Phys. Rev. C 68, 044902 (2003).
- [24] (ALICE Collaboration) J. Adam *et al.* Phys. Rev. C 95, 064606 (2017).
- [25] R. Barlow, arXiv:0207026 (2002).

Chapter 6

A transport model study of hadronic phase in heavy-ion collisions using K^{*0} and ϕ

According to quantum chromodynamics (QCD) at very high temperature and/or at high density, a de-confined phase of quarks and gluons, known as quark-gluon plasma (QGP) is expected to be formed. In the heavy-ion experiment, the study of QCD matter is performed by colliding nuclei at ultra-relativistic velocity. A hot and dense medium with color degree of freedom which is short lived ($\sim 5-10$ fm/c) is created in the heavy-ion collisions. This is followed by hadronic phase. The resonances K^{*0} and ϕ are considered as a good probe due to their unique properties to study the QCD matter created in relativistic collisions [1, 2, 3, 4, 5, 6, 7]. The ϕ is a vector meson, which is the lightest bound state of s and \bar{s} quarks and has a lifetime of 46.3 ± 0.4 fm/c [8]. Because of long lifetime (relative to fireball lifetime) the ϕ meson mostly decay outside the fireball and hence its daughters do not have much time to re-scatter in the hadronic medium. The hadronic interaction cross-section of ϕ

is expected to have a small value and hence seems to freeze out early compared to other lighter hadrons [1, 2, 3, 4, 5, 6, 7]. On the other hand, K^{*0} meson has mass of 896 MeV/ c^2 which is comparable to the mass ϕ (1020 MeV/ c^2). The lifetime of K^{*0} meson is 4.16 ± 0.05 fm/ c and it mostly decays inside the medium [8]. Therefore, the decay daughters of K^{*0} are suffered by the interactions in the hadronic phase of the QCD medium. The momentum of these decay daughters may get changed if they re-scattered by other hadrons present in the medium [9, 10, 11]. This would lead to a loss in the reconstruction of the parent resonance. On the other hand, after chemical freeze-out, pseudo-elastic interactions could regenerate resonances in the medium leading to enhancement in their yields. The amount of loss or gain could depend on the lifetime of hadronic phase, hadronic interaction cross section of decay daughters, particle density in the medium. Study of the yield and flow coefficient of K^{*0} and ϕ simultaneously in heavy-ion collisions might help us to better understand the late stage hadronic effects.

In this part of the thesis, a multi phase transport (AMPT) model study in Pb–Pb collisions at $\sqrt{s_{NN}} = 2.76$ TeV, in mid-rapidity ($|y| < 1$) is performed by varying hadronic cascade termination time (τ_{HC}) from 0.6 fm/ c to 30 fm/ c to see the in-medium (re-scattering and regeneration) effects on the p_T -spectra and v_2 of K^{*0} and ϕ resonances.

6.1 A Multi Phase Transport (AMPT) model

In this analysis, the string melting version of AMPT model (2.25t9b) [12, 13, 14, 15] is used. The AMPT model has four main stages: (i) the initial conditions, (ii) partonic interactions, (iii) the conversion from the partonic to the hadronic matter, and (iv) hadronic interactions. The first stage i.e initial conditions are obtained from the HIJING model [16]. Zhang’s parton cascade (ZPC) takes care the scatterings

among parton) [17]. The parton-parton interaction cross section is taken to be 3 mb. Hadronization is done via a quark coalescence model. The subsequent hadronic matter interaction is described by a hadronic cascade, which is based on a relativistic transport (ART) model [18]. The termination time of the hadronic cascade is varied from 0.6 to 30 fm/ c to study the effect of the hadronic phase on the observables presented in this analysis [21]. For our study, approximately 150 thousand events for each hadronic cascade time are generated for minimum bias Pb–Pb collisions at $\sqrt{s_{\text{NN}}} = 2.76$ TeV.

The K^* and their anti-particles are included implicitly via elastic πK scattering having a Breit-Wigner form of cross section [18] and explicitly by adding them in the hadronic phase of AMPT model [22]. In addition to scattering of πK , the K^* scattering with other mesons such as ρ , ω and η are also included using 10 mb cross section (the same cross section is used for kaons). The reaction channels such as $(\pi\eta)(\rho\omega) \leftrightarrow K^*\bar{K}$ or \bar{K}^*K and $\pi K \leftrightarrow K^*(\rho\omega)$ are also included as they also contribute to the formation and decays of K^* resonances.

The ϕ meson formation and decays to KK pairs are also included in the AMPT model and the formation cross section is given by Breit-Wigner form [23]. Inelastic reactions i.e baryon-baryon $[(N\Delta N^*)(N\Delta N^*) \rightarrow \phi NN]$ and meson-meson $[(\pi\rho \leftrightarrow \phi N)]$, where the forward-going cross section is taken from one-boson-exchange model [24] are also included. The baryon-meson reactions of the ϕ meson include $K(\Lambda\Sigma) \leftrightarrow \phi N$ with cross section from kaon-exchange model [25]. Some other reactions of ϕ with pseudo-scalar (π , K) and vector mesons (ρ , ω and K^*) i.e $\phi(\pi\rho\omega) \leftrightarrow (KK^*)(\bar{K}\bar{K}^*)$ and $\phi(KK^*) \leftrightarrow (\pi\rho\omega)(KK^*)$ are included with cross sections obtained from the partial collisional widths taken from the Ref [19]. The elastic cross section of ϕ meson with nucleon and meson is set to be 8 mb and 5 mb, respectively [25, 20].

6.2 Results

6.2.1 Transverse Momentum Spectra

The p_T -spectra of produced (prod) and reconstructable (reco) K^{*0} and ϕ for three different lifetime, τ_{HC} (0.6, 15 and 30 fm/c) of hadronic phase are obtained in Pb–Pb collisions at mid-rapidity ($|y| < 1$) Fig. 6.1. The reconstructable K^{*0} and ϕ are those for which the each component of decay daughter's momentum remains unchanged during the system's evolution. The $\tau_{\text{HC}} = 0.6$ fm/c represent particle productions from quark coalescence without hadronic interactions. A higher value of hadronic cascade time reflects larger hadronic re-scattering and regeneration. The p_T -spectra of all produced and reconstructable particles are shown by solid and open markers, respectively. The ratio between produced and reconstructable K^{*0} (and ϕ) at corresponding τ_{HC} are shown at the bottom of Fig. 6.1. The left panel of Fig. 6.1 shows number of reconstructable K^{*0} decreases with increasing lifetime of hadronic phase. This is due to the effect of hadronic re-scattering for which momenta of decay daughters gets changed and this lead to loss in the reconstruction of the parent resonance. The re-scattering effect is found to be more dominant at low- p_T . There are experimental evidences which show a prominent hadronic re-scattering effect of K^{*0} at low- p_T [26, 27]. The right panel of Fig. 6.1 shows the hadronic re-scattering effect on ϕ mesons which is significantly smaller than that of K^{*0} . This is due to the small hadronic interaction cross-section of ϕ meson and also due to the long lifetime of ϕ meson for which its daughters do not have much time to re-scatter in the hadronic phase.

Fig. 6.2 shows p_T integrated yield (dN/dy) of K^{*0} and ϕ for different τ_{HC} of hadronic phase. The change in dN/dy between produced and reconstructable hadron

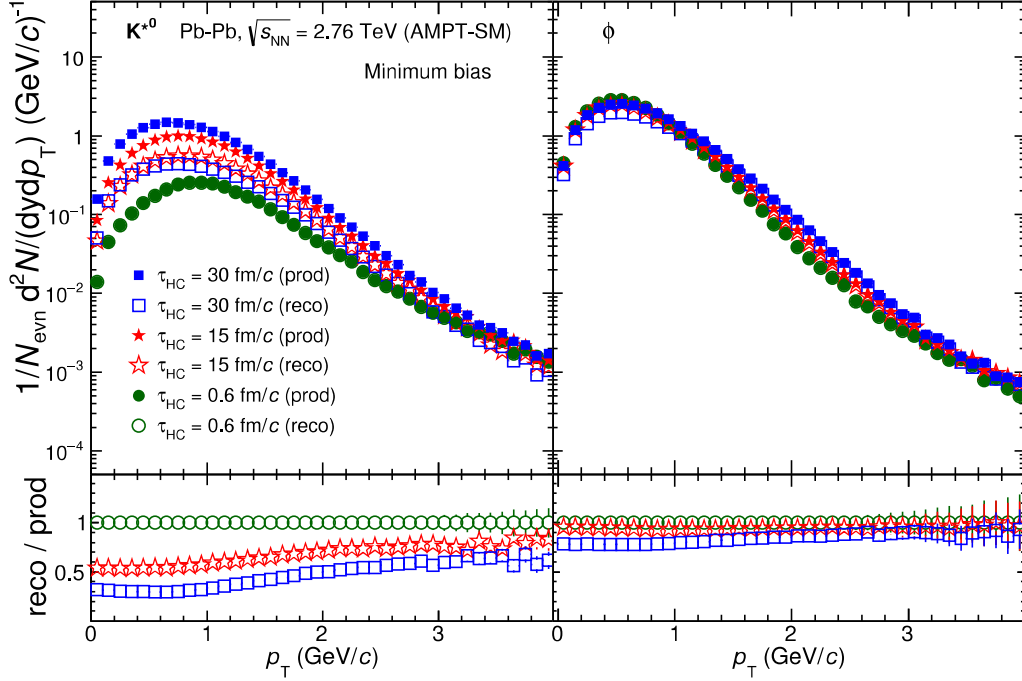


Figure 6.1: p_T spectra of K^{*0} (left panel) and ϕ (right panel) for different hadronic cascade, τ_{HC} , values in minimum bias measured at mid-rapidity ($|y| < 1$) in Pb-Pb collisions at $\sqrt{s_{NN}} = 2.76$ TeV (AMPT-SM).

at a fixed τ_{HC} gives loss due to re-scattering. Whereas change in dN/dy of produced hadron between two different τ_{HC} gives amount of regeneration. The dN/dy of K^{*0} increases with increasing the hadronic cascade time because K^{*0} is added in the hadronic phase as a effect of regeneration [13]. In case of ϕ , we observe a small change in dN/dy with increasing τ_{HC} . Table 6.1 lists dN/dy values of K^{*0} and ϕ at different τ_{HC} and the fraction of resonances re-scattered at $\tau_{HC} = 15$ and 30 fm/c are shown in Tab. 6.2. The re-scattered fraction percentage is the ratio between all reconstructable to produced resonance for corresponding τ_{HC} . The effect of re-scattering increases with increase in τ_{HC} , however re-scattering effect is more dominant for K^{*0} than ϕ .

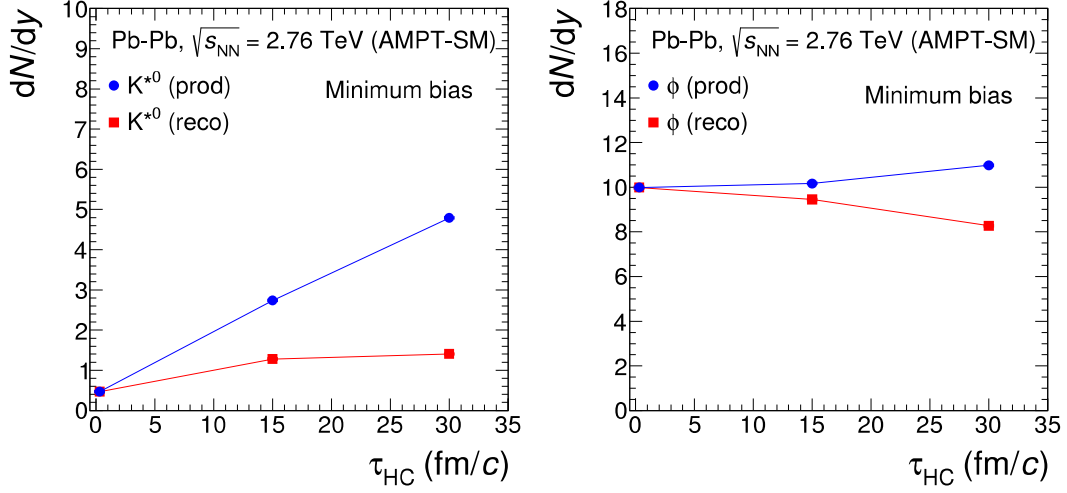


Figure 6.2: dN/dy of K^{*0} (left panel) and ϕ (right panel) as function of τ_{HC} minimum bias Pb-Pb collisions at $\sqrt{s_{\text{NN}}} = 2.76$ TeV (AMPT-SM).

Figure 6.3 shows the resonance to stable particle ratios as function of average number of charged particle ($\langle N_{\text{ch}} \rangle$), obtained with $|y| < 0.5$ for $\tau_{\text{HC}} = 30$ fm/c in Pb-Pb collisions at $\sqrt{s_{\text{NN}}} = 2.76$ TeV. It is observed that the K^{*0}/K (reco) ratios decreases while moving peripheral (low $\langle N_{\text{ch}} \rangle$) to central (high $\langle N_{\text{ch}} \rangle$) collision unlike ϕ/K ratio. This decreasing trend is attributed to rescattering effect of K^{*0} daughter particles in the hadronic medium in Pb-Pb collisions at $\sqrt{s_{\text{NN}}} = 2.76$ TeV.

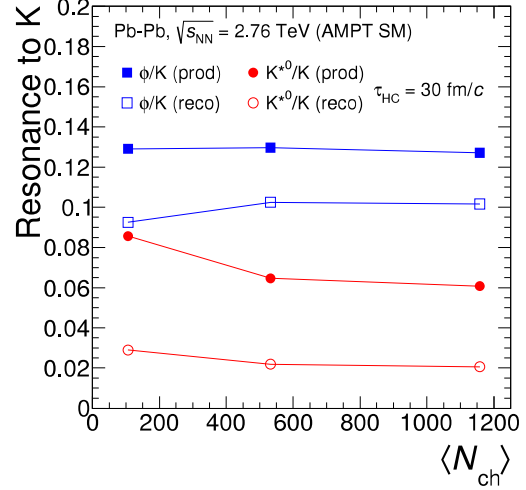


Figure 6.3: Resonance to stable particle (kaon) ratio as function of average number of charged particle, $\langle N_{\text{ch}} \rangle$, for $\tau_{\text{HC}} = 30$ fm/c in Pb-Pb collisions at $\sqrt{s_{\text{NN}}} = 2.76$ TeV (AMPT-SM).

	$\tau_{\text{HC}} = 0.6 \text{ fm}/c$		$\tau_{\text{HC}} = 15 \text{ fm}/c$		$\tau_{\text{HC}} = 30 \text{ fm}/c$	
	produced	reconstructable	produced	reconstructable	produced	reconstructable
dN/dy of K^{*0}	0.47	0.47	2.74	1.28	4.8	1.4
dN/dy of ϕ	9.98	9.98	10.17	9.45	10.97	8.27

Table 6.1: p_T integrated yield (dN/dy) of K^{*0} and ϕ for different τ_{HC} of hadronic phase.

	$\tau_{\text{HC}} = 15 \text{ fm}/c$	$\tau_{\text{HC}} = 30 \text{ fm}/c$
	re-scattering (%)	re-scattering (%)
K^{*0}	53.3	70.8
ϕ	7.0	24.6

Table 6.2: Fraction of K^{*0} and ϕ re-scattered at different τ_{HC} of the hadronic phase.

6.2.2 Elliptic Flow (v_2)

The elliptic flow (v_2), a measure of the azimuthal anisotropy in the momentum space is considered as a sensitive probe of the early stages of heavy-ion collisions [28, 29, 30]. This flow parameter v_2 is extracted by studying the correlation of produced particles with respect to the reaction plane (Ψ) as

$$v_2 = \langle \cos[2(\Phi - \Psi)] \rangle \quad (6.1)$$

where Φ is the azimuthal angle of the produced particles [31]. The reaction plane angle, Ψ is taken as zero in this analysis which produces within AMPT. Figure 6.4 shows v_2 of K^{*0} and ϕ , as a function of p_T , at different τ_{HC} in Pb–Pb collisions at $\sqrt{s_{\text{NN}}} = 2.76 \text{ TeV}$. We see that the v_2 of K^{*0} largely depend on τ_{HC} and this is because of the fact that the flow is developed during the late stage of the hadronic phase due to interactions of K^{*0} with other hadrons. The interaction cross-section of ϕ -meson with

other hadrons is very small, hence its flow is not affected significantly with change in τ_{HC} , as shown in the right panel of Fig 6.4.

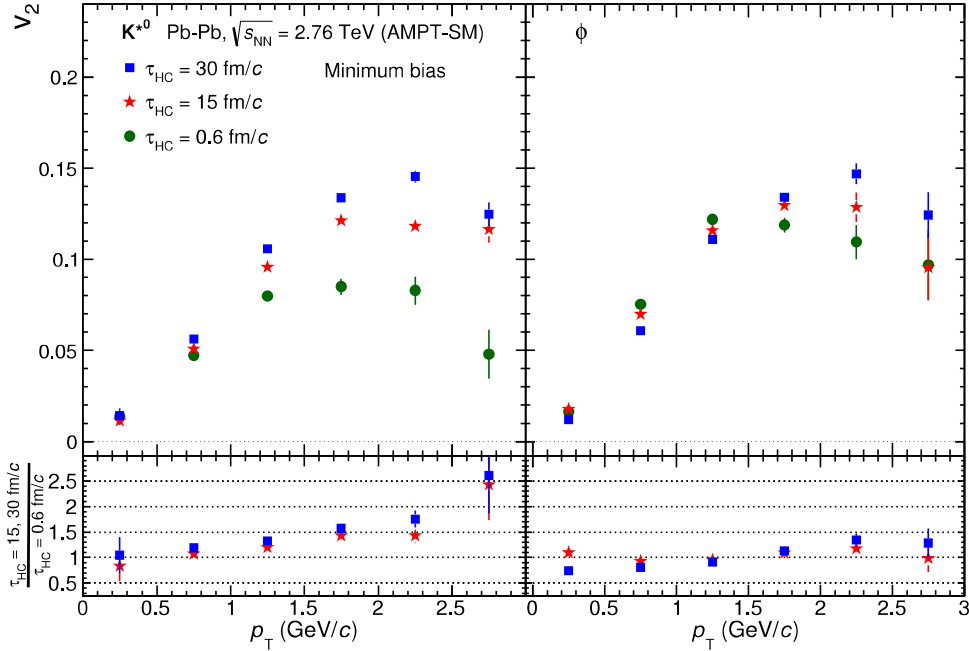


Figure 6.4: v_2 of K^{*0} (left panel) and ϕ (right panel) as a function of p_T in different τ_{HC} for minimum bias Pb–Pb collisions at $\sqrt{s_{\text{NN}}} = 2.76$ TeV (AMPT-SM).

We have compared $v_2(p_T)$ of K^{*0} and ϕ with other identified particles (π , K , p) at different τ_{HC} in Pb–Pb collisions at $\sqrt{s_{\text{NN}}} = 2.76$ TeV using AMPT model as shown in Fig. 6.5. The left, middle and right panel of Fig. 6.5 shows comparison at $\tau_{\text{HC}} = 30$, 15 and 0.6 fm/c, respectively. We have seen a mass ordering in v_2 at low p_T and a clear baryon-meson separation at intermediate p_T among π , K , p and ϕ for all values of τ_{HC} . However, K^{*0} v_2 does not seem to follow similar trend as other mesons. At $\tau_{\text{HC}} = 0.6$ fm/c, it is found that K^{*0} v_2 does not follow mass ordering at low p_T as well as baryon-meson separation at intermediate p_T . This is a striking observation. At $\tau_{\text{HC}} = 0.6$ fm/c, v_2 of hadrons are just after the quark coalescence and there is no hadronic interaction. Therefore, one should expect that all hadron's v_2

should follow baryon-meson separation (base line for number-of-constituent scaling) at intermediate p_T . However, we have seen that K^{*0} v_2 in AMPT model does not follow the expectation. With increasing τ_{HC} , K^{*0} v_2 increases and at $\tau_{\text{HC}} = 30$ fm/c, K^{*0} v_2 follows the mass ordering (at low p_T) and other mesons at intermediate p_T . This observation from AMPT model tells us that the hadronic interaction is needed for K^{*0} v_2 to follow number-of-constituent quark scaling, which is against the expectation from a quark coalescence model.

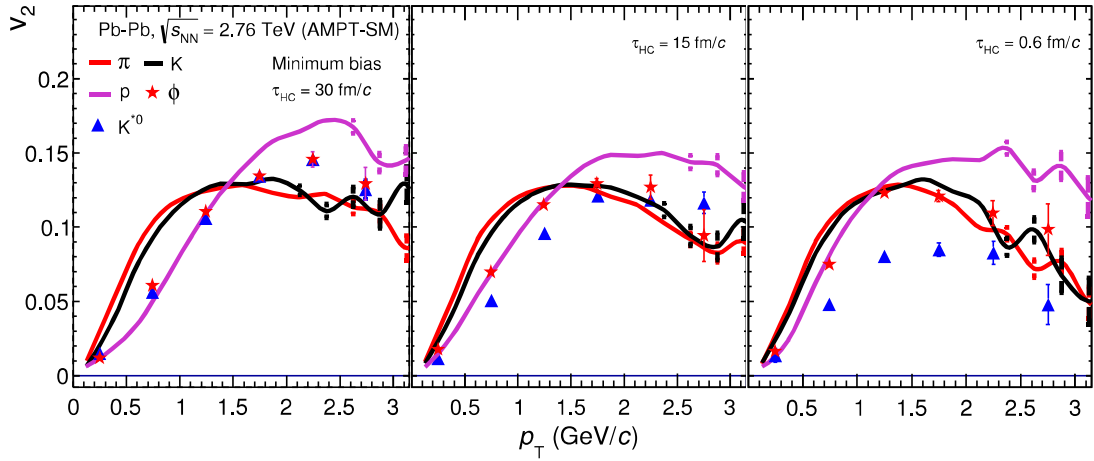


Figure 6.5: v_2 of identified hadrons (π , K , p , K^{*0} and ϕ) as a function of p_T for $\tau_{\text{HC}} = 30$ fm/c (left), 15 fm/c (middle) and 0.6 fm/c (right) in minimum bias Pb–Pb collisions at $\sqrt{s_{\text{NN}}} = 2.76$ TeV (AMPT-SM).

6.3 Summary

We have studied the effect of late stage hadronic interaction on the production of K^{*0} and ϕ meson using the string melting version of AMPT model at mid-rapidity ($|y| < 1$) in Pb–Pb collisions at $\sqrt{s_{\text{NN}}} = 2.76$ TeV. The p_T -spectra of reconstructable K^{*0} decreases as the hadronic cascade time increases, whereas for ϕ mesons this change is much smaller. Increasing the hadronic interaction (re-scattering and regeneration)

by increasing the hadron cascade time period does not change the v_2 of ϕ mesons. In contrast to ϕ mesons, the v_2 of K^{*0} increases with increase in hadronic interaction. It was found that the hadronic interaction is needed for K^{*0} v_2 to follow number-of-constituent quark scaling, which is against the expectation from a quark coalescence model. The violation of number of constituent quark scaling in Pb–Pb collisions at $\sqrt{s_{\text{NN}}} = 2.76$ TeV is also not explained by hadronic cascade time variations.

Bibliography

- [1] M. Nasim, Phys. Rev. C, 89, 034909 (2014).
- [2] M. Nasim, B. Mohanty and N. Xu, Phys. Rev. C, 87, 014903 (2013).
- [3] B. Mohanty and N. Xu, J. Phys. G, 38, 124023 (2011).
- [4] (STAR Collaboration) M. M. Aggarwal *et al.*, Phys. Rev. C, 84, 034909 (2011).
- [5] (STAR Collaboration) B. I. Abelev *et al.*, Phys. Rev. C, 78, 044906 (2008).
- [6] (STAR Collaboration) (J. Adam *et al.*), Phys. Rev. C, 71, 064902 (2005).
- [7] A. Shor, Phys. Rev. Lett., 54, 1122 (1985).
- [8] (Particle Data Group) K. A. Olive *et al.* , Chin. Phys. C, 38, 090001 (2014).
- [9] R. Rapp and E. V. Shuryak, Phys. Rev. Lett., 86, 2980 (2001).
- [10] C. Song and V. Koch, Phys. Rev. C, 55, 3026 (1997).
- [11] J. Rafelski, J. Letessier and G. Torrieri, Phys. Rev. C, 64, 054907 (2001);
Erratum-ibid. C, 65, 069902 (2002).
- [12] Zi-Wei Lin, C. M. Ko, Phys. Rev. C, 65, 034904 (2002).
- [13] Zi-Wei Lin, C. M. Ko, Bao-An *et al.*, Phys. Rev. C, 72, 064901 (2005).

- [14] Lie-Wen Chen *et al.*, Phys. Lett. B, 605, 95 (2005).
- [15] Z. W. Lin, S. Pal, C. M. Ko, *et al.*, Phys. Rev. C, 64, 011902 (2001).
- [16] X. N. Wang and M. Gyulassy, Phys. Rev. D, 44, 3501 (1991).
- [17] B. Zhang, Comput. Phys. Commun., 109, 193 (1998).
- [18] B. A. Li and C. M. Ko, Phys. Rev. C, 52, 2037 (1995).
- [19] L. Alvarez-Ruso and V. Koch, Phys. Rev. C, 65, 054901 (2002).
- [20] H. J. Behrend *et al.*, Phys. Lett. B, 56, 408 (1975).
- [21] S. Singha, B. Mohanty and Zi-Wei Lin, Int. J. of Mod. Phys. E, 24, 5 1550041 (2015).
- [22] G. E. Brown, C.M. Ko, Z. G. Wu *et al.*, Phys. Rev. C, 43, 1881 (1991).
- [23] S. Pal, C. M. Ko, and Z. W. Lin, Nucl. Phys. A, 707, 525 (2002).
- [24] W. S. Chung, G. Q. Li, and C. M. Ko, Nucl. Phys. A, 625, 347 (1997).
- [25] C. M. Ko and B. H. Sa, Phys. Lett. B, 258, 6 (1991).
- [26] (ALICE Collaboration) B. Abelev *et al.*, Phys. Rev. C, 91, 024609 (2015).
- [27] (ALICE Collaboration) J. Adam *et al.*, Phys. Rev. C, 95, 064606 (2017).
- [28] J. Y. Ollitrault, Phys. Rev. D, 46, 229 (1992).
- [29] H. Sorge, Phys. Rev. Lett., 78, 2309 (1997).
- [30] P. Huovinen, P. F. Kolb, U. Heinz *et al.*, Phys. Lett. B, 503, 58 (2001).
- [31] S. A. Voloshin, A. M. Poskanzer and R. Snellings, arXiv:0809.2949 (2008).

Chapter 7

Summary

The thesis deals with the study of K^{*0} resonance production as the probe to understand the novel QCD matter produced in the Pb–Pb collisions at LHC. Resonances by definition are very short-lived ($\sim \text{fm}/c$) particles and hence they are very useful to study the in-medium dynamics of the strongly interacting QCD matter. The K^{*0} is one of the best suited resonance particle for this purpose because of its lifetime ($\sim 4.2 \text{ fm}/c$), which is comparable to the timescale of the hot and dense matter produced. As K^{*0} contains strange (s) quark, so it may also give information about the mechanism and dynamics of strange particle production in the medium. Specifically, we measured the nuclear modification factor (R_{AA} , R_{CP}) of K^{*0} at high transverse momentum (p_T) to understand energy loss of parton in strange sector. The azimuthal anisotropy or elliptic flow (v_2) of K^{*0} is also measured in various centralities to understand the in-mediums dynamics and particle production mechanism.

In this thesis, a comprehensive study of the K^{*0} resonance production in Pb–Pb collisions at $\sqrt{s_{NN}} = 2.76 \text{ TeV}$ using the high statistics data set collected in the year 2011 with the ALICE detector is performed. The K^{*0} signal is reconstructed via its hadronic decay channel $K^{*0} (\bar{K}^{*0}) \rightarrow \pi^- K^+ (\pi^+ K^-)$ having branching ratio of 66.6%.

The K^{*0} p_T -spectra is measured in finer centrality classes with high- p_T reach up to 20 GeV/ c . The p_T -integrated K^{*0} yield is also calculated and resonance to stable particle (K^{*0}/K) ratio is obtained. The K^{*0}/K ratio decreases as a function of system size, unlike ϕ/K ratio. This observation is understood by considering the lifetime of these resonance particles i.e 4.16 ± 0.05 fm/ c and 46.3 ± 0.4 fm/ c for K^{*0} and ϕ , respectively. The K^{*0} decays inside the hadronic medium and the decay daughters (pions and kaons) re-scatter with the other medium particles by changing their momentum. Due to this momentum exchange, the parent K^{*0} can't be reconstructed from its decayed daughters' energy and momentum information via the invariant mass method. So the K^{*0} signal is lost because of re-scattering of decay daughters in the medium. The system size and also the dense medium formation is more in central as compared to peripheral Pb–Pb collisions and hence the loss of K^{*0} signal in central Pb–Pb collisions is more prominent. However, ϕ decays outside the medium and hence the effect of re-scattering is not reflected in the ϕ/K ratio. The presence of the re-scattering effect is further confirmed by comparison of the measurement to the Thermal and EPOS3 model predictions. The Thermal model over-predicts the K^{*0}/K ratio and well describes the ϕ/K ratio as the re-scattering effect was not incorporated into the thermal model. EPOS3 which includes re-scattering effect reproduces the observed trend of the K^{*0}/K ratio qualitatively. The p_T -dependent K^{*0}/K , K^{*0}/π , ϕ/K and ϕ/π ratios are also measured for understanding the particle production mechanism in different p_T regions. The p_T -dependent K^{*0}/K and K^{*0}/π ratios in central Pb–Pb show an enhancement at $p_T \sim 3$ GeV/ c as compared to minimum bias pp collisions, indicating the presence of strong radial flow effect at LHC energies. In central Pb–Pb collisions, the p_T -dependent K^{*0}/K ratio is also suppressed for $p_T < 2$ GeV/ c with respect to pp collisions, indicating the dominance of the re-scattering effect at low- p_T .

The nuclear modification factor (R_{AA}) is defined as the ratio yield of particles

in heavy-ion collisions to that in elementary pp collisions, scaled with the average nuclear overlap function. The R_{AA} measurement is sensitive to the dynamics of particle production, in-medium effects and the energy loss mechanism of partons in the medium. If a nuclear collision were simply a superposition of nucleon-nucleon collisions, the R_{AA} would be equal to unity at high- p_T . Any deviation of the R_{AA} from unity at high- p_T may indicate the presence of in-medium effects. The R_{AA} of K^{*0} is compared to other identified particles such as π , K , p and ϕ . The R_{AA} of K^{*0} is found to be less than unity for central collisions as was observed for other hadrons indicating the dense medium formation at LHC energies. At low- p_T (< 2 GeV/ c), the K^{*0} R_{AA} is smaller than the ϕ meson and the charged hadron R_{AA} . This additional suppression of K^{*0} at low- p_T with respect to ϕ is reduced as one goes from central to peripheral collisions, consistent with the expectation of more re-scattering in central Pb-Pb collisions. At high- p_T the suppression (R_{AA} value) of all these particles are found to be of similar order. This indicates that the energy loss mechanism for all light flavour hadrons are similar and rejects those models where the energy loss mechanism depends on light quark content (u, d, s) and hadron masses.

The nuclear modification factor, R_{CP} , measurement does not require the pp reference unlike the R_{AA} are also presented in this thesis. It is defined as the p_T -spectra ratio between the central and peripheral collisions scaled with the corresponding binary collisions. The R_{CP} of K^{*0} is compared with K_S^0 , ϕ and Λ in Pb-Pb collisions at $\sqrt{s_{NN}} = 2.76$ TeV. The suppression of K^{*0} as observed in R_{AA} is approximately 2.5 times more than the corresponding R_{CP} measurement at low- p_T . This significant difference between the K^{*0} R_{AA} and R_{CP} is might be due to pp reference rather than nuclear effects. At low- p_T (< 2 GeV/ c), particles with similar mass are found to have a similar value of suppression. The peak value in the R_{CP} of Λ is observed at relatively higher p_T as compared to K^{*0} and K_S^0 . This peak shift might be due to the

radial flow of the particle which is more for a heavier mass particle.

The measurement of K^{*0} meson elliptic flow at mid-rapidity ($|\eta| < 0.8$) in Pb–Pb collisions at $\sqrt{s_{NN}} = 2.76$ TeV using ALICE detector has been performed. The K^{*0} v_2 for 0-80% is calculated by using two different methods (event plane with $(\phi - \psi)$ bin and invariant mass fit) and compared. The results using both the methods are consistent within 5%. The invariant mass method has been used for v_2 calculation in various centralities. The centrality dependent on K^{*0} v_2 is observed. The v_2 of K^{*0} is compared with other identified hadrons (π , K, p, K_S^0 , ϕ , Λ , Ξ and Ω) which suggest that mass ordering hypothesis is supported by K^{*0} v_2 . At about $p_T = 3$ GeV/ c , the trend of K^{*0} v_2 is seemed high as compared to other hadrons in certain centralities although the larger uncertainties do not allow a firm conclusion. This increase of K^{*0} v_2 around mid- p_T might be due to the hadronic in-medium effect which increases the flow value. One observes a violation of NCQ scaling by K^{*0} v_2 although error bars are very large. So, more statistics is the need of the time for further confirmation and conclusions.

A detailed study of event multiplicity dependence of K^{*0} production in pp collisions at $\sqrt{s} = 7$ TeV is carried out in this thesis. In the recent LHC measurements, some collective features similar to Pb–Pb collisions have been observed in high multiplicity pp and p–Pb collisions. From the two-particle correlation study, there is an indication of a flow-like effect in high-multiplicity pp and p–Pb collisions which resembles to the observation in Pb–Pb. The particle ratios such as K^{*0}/K in p–Pb show some analogous features to Pb–Pb collisions. In order to understand the origin of these features a comprehensive study of a fundamental observable like p_T -spectra of K^{*0} is performed in pp collisions for various multiplicity classes of events. The p_T -spectra are measured in different V0M event multiplicity classes. A spectral modification is observed when the ratios of p_T -spectra in different multiplicity classes with

respect to 0-100% multiplicity event class is calculated. The p_T -spectra get harder with increasing multiplicity event classes. This indicates the presence of radial flow effect in high multiplicity event classes measured in pp collisions at $\sqrt{s} = 7$ TeV. A mass ordering of $\langle p_T \rangle$ value is observed for different identified particles, but, when the K^{*0} (and also ϕ) $\langle p_T \rangle$ is compared, there observed a deviation from the trend of mass ordering. The reason for this deviation still needs to be understood. The p_T -integrated K^{*0}/K ratio shows a decreasing trend, having a non-zero slope with respect to the average charged particle multiplicity, this feature is similar what observed in p-Pb and Pb-Pb collisions systems. The decreasing trend of K^{*0}/K ratio in Pb-Pb collisions are attributed to hadronic re-scattering effects. A similar decreasing trend in high multiplicity pp collisions at LHC energies might indicate the onset of a small-medium formation or the effect of multi-partonic interaction.

A major conclusion of the thesis is an experimental demonstration of the re-scattering effect in the QCD medium formed at LHC using K^{*0} hadron. In order to get a better understanding of the effect, a simulation study is performed in the last part of the thesis. The late stage hadronic interaction on the production of K^{*0} and ϕ meson using the string melting version of AMPT model at mid-rapidity ($|y| < 1$) in Pb-Pb collisions at $\sqrt{s_{NN}} = 2.76$ TeV is performed. The p_T -spectra of reconstructable K^{*0} decreases as the hadronic cascade time increases, whereas for ϕ mesons this change is much smaller. Increasing the hadronic interaction (re-scattering and regeneration) by increasing the hadron cascade time period does not change the v_2 of ϕ mesons. In contrast to ϕ mesons, the v_2 of K^{*0} increases with increase in hadronic interaction. It was found that the hadronic interaction is needed for K^{*0} v_2 to follow NCQ scaling, which is against the expectation from a quark coalescence model. The violation of NCQ in Pb-Pb collisions at $\sqrt{s_{NN}} = 2.76$ TeV is also not explained by the variation of hadronic cascade time.

Bibliography

1. Torre LA, Bray F, Siegel RL, Ferlay J, Lortet-Tieulent J, Jemal A. Global cancer statistics, 2012. *CA Cancer J Clin.* 2015; 65:87-108.
2. Ferlay J, Soerjomataram I, Dikshit R, Eser S, Mathers C, Rebelo M, Parkin DM, Forman D, Bray F. Cancer incidence and mortality worldwide: sources, methods and major patterns in GLOBOCAN 2012. *Int J Cancer.* 2015; 136: E359-386.
3. Ali I, Wani WA, Saleem K, Cancer Scenario in India with Future Perspectives, *Cancer Therapy.* 2011; 8: 56-70.
4. Mallath MK, Taylor DG, Badwe RA, Rath GK, Shanta V, Pramesh CS, Digumarti R, Sebastian P, Borthakur BB, Kalwar A, Kapoor S. The growing burden of cancer in India: epidemiology and social context. *Lancet Oncol.* 2014; 15: e205-212.
5. Devi PU. Basics of carcinogenesis. *Health Adm.* 2004; 17: 16-24.
6. Bakhya Shree and Radhasaraswathy. Incidence and risk factors of most prevalent cancers in India. *Int J Pharm Bio Sci.* 2015; 6: 436 - 443.
7. Bartek J, Lukas J, Bartkova J. Perspective: defects in cell cycle control and cancer. *J Pathol.* 1999; 187: 95-99.
8. Kastan MB, Bartek J. Cell-cycle checkpoints and cancer. *Nature.* 2004; 432:316-323.
9. Chambers AF, Groom AC, MacDonald IC. Metastasis: dissemination and growth of cancer cells in metastatic sites. *Nat Rev Cancer.* 2002; 2: 563- 572.
10. Iliakis G, Wang YA, Guan J, Wang H. DNA damage checkpoint control in cells exposed to ionizing radiation. *Oncogene.* 2003; 22: 5834-5847.

11. Pawlik TM, Keyomarsi K. Role of cell cycle in mediating sensitivity to radiotherapy. *Int J Radiat Oncol Biol Phys*. 2004; 59: 928-942.
12. DeVita Jr VT, Rosenberg SA. Two hundred years of cancer research. *N Engl J Med*. 2012; 366: 2207-2214.
13. Liauw SL, Connell PP, Weichselbaum RR. New paradigms and future challenges in radiation oncology: an update of biological targets and technology. *Sci Transl Med*. 2013; 5: 173sr2.
14. Bernier J, Hall EJ, Giaccia A. Radiation oncology: a century of achievements. *Nature reviews. Cancer*. 2004; 4: 737-747.
15. Connell PP, Hellman S. Advances in radiotherapy and implications for the next century: a historical perspective. *Cancer Res*. 2009 Jan 15; 69: 383-392.
16. Thariat J, Hannoun-Levi JM, Myint AS, Vuong T, Gérard JP. Past, present, and future of radiotherapy for the benefit of patients. *Nat. Rev. Clin. Oncol*. 2013; 10: 52-60.
17. Baskar R, Lee KA, Yeo R, Yeoh KW. Cancer and radiation therapy: current advances and future directions. *Int J Med Sci*. 2012; 9: 193-199.
18. Chabner BA, Roberts Jr TG. Chemotherapy and the war on cancer. *Nat. Rev. Cancer*. 2005; 5: 65-72.
19. Morrison WB. Cancer chemotherapy: an annotated history. *J Vet Intern Med*. 2010; 24: 1249-1262.
20. Rosenberg B, Vancamp L, Trosko JE, Mansour VH. Platinum compounds: a new class of potent antitumour agents. *Nature*. 1969; 222: 385-386.
21. Blagosklonny MV. Analysis of FDA approved anticancer drugs reveals the future of cancer therapy. *Cell Cycle*. 2004; 3: 1033-1040.

22. DeVita VT, Chu E. A history of cancer chemotherapy. *Cancer Res.* 2008; 68: 8643-8653.
23. Center Watch, www.centerwatch.com/drug-information/fda-approved-drugs/therapeutic-area/12/oncology.
24. Imai K, Takaoka A. Comparing antibody and small-molecule therapies for cancer. *Nat. Rev. Cancer.* 2006; 6:714-727.
25. Gerber DE. Targeted therapies: a new generation of cancer treatments. *Am Fam Physician.* 2008; 77: 311-319.
26. Hoelder S, Clarke PA, Workman P. Discovery of small molecule cancer drugs: successes, challenges and opportunities. *Mol Oncol.* 2012; 6: 155-176.
27. Seiwert TY, Salama JK, Vokes EE. The concurrent chemoradiation paradigm—general principles. *Nat Clin Pract Oncol.* 2007; 4: 86-100.
28. Brunner TB. The rationale of combined radiotherapy and chemotherapy—Joint action of Castor and Pollux. *Best Pract Res Clin Gastroenterol.* 2016; 30: 515-528.
29. Wilson GD, Bentzen SM, Harari PM. Biologic basis for combining drugs with radiation. *Semin Radiat Oncol.* 2006; 16: 2-9.
30. Mondal J, Panigrahi AK, Khuda-Bukhsh AR. Conventional Chemotherapy: Problems and Scope for Combined Therapies with Certain Herbal Products and Dietary Supplements. *Austin J Mol & Cell Biol.* 2014; 1: 10.
31. Sharma RA, Plummer R, Stock JK, Greenhalgh TA, Ataman O, Kelly S, Clay R, Adams RA, Baird RD, Billingham L, Brown SR. Clinical development of new drug-radiotherapy combinations. *Nat Rev Clin Oncol.* 2016; 13: 627-642.

32. Li J, Chen F, Cona MM, Feng Y, Himmelreich U, Oyen R, Verbruggen A, Ni Y. A review on various targeted anticancer therapies. *Target Oncol.* 2012; 7: 69-85.
33. Marusyk A, Polyak K. Tumor heterogeneity: causes and consequences. *Biochim Biophys Acta.* 2010; 1805: 105-117.
34. Dean M, Fojo T, Bates S. Tumour stem cells and drug resistance. *Nat. Rev. Cancer.* 2005 ; 5: 275-284.
35. Laster BH, Thomlinson WC, Fairchild RG. Photon activation of iododeoxyuridine: biological efficacy of Auger electrons. *Radiat. Res.* 1993; 133: 219-224.
36. Gil S, Fernández M, Prezado Y, Biete A, Bravin A, Sabés M. Synchrotron radiation in cancer treatments and diagnostics: an overview. *Clin Transl Oncol.* 2011; 13: 715-720.
37. Kobayashi K, Usami N, Porcel E, Lacombe S, Le Sech C. Enhancement of radiation effect by heavy elements. *Mutat Res.* 2010; 704: 123-131.
38. Fairchild RG, Brill AB, Ettinger KV. Radiation enhancement with iodinated deoxyuridine. *Invest Radiol.* 1982; 17: 407-416.
39. Shinohara K, Ohara H, Kobayashi K, Maezawa H, Hieda K, Okada S, Ito T. Enhanced killing of HeLa cells pre-labeled with 5-bromodeoxyuridine by monochromatic synchrotron radiation at 0.9 Å: an evidence for Auger enhancement in mammalian cells. *J.Radiat. Res.* 1985; 26: 334-338.
40. Ohara H, Shinohara K, Yamada T, Kobayashi K, Maesawa H, Hieda K, Ito T. Enhancement of chromosome aberrations induced in 5'-bromodeoxyuridine-

- labeled Chinese hamster ovary cells by monochromatic radiation. Workshop on photon activation therapy: proceedings. 1985:40.
41. Larson D, Bodell WJ, Ling C, Phillips TL, Schell M, Shrieve D, Troxel T. Auger electron contribution to bromodeoxyuridine cellular radiosensitization. *Int J Radiat Oncol Biol Phys*. 1989; 16: 171-176.
 42. Biston MC, Joubert A, Adam JF, Elleaume H, Bohic S, Charvet AM, Estève F, Foray N, Balosso J. Cure of Fisher rats bearing radioresistant F98 glioma treated with cis-platinum and irradiated with monochromatic synchrotron X-rays. *Cancer Res*. 2004; 64: 2317-2323.
 43. Adam JF, Joubert A, Biston MC, Charvet AM, Peoc'h M, Le Bas JF, Balosso J, Estève F, Elleaume H. Prolonged survival of Fischer rats bearing F98 glioma after iodine-enhanced synchrotron stereotactic radiotherapy. *Int J Radiat Oncol Biol Phys*. 2006; 64: 603-611.
 44. Adam JF, Biston MC, Rousseau J, Boudou C, Charvet AM, Balosso J, Estève F, Elleaume H. Heavy element enhanced synchrotron stereotactic radiotherapy as a promising brain tumour treatment. *Phys Med*. 2008; 24: 92-97.
 45. Rousseau J, Adam JF, Deman P, Wu TD, Guerquin-Kern JL, Gouget B, Barth RF, Estève F, Elleaume H. Intracerebral delivery of 5-iodo-2'-deoxyuridine in combination with synchrotron stereotactic radiation for the therapy of the F98 glioma. *J Synchrotron Radiat*. 2009; 16:573-581.
 46. Ricard C, Fernandez M, Requardt H, Wion D, Vial JC, Segebarth C, van der Sanden B. Synergistic effect of cisplatin and synchrotron irradiation on F98 gliomas growing in nude mice. *J Synchrotron Radiat*. 2013; 20: 777-784.

47. Ceresa C, Nicolini G, Semperboni S, Requardt H, Le Duc G, Santini C, Pellei M, Bentivegna A, Dalpra L, Cavaletti G, Bravin A. Synchrotron-based photon activation therapy effect on cisplatin pre-treated human glioma stem cells. *Anticancer Res.* 2014; 34: 5351-5355.
48. Chilakamarthi U, Giribabu L. Photodynamic Therapy: Past, Present and Future. *Chem Rec.* 2017; 17: 775-802.
49. van Straten D, Mashayekhi V, de Bruijn HS, Oliveira S, Robinson DJ. Oncologic Photodynamic Therapy: Basic Principles, Current Clinical Status and Future Directions. *Cancers (Basel).* 2017; 9. pii: E19.
50. Abrahamse H, Hamblin MR. New photosensitizers for photodynamic therapy. *Biochem. J.* 2016; 473: 347-364.
51. Agostinis P, Berg K, Cengel KA, Foster TH, Girotti AW, Gollnick SO, Hahn SM, Hamblin MR, Juzeniene A, Kessel D, Korbelik M. Photodynamic therapy of cancer: an update. *CA: a cancer journal for clinicians.* 2011; 61: 250-281.
52. Olivo M, Bhuvaneswari R, Lucky SS, Dendukuri N, Soo-Ping Thong P. Targeted Therapy of Cancer Using Photodynamic Therapy in Combination with Multi-faceted Anti-Tumor Modalities. *Pharmaceuticals (Basel).* 2010; 3: 1507-1529.
53. Robertson CA, Evans DH, Abrahamse H. Photodynamic therapy (PDT): a short review on cellular mechanisms and cancer research applications for PDT. *J Photochem Photobiol B.* 2009; 96: 1-8.
54. Huang Z. A review of progress in clinical photodynamic therapy. *Technol Cancer Res Treat.* 2005; 4: 283-293.

55. Fayter D, Corbett M, Heirs M, Fox D, Eastwood A. A systematic review of photodynamic therapy in the treatment of pre-cancerous skin conditions, Barrett's oesophagus and cancers of the biliary tract, brain, head and neck, lung, oesophagus and skin. *Health Technol Assess.* 2010; 14: 1-288.
56. Allison RR, Sibata CH. Oncologic photodynamic therapy photosensitizers: a clinical review. *Photodiagnosis Photodyn Ther.* 2010; 7: 61-75.
57. Berg K, Selbo PK, Weyergang A, Dietze A, Prasmickaite L, Bonsted A, Engesaeter BØ, Angell-Petersen E, Warloe T, Frandsen N, Høgset A. Porphyrin-related photosensitizers for cancer imaging and therapeutic applications. *J Microsc.* 2005; 218:133-147.
58. Dolmans DE, Fukumura D, Jain RK. Photodynamic therapy for cancer. *Nat. Rev. Cancer.* 2003; 3: 380-387.
59. Josefsen LB, Boyle RW. Photodynamic therapy and the development of metal-based photosensitisers. *Met Based Drugs.* 2008; 2008: 276109.
60. Redmond RW. Photophysics and photochemistry in photodynamic therapy In Hamblin MR, Mróz P (Ed.) *Advances in photodynamic therapy: basic, translational, and clinical.* Boston:Artech House; 2008: 41- 58.
61. Bacellar IO, Tsubone TM, Pavani C, Baptista MS. Photodynamic Efficiency: From Molecular Photochemistry to Cell Death. *Int J Mol Sci.* 2015; 16: 20523-20559.
62. Ormond AB, Freeman HS. Dye sensitizers for photodynamic therapy. *Materials.* 2013; 6: 817-840.

63. Abdel-kader MH. The Journey of PDT Throughout History: PDT from Pharos to Present. In Kostron H, Hasan T. (Ed.) Photodynamic Medicine: From Bench to Clinic; Royal society of chemistry; 2016: 1-21.
64. Abdel-kader MH. The Journey of PDT Throughout History: PDT from Pharos to Present. In Kostron H, Hasan T. (Ed.) Photodynamic Medicine: From Bench to Clinic; Royal Society of Chemistry, 2016; 1-21.
65. Nyman ES, Hynninen PH. Research advances in the use of tetrapyrrolic photosensitizers for photodynamic therapy. J Photochem Photobiol B. 2004; 73: 1-28.
66. O'Connor AE, Gallagher WM, Byrne AT. Porphyrin and nonporphyrin photosensitizers in oncology: preclinical and clinical advances in photodynamic therapy. Photochem Photobiol. 2009; 85: 1053-1074.
67. Szaciłowski K, Macyk W, Drzewiecka-Matuszek A, Brindell M, Stochel G. Bioinorganic photochemistry: frontiers and mechanisms. Chem Rev. 2005; 105: 2647-2694.
68. Kuznetsova NA, Gretsova NS, Derkacheva VM, Kaliya OL, Lukyanets EA. Sulfonated phthalocyanines: aggregation and singlet oxygen quantum yield in aqueous solutions J Porphyr Phthalocyanines. 2003;7: 147-154.
69. Chin Y, Lim SH, Zorlu Y, Ahsen V, Kiew LV, Chung LY, Dumoulin F, Lee HB. Improved photodynamic efficacy of Zn(II) phthalocyanines via glycerol substitution. PLoS One. 2014; 9: e97894.
70. Ji W, Yoo JW, Bae EK, Lee JH, Choi CM. The effect of Radachlorin® PDT in advanced NSCLC: a pilot study. Photodiagnosis Photodyn Ther. 2013; 10: 120-126.

71. Yoon I, Li JZ, Shim YK. Advance in photosensitizers and light delivery for photodynamic therapy. *Clin Endosc.* 2013; 46: 7-23.
72. Chen Y, Potter WR, Missert JR, Morgan J, Pandey RK. Comparative in vitro and in vivo studies on long-wavelength photosensitizers derived from bacteriopurpurinimide and Bacteriochlorin p6: fused imide ring enhances the in vivo PDT efficacy. *Bioconjug Chem.* 2007; 18: 1460-1473.
73. Huang YY, Mroz P, Zhiyentayev T, Sharma SK, Balasubramanian T, Ruzié C, Krayner M, Fan D, Borbas KE, Yang E, Kee HL, Kirmaier C, Diers JR, Bocian DF, Holten D, Lindsey JS, Hamblin MR. In vitro photodynamic therapy and quantitative structure-activity relationship studies with stable synthetic near-infrared-absorbing bacteriochlorin photosensitizers. *J Med Chem.* 2010; 53: 4018-4027.
74. Photodynamic Therapy with LUZ11 in Advanced Head and Neck Cancer, Clinical Trials. Gov NCT02070432. <https://clinicaltrials.gov/ct2/show/NCT02070432>.
75. Jacques SL. How tissue optics affect dosimetry of photodynamic therapy. *J Biomed Opt.* 2010; 15: 051608.
76. Stolik S, Delgado JA, Pérez A, Anasagasti L. Measurement of the penetration depths of red and near infrared light in human "ex vivo" tissues. *J Photochem Photobiol B.* 2000; 57: 90-93.
77. Han G, Xie J. Light-Mediated Deep-Tissue Theranostics. *Theranostics.* 2016; 6: 2292-2294.
78. Quirk BJ, Brandal G, Donlon S, Vera JC, Mang TS, Foy AB, Lew SM, Girotti AW, Jogonal S, LaViolette PS, Connelly JM, Whelan HT.

Photodynamic therapy (PDT) for malignant brain tumors--where do we stand?

Photodiagnosis Photodyn Ther. 2015; 12: 530-544.

79. Webber J, Herman M, Kessel D, Fromm D. Current concepts in gastrointestinal photodynamic therapy. *Ann Surg.* 1999 ; 230: 12-23.
80. Starkey JR, Rebane AK, Drobizhev MA, Meng F, Gong A, Elliott A, McInnerney K, Spangler CW. New two-photon activated photodynamic therapy sensitizers induce xenograft tumor regressions after near-IR laser treatment through the body of the host mouse. *Clin Cancer Res.* 2008; 14: 6564-6573.
81. Henderson BW, Fingar VH. Oxygen limitation of direct tumor cell kill during photodynamic treatment of a murine tumor model. *Photochem Photobiol.* 1989; 49: 299-304.
82. Ma L, Moan J, Berg K. Evaluation of a new photosensitizer, meso-tetrahydroxyphenyl-chlorin, for use in photodynamic therapy: a comparison of its photobiological properties with those of two other photosensitizers. *Int J Cancer.* 1994; 57: 883-888.
83. Melnikova VO, Bezdetnaya LN, Potapenko AY, Guillemin F. Photodynamic properties of meta-tetra(hydroxyphenyl)chlorin in human tumor cells. *Radiat Res.* 1999; 152: 428-435.
84. Weishaupt KR, Gomer CJ, Dougherty TJ. Identification of singlet oxygen as the cytotoxic agent in photoinactivation of a murine tumor. *Cancer Res.* 1976; 36: 2326-2329.

85. Huang Z, Xu H, Meyers AD, Musani AI, Wang L, Tagg R, Barqawi AB, Chen YK. Photodynamic therapy for treatment of solid tumors--potential and technical challenges. *Technol Cancer Res Treat*. 2008; 7: 309-320.
86. Moan J and Juzeniene A. The role of oxygen in photodynamic therapy. In Hamblin MR, Mróz P (Ed.) *Advances in photodynamic therapy: basic, translational, and clinical*. Boston: Artech House; 2008: 135- 149.
87. Melnikova VO, Bezdetnaya LN, Brault D, Potapenko AY, Guillemin F. Enhancement of meta-tetrahydroxyphenylchlorin-sensitized photodynamic treatment on human tumor xenografts using a water-soluble vitamin E analogue, Trolox. *Int J Cancer*. 2000; 88: 798-803.
88. Umar MN, Khan K, Anjum MN, Yaseen M. Synthesis and relaxivity measurement of porphyrin-based Magnetic Resonance Imaging (MRI) contrast agents. *Journal of Structural Chemistry*. 2014; 55: 910-915.
89. Zhang S, Patel NJ, Pandey RK. Chlorophyll-a analogs for cancer imaging and therapy (theranostics). In Paolesse R. (Ed.) *Applications of Porphyrinoids*. Springer Berlin Heidelberg: 2014: pp. 1-30.
90. Patel NJ, Chen Y, Joshi P, Pera P, Baumann H, Missert JR, Ohkubo K, Fukuzumi S, Nani RR, Schnermann MJ, Chen P, Zhu J, Kadish KM, Pandey RK. Effect of Metalation on Porphyrin-Based Bifunctional Agents in Tumor Imaging and Photodynamic Therapy. *Bioconjug Chem*. 2016; 27: 667-680.
91. Pandey SK, Gryshuk AL, Sajjad M, Zheng X, Chen Y, Abouzeid MM, Morgan J, Charamisinau I, Nabi HA, Oseroff A, Pandey RK. Multimodality agents for tumor imaging (PET, fluorescence) and photodynamic therapy. A possible "see and treat" approach. *J Med Chem*. 2005; 48: 6286-6295.

92. Zhang Y, Lovell JF. Porphyrins as theranostic agents from prehistoric to modern times. *Theranostics*. 2012; 2: 905-915.
93. Huang H, Song W, Rieffel J, Lovell JF. Emerging applications of porphyrins in photomedicine. *Front Phys*. 2015. pii: 23.
94. Chen H, Wang GD, Chuang YJ, Zhen Z, Chen X, Biddinger P, Hao Z, Liu F, Shen B, Pan Z, Xie J. Nanoscintillator-mediated X-ray inducible photodynamic therapy for in vivo cancer treatment. *Nano Lett*. 2015; 15: 2249-2256.
95. Kaščáková S, Giuliani A, Lacerda S, Pallier A, Mercère P, Tóth É, Réfrégiers M. X-ray-induced radiophotodynamic therapy (RPDT) using lanthanide micelles: Beyond depth limitations. *Nano Research*. 2015; 8: 2373-2379.
96. Wang GD, Nguyen HT, Chen H, Cox PB, Wang L, Nagata K, Hao Z, Wang A, Li Z, Xie J. X-Ray Induced Photodynamic Therapy: A Combination of Radiotherapy and Photodynamic Therapy. *Theranostics*. 2016; 6: 2295-2305.
97. Mehraban N, Freeman HS. Developments in PDT Sensitizers for Increased Selectivity and Singlet Oxygen Production. *Materials (Basel)*. 2015; 8: 4421-4456.
98. Solov'ev KN, Borisevich EA. Intramolecular heavy-atom effect in the photophysics of organic molecules. *Physics-Uspekhi*. 2005; 48: 231-53.
99. Gorman A, Killoran J, O'Shea C, Kenna T, Gallagher WM, O'Shea DF. In vitro demonstration of the heavy-atom effect for photodynamic therapy. *J Am Chem Soc*. 2004; 126: 10619-10631.

100. Dąbrowski JM, Pucelik B, Regiel-Futyra A, Brindell M, Mazuryk O, Kyzioł A, Stochel G, Macyk W, Arnaut LG. Engineering of relevant photodynamic processes through structural modifications of metallotetrapyrrolic photosensitizers. *Coordination Chemistry Reviews*. 2016; 325: 67-101.
101. Küpper H, Dedic R, Svoboda A, Hála J, Kroneck PM. Kinetics and efficiency of excitation energy transfer from chlorophylls, their heavy metal-substituted derivatives, and pheophytins to singlet oxygen. *Biochim Biophys Acta*. 2002; 1572:107-113.
102. Marydasan B, Nair AK, Ramaiah D. Optimization of triplet excited state and singlet oxygen quantum yields of picolylamine-porphyrin conjugates through zinc insertion. *J Phys Chem B*. 2013; 117: 13515-13522.
103. Ando T, Irie K, Koshimizu K, Takemura T, Nishino H, Iwashima A, Takeda N, Nakajima S, Sakata I. Photocytotoxicity of water – soluble metalloporphyrins derivatives. *J. Photochem. Photobiol*. 1993; 57: 629-633.
104. Obata M, Hirohara S, Tanaka R, Kinoshita I, Ohkubo K, Fukuzumi S, Tanihara M, Yano S. In vitro heavy-atom effect of palladium(II) and platinum(II) complexes of pyrrolidine-fused chlorin in photodynamic therapy. *J Med Chem*. 2009; 52: 2747-2753.
105. Chen Y, Zheng X, Dobhal MP, Gryshuk A, Morgan J, Dougherty TJ, Oseroff A, Pandey RK. Methyl pyropheophorbide-a analogues: potential fluorescent probes for the peripheral-type benzodiazepine receptor. Effect of central metal in photosensitizing efficacy. *J Med Chem*. 2005; 48: 3692-3695.

106. Malina L, Tomankova KB, Malohlava J, Jiravova J, Manisova B, Zapletalova J, Kolarova H. The in vitro cytotoxicity of metal-complexes of porphyrin sensitizer intended for photodynamic therapy. *Toxicol In Vitro*. 2016; 34: 246-256.
107. Brandis A, Mazor O, Neumark E, Rosenbach-Belkin V, Salomon Y, Scherz A. Novel water-soluble bacteriochlorophyll derivatives for vascular-targeted photodynamic therapy: synthesis, solubility, phototoxicity and the effect of serum proteins. *Photochem Photobiol*. 2005; 81: 983-993.
108. Shi L, Jiang YY, Jiang T, Yin W, Yang JP, Cao ML, Fang YQ, Liu HY. Water-soluble Manganese and Iron Mesotetrakis(carboxyl)porphyrin: DNA Binding, Oxidative Cleavage, and Cytotoxic Activities. *Molecules*. 2017; 22. pii: E1084.
109. Er O, Lambrecht FY, Ocakoglu K, Kayabasi C, Gunduz C. Primary evaluation of a nickel-chlorophyll derivative as a multimodality agent for tumor imaging and photodynamic therapy. *J. Radioanal. Nucl. Chem*. 2015; 306: 155-163.
110. Ocakoglu K, Er Ö, Yurt Lambrecht F, Yılmaz Süslüer S, Kayabasi C, Gündüz C, Yılmaz O. Evaluation of cancer imaging potential and photodynamic therapy efficacy of copper (II) benzyloxypheophorbide-a. *J. Drug Target*. 2015; 23: 89-95.
111. Ocakoglu K, Er O, Kiyak G, Lambrecht FY, Gunduz C, Kayabasi C. 131 I–Zn–Chlorophyll derivative photosensitizer for tumor imaging and photodynamic therapy. *Int. J. Pharm*. 2015; 493: 96-101.

112. Yoon I, Park HS, Cui BC, Li JZ, Kim JH, Lkhagvadulam B, Shim YK. Photodynamic and Antioxidant Activities of Divalent Transition Metal Complexes of Methyl Pheophorbide-a. *Bull. Korean Chem. Soc.* 2011; 32: 2981-2987.
113. Arnaut LG. Design of porphyrin-based photosensitizers for photodynamic therapy. *Adv. Inorg. Chem.* 2011; 63: 187-233.
114. Marin DM, Payerpaj S, Collier GS, Ortiz AL, Singh G, Jones M, Walter MG. Efficient intersystem crossing using singly halogenated carbomethoxyphenyl porphyrins measured using delayed fluorescence, chemical quenching, and singlet oxygen emission. *Phys Chem Chem Phys.* 2015; 17: 29090-29096.
115. Topkaya D, Arnoux P, Dumoulin F. Modulation of singlet oxygen generation and amphiphilic properties of trihydroxylated monohalogenated porphyrins. *J Porphyr Phthalocyanines.* 2015; 19: 1081-1087.
116. Rey YP, Abradelo DG, Santschi N, Strassert CA, Gilmour R. Quantitative Profiling of the Heavy-Atom Effect in BODIPY Dyes: Correlating Initial Rates, Atomic Numbers, and 1O_2 Quantum Yields. *Eur. J. Org. Chem.* 2017; 2017: 2170-2178.
117. Avirah RR, Jayaram DT, Adarsh N, Ramaiah D. Squaraine dyes in PDT: from basic design to in vivo demonstration. *Org Biomol Chem.* 2012; 10: 911-920.
118. Bogoeva V, Siksjø M, Sæterbø KG, Melø TB, Bjørkøy A, Lindgren M, Gederaas OA. Ruthenium porphyrin-induced photodamage in bladder cancer cells. *Photodiagnosis Photodyn Ther.* 2016; 14: 9-17.

119. Schmitt F, Govindaswamy P, Süss-Fink G, Ang WH, Dyson PJ, Juillerat-Jeanneret L, Therrien B. Ruthenium porphyrin compounds for photodynamic therapy of cancer. *J Med Chem.* 2008; 51: 1811-1816.
120. Kessel D, Morgan A. Photosensitization with etiobenzochlorins and octaethylbenzochlorins. *Photochem Photobiol.* 1993; 58: 521-526.
121. Chen CY, Sun E, Fan D, Taniguchi M, McDowell BE, Yang E, Diers JR, Bocian DF, Holten D, Lindsey JS. Synthesis and physicochemical properties of metallobacteriochlorins. *Inorg Chem.* 2012; 51: 9443-9464.
122. Lottner C, Knuechel R, Bernhardt G, Brunner H. Combined chemotherapeutic and photodynamic treatment on human bladder cells by hematoporphyrin-platinum(II) conjugates. *Cancer Lett.* 2004; 203: 171-180.
123. Brunner H, Arndt MR, Treitinger B. Porphyrin platinum conjugates—new aims. *Inorg. Chim. Acta.* 2004; 357:1649-1669.
124. Brunner H, Schellerer KM. New porphyrin platinum conjugates for the cytostatic and photodynamic tumor therapy. *Inorganica chimica acta.* 2003; 350: 39-48.
125. Kim YS, Song R, Hyun Kim D, Jun MJ, Sohn YS. Synthesis, biodistribution and antitumor activity of hematoporphyrin-platinum(II) conjugates. *Bioorg Med Chem.* 2003; 11: 1753-1760.
126. Kim YS, Song R, Lee CO, Sohn YS. Synthesis and biological activity of novel platinum(II) complexes of glutamate tethered to hydrophilic hematoporphyrin derivatives. *Bioorg Med Chem Lett.* 2004; 14: 2889-2892.
127. Momekov G, Karaivanova M, Ugrinova I, Pasheva E, Gencheva G, Tsekova D, Arpadjan S, Bontchev PR. In vitro pharmacological study of monomeric

- platinum(III) hematoporphyrin IX complexes. *Invest New Drugs*. 2011; 29: 742-751.
128. Naik A, Rubbiani R, Gasser G, Spingler B. Visible-light-induced annihilation of tumor cells with platinum-porphyrin conjugates. *Angew Chem Int Ed Engl*. 2014; 53: 6938-6941.
129. Sun RW. Strategies to improve the anti-cancer properties of gold (III) complexes. *Mod Chem Appl*. 2013; 1: 1000102.
130. Sun RW, Che CM. The anti-cancer properties of gold (III) compounds with dianionic porphyrin and tetradentate ligands. *Coord Chem Rev*. 2009; 253: 1682-1691.
131. Che CM, Sun RW, Yu WY, Ko CB, Zhu N, Sun H. Gold(III) porphyrins as a new class of anticancer drugs: cytotoxicity, DNA binding and induction of apoptosis in human cervix epitheloid cancer cells. *Chem Commun (Camb)*. 2003; 14:1718-1719.
132. Wang Y, He QY, Sun RW, Che CM, Chiu JF. Gold(III) porphyrin 1a induced apoptosis by mitochondrial death pathways related to reactive oxygen species. *Cancer Res*. 2005; 65: 11553-11564.
133. Momekov G, Ferdinandov D, Konstantinov S, Arpadjan S, Tsekova D, Gencheva G, Bontchev PR, Karaivanova M. In vitro evaluation of a stable monomeric gold(II) complex with hematoporphyrin IX: cytotoxicity against tumor and kidney cells, cellular accumulation, and induction of apoptosis. *Bioinorg Chem Appl*. 2008: 367471.

134. Hartmann M, Robert A, Duarte V, Keppler BK, Meunier B. Synthesis of water-soluble ruthenium porphyrins as DNA cleavers and potential cytotoxic agents J Biol Inorg Chem. 1997; 2: 427-432.
135. Gianferrara T, Bergamo A, Bratsos I, Milani B, Spagnul C, Sava G, Alessio E. Ruthenium-porphyrin conjugates with cytotoxic and phototoxic antitumor activity. J Med Chem. 2010; 53: 4678-4690.
136. Antoni PM, Naik A, Albert I, Rubbiani R, Gupta S, Ruiz-Sanchez P, Munikorn P, Mateos JM, Luginbuehl V, Thamyongkit P, Ziegler U, Gasser G, Jeschke G, Spingler B. (Metallo)porphyrins as potent phototoxic anticancer agents after irradiation with red light. Chemistry. 2015; 21: 1179-1183.
137. Tovmasyan AG, Babayan NS, Sahakyan LA, Shahkhatuni AG, Gasparyan GH, Aroutiounian RM, Ghazaryan RK. Synthesis and in vitro anticancer activity of water-soluble cationic pyridylporphyrins and their metallocomplexes. J Porphyr Phthalocyanines. 2008; 12: 1100-1110.
138. Tovmasyan A, Babayan N, Poghosyan D, Margaryan K, Harutyunyan B, Grigoryan R, Sarkisyan N, Spasojevic I, Mamyan S, Sahakyan L, Aroutiounian R, Ghazaryan R, Gasparyan G. Novel amphiphilic cationic porphyrin and its Ag(II) complex as potential anticancer agents. J Inorg Biochem. 2014; 140: 94-103.
139. Tsekova D, Gorolomova P, Gochev G, Skumryev V, Momekov G, Momekova D, Gencheva G. Synthesis, structure and in vitro cytotoxic studies of novel paramagnetic palladium(III) complexes with hematoporphyrin IX. J Inorg Biochem. 2013; 124: 54-62.

140. Chen W, Zhang J. Using nanoparticles to enable simultaneous radiation and photodynamic therapies for cancer treatment. *J Nanosci Nanotechnol.* 2006; 6: 1159-1166.
141. Morgan NY, Kramer-Marek G, Smith PD, Camphausen K, Capala J. Nanoscintillator conjugates as photodynamic therapy-based radiosensitizers: calculation of required physical parameters. *Radiat Res.* 2009; 171: 236-244.
142. Kamkaew A, Chen F, Zhan Y, Majewski RL, Cai W. Scintillating Nanoparticles as Energy Mediators for Enhanced Photodynamic Therapy. *ACS Nano.* 2016; 10: 3918-3935.
143. Astolfi L, Ghiselli S, Guaran V, Chicca M, Simoni E, Olivetto E, Lelli G, Martini A. Correlation of adverse effects of cisplatin administration in patients affected by solid tumours: a retrospective evaluation. *Oncol Rep.* 2013; 29: 1285-1292.
144. Tsuchida T, Kato H, Okunaka T, Harada M, Ichinose S, Hirata T. P-168 Diagnosis and treatment of neoplasms by synchrotron radiation combined with mono-L-aspartyl aurochlorin e6. *Lung Cancer.* 2003; 41: S133.
145. Ishibashi N, Fujiwara K, Pandey RK, Kataba M, Oguni A, Igarashi J, Soma M, Shizukuishi T, Maebayashi T, Abe K. An Iodine labeled porphyrin as a new radiation sensitizer in human bladder cancer cells in vitro and in vivo, combining photodynamic therapy (PDT) with photon activation therapy (PAT). *Nihon Univ J Med.* 2013; 72: 212-219.
146. Sharma M, Dube A, Bansal H, Kumar Gupta P. Effect of pH on uptake and photodynamic action of chlorin p6 on human colon and breast adenocarcinoma cell lines. *Photochem Photobiol Sci.* 2004; 3: 231-235.

147. Parihar A, Dube A, Gupta PK. Conjugation of chlorin p(6) to histamine enhances its cellular uptake and phototoxicity in oral cancer cells. *Cancer Chemother Pharmacol.* 2011; 68: 359-369.
148. Dube A, Sharma S, Gupta PK. Evaluation of chlorin p6 for photodynamic treatment of squamous cell carcinoma in the hamster cheek pouch model. *Oral Oncol.* 2006; 42: 77-82.
149. Dube A, Sharma S, Gupta PK. Tumor regression induced by photodynamic treatment with chlorin p(6) in hamster cheek pouch model of oral carcinogenesis: Dependence of mode of tumor cell death on the applied drug dose. *Oral Oncol.* 2011; 47: 467-471.
150. Santini C, Pellei M, Gandin V, Porchia M, Tisato F, Marzano C. Advances in copper complexes as anticancer agents. *Chem Rev.* 2014; 114: 815-862.
151. Hao G, N Singh A, K Oz O, Sun X. Recent advances in copper radiopharmaceuticals. *Current radiopharmaceuticals.* 2011; 4: 109-121.
152. Zhang CX, Lippard SJ. New metal complexes as potential therapeutics. *Curr Opin Chem Biol.* 2003; 7: 481-489.
153. Ganguly A, Basu S, Banerjee K, Chakraborty P, Sarkar A, Chatterjee M, Chaudhuri SK. Redox active copper chelate overcomes multidrug resistance in T-lymphoblastic leukemia cell by triggering apoptosis. *Mol Biosyst.* 2011; 7: 1701-1712.
154. Wang J, Yi J. Cancer cell killing via ROS: to increase or decrease, that is the question. *Cancer Biol Ther.* 2008; 7: 1875-1884.

155. Prashanth L, Kattapagari KK, Chitturi RT, Baddam VR, Prasad LK. A review on role of essential trace elements in health and disease. *J Dr NTR Univ Health Sci.* 2015; 4: 75-85.
156. Hooper JK, Sery TW, Yamamoto N. Photodynamic sensitizers from chlorophyll:purpurin-18 and chlorin p6. *Photochem Photobiol.* 1988; 48: 579-582.
157. Mosmann T. Rapid colorimetric assay for cellular growth and survival: application to proliferation and cytotoxicity assays. *J Immunol Methods.* 1983; 65: 55-63.
158. Price P, McMillan TJ. Use of the tetrazolium assay in measuring the response of human tumor cells to ionizing radiation. *Cancer Res.* 1990; 50: 1392-1396.
159. Rappole CA, Mitra K, Wen H. Dynamic fluorescence imaging of the free radical products of X-ray absorption in live cells. *Opt Nanoscopy.* 2012; 1: 5.
160. Guo WJ, Ye SS, Cao N, Huang J, Gao J, Chen QY. ROS-mediated autophagy was involved in cancer cell death induced by novel copper(II) complex. *Exp Toxicol Pathol.* 2010; 62: 577-582.
161. Tiwari MK, Gupta P, Sinha AK, Kane SR, Singh AK, Garg SR, Garg CK, Lodha GS, Deb SK. A microfocus X-ray fluorescence beamline at Indus-2 synchrotron radiation facility. *J Synchrotron Radiat.* 2013; 20: 386-389.
162. Gollmer A, Arnbjerg J, Blaikie FH, Pedersen BW, Breitenbach T, Daasbjerg K, Glasius M, Ogilby PR. Singlet Oxygen Sensor Green®: photochemical behavior in solution and in a mammalian cell. *Photochem Photobiol.* 2011; 87: 671-679.

163. Bourré L, Thibaut S, Briffaud A, Rousset N, Eléouet S, Lajat Y, Patrice T. Indirect detection of photosensitizer ex vivo. *J Photochem Photobiol B*. 2002; 67: 23-31.
164. Price M, Reiners JJ, Santiago AM, Kessel D. Monitoring singlet oxygen and hydroxyl radical formation with fluorescent probes during photodynamic therapy. *Photochem Photobiol*. 2009; 85:1177-1181.
165. Lakowicz JR, *Principles of Fluorescence Spectroscopy*, Springer, New York, USA, 1st edition 1983.
166. Reichmann ME, Rice SA, Thomas CA, Doty P. A further examination of the molecular weight and size of desoxypentose nucleic acid. *J. Am. Chem. Soc*. 1954; 76: 3047-3053.
167. Liu J, Shi S, Ji LN, Mei WJ. Investigation on DNA binding and photocleavage properties of water-soluble porphyrin and metalloporphyrins. *Transit metal chem*. 2005; 30: 684-690.
168. Mroz P, Bhaumik J, Dogutan DK, Aly Z, Kamal Z, Khalid L, Kee HL, Bocian DF, Holten D, Lindsey JS, Hamblin MR. Imidazole metalloporphyrins as photosensitizers for photodynamic therapy: role of molecular charge, central metal and hydroxyl radical production. *Cancer Lett*. 2009; 282: 63-76.
169. Sapan CV, Lundblad RL, Price NC. Colorimetric protein assay techniques. *Biotechnol. Appl. Biochem*. 1999; 29: 99-108.
170. Del Rio MS, Dejus RJ. XOP: Recent developments. In *SPIE proceedings* 1998; 3448: 340-345.

171. Dhamgaye VP, Lodha GS, Gowri Sankar B, Kant C. Beamline BL-07 at Indus-2: a facility for microfabrication research. *J Synchrotron Radiat.* 2014 ; 21: 259-263.
172. El Gohary MI, Shabban YS, Amin EA, Gawad MA, Desouky OS. Preparation and Characterization of Frick gel dosimeter. *Nat Sci* 2015; 13:139-143.
173. Mah LJ, El-Osta A, Karagiannis TC. gammaH2AX: a sensitive molecular marker of DNA damage and repair. *Leukemia.* 2010; 24: 679-686.
174. Darzynkiewicz Z, Halicka HD, Zhao H. Analysis of cellular DNA content by flow and laser scanning cytometry. *Adv Exp Med Biol.* 2010; 676: 137-147.
175. Bernhardt G, Reile H, Birnböck H, Spruss T, Schönenberger H. Standardized kinetic microassay to quantify differential chemosensitivity on the basis of proliferative activity. *J Cancer Res Clin Oncol.* 1992; 118: 35-43.
176. Low ML, Chan CW, Ng PY, Ooi IH, Maah MJ, Chye SM, Tan KW, Ng SW, Ng CH. Ternary and binary copper (II) complexes: synthesis, characterization, ROS-inductive, proteasome inhibitory, and anticancer properties. *J. Coord. Chem.* 2017;70: 223-241.
177. Brunner H, Gruber N. Carboplatin-containing porphyrin-platinum complexes as cytotoxic and phototoxic antitumor agents. *Inorg. Chim. Acta.*2004; 357: 4423-4451.
178. Shoemaker RH. The NCI60 human tumour cell line anticancer drug screen. *Nat Rev Cancer.* 2006; 6: 813-823.

179. White WI. Aggregation of porphyrins and metalloporphyrins. In D. Dolphin (Ed.) The porphyrins, physical chemistry part C. Academic Press, inc., London, UK 1978; 5: 303-339.
180. Fleischer EB, Choi EI, Hambright P, Stone A. Porphyrin studies: kinetics of metalloporphyrin formation. *Inorg Chem.* 1964; 3: 1284-1287.
181. Merlot AM, Kalinowski DS, Richardson DR. Unraveling the mysteries of serum albumin-more than just a serum protein. *Front Physiol.* 2014; 5: 299.
182. Buxton ILO, Benet LZ, Pharmacokinetics: The dynamics of drug absorption, distribution, and elimination. In Brunton LL, Chabner BA, Knollmann BC (Ed.) Goodman and Gilman's the pharmacological basis of therapeutics. McGraw-Hill Companies, Inc, 12th edition:17-39
183. Komor AC, Barton JK. The path for metal complexes to a DNA target. *Chem Commun (Camb).* 2013; 49: 3617-3630.
184. Pages BJ, Ang DL, Wright EP, Aldrich-Wright JR. Metal complex interactions with DNA. *Dalton Trans.* 2015; 44: 3505-3526.
185. Raman N, Ravichandran S, Thangaraja C. Copper (II), cobalt (II), nickel (II) and zinc (II) complexes of Schiff base derived from benzil-2, 4-dinitrophenylhydrazone with aniline. *J. Chem. Sci.* 2004; 116: 215-219.
186. Gladkova OL, Parkhats MV, Gorbachova AN, Terekhov SN. FTIR spectra and normal-mode analysis of chlorin e(6) and its degradation-induced impurities. *Spectrochim Acta A Mol Biomol Spectrosc.* 2010; 76: 388-394.
187. Zhang MQ, Zhu YC, Wu JG, Shi P, Deng RW, Chen ZN. Some transition metal complexes with naproxen. *Chemical Papers- Slovak Academy of Sciences.* 2001; 55: 202-206.

188. Petrović J, Nikolić G, Marković D. In vitro complexes of copper and zinc with chlorophyll. *J Serb Chem Soc.* 2006; 71: 501-512.
189. Bold B, Barkhuu B, Lee WK, Shim YK. Photodynamic Inactivation of *Staphylococcus aureus* by Novel Troponyl Methyl (Pyro) pheophorbides. *Bull. Korean Chem. Soc.* 2008; 29: 237-240.
190. Jarvi MT, Patterson MS, Wilson BC. Insights into photodynamic therapy dosimetry: simultaneous singlet oxygen luminescence and photosensitizer photobleaching measurements. *Biophys J.* 2012; 102: 661-671.
191. Moan J. Effect of bleaching of porphyrin sensitizers during photodynamic therapy. *Cancer Lett.* 1986; 33: 45-53.
192. Mishra PP, Patel S, Datta A. Effect of increased hydrophobicity on the binding of two model amphiphilic chlorin drugs for photodynamic therapy with blood plasma and its components. *J Phys Chem B.* 2006; 110: 21238-21244.
193. Yamasaki K, Chuang VT, Maruyama T, Otagiri M. Albumin-drug interaction and its clinical implication. *Biochim Biophys Acta.* 2013; 1830: 5435-5443.
194. Abou-Zied OK, Al-Shihi OI. Characterization of subdomain IIA binding site of human serum albumin in its native, unfolded, and refolded states using small molecular probes. *J Am Chem Soc.* 2008; 130: 10793-10801.
195. Yang F, Zhang Y, Liang H. Interactive association of drugs binding to human serum albumin. *Int J Mol Sci.* 2014; 15: 3580-3595.
196. Bohnert T, Gan LS. Plasma protein binding: from discovery to development. *J. Pharm. Sci.* 2013; 102: 2953-2994.

197. The U.S. Food and Drug Administration website: <http://www.fda.gov/OHRMS/DOCKETS/98fr/00n-1269-nfr0001-03.pdf>.
198. Lakowicz JR, Weber G. Quenching of fluorescence by oxygen. A probe for structural fluctuations in macromolecules. *Biochemistry*. 1973; 12: 4161-4170.
199. Patel S, Datta A. Steady state and time-resolved fluorescence investigation of the specific binding of two chlorin derivatives with human serum albumin. *J Phys Chem B*. 2007; 111: 10557-10562.
200. Yousefi R, Taheri-Kafrani A, Nabavizadeh SM, Pouryasini Z, Shahsavani MB, Khoshaman K, Rashidi M. The binding assessment with human serum albumin of novel six-coordinate Pt(IV) complexes, containing bidentate nitrogen donor/methyl ligands. *Mol Biol Res Commun*. 2015; 4: 167-179.
201. Shahabadi N, Maghsudi M. Binding studies of a new copper (II) complex containing mixed aliphatic and aromatic dinitrogen ligands with bovine serum albumin using different instrumental methods. *Journal of Molecular Structure*. 2009; 929: 193-199.
202. Ma HM, Chen X, Zhang N, Han YY, Wu D, Du B, Wei Q. Spectroscopic studies on the interaction of a water-soluble cationic porphyrin with proteins. *Spectrochim Acta A Mol Biomol Spectrosc*. 2009; 72: 465-469.
203. Aliaga-Alcalde N, Marqués-Gallego P, Kraaijkamp M, Herranz-Lancho C, den Dulk H, Görner H, Roubeau O, Teat SJ, Weyhermüller T, Reedijk J. Copper curcuminoids containing anthracene groups: fluorescent molecules with cytotoxic activity. *Inorg Chem*. 2010; 49: 9655-9663.

204. Mettath S, Munson BR, Pandey RK. DNA interaction and photocleavage properties of porphyrins containing cationic substituents at the peripheral position. *Bioconjug Chem.* 1999; 10: 94-102.
205. Moreira LM, Lima A, Soares RR, Batistela VR, Gerola AP, Hioka N, Bonacin JA, Severino D, Baptista MS, Machado AE, Rodrigues MR. Metallochlorophylls of magnesium, copper and zinc: evaluation of the influence of the first coordination sphere on their solvatochromism and aggregation properties. *J. Braz. Chem. Soc.* 2009; 20: 1653-1658.
206. Boscencu R. Unsymmetrical mesoporphyrinic complexes of Copper (II) and Zinc (II). microwave-assisted synthesis, spectral characterization and cytotoxicity evaluation. *Molecules.* 2011; 16: 5604-5617.
207. Nonomura Y, Yoshioka N, Inoue H. ESR studies on distortion in the macrocyclic ring of copper (II) chlorophylls. *Inorg. Chim. Acta.* 1994; 224:181-184.
208. Hoffmann SK, Goslar J, Lijewski S, Zalewska A. EPR and ESE of CuS₄ complex in Cu(dmit)₂: g-factor and hyperfine splitting correlation in tetrahedral Cu-sulfur complexes. *J Magn Reson.* 2013; 236: 7-14.
209. Ethirajan M, Joshi P, William WH 3rd, Ohkubo K, Fukuzumi S, Pandey RK. Remarkable regioselective position-10 bromination of bacteriopyropheophorbide-a and ring-B reduced pyropheophorbide-a. *Org Lett.* 2011; 13: 1956-1959.
210. Tamiaki H, Kotegawa Y, Mizutani K. Rotational deviation of 3-acetyl group from cyclic tetrapyrrole pi-plane in synthetic bacteriochlorophyll-a analogs by 20-substitution. *Bioorg Med Chem Lett.* 2008; 18: 6037-6040.

211. Tamiaki H, Ariki N, Yasuda S, Miyatake T, Oba T. Synthesis of 20-iodochlorophyll derivatives and their properties including reactivity, electronic absorption, and self-aggregation. *Tetrahedron*. 2014; 70: 9768-9775.
212. Usacheva M, Swaminathan SK, Kirtane AR, Panyam J. Enhanced photodynamic therapy and effective elimination of cancer stem cells using surfactant-polymer nanoparticles. *Mol Pharm*. 2014; 11: 3186-3195.
213. Ding H, Yu H, Dong Y, Tian R, Huang G, Boothman DA, Sumer BD, Gao J. Photoactivation switch from type II to type I reactions by electron-rich micelles for improved photodynamic therapy of cancer cells under hypoxia. *J Control Release*. 2011; 156: 276-280.
214. Park W, Bae BC, Na K. A highly tumor-specific light-triggerable drug carrier responds to hypoxic tumor conditions for effective tumor treatment. *Biomaterials*. 2016; 77: 227-234.
215. Yuan F, Dellian M, Fukumura D, Leunig M, Berk DA, Torchilin VP, Jain RK. Vascular permeability in a human tumor xenograft: molecular size dependence and cutoff size. *Cancer Res*. 1995; 55: 3752-3756.
216. Patel S, Sharma KK, Datta A. Competitive binding of Chlorin p6 and Dansyl-L-Proline to Sudlow's site II of human serum albumin. *Spectrochim Acta A Mol Biomol Spectrosc*. 2015; 138: 925-931.
217. Fasano M, Curry S, Terreno E, Galliano M, Fanali G, Narciso P, Notari S, Ascenzi P. The extraordinary ligand binding properties of human serum albumin. *IUBMB Life*. 2005; 57: 787-796.

218. Ahmed-Ouameur A, Diamantoglou S, Sedaghat-Herati MR, Nafisi Sh, Carpentier R, Tajmir-Riahi HA. The effects of drug complexation on the stability and conformation of human serum albumin: protein unfolding. *Cell Biochem Biophys*. 2006; 45: 203-213.
219. Bal W, Sokołowska M, Kurowska E, Faller P. Binding of transition metal ions to albumin: sites, affinities and rates. *Biochim Biophys Acta*. 2013; 1830: 5444-5455.
220. Moi MK, DeNardo SJ, Meares CF. Stable bifunctional chelates of metals used in radiotherapy. *Cancer Res*. 1990; 50(3 Suppl): 789s-793s.
221. da Silveira VC, Caramori GF, Abbott MP, Gonçalves MB, Petrilli HM, da Costa Ferreira AM. Oxindole-Schiff base copper(II) complexes interactions with human serum albumin: spectroscopic, oxidative damage, and computational studies. *J Inorg Biochem*. 2009; 103: 1331-1341.
222. Azzellini MA, Abbott MP, Machado A, Miranda MT, Garcia LC, Caramori GF, Gonçalves MB, Petrilli HM, Ferreira A. Interactions of diimine copper (II) complexes with albumin: competitive equilibria, promoted oxidative damage and DFT studies. *J. Braz. Chem. Soc*. 2010; 21: 1303-1317.
223. Tabassum S, Al-Asbahy WM, Afzal M, Arjmand F. Synthesis, characterization and interaction studies of copper based drug with Human Serum Albumin (HSA): spectroscopic and molecular docking investigations. *J Photochem Photobiol B*. 2012; 114: 132-139.
224. Marzano C, Pellei M, Tisato F, Santini C. Copper complexes as anticancer agents. *Anticancer Agents Med Chem*. 2009; 9: 185-211.

225. Sari MA, Battioni JP, Dupré D, Mansuy D, Le Pecq JB. Interaction of cationic porphyrins with DNA: importance of the number and position of the charges and minimum structural requirements for intercalation. *Biochemistry*. 1990; 29: 4205-4215.
226. Karunakaran SC, Ramaiah D, Schulz I, Epe B. Study of the mode and efficiency of DNA binding in the damage induced by photoactivated water soluble porphyrins. *Photochem Photobiol*. 2013; 89: 1100-1105.
227. Chitrapriya N, Park J, Wang W, Lee H, Kim SK. Photo-induced DNA scission by Cu(ii)-meso-tetrakis(n-N-methylpyridiniumyl)porphyrins (n = 2, 3, 4) and their binding modes to supercoiled DNA. *Metallomics*. 2012; 4: 417-421.
228. Benov L. Photodynamic therapy: current status and future directions. *Med Princ Pract*. 2015; 24 Suppl 1:14-28.
229. Rosenkranz AA, Jans DA, Sobolev AS. Targeted intracellular delivery of photosensitizers to enhance photodynamic efficiency. *Immunol Cell Biol*. 2000; 78: 452-464.
230. Begum G, Dube A, Joshi PG, Gupta PK, Joshi NB. Chlorin p6 preferentially localizes in endoplasmic reticulum and golgi apparatus and inhibits Ca²⁺ release from intracellular store. *J. Photochem. Photobiol. B: Biology*. 2009; 95: 177-184.
231. Mulherkar R, Goud AP, Wagle AS, Naresh KN, Mahimkar MB, Thomas SM, Pradhan SA, Deo MG. Establishment of a human squamous cell carcinoma cell line of the upper aero-digestive tract. *Cancer Lett*. 1997; 118: 115-121.

232. Zölzer F, Hillebrandt S, Streffer C. Radiation induced G1-block and p53 status in six human cell lines. *Radiother Oncol.* 1995; 37: 20-28.
233. Basu-Modak S, Tyrrell RM. Singlet oxygen: a primary effector in the ultraviolet A/near-visible light induction of the human heme oxygenase gene. *Cancer Res.* 1993; 53: 4505-4510.
234. Grossweiner LI, Patel AS, Grossweiner JB. Type I and type II mechanisms in the photosensitized lysis of phosphatidylcholine liposomes by hematoporphyrin. *Photochem Photobiol.* 1982; 36: 159-167.
235. Mojzisoava H, Bonneau S, Maillard P, Berg K, Brault D. Photosensitizing properties of chlorins in solution and in membrane-mimicking systems. *Photochem Photobiol Sci.* 2009; 8: 778-787.
236. Moan J, Sommer S. Oxygen dependence of the photosensitizing effect of hematoporphyrin derivative in NHIK 3025 cells. *Cancer Res.* 1985; 45: 1608-1610.
237. Mitchell JB, McPherson S, DeGraff W, Gamson J, Zabell A, Russo A. Oxygen dependence of hematoporphyrin derivative-induced photoinactivation of Chinese hamster cells. *Cancer Res.* 1985; 45: 2008-2011.
238. Henderson BW, Fingar VH. Relationship of tumor hypoxia and response to photodynamic treatment in an experimental mouse tumor. *Cancer Res.* 1987; 47: 3110-3114.
239. Liu Y, Chen W, Wang S, Joly AG. Investigation of water-soluble x-ray luminescence nanoparticles for photodynamic activation. *Appl. Phys. Lett.* 2008; 92: 043901.

240. Chapman JD, Stobbe CC, Arnfield MR, Santus R, Lee J, McPhee MS. Oxygen dependency of tumor cell killing in vitro by light-activated Photofrin II. *Radiat Res.* 1991; 126: 73-79.
241. Moan J, Sommer S. Oxygen dependence of the photosensitizing effect of hematoporphyrin derivative in NHIK 3025 cells. *Cancer Res.* 1985; 45: 1608-1610.
242. Anderson DL, Mirzayans R, Andrais B, Siegbahn EA, Fallone BG, Warkentin B. Spatial and temporal distribution of γ H2AX fluorescence in human cell cultures following synchrotron-generated X-ray microbeams: lack of correlation between persistent γ H2AX foci and apoptosis. *J Synchrotron Radiat.* 2014; 21: 801-810.
243. Takahashi A, Matsumoto H, Yuki K, Yasumoto J, Kajiwara A, Aoki M, Furusawa Y, Ohnishi K, Ohnishi T. High-LET radiation enhanced apoptosis but not necrosis regardless of p53 status. *Int J Radiat Oncol Biol Phys.* 2004; 60: 591-597.
244. Zhang J, Shen L, Sun LQ. The regulation of radiosensitivity by p53 and its acetylation. *Cancer Lett.* 2015; 363: 108-118.
245. Turchi JJ, Henkels KM, Zhou Y. Cisplatin-DNA adducts inhibit translocation of the Ku subunits of DNA-PK. *Nucleic Acids Res.* 2000; 28: 4634-4641.
246. Biston MC, Joubert A, Charvet AM, Balosso J, Foray N. In vitro and in vivo optimization of an anti-glioma modality based on synchrotron X-ray photoactivation of platinated drugs. *Radiat Res.* 2009; 172: 348-358.

247. Bayart E, Pouzoulet F, Calmels L, Dadoun J, Allot F, Plagnard J, Ravanat JL, Bridier A, Denozière M, Bourhis J, Deutsch E. Enhancement of IUdR Radiosensitization by Low-Energy Photons Results from Increased and Persistent DNA Damage. *PLoS One*. 2017; 12: e0168395.
248. Guicciardi ME, Leist M, Gores GJ. Lysosomes in cell death. *Oncogene*. 2004; 23: 2881.
249. Lan YY, Londoño D, Bouley R, Rooney MS, Hacohen N. Dnase2a deficiency uncovers lysosomal clearance of damaged nuclear DNA via autophagy. *Cell Rep*. 2014; 9:180-192.
250. Roos WP, Kaina B. DNA damage-induced cell death: from specific DNA lesions to the DNA damage response and apoptosis. *Cancer Lett*. 2013; 332: 237-248.
251. Battogtokh G, Liu HB, Bae SM, Chaturvedi PK, Kim YW, Kim IW, Ahn WS. Synthesis of di-pyropheophorbide-a-platinum (II) complex and the in vitro cytotoxicity against TC-1 tumor cells. *J Porphyr Phthalocyanines*. 2012; 16: 1024-1031.
252. Lum CT, Yang ZF, Li HY, Wai-Yin Sun R, Fan ST, Poon RT, Lin MC, Che CM, Kung HF. Gold(III) compound is a novel chemocytotoxic agent for hepatocellular carcinoma. *Int J Cancer*. 2006; 118: 1527-1538.
253. Tu S, Wai-Yin Sun R, Lin MC, Tao Cui J, Zou B, Gu Q, Kung HF, Che CM, Wong BC. Gold (III) porphyrin complexes induce apoptosis and cell cycle arrest and inhibit tumor growth in colon cancer. *Cancer*. 2009; 115: 4459-4469.

254. Zhang JX, Zhou JW, Chan CF, Lau TC, Kwong DW, Tam HL, Mak NK, Wong KL, Wong WK. Comparative studies of the cellular uptake, subcellular localization, and cytotoxic and phototoxic antitumor properties of ruthenium(II)-porphyrin conjugates with different linkers. *Bioconjug Chem*. 2012; 23: 1623-1638.
255. Kamat JP, Bloor KK, Devasagayam TP. Chlorophyllin as an effective antioxidant against membrane damage in vitro and ex vivo. *Biochim Biophys Acta*. 2000; 1487: 113-127.
256. Lanfer-Marquez UM, Barros RM, Sinnecker P. Antioxidant activity of chlorophylls and their derivatives. *Food Res Int*. 2005; 38: 885-891.
257. Boya P, Kroemer G. Lysosomal membrane permeabilization in cell death. *Oncogene*. 2008; 27: 6434.
258. Jungwirth U, Kowol CR, Keppler BK, Hartinger CG, Berger W, Heffeter P. Anticancer activity of metal complexes: involvement of redox processes. *Antioxid Redox Signal*. 2011; 15: 1085-1127.
259. Suntharalingam K, Mendoza O, Duarte AA, Mann DJ, Vilar R. A platinum complex that binds non-covalently to DNA and induces cell death via a different mechanism than cisplatin. *Metallomics*. 2013; 5: 514-523.
260. Rixe O, Fojo T. Is cell death a critical end point for anticancer therapies or is cytostasis sufficient? *Clin Cancer Res*. 2007; 13: 7280-7287.
261. Kornienko A, Mathieu V, Rastogi SK, Lefranc F, Kiss R. Therapeutic agents triggering nonapoptotic cancer cell death. *J Med Chem*. 2013; 56: 4823-4839.
262. Badisa RB, Kumar SS, Mazzio E, Haughbrook RD, Allen JR, Davidson MW, Fitch-PyeCA, Goodman CB. N-acetyl cysteine mitigates the acute effects of

- cocaine-induced toxicity in astroglia-like cells. *PLoS One*. 2015; 10: e0114285.
263. Focaccetti C, Bruno A, Magnani E, Bartolini D, Principi E, Dallaglio K, Bucci EO, Finzi G, Sessa F, Noonan DM, Albini A. Effects of 5-fluorouracil on morphology, cell cycle, proliferation, apoptosis, autophagy and ROS production in endothelial cells and cardiomyocytes. *PLoS One*. 2015; 10: e0115686.
264. Farah ME, Sirotkin V, Haarer B, Kakhniashvili D, Amberg DC. Diverse protective roles of the actin cytoskeleton during oxidative stress. *Cytoskeleton (Hoboken)*. 2011; 68: 340-354.
265. Kavčič N, Pegan K, Turk B. Lysosomes in programmed cell death pathways: from initiators to amplifiers. *Biol Chem*. 2016; 398: 289-301.
266. Ahamad MS, Siddiqui S, Jafri A, Ahmad S, Afzal M, Arshad M. Induction of apoptosis and antiproliferative activity of naringenin in human epidermoid carcinoma cell through ROS generation and cell cycle arrest. *PLoS One*. 2014; 9: e110003
267. Wimardhani YS, Suniarti DF, Freisleben HJ, Wanandi SI, Siregar NC, Ikeda MA. Chitosan exerts anticancer activity through induction of apoptosis and cell cycle arrest in oral cancer cells. *J Oral Sci*. 2014; 56: 119-126.
268. Akladios FN, Andrew SD, Parkinson CJ. Selective induction of oxidative stress in cancer cells via synergistic combinations of agents targeting redox homeostasis. *Bioorg Med Chem*. 2015; 23: 3097-3104.

269. Galadari S, Rahman A, Pallichankandy S, Thayyullathil F. Reactive oxygen species and cancer paradox: To promote or to suppress? *Free Radic Biol Med.* 2017; 104: 144-164.

Appendix

Appendix A. Supplementary Information

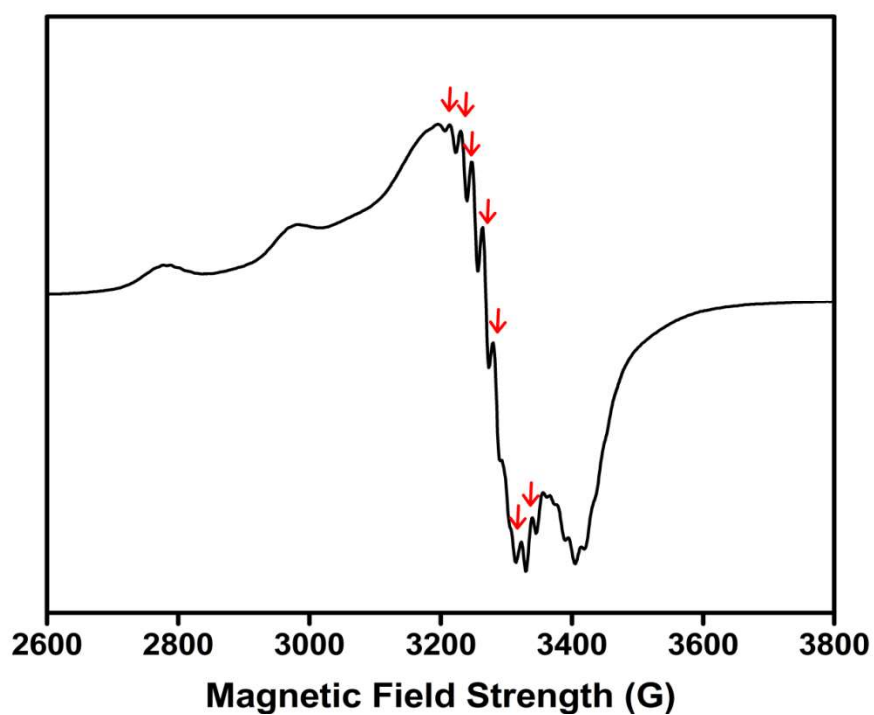


Figure A.1. ESR spectrum of Copper- Chlorophyllin at 100 K in methanol. Arrows represents the hyperfine splitting in g_{\perp} region.

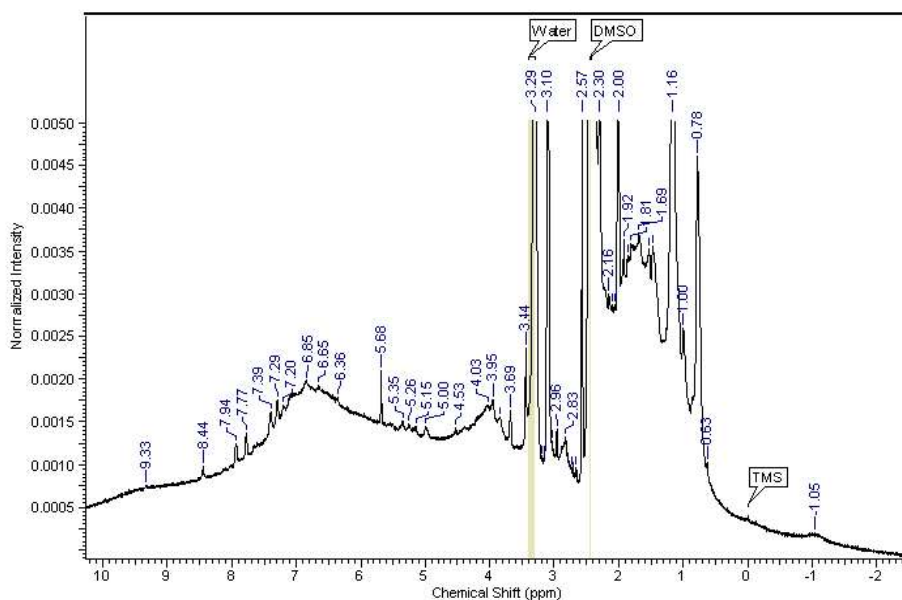


Figure A.2. 500MHz ^1H NMR spectrum of ICp₆-Cu

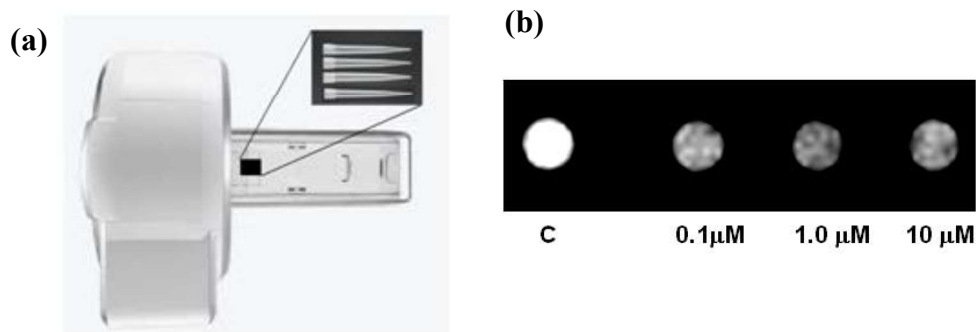


Figure A.3. Magnetic resonance (T2-weighted) images of sample tubes which were filled with tissue phantom (solidified gelatin-agarose) containing 0, 0.1, 1.0 and 10 micromolar iodo-chlorin p6 copper complex. (a) Experimental setup of MRI imaging setup (b) The circular spot represents cross section image (slice) of each tube. [Source: Indian patent application No. 4912/MUM/2015, filed on 29 Dec. 2015: A Metal complex of chlorophyll derivative for magnetic resonance imaging and photodynamic therapy.]

Appendix B. Research Output (Reprint of Publications)

PAPER

Cite this: *RSC Adv.*, 2016, 6, 75782Synthesis and characterization of photodynamic activity of an iodinated Chlorin p_6 copper complex†Paromita Sarbadhikary,^a Alok Dube^{*ab} and Pradeep Kumar Gupta^{ab}

We report the synthesis of a new iodinated Chlorin p_6 copper complex (IC p_6 -Cu) and its efficacy for photodynamic treatment (PDT) of cancer cells. The metal complex is obtained by reacting Chlorin p_6 (C p_6) with copper iodide (CuI). The complex formation results in a shift in the Q absorption band of C p_6 from 663 nm to 634 nm and X-ray fluorescence of the complex showed the presence of both copper and iodine. FTIR and EPR spectroscopy suggests that the copper is attached to C p_6 at the two adjacent carboxylic groups. Studies on the photochemical generation of singlet oxygen (1O_2) and other reactive oxygen species (ROS) using fluorescence probes revealed that IC p_6 -Cu acts predominantly through the type I process. PDT of oral cancer cells with IC p_6 -Cu (10 μ M, 3 h) and red light (630 \pm 20 nm, \sim 12 J cm $^{-2}$) led to \sim 90% phototoxicity. Furthermore, in contrast to C p_6 , the phototoxicity induced by IC p_6 -Cu is not significantly affected under hypoxic conditions.

Received 30th May 2016

Accepted 31st July 2016

DOI: 10.1039/c6ra14026b

www.rsc.org/advances

Introduction

Photodynamic therapy (PDT) of cancer utilizes a photosensitive drug referred to as a photosensitizer (PS) and irradiation with light of appropriate wavelengths to induce tumor damage *via* generation of ROS.^{1,2} The absorption of light by the PS results in its excitation to a singlet excited state ($^1PS^*$) which undergoes inter system crossing (ISC), to form a relatively long lived excited-triplet state (3PS). The 3PS can undergo two types of reactions defined as type I and type II process. In type I process, the 3PS reacts with surrounding substrates involving transfer of hydrogen atom or electron to result in formation of ion radicals or ROS such as superoxide ($O_2^{\cdot-}$) and hydroxyl radicals ($\cdot OH$). In type II process, 3PS reacts directly with 3O_2 through transfer of energy to result in formation of 1O_2 .³ It is generally accepted that the 1O_2 is the major species responsible for PDT efficacy of most PSs.³ Although, PSs which acts *via* type I process have also been considered useful for PDT.⁴

Currently, PSs such as Photofrin, ALA, Foscan and Verteporfin have been clinically approved and some more PSs are under clinical trials.¹ For improving, the tumor selectivity and efficacy of PDT, PSs complexed to metal ions have been actively

explored.⁵ The insertion of metal in PS provides two significant advantages. First, the metal through heavy atom effect can enhance triplet state yield of the PS and second because of cationic charge the PS can accumulate more efficiently in cancer cells.^{5,6} In addition, metal based PS have received considerable attention for potential use as multimodal agents in tumor imaging and therapy such as magnetic resonance imaging (MRI), positron emission tomography (PET) imaging,^{7,8} X-ray photon activation therapy (PAT),⁹⁻¹¹ and radiotherapy of cancer.¹²

Our earlier studies in hamster cheek pouch model have shown that C p_6 , a water soluble chlorophyll derivative is a promising PS for PDT of tumors.^{13,14} C p_6 is anionic due to the presence of carboxylic groups in the molecule. For further developing its use as a multimodal agent for PDT and PAT, we have explored the possibility to obtain its metal complex by chelation of metal ion at the carboxylic groups. We choose CuI to prepare complex with C p_6 because of several considerations; copper complexes are potential agents for chemo and radiotherapy of cancer,^{15,16} iodinated compounds are useful for PAT and contrast imaging,^{17,18} the radioisotopes of both copper and iodine can provide modality for PET and single-photon emission computed tomography (SPECT) imaging of tumor,^{19,20} and both copper and iodine are considered to be relatively well tolerated metabolically because these are required as trace elements.²¹ In this report, we describe the synthesis of an iodinated-Chlorin p_6 copper complex (IC p_6 -Cu) and its characterization as a PS. Unlike the tetrapyrrole copper complex reported in literatures which are metallated at the pyrrole NH, the copper in IC p_6 -Cu is attached to the carboxylic groups. Studies on 1O_2 and ROS generation showed that IC p_6 -Cu predominantly acts through type I photochemical pathway and

^aHomi Bhabha National Institute, Raja Ramanna Centre for Advanced Technology, Indore 452013, India

^bLaser Biomedical Application and Instrumentation Division, Raja Ramanna Centre for Advanced Technology, Indore 452013, India. E-mail: okdube@rrcat.gov.in; Tel: +91 731 2488437

† Electronic supplementary information (ESI) available: Table S1: percent cytotoxicity of IC p_6 -Cu in dark at 10–15 μ M concentration; Fig. S1: absorption spectra of IC p_6 -Cu in buffer and methanol; Table S2: Absorption characteristics of IC p_6 -Cu in methanol and buffer; Table S3: octanol/water partition coefficient of C p_6 and IC p_6 -Cu. See DOI: 10.1039/c6ra14026b

as compared to Cp_6 , it is more effective for PDT of cancer cells under hypoxic condition.

Results and discussion

Formation of complex of Cp_6 with CuI

The changes in the absorption spectrum of Cp_6 upon addition of different concentrations of CuI are shown in Fig. 1a. With the increase in the concentration of CuI, the absorbance of Q band at 663 nm gradually decreases with concomitant appearance of a new band at 634 nm. This is also accompanied by a decrease in absorbance at the Soret band (400 nm) and the minor Q band (500 nm). Beyond 5 μ M concentration of CuI which is equimolar to Cp_6 , no further changes were observed. This indicates that the complex formation between Cp_6 and CuI is completed at 1 : 1 stoichiometry. Complex thus formed displays a Soret band with sharp peak at 408 nm with a shoulder at 380

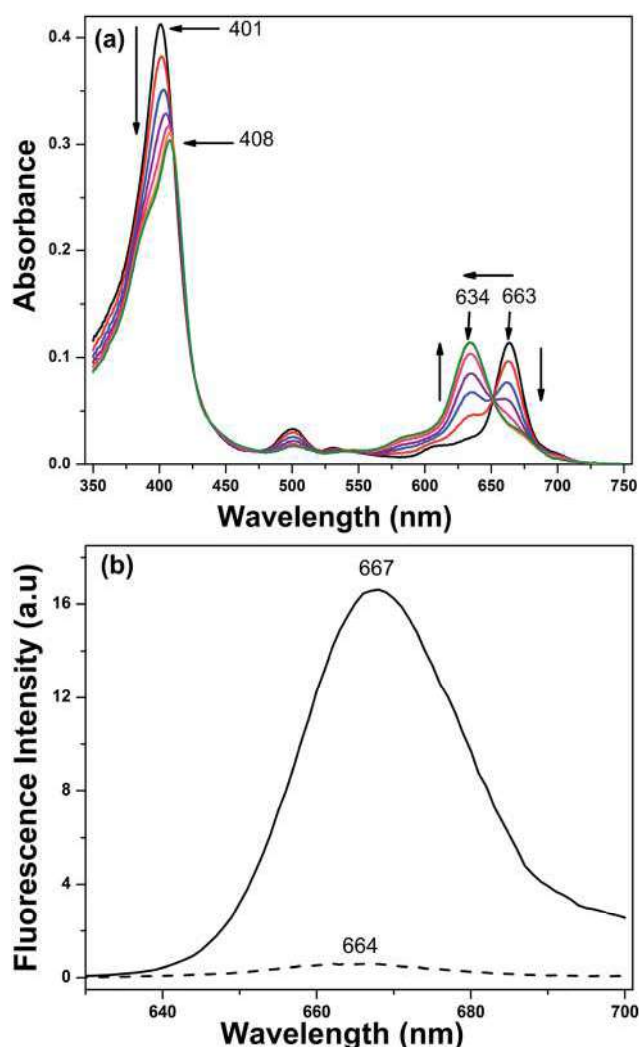


Fig. 1 (a) Changes in absorption spectra of 5 μ M Cp_6 solid line (black) with subsequent increase in concentration of CuI in methanol; 1 μ M (red), 2 μ M (blue), 3 μ M (purple), 4 μ M (pink), 5 μ M (orange), 10 μ M (green). (b) Fluorescence spectra ($\lambda_{\text{ext}} = 400$ nm) of Cp_6 (solid line) and $ICp_6\text{-Cu}$ (dashed line) in methanol.

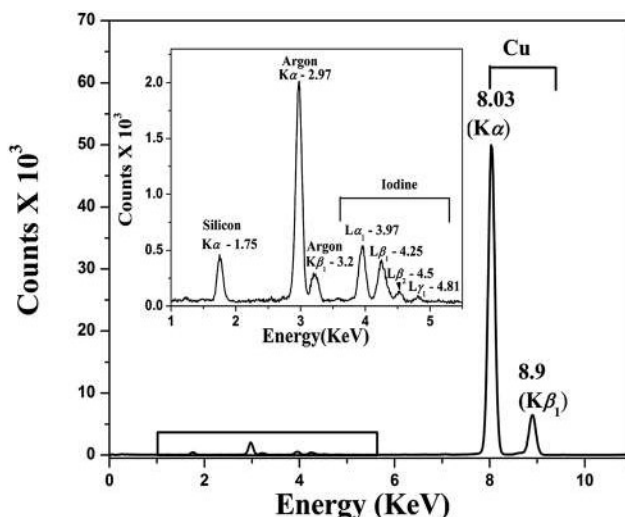


Fig. 2 XRF spectrum of $ICp_6\text{-Cu}$ showing characteristic X-ray emission lines for copper and iodine (inset). X-ray emission lines for copper at 8.03 keV (K_{α}) and 8.9 keV ($K_{\beta 1}$) and for iodine at 3.97, 4.25, 4.5, 4.81 keV ($L_{\alpha 1}$, $L_{\beta 1}$, $L_{\beta 2}$, $L_{\gamma 1}$). The peak at 2.97 keV and 3.2 keV is due to atmospheric argon and the peak at 1.75 keV is due to silicon wafer on which powdered sample is deposited.

nm, a minor Q_x band at 500 nm and the major Q_y band at 634 nm. The molar extinction coefficient (ϵ) of the complex at Q_y band is almost same ($24\,000\text{ M}^{-1}\text{ cm}^{-1}$) as that for Cp_6 , whereas at the Soret band the ϵ is $\sim 30\%$ lower ($63\,000\text{ M}^{-1}\text{ cm}^{-1}$). In Fig. 1b the fluorescence spectra of Cp_6 and $ICp_6\text{-Cu}$ complex are shown. As compared to Cp_6 , the fluorescence yield for $ICp_6\text{-Cu}$ is reduced by a factor of ~ 16 . This is because of insertion of paramagnetic copper in Cp_6 and is consistent with the quenching of fluorescence reported for copper complex of some chlorophyll derivatives.²² X-Ray fluorescence (XRF) spectrum of the complex (Fig. 2) shows the characteristic X-ray emission lines for copper at 8.03 keV (K_{α}) and 8.9 keV ($K_{\beta 1}$) and for iodine at 3.97, 4.25, 4.5, 4.81 keV ($L_{\alpha 1}$, $L_{\beta 1}$, $L_{\beta 2}$, $L_{\gamma 1}$). This also confirms the presence of both copper and iodine in the complex.

Position of copper and iodine in the complex

Generally, metallation of tetrapyrrole compounds leads to insertion of metal atom in the centre of the tetrapyrrole ring by substitution with two hydrogen at the pyrrole NH. However for tetrapyrrolic compound containing carboxylic groups, it has been reported that the insertion of metal ion at pyrrole NH is not favoured due to preferential binding of metal ion at the carboxylic groups through coordination.²³ Cp_6 contains three carboxylic groups, one is as propionate side chain at C17 position and remaining two are adjacently attached at C13 and C15 position.

To confirm the coordination site of copper in $ICp_6\text{-Cu}$, its Electron Paramagnetic Resonance (EPR) spectrum was measured at 100 K in methanol (Fig. 3). The spectrum is anisotropic with characteristic intense absorption in high field region and well resolved hyperfine splitting in low field region. It is important to mention that the EPR spectra of copper

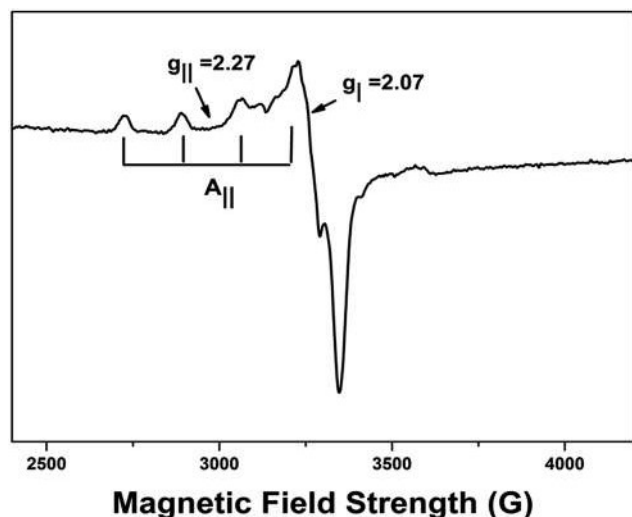


Fig. 3 EPR spectrum of $\text{ICp}_6\text{-Cu}$ at 100 K in methanol.

complexes of porphyrin and chlorophyll derivatives show characteristic multiple super hyperfine splitting in g_{\perp} region due to interaction of unpaired electron of metal with neighbouring nitrogen nucleus.²⁴ Such hyperfine splitting is absent in the EPR spectrum of $\text{ICp}_6\text{-Cu}$ which suggests that copper is not coordinated to pyrrole nitrogen. This is in agreement with a previous report on platinum(III) complex of hematoporphyrin where the EPR spectra of the complex having platinum attached to tetrapyrrole ring and the one in which platinum is attached to side chain carboxylic groups show similar difference.²⁵ Further, the value of g -tensor and hyperfine splitting can be used to infer the coordination of copper with oxygen, nitrogen or sulphur based on the Peisach–Blumberg correlation.²⁶ The value of g_{\parallel} (2.27) and A_{\parallel} ($174 \times 10^{-4} \text{ cm}^{-1}$) obtained from the EPR spectrum are within the range of copper coordinating with oxygen atom. These findings unequivocally confirm that copper is attached to carboxylic groups. The nature of metal ligand bond can be predicted by calculating covalency parameter α^2 from the following equation.

$$\alpha_{\text{Cu}}^2 = -(A_{\parallel}/0.036) + (g_{\parallel} - 2.003) + 3/7(g_{\parallel} - 2.003) + 0.04$$

A value of $\alpha^2 = 0.5$ indicates complete covalent nature and if the value is 1.0 it indicates ionic bonding.²⁷ The value of α^2 for $\text{ICp}_6\text{-Cu}$ is 0.82 which indicates that the nature of bonding between ligand and copper has some covalent character. Moreover, the value of α^2 is higher than that reported for copper chlorophyll derivatives for Cu–N bond (0.63–0.68). This also suggests that the nature of copper–ligand bond in $\text{ICp}_6\text{-Cu}$ is significantly different.²⁴

In Fig. 4, we show the FTIR spectra of $\text{ICp}_6\text{-Cu}$ and Cp_6 . The FTIR spectrum of Cp_6 is very similar to the FTIR spectrum of Chlorin e6 reported by Gladkova *et al.*²⁸ This is to be expected because the chemical structure of Ce6 is similar to Cp_6 except the presence of one extra methylene ($-\text{CH}_2-$) group at C15 position. The FTIR spectra of Cp_6 in the region

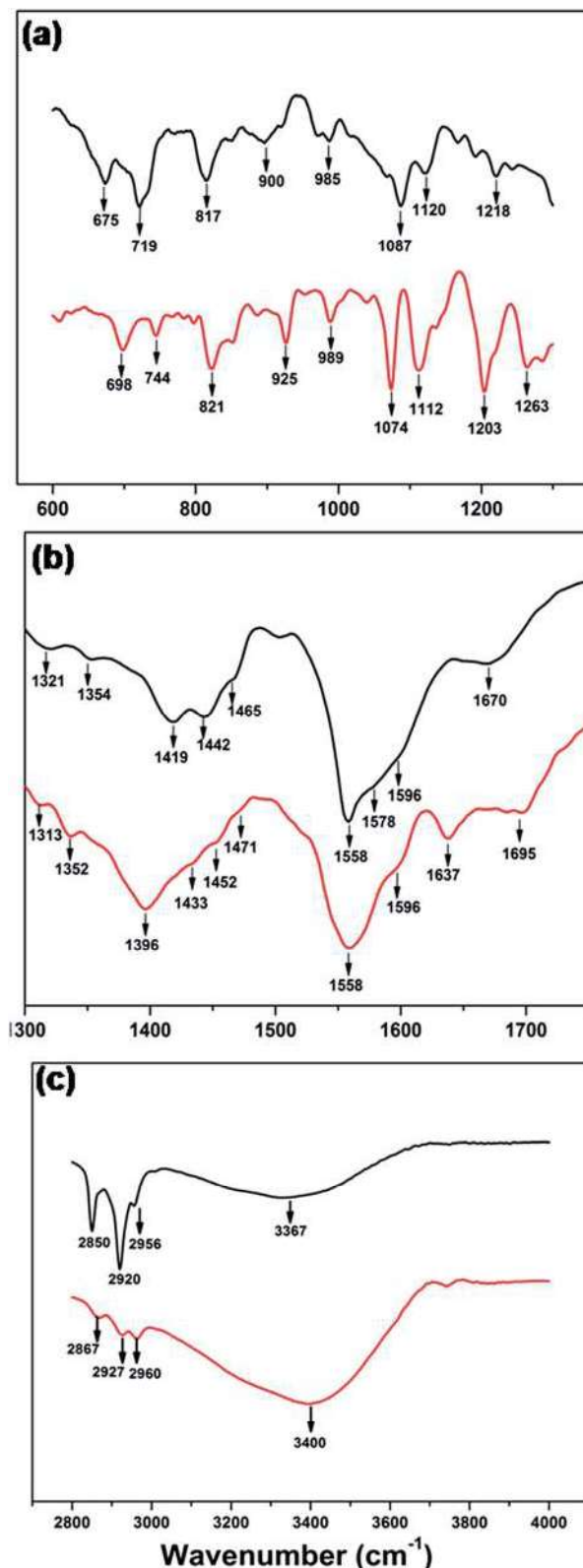


Fig. 4 FTIR spectra of Cp_6 (black) and $\text{ICp}_6\text{-Cu}$ (red) plotted in the range of (a) 600–1250 cm^{-1} , (b) 1300–1750 cm^{-1} and (c) 2800–4000 cm^{-1} .

from 1300 cm^{-1} to 1750 cm^{-1} shows absorption bands due to C=O and COO stretching vibrations of the carboxylic groups (Fig. 4b). The major changes observed upon complex

formation are as follows (1) appearance of three new bands for $\text{ICp}_6\text{-Cu}$, one at 1637 cm^{-1} which is characteristic of CO-metal stretch^{29,30} and two prominent bands at 1112 cm^{-1} and 1203 cm^{-1} due to CO stretching. In a previous report, the appearance of later two bands have been shown as direct proof for the formation of chelate of copper and zinc with C13 keto group of chlorophyll.³⁰ (2) The COO vibration bands in Cp_6 arise as a prominent band resolved into a peak at 1558 cm^{-1} and shoulders at 1578 cm^{-1} and 1596 cm^{-1} . This band in $\text{ICp}_6\text{-Cu}$ is broad and one of the band at 1578 cm^{-1} disappeared. (3) The CO vibrations of C13 and C15 carboxylic group (at 1419 cm^{-1} and 1321 cm^{-1}) are shifted to lower frequency at 1396 cm^{-1} and 1313 cm^{-1} , respectively. These observations suggest that the two adjacent carboxylic groups at C13 and C15 position participate in formation of the metal coordination complex. The third carboxylic group at C17 propionic side chain is likely to remain attached to sodium because the region $\sim 1740\text{ cm}^{-1}$ which is characteristic of C=O vibrational band of this carboxylate show no change. In addition to above noted changes, the FTIR spectrum of $\text{ICp}_6\text{-Cu}$ also revealed an intense broad absorption band at $\sim 3400\text{ cm}^{-1}$ (Fig. 4c) which is expected to appear due to the presence of water molecules in the co-ordination sphere of copper.²⁹

The mass spectrum of $\text{ICp}_6\text{-Cu}$ is shown in Fig. 5. The molecular ion containing copper is identified by the characteristic isotopic splitting at 724.12 m/z and 726.12 m/z which represent loss of C17 carboxylate from the molecule. The largest peak observed at 701 m/z shows no such splitting and represents molecular ion with loss of metal and vinyl side group. This also rules out the possibility of iodination at vinyl group of Cp_6 . Previous reports on iodination of chlorophyll derivatives have

shown that of the three *meso* positions at C5, C10, and C20, the *meso* position at C20 is relatively more reactive towards halogenation.³¹ The selective iodination of chlorophyll-a derivatives at C20 position has been reported in several studies.^{31–33} The replacement of *meso*-H with halogen in tetrapyrrole ring is identified by disappearance of characteristic proton peak in the ^1H NMR spectrum. However, because the presence of paramagnetic copper leads to broadening of lines, a well resolved ^1H NMR spectrum of $\text{ICp}_6\text{-Cu}$ could not be obtained. Based on evidence gathered from XRF (Fig. 2), EPR (Fig. 3), FTIR (Fig. 4), and HRMS (Fig. 5), the proposed chemical structure of $\text{ICp}_6\text{-Cu}$ is shown in Fig. 6. The site of iodination is indicated as most probable based on literature discussed above and needs to be confirmed.

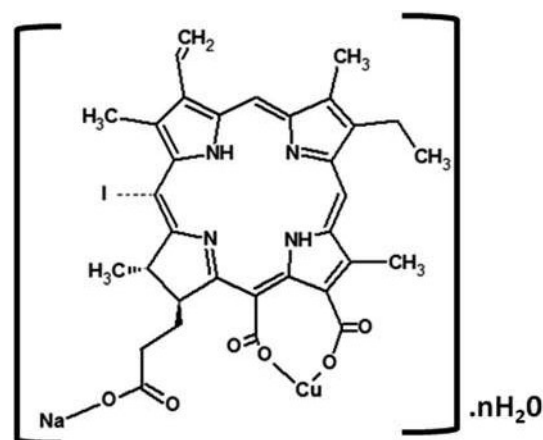


Fig. 6 Proposed structure of $\text{ICp}_6\text{-Cu}$. The probable site of iodine is indicated by dashed bond.

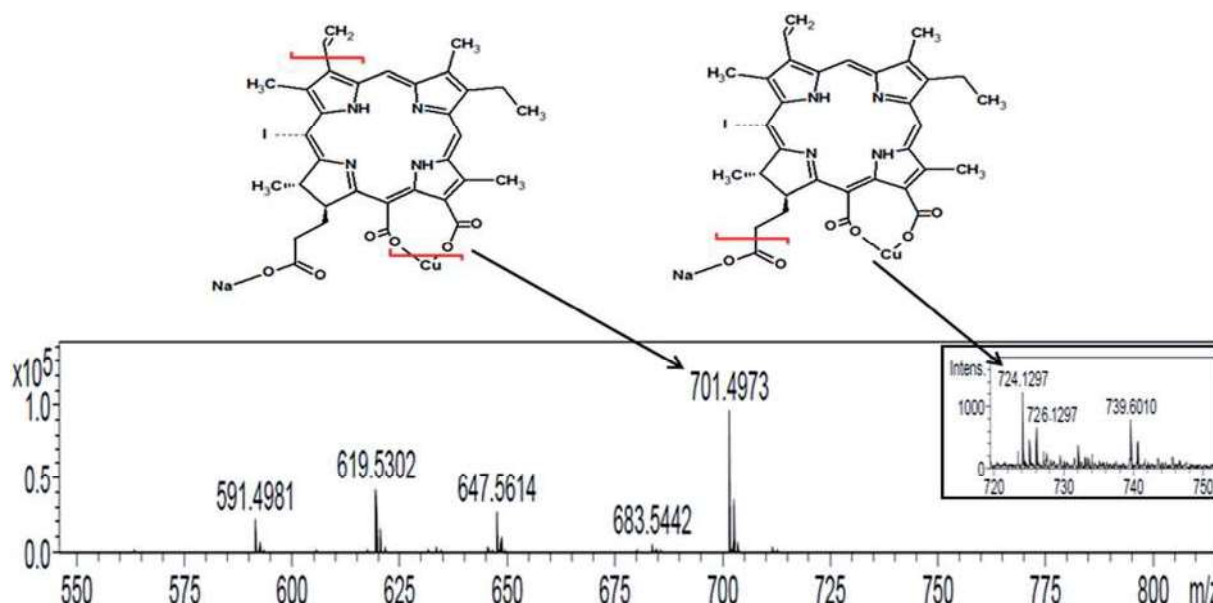


Fig. 5 Mass spectrum of $\text{ICp}_6\text{-Cu}$ in the range $550\text{--}800\text{ m/z}$, showing molecular ion at 701 m/z (after loss of Cu and a vinyl (C_2H_3) from parent molecule) and spectrum magnified in the range $720\text{--}750$ (inset) to show peaks of isotopic ion at 724.12 m/z and 726.12 m/z due to presence of natural isotopes of copper ^{63}Cu and ^{65}Cu (after loss of $-\text{COONa}$ from parent molecule).

$^1\text{O}_2$ and ROS generation efficiency of $\text{ICp}_6\text{-Cu}$

The $^1\text{O}_2$ and ROS generation efficiency of $\text{ICp}_6\text{-Cu}$ was measured using three different fluorescence probes Singlet Oxygen Sensor green (SOSG), 2',7'-dichlorodihydrofluorescein (DCFH) and 3'-(*p*-aminophenyl) fluorescein (APF). SOSG is specific for $^1\text{O}_2$,³⁴ DCFH detects total ROS³⁵ and APF can detect $\cdot\text{OH}$ as well as $^1\text{O}_2$.³⁶ The $^1\text{O}_2$ or ROS generated in photochemical reaction converts these probes into highly fluorescent species. The change in fluorescence intensity (F_t/F_0) of SOSG and DCF as a function of irradiation time were plotted to compare the $^1\text{O}_2$ and ROS generation capability of Cp_6 (Fig. 7a) and $\text{ICp}_6\text{-Cu}$ (Fig. 7b). For $\text{ICp}_6\text{-Cu}$, the relative increase in SOSG fluorescence is ~ 10 times less than that for Cp_6 (Fig. 7a

and b), which suggest that as compared to Cp_6 , the efficiency of $\text{ICp}_6\text{-Cu}$ to produce $^1\text{O}_2$ is reduced. It may be noted here that while the presence of heavy atom in the PS can improve the yield of $^1\text{O}_2$ by increasing the efficiency of ISC from $^1\text{PS}^*$ to the ^3PS ,^{5,37} any shortening of excited state life time would result in a loss of $^1\text{O}_2$ generation ability of the PS.³⁸ Copper being paramagnetic results in reduction in excited state lifetime because of which most of the copper complex of porphyrin and chlorophyll derivatives reported in literature are photodynamically inactive.^{22,39} In contrast to copper, the presence of iodine on the PS

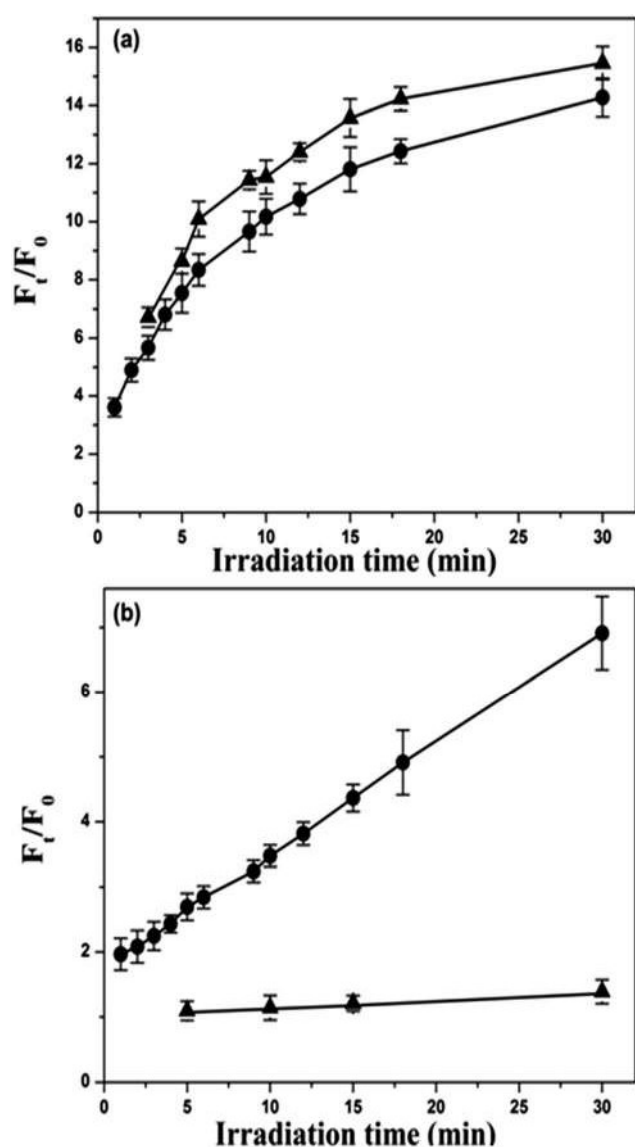


Fig. 7 Cp_6 (a) and $\text{ICp}_6\text{-Cu}$ (b) induced photodynamic generation of $^1\text{O}_2$ and total ROS plotted as increase in fluorescence (F_t/F_0) of SOSG (upside arrow) and DCF (circle), respectively. The solution of PS and fluorescence probe in phosphate buffer (pH 7.4) was irradiated with red light (3.5 mW cm^{-2}) for different time periods. Each data point represents mean \pm SD value of three independent experiments.

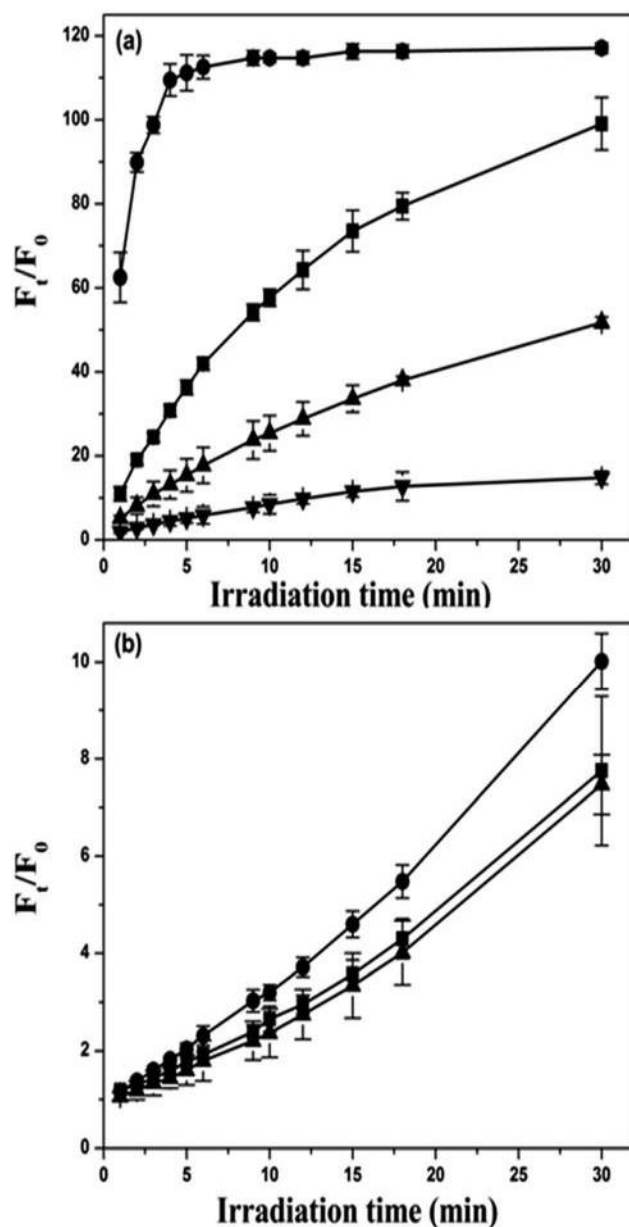


Fig. 8 Cp_6 (a) and $\text{ICp}_6\text{-Cu}$ (b) induced photodynamic generation of ROS plotted as increase in fluorescence (F_t/F_0) of APF in H_2O (square), D_2O (circle) and in H_2O containing NaN_3 at 5 mM (upward arrow) and 10 mM (downward arrow) concentration. The solution of PS and fluorescence probe in phosphate buffer (pH 7.4) was irradiated with red light (3.5 mW cm^{-2}) for different time periods. Each data point represents mean \pm SD value of three independent experiments.

usually increase the yield of ^3PS and results in enhancement in the $^1\text{O}_2$ yield.^{40,41} However, iodine depending on its position on the PS molecule can also results in shortening of ^3PS life time and decrease in $^1\text{O}_2$ yield.³⁷ This is due to the fact that the orbital overlap between tetrapyrrole ring and iodine atom facilitates non-radiative decay of the ^3PS .³⁷ Thus the decrease in $^1\text{O}_2$ yield of $\text{ICp}_6\text{-Cu}$ can be attributed to the presence of both copper and iodine. It is also pertinent to note that PS with short life time of ^3PS can be photodynamically active *via* type I process. For example, copper octaethylbenzochlorin despite short ^3PS life time induce efficient photosensitization *via* type I process and has been found useful for PDT of cancer both in *in vitro* and *in vivo* studies.⁴²

The total ROS generation ability of $\text{ICp}_6\text{-Cu}$ was measured using fluorescence probe dichlorofluorescein (DCF). Fig. 7b show changes in DCF fluorescence induced by photoactivation of Cp_6 or $\text{ICp}_6\text{-Cu}$ as a function of irradiation time. Here, the increase in DCF fluorescence is higher in Cp_6 than for $\text{ICp}_6\text{-Cu}$. However, since the yield of $^1\text{O}_2$ for $\text{ICp}_6\text{-Cu}$ is low, the increase

in DCF fluorescence is mainly due to generation of other ROS. Whereas for Cp_6 , the increase in DCF fluorescence is contributed predominantly by generation of $^1\text{O}_2$ as seen in SOSG assay (Fig. 7b). These results show that the generation of other ROS by $\text{ICp}_6\text{-Cu}$ is substantially higher than the generation of $^1\text{O}_2$. To confirm this, increase in DCF fluorescence was monitored in the presence of Sodium azide (NaN_3), a quencher of $^1\text{O}_2$. However, it was observed that the addition of NaN_3 to DCF solution led to alteration in fluorescence of DCF which interfered with the measurement. In a previous report, fluorescence probe APF together with NaN_3 and D_2O (enhances life time of $^1\text{O}_2$) has been effectively used to distinguish type I or type II photochemical mechanism of PDT drug.³⁶ For Cp_6 and $\text{ICp}_6\text{-Cu}$, the changes in fluorescence of APF (F_t/F_0) as a function of irradiation time is shown in Fig. 8a and b. For Cp_6 , the increase in fluorescence of APF is inhibited to $\sim 50\%$ and $\sim 90\%$ in the presence of 5 mM and 10 mM NaN_3 , respectively and it is enhanced by a factor of ~ 4 in D_2O (Fig. 8a). These results show that $^1\text{O}_2$ is predominant species in photodynamic action of Cp_6

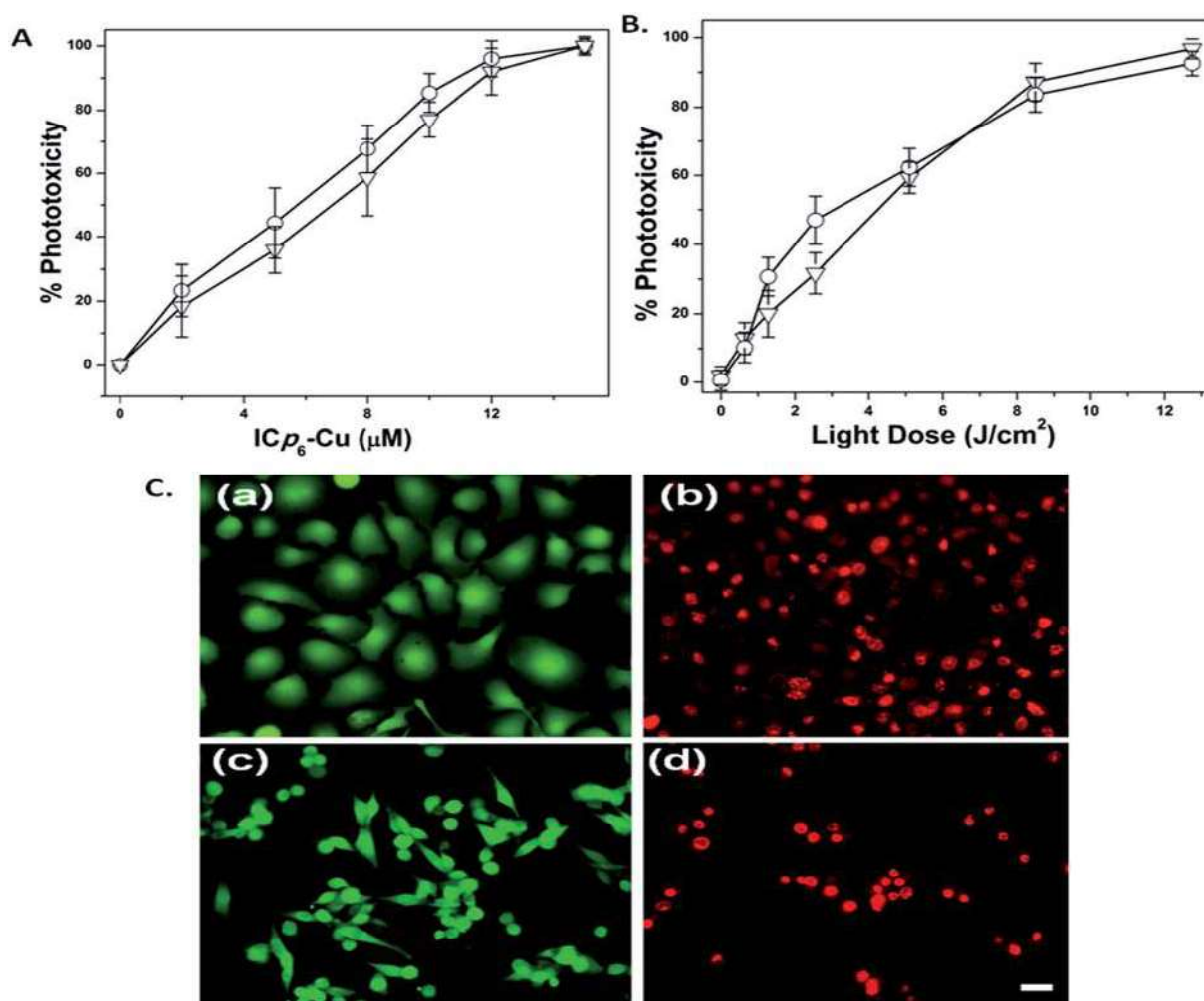


Fig. 9 (A) Concentration dependent phototoxicity of $\text{ICp}_6\text{-Cu}$ in NT8e (open circle) and 4451 (open downward arrow) at fixed light dose of 7 J cm^{-2} . (B) Phototoxicity of $\text{ICp}_6\text{-Cu}$ in NT8e (open circle) and 4451 (open downward arrow) cell lines as a function of light dose, (C) fluorescence microphotograph of NT8e and 4451 cells in control (a, c) and at 24 h after PDT (b, d) with light dose of 8 J cm^{-2} showing live and dead cells after staining with live/dead fluorescence probe, scale bar = $20 \mu\text{m}$.

which is also consistent with our previous report.⁴³ In contrast, for ICp_6 -Cu induced increase in APF fluorescence is not significantly influenced by either NaN_3 or D_2O (Fig. 8b). These results clearly show that the photodynamic action of ICp_6 -Cu is mediated predominantly *via* type I process.

Phototoxicity of ICp_6 -Cu in cancer cells

The dependence of phototoxicity of ICp_6 -Cu on the concentration and the light dose in two oral cancer cell lines (4451 and NT8e) is shown in Fig. 9A and B, respectively. Treatment of cells with various concentration of ICp_6 -Cu followed by light exposure at fixed light dose of 7 J cm^{-2} led to concentration dependent increase in phototoxicity (Fig. 9A). At $10\text{ }\mu\text{M}$ ICp_6 -Cu, the phototoxicity was $\sim 80\%$ which increased further upto $\sim 95\%$ at higher concentrations. However, there was also some ($\sim 10\%$) dark toxicity in both cell lines beyond $10\text{ }\mu\text{M}$ ICp_6 -Cu (see ESI Table S1†). Based on this, $10\text{ }\mu\text{M}$ concentration of ICp_6 -Cu was selected to study the dependence of phototoxicity on light dose. As shown in Fig. 9B, PDT with $10\text{ }\mu\text{M}$ ICp_6 -Cu led to a dose dependent increase in phototoxicity. The phototoxicity was $\sim 60\%$ at light dose of 5 J cm^{-2} and increased to $\sim 90\%$ at 12 J cm^{-2} . The changes in cell viability observed after staining with LIVE/DEAD kit is shown in Fig. 9C. In both NT8e and 4451, while all cells in control appear green (Fig. 9C(a) and (c)), the cells after PDT take up the red fluorescence due to loss of cell viability (Fig. 9C(b) and (d)). The morphological changes in two cell lines after PDT are shown in Fig. 10A. The cells in control appear healthy with intact cell membrane (Fig. 10A(a) and (c)). At 3 h after PDT (LD_{90} dose), almost all NT8e cells show formation of membrane blebs whereas, 4451 cells display damaged plasma membrane and swelling, indicated by arrows (Fig. 10A(b) and (d)). The percentages of live, apoptotic and necrotic cells in control and PDT treated cells for the two cell lines is shown in Fig. 10B. As expected, the mode of cell death in

NT8e and 4451 cells occurred mainly *via* apoptosis and necrosis, respectively. This is due to the fact that the tumor suppressor p53 gene responsible for apoptotic death is wild type in NT8e cells whereas it is mutated in 4451 cells.⁴⁴ These results are consistent with our earlier report on the mode of cell death induced by Cp_6 and its histamine conjugate in these cell lines.⁴⁴ The influence of quenchers of 1O_2 (NaN_3 , L-histidine) and free radicals (dimethyl sulfoxide (DMSO), D-mannitol) on ICp_6 -Cu induced phototoxicity is shown in Fig. 11. As compared to control, the level of phototoxicity is significantly reduced in the presence of all the quenchers. Treatment of cells with quenchers alone under similar conditions did not result in any toxicity. It is important to mention that NaN_3 and histidine can

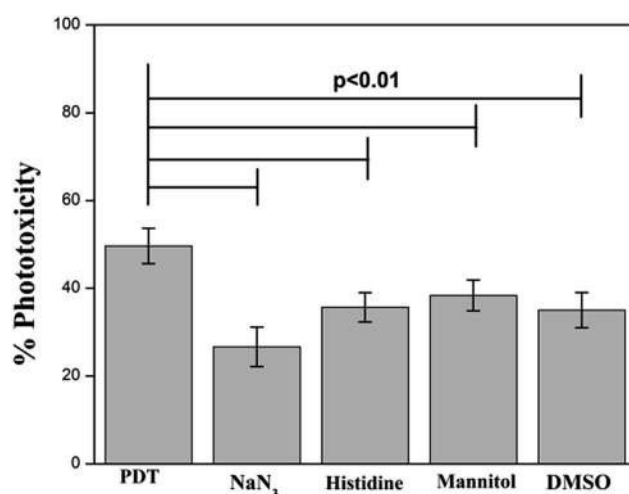


Fig. 11 Percent phototoxicity induced by ICp_6 -Cu in NT8e cells in absence and presence of quenchers of ROS. The cells were subjected to PDT using light dose of 4 J cm^{-2} which led to $\sim 50\%$ phototoxicity in absence of any quencher. Data are mean \pm SD of three independent experiments in triplicates.

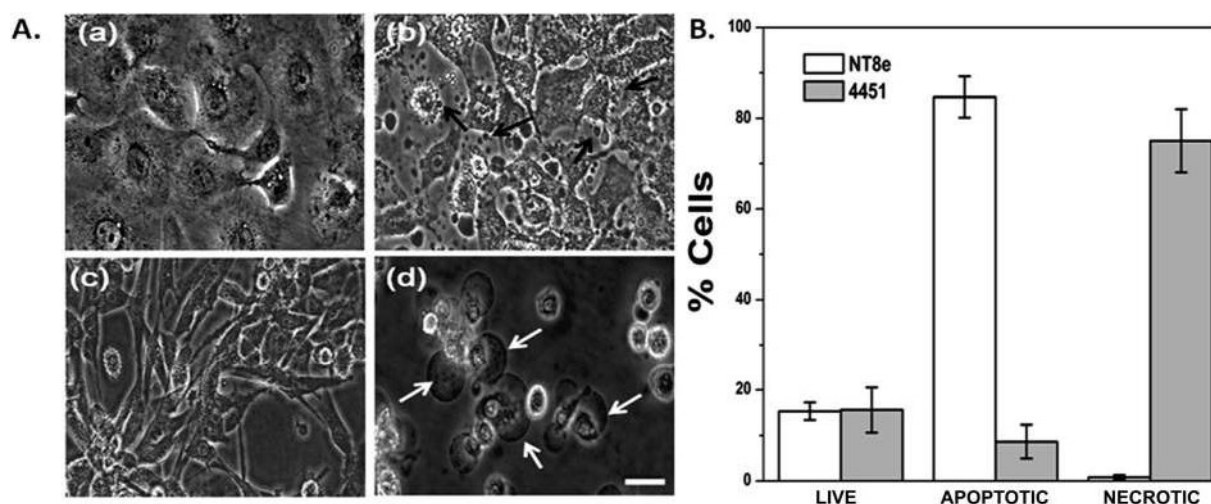


Fig. 10 (A) Microphotograph of NT8e and 4451 cells in control (a, c) and at 3 h after PDT (b, d) showing cell morphology in phase contrast, magnification $20\times$, scale bar – $20\text{ }\mu\text{m}$. Arrows showing formation of apoptotic blebs in NT8e (b), and plasma membrane damage and swelling in 4451 (d). (B) Percentage of live, apoptotic and necrotic cells at 3 h after PDT in NT8e (white bar) and 4451 (shaded bar) cell lines. Light dose used in A and B, is 8 J cm^{-2} . Data are mean \pm SD of three independent experiments in triplicates.

also quench $\cdot\text{OH}$ radicals.⁴⁵ However, since the rate constant of NaN_3 and histidine for reaction with $\cdot\text{OH}$ radicals is almost same, both should lead to inhibition of phototoxicity to the same extent. In contrast, the inhibition of phototoxicity by NaN_3 is higher than that for histidine (Fig. 11) which correlates with their efficiency to quench $^1\text{O}_2$.⁴⁵ This suggests that in addition to free radicals, $^1\text{O}_2$ also contributes to the phototoxicity of $\text{ICp}_6\text{-Cu}$. The contribution of $^1\text{O}_2$ to the phototoxicity of $\text{ICp}_6\text{-Cu}$ was not expected because studies on ROS generation in aqueous solution showed that the $^1\text{O}_2$ generation ability of $\text{ICp}_6\text{-Cu}$ is very low (Fig. 7b and 8b). Here it is pertinent to note that the efficacy of the PS to generate $^1\text{O}_2$ also depends on its environment. In aqueous solution, the PSs with higher hydrophobicity tend to aggregate and show decrease in $^1\text{O}_2$ generation efficiency whereas the localization of PS in cellular membrane results in dis-aggregation and increase in photosensitization *via* type II process.^{46,47} A comparison of the absorption spectra of $\text{ICp}_6\text{-Cu}$ in aqueous medium and methanol (see ESI Fig. S1†) suggested that it is slightly aggregated in aqueous condition as indicated by significant blue shift and broadening of Soret and Q bands (see ESI Table S2†). Further, the octanol : water partition coefficient (Log P) of $\text{ICp}_6\text{-Cu}$ is 0.94 which is ~ 2 times higher than Cp_6 (see ESI Table S3†). Therefore due to higher hydrophobicity, $\text{ICp}_6\text{-Cu}$ can localize efficiently in cellular membrane.⁴⁸ This and the fact that the life time of $^1\text{O}_2$ in cellular environment is considerably longer (10 μs) as compared to that in aqueous media (3.5 μs)⁴⁹ can explain the contribution of $^1\text{O}_2$ to the phototoxicity for $\text{ICp}_6\text{-Cu}$.

Phototoxicity under hypoxic conditions

Availability of molecular oxygen is an important factor for the PDT efficacy of majority of PSs. It has been reported that low oxygen concentration can reduce the $^1\text{O}_2$ yield and compromise the PDT efficacy.^{50–52} Alternatively, studies on PDT of human tumor xenografts with meta-tetrahydroxyphenylchlorin have shown that photochemical process leading to radical formation can work better under hypoxic condition.⁵² Several recent studies also showed that PS which act *via* type I photochemical mechanism induce better PDT efficacy under hypoxia. For example, phototoxicity mediated by methylene blue encapsulated in polymer nanoparticle⁵³ and 5,10,15,20-tetrakis(meso-hydroxyphenyl)porphyrin incorporated in electron-rich poly(2-(diisopropylamino)ethyl methacrylate) micelles is not affected under hypoxia.⁵⁴ Similarly, photodynamic release of doxorubicin induced by chondroitin sulfate conjugated Pheophorbide-*a* *via* type I mechanism led to higher toxicity under hypoxic conditions than that under normoxic conditions.⁵⁵

The effect of hypoxia on the phototoxicity of $\text{ICp}_6\text{-Cu}$ and Cp_6 at LD_{50} and LD_{80} dose (for normoxic condition) is shown in Fig. 12. For Cp_6 , hypoxia led to decrease in phototoxicity by almost 1/2 ($\sim 30\%$ and 40%). In contrast, phototoxicity induced by $\text{ICp}_6\text{-Cu}$ under normoxic and hypoxic condition show no significant difference. Thus, as compared to Cp_6 , $\text{ICp}_6\text{-Cu}$ led to higher phototoxicity under hypoxic condition. It is important to mention that hypoxia has also been shown to affect the phototoxicity of bacteriopheophorbide which acts only *via*

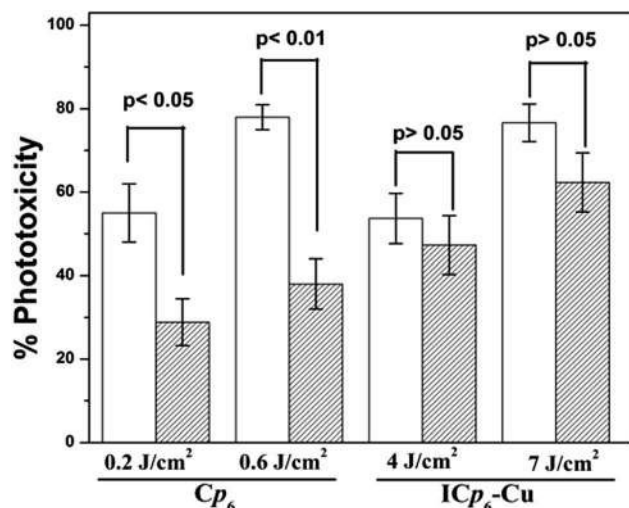


Fig. 12 Percent phototoxicity of $\text{ICp}_6\text{-Cu}$ and Cp_6 in NT8e cells after PDT under normoxia (white bar) and hypoxia (shaded bar). The light dose used corresponds to LD_{50} and LD_{80} for cells under normoxic condition. Data are mean \pm SD of three independent experiments in triplicates.

oxygen radicals, whereas the phototoxicity of Type II PS Npe_6 was found to be unaffected.⁵⁶ The possible reason for PDT efficacy of Npe_6 under hypoxia was referred to superior ability of its ^3PS to interact with oxygen.⁵⁶ Although in our studies, as compared to Cp_6 which also acts mainly *via* $^1\text{O}_2$, the ability of $\text{ICp}_6\text{-Cu}$ to act *via* type I process appear important for its PDT efficacy under hypoxic condition.

Conclusions

To summarize, we have synthesized iodinated Chlorin p_6 copper complex for PDT applications. EPR and FTIR studies suggest that copper is attached to the two adjacent carboxylic groups through co-ordination and the site of iodination may be *meso* position in the tetrapyrrole ring. Results of studies on the photodynamic efficacy of $\text{ICp}_6\text{-Cu}$ show that it is able to induce high phototoxicity in cancer cells and the phototoxicity is not affected significantly under hypoxic condition. In conclusion, results suggest that the novel copper complex is useful for PDT of cancer.

Experimental section

Preparation of Cp_6 and $\text{ICp}_6\text{-Cu}$

Chlorophyll-*a* was extracted from dried spirulina powder and converted into Cp_6 following the procedure described by Hooper *et al.*⁵⁷ Cp_6 was converted into $\text{ICp}_6\text{-Cu}$ according to our patent specifications (no. 4912/MUM/2015). In brief, the solution of Cp_6 and CuI in methanol : acetonitrile (1 : 10 v/v) was mixed at equimolar concentration at room temperature. The solvent was partially evaporated to result in precipitation of the metal complex. The precipitates were collected by centrifugation (6000g, 10 min). The metal complex was further purified by silica column chromatography using methanol : acetonitrile

solvent system. The stock solution of ICp_6 -Cu was prepared in ethanol : PEG (400) : water (20 : 30 : 50) to prevent aggregation and contamination of the concentrated solution during storage.

Spectroscopy

The UV/VIS absorption spectra of the Cp_6 and ICp_6 -Cu were recorded from 350–750 nm, at 1 nm bandpass on a Cintra-20 spectrophotometer (GBC, Australia). The fluorescence emission spectra of Cp_6 and ICp_6 -Cu were recorded on a Fluorolog-2 spectrofluorometer (Spex, USA) by setting excitation wavelength at ~400 nm, scan range from 500–700 nm and band pass of ~1.7 nm and ~3.7 nm for excitation and emission slits, respectively. FTIR spectra were recorded on a spectrometer model (FTLA 2000 MB 104) using powdered sample deposited on Zinc Selenide window. The X band EPR spectrum of ICp_6 -Cu was recorded on Spectrometer model JES – (Jeol, Japan) at 100 K. Methanol was used as solvent.

The X-ray fluorescence of ICp_6 -Cu was monitored using microprobe XRF beamline (BL-16) of the synchrotron radiation source (Indus-2).⁵⁸ For preparation of sample for XRF, 10 μ l concentrated solution of ICp_6 -Cu in methanol was applied on a piece of Silicon wafer and air dried. Monochromatic X-ray of energy 12.0 keV (beam size 4 mm \times 4 mm) was used to excite the fluorescence from the sample. XRF spectra were recorded using a Vortex energy-dispersive detector (SII NanoTechnology, USA).

Cell culture

Human oral cancer cell lines NT8e derived from upper aerodigestive tract (pyriform fossa) and 4451 derived from recurrent tumor in the lower jaw were obtained from ACTREC, Mumbai and INMAS, Delhi respectively. Both the cell lines were maintained in Dulbecco's Modified Eagle's Medium (DMEM) containing 4.5 g L⁻¹ glucose, 4 mM L-glutamine, 25 mM of HEPES, antibiotics (streptomycin, nystatin, penicillin) and 10% fetal bovine serum. The cells were grown at 37 °C in a humidified incubator (Galaxy R, RS Biotech) under 5% CO₂ + 95% air atmosphere. The cells were harvested by trypsinization and seeded in 35 mm Petri dishes or 96 well plate. After 18 h of incubation, the cells in exponential phase were used for the experiments.

Irradiation

For assay of ROS generation and phototoxicity with ICp_6 -Cu, the irradiation was done using an LED lamp (Dia 4 cm) emitting red light (630 \pm 20 nm). To ensure homogenous illumination, a diffuser glass plate was placed below the LED lamp. For similar studies with Cp_6 , a diode laser source (Thorlabs, USA) emitting red light (660 \pm 5 nm) was used. Power of light was measured using a power meter model AN/2 (Ophir) and the power density was kept nearly same (~3.5 mW cm⁻²) for both the light source.

Generation of ¹O₂ and ROS

To determine the ¹O₂ and other ROS yield for ICp_6 -Cu and Cp_6 we used three different fluorescence probes; SOSG and APF both from Invitrogen (USA) and 2',7'-dichlorodihydrofluorescein diacetate (DCFH-DA) from Sigma, USA. SOSG reacts specifically with ¹O₂ to result in formation of highly fluorescent endoperoxide product.³⁴ DCFH-DA is a fluorescence probe for detection of intracellular generation of broad range of ROS such as O₂^{•-} and [•]OH, hydrogen peroxide (H₂O₂) and ¹O₂. In cells, DCFH-DA is first converted enzymatically into DCFH which upon reaction with ROS is oxidized into green fluorescent DCF. For detection of ROS in solution, DCFH-DA is chemically converted into DCFH by hydrolysis according to the protocol described by Bourré *et al.*³⁵ For this, DCFH-DA was mixed with 0.01 N NaOH in absolute ethanol and the solution was kept at room temperature for 30 min to allow hydrolysis. After neutralization with 25 mM sodium phosphate buffer (pH 7.4), the solution was stored on ice in dark until use. The fluorescence probe APF has been used to detect [•]OH and ¹O₂ both.³⁶ APF upon reaction with [•]OH and ¹O₂ is converted to a fluorescent form due to the cleavage of the aminophenyl ring from fluorescein ring system.

For monitoring generation of ¹O₂ and other ROS, ICp_6 -Cu or Cp_6 (5 μ M) was added to 3.5 ml sodium phosphate buffer (pH 7.4) in a plastic petridish (3.5 cm dia). After addition of the fluorescence probe, the solution was irradiated with narrow bandwidth light of appropriate wavelengths 630 \pm 20 nm or 660 \pm 5 nm for photoactivation of ICp_6 -Cu or Cp_6 respectively, using light source described in section 'Irradiation'. The irradiation was done in diffused dim light and the solution was continuously stirred during irradiation. At different time interval, 200 μ l aliquot was withdrawn and fluorescence was measured on a spectrofluorometer. The wavelength used for fluorescence excitation of SOSG, DCF and APF were 485 nm, 488 nm and 490 nm respectively. The change in fluorescence intensity at 530 nm, 525 nm and 515 nm for SOSG, DCF and APF respectively were plotted as F_t/F_0 vs. irradiation time, where F_0 and F_t are the fluorescence intensity before and after irradiation.

Photosensitizer treatment

The growth medium from 35 mm petri dishes or 96 well plate containing cell monolayer was removed and replaced with fresh media containing ICp_6 -Cu. After incubation for 3 h at 37 °C in a humidified CO₂ incubator in dark, the growth medium was aspirated and the cell monolayer was washed twice using plain medium (DMEM without serum). After adding fresh growth medium, the cells were subjected to photodynamic treatment. For concentration dependent PDT experiments, concentration of ICp_6 -Cu was varied from 2–15 μ M and cells were irradiated with a fixed light dose of 7 J cm⁻². For experiments where the light dose was varied, cells were treated with fixed concentration of 10 μ M and irradiated with different light doses (0–12.7 J cm⁻²). For PDT under hypoxia, a fresh growth medium which was de-oxygenated by bubbling nitrogen gas for 1 h was used. The de-oxygenated medium was added to the cells after PS treatment and the cells were transferred to humidified

incubator (ESCO) under controlled environment (1% O₂ + 5% CO₂) at 37 °C for 1 h. To maintain the hypoxia during irradiation, the 96 well plate containing cells was placed in a sealed glass chamber and the chamber was flushed with nitrogen. For studies with quenchers of ROS (NaN₃, histidine, DMSO and mannitol), the cells prior to the photodynamic treatment were incubated for 1 h in growth medium containing specified concentration of each quencher and then irradiated at LD₅₀ light dose.

MTT assay

The dark and light induced cytotoxicity was determined using MTT (3-[4,5-dimethylthiazol-2-yl]-2,5 diphenyl tetrazolium bromide) assay.⁵⁹ Briefly, at 24 h after PDT, the growth medium of the treated cells was replaced with plain medium containing 0.5 mg ml⁻¹ MTT and the cells were incubated at 37 °C for 3 h in dark. After incubation, the medium was removed and 100 µl of DMSO was added and kept for 15 min to solubilise the formazan crystals formed within the cells. A microplate reader (Power Wave 340, Bio-tek instruments Inc., USA) was used to read the absorbance of the samples at 570 nm with reference wavelength at 690 nm. The percent phototoxicity was calculated with respect to the absorbance value in control samples. The cells treated with ICp₆-Cu but not exposed to light were used as dark control. In each experiment at least four replicates were used and mean value was used to determine the percent cytotoxicity.

Cell morphology and viability

PDT-induced cell damage and loss of cell viability was examined by bright field and fluorescence microscopy at 20× magnification using inverted microscope (Olympus, Japan). For cell viability, the cells after 24 h of PDT were stained with LIVE/DEAD cytotoxicity kit (Invitrogen, Molecular Probes, Eugene OR). The kit contains a green fluorescent dye calcein, which is retained in the cytoplasm by live cells and a DNA binding red fluorescent dye ethidium homodimer, that enter the cells only upon loss of plasma membrane integrity. After staining the cells were washed with phosphate buffered saline (PBS) and observed under fluorescence microscope using blue (450–480 nm) and green excitation (510–550 nm).

Assessment of apoptosis and necrosis

To determine the percentage of cells undergoing apoptosis and necrosis, the cells after PDT were stained with Hoechst 33 342 (10 µg ml⁻¹) and propidium iodide (PI, 2.5 µg ml⁻¹) for 5 min, washed twice with PBS and observed under inverted microscope (Olympus, Japan). PI is a cell impairment dye and can only stain the cells in which plasma membrane integrity is lost due to necrotic damage. Hoechst 33 342 is cell permeable, which stains nuclei and allows visualization of chromatin condensation and fragmentation of apoptotic cells. The blue fluorescence of Hoechst 33342 and red fluorescence of PI was visualized using excitation with 380–400 nm, barrier filter 440 nm. Images were recorded using a color CCD camera model 'Prog Res Cfscan' and a ProgRes Capture Pro Software (Jenoptik,

Germany). A minimum of 500 cells were counted in each group and percentage of apoptotic, necrotic and live cells was calculated from the total number of cells counted.

Disclosure

Alok Dube, Paromita Sarbadhikary and Pradeep Kumar Gupta are named patent inventors for Indian Patent Application no. 4912/MUM/2015 titled 'A metal complex of chlorophyll derivative for magnetic resonance imaging and photodynamic therapy', filed on December 29, 2015.

Acknowledgements

We are thankful to Dr G. S. Lodha and Dr M. K. Tiwari for helping with XRF measurement, Dr B. Jain for helping with FTIR measurements at our centre and Dr M. Shanmugam, IIT Bombay, Mumbai for EPR measurement. We also thank Dr B. S. Dwarakanath, INMAS, Delhi and Dr U. M. Warawdekar, ACTREC, Mumbai for providing oral cancer cell lines. S Paromita thanks Homi Bhabha National Institute, Mumbai for senior research fellowship.

References

- 1 P. Agostinis, K. Berg, K. A. Cengel, T. H. Foster, A. W. Girotti, S. O. Gollnick, S. M. Hahn, M. R. Hamblin, A. Juzeniene, D. Kessel, M. Korbelik, J. Moan, P. Mroz, D. Nowis, J. Piette, B. C. Wilson and J. Golab, *Ca-Cancer J. Clin.*, 2011, **61**, 250–281.
- 2 R. R. Allison and K. Moghissi, *Photodiagn. Photodyn. Ther.*, 2013, **10**, 331–341.
- 3 A. P. Castano, T. N. Demidova and M. R. Hamblin, *Photodiagn. Photodyn. Ther.*, 2004, **1**, 279–293.
- 4 Y. M. Riyad, S. Naumov, S. Schastak, J. Griebel, A. Kahnt, T. Häupl, J. Neuhaus, B. Abel and R. Hermann, *J. Phys. Chem. B*, 2014, **118**, 11646–11658.
- 5 L. B. Josefsen and R. W. Boyle, *Met.-Based Drugs*, 2008, **2008**, 276109.
- 6 L. Benov, *Med. Princ. Pract.*, 2015, **24**, 14–28.
- 7 R. K. Pandey, N. S. James, Y. Chen, J. Missert and M. Sajjad, *Methods Mol. Biol.*, 2010, **635**, 223–259.
- 8 H. U. Rashid, M. N. Umar, K. Khan, M. N. Anjum and M. Yaseen, *J. Struct. Chem.*, 2014, **55**, 910–915.
- 9 J. Gastaldo, Z. Bencokova, C. Massart, A. Joubert, J. Balosso, A. M. Charveta and N. Foraya, *J. Synchrotron Radiat.*, 2011, **18**, 456–463.
- 10 T. Ishizumi, K. Aizawa, T. Tsuchidaa, T. Okunakaa and H. Katoa, *Photodiagn. Photodyn. Ther.*, 2004, **1**, 295–301.
- 11 M. Miura, G. M. Morris, J. W. Hopewell, P. L. Micca, M. S. Makar, M. M. Nawrocky and M. W. Renner, *Br. J. Radiol.*, 2012, **85**, 443–450.
- 12 P. A. Waghorn, *J. Labelled Compd. Radiopharm.*, 2014, **57**, 304–309.
- 13 A. Dube, S. Sharma and P. K. Gupta, *Oral Oncol.*, 2006, **42**, 77–82.

- 14 A. Dube, S. Sharma and P. K. Gupta, *Oral Oncol.*, 2011, **47**, 467–471.
- 15 C. Santini, M. Pellei, V. Gandin, M. Porchia, F. Tisato and C. Marzano, *Chem. Rev.*, 2014, **114**, 815–862.
- 16 G. Hao, A. N. Singh, O. K. Oz and X. Sun, *Curr. Radiopharm.*, 2011, **4**, 109–121.
- 17 R. W. Miller, W. DeGraff, T. J. Kinsella and J. B. Mitchell, *Int. J. Radiat. Oncol., Biol., Phys.*, 1987, **13**, 1193–1197.
- 18 J. M. Widmark, *Proc. Bayl. Univ. Med. Cent.*, 2007, **20**, 408–417.
- 19 C. J. Anderson and R. Ferdani, *Cancer Biother. Radiopharm.*, 2009, **24**, 379–393.
- 20 B. Gutfilen and G. Valentini, *BioMed Res. Int.*, 2014, **2014**, 426892.
- 21 L. Prashanth, K. K. Kattapagari, R. T. Chitturi, V. R. Baddam and L. K. Prasad, *J. NTR Univ. Health Sci.*, 2015, **4**, 75–85.
- 22 L. M. Moreira, A. Lima, R. R. S. Soares, V. R. Batistela, A. P. Gerola, N. Hioka, J. A. Bonacin, D. Severino, M. S. Baptista, A. E. H. Machado, M. R. Rodrigues, L. Codognotoa and H. P. M. Oliveira, *J. Braz. Chem. Soc.*, 2009, **20**, 1653–1658.
- 23 E. B. Fleischer, E. I. Choi, P. Hambright and A. Stose, *Inorg. Chem.*, 1964, **3**, 1284–1287.
- 24 Y. Nonomura, N. Yoshioka and H. Inoue, *Inorg. Chim. Acta*, 1994, **224**, 181–184.
- 25 G. Momekov, M. Karaivanova, I. Ugrinova, E. Pasheva, G. Gencheva, D. Tsekova, S. Arpadjan and P. R. Bontchev, *Invest. New Drugs*, 2011, **29**, 742–751.
- 26 S. K. Hoffmann, J. Goslar, S. Lijewski and A. Zalewska, *J. Magn. Reson.*, 2013, **236**, 7–14.
- 27 N. Raman, S. Ravichandran and C. Thangaraja, *J. Chem. Sci.*, 2004, **116**, 215–219.
- 28 O. L. Gladkova, M. V. Parkhats, A. N. Gorbachova and S. N. Terekhov, *Spectrochim. Acta, Part A*, 2010, **76**, 388–394.
- 29 M. Q. Zhang, Y. C. Zhu, J. G. Wu, P. Shi, R. W. Deng and Z. N. Chen, *Chem. Pap.*, 2001, **55**, 202–205.
- 30 J. Petrovic, G. Nikolic and D. Markovic, *J. Serb. Chem. Soc.*, 2006, **71**, 501–512.
- 31 M. Ethirajan, P. Joshi, W. H. William, K. Ohkubo, K. S. Fukuzumi and R. K. Pandey, *Org. Lett.*, 2011, **13**, 1956–1959.
- 32 H. Tamiaki, N. Arik, S. Yasuda, T. Miyatake and T. Oba, *Tetrahedron*, 2014, **70**, 9768–9775.
- 33 H. Tamiaki, Y. Kotegawa and K. Mizutani, *Bioorg. Med. Chem. Lett.*, 2008, **18**, 6037–6040.
- 34 A. Gollmer, J. Arnberg, F. H. Blaikie, B. W. Pedersen, T. Breitenbach, K. Daasbjerg, M. Glasius and P. R. Ogilby, *Photochem. Photobiol.*, 2011, **87**, 671–679.
- 35 L. Bourré, S. Thibaut, A. Briffaud, N. Rousset, S. Eléouet, Y. Lajat and T. Patrice, *J. Photochem. Photobiol., B*, 2002, **67**, 23–31.
- 36 M. Price, J. J. Reiners, A. M. Santiago and D. Kessel, *Photochem. Photobiol.*, 2009, **85**, 1177–1181.
- 37 F. Nifiatis, J. C. Athas, K. D. D. Gunaratne, Y. Gurung, K. M. Monette and P. J. Shivokevich, *Open Spectrosc. J.*, 2011, **5**, 1–12.
- 38 S. Mathai, T. A. Smith and K. P. Ghiggino, *Photochem. Photobiol. Sci.*, 2007, **6**, 995–1002.
- 39 M. C. DeRosa and R. J. Crutchley, *Coord. Chem. Rev.*, 2002, **233**, 351–371.
- 40 A. C. Serra, M. Pineiro, A. M. Rocha Gonsalves, M. Abrantes, M. Laranjo, A. C. Santos and M. F. Botelho, *J. Photochem. Photobiol., B*, 2008, **92**, 59–65.
- 41 S. H. Lim, C. Thivierge, P. Nowak-Sliwinska, J. Han, H. van den Bergh, G. Wagnières, K. Burgess and H. B. Lee, *J. Med. Chem.*, 2010, **53**, 2865–2874.
- 42 G. M. Garbo, V. H. Fingar, T. J. Wieman, E. B. Noakes 3rd, P. S. Haydon, P. B. Cerrito, D. H. Kessel and A. R. Morgan, *Photochem. Photobiol.*, 1998, **68**, 561–568.
- 43 B. Bose and A. Dube, *J. Photochem. Photobiol., B*, 2008, **93**, 32–35.
- 44 A. Parihar, A. Dube and P. K. Gupta, *Cancer Chemother. Pharmacol.*, 2011, **68**, 359–369.
- 45 S. Basu-Modak and R. M. Tyrrell, *Cancer Res.*, 1993, **53**, 4505–4510.
- 46 L. I. Grossweiner, A. S. Patel and J. B. Grossweiner, *Photochem. Photobiol.*, 1982, **36**, 159–167.
- 47 H. Mojziso, S. Bonneau, P. Maillard, K. Berg and D. Brault, *Photochem. Photobiol. Sci.*, 2009, **8**, 778–787.
- 48 F. M. Engelmann, S. V. Rocha, H. E. Toma, K. Araki and M. S. Baptista, *Int. J. Pharm.*, 2007, **329**, 12–18.
- 49 J. Baier, M. Maier, R. Engl, M. Landthaler and W. Bäuml, *J. Phys. Chem. B*, 2005, **109**, 3041–3046.
- 50 J. Moan and S. Sommer, *Cancer Res.*, 1985, **45**, 1608–1610.
- 51 J. D. Chapman, C. C. Stobbe, M. R. Arnfield, R. Santus, J. Lee and M. S. McPhee, *Radiat. Res.*, 1991, **126**, 73–79.
- 52 V. O. Melnikova, L. N. Bezdetnaya, D. Brault, A. Y. Potapenko and F. Guillemin, *Int. J. Cancer*, 2000, **88**, 798–803.
- 53 M. Usacheva, S. K. Swaminathan, A. R. Kirtane and J. Panyam, *Mol. Pharm.*, 2014, **11**, 3186–3195.
- 54 H. Ding, H. Yu, Y. Dong, R. Tian, G. Huang, D. A. Boothman, B. D. Sumer and J. Gao, *J. Controlled Release*, 2011, **156**, 276–280.
- 55 W. Park, B. C. Bae and K. Na, *Biomaterials*, 2016, **77**, 227–234.
- 56 M. Price, L. Heilbrun and D. Kessel, *Photochem. Photobiol.*, 2013, **89**, 683–686.
- 57 J. K. Hooper, T. W. Sery and N. Yamamoto, *Photochem. Photobiol.*, 1988, **48**, 579–582.
- 58 M. K. Tiwari, P. Gupta, A. K. Sinha, S. R. Kane, A. K. Singh, S. R. Garg, C. K. Garg, G. S. Lodha and S. K. Deb, *J. Synchrotron Radiat.*, 2013, **20**, 386–389.
- 59 T. Mosmann, *J. Immunol. Methods*, 1983, **65**, 55–63.



Contents lists available at ScienceDirect

Chemico-Biological Interactions

journal homepage: www.elsevier.com/locate/chembioint

Iodinated chlorin p_6 copper complex induces anti-proliferative effect in oral cancer cells through elevation of intracellular reactive oxygen species

Paromita Sarbadhikary ^{a, b}, Alok Dube ^{a, b, *}^a Raja Ramanna Centre for Advanced Technology, Indore, Madhya Pradesh, India^b Homi Bhabha National Institute, Training School Complex, Anushakti Nagar, Mumbai 400094, India

ARTICLE INFO

Article history:

Received 7 April 2017

Received in revised form

26 July 2017

Accepted 11 September 2017

Available online 14 September 2017

Keywords:

Anticancer drug

Chlorophyll derivative

Copper complex

Cytotoxicity

Reactive oxygen species

ABSTRACT

We investigated the anticancer chemotoxicity of previously reported iodinated chlorin p_6 copper complex (IC p_6 -Cu), a novel chlorophyll derivative in which copper is attached to the side chain carboxylate groups via coordination. Human oral carcinoma cells NT8e, 4451 and the non-cancerous keratinocyte HaCaT cells were treated with IC p_6 -Cu for 48 h in dark and cell viability, proliferation and morphological alterations were examined. IC p_6 -Cu showed pronounced cytotoxicity in cancer cells with IC₅₀ ~40 μ M, whereas, the viability of HaCaT cells was not affected. Cell proliferation assay revealed that IC p_6 -Cu at IC₅₀ concentration led to complete inhibition of cell proliferation in both the cell lines. Cell morphology studied by confocal microscopy showed absence of cell death via necrosis or apoptosis. Instead, the treated cells displayed distinct features of non-apoptotic death such as highly vacuolated cytoplasm, lysosomal membrane permeabilization and damage to cytoskeleton F-actin filaments. In addition, IC p_6 -Cu treatment led to time dependent increase in the intracellular level of reactive oxygen species (ROS) and the cytotoxicity of IC p_6 -Cu was significantly inhibited by pre-treatment of cells with antioxidants (glutathione and trolox). These findings revealed that IC p_6 -Cu is a potent chemotoxic agent which can induce cytotoxic effect in cancer cells through elevation of intracellular ROS. It is suggested that IC p_6 -Cu may provide tumor selective chemotoxicity by exploiting difference of redox environment in normal and cancer cells.

© 2017 Elsevier B.V. All rights reserved.

1. Introduction

Copper coordination compounds have received significant attention as promising anticancer agents as these offer some important advantages over other metal based drugs [1]. Copper being an essential trace element is relatively less toxic than the non-essential metals [2–4]. Further, copper complexes due to different mode of action than the platinum based drugs holds considerable promise for the treatment of platinum resistant cancer cells. While platinum based drugs inhibit DNA replication and transcription by forming platinum-DNA adduct, copper complexes exert chemotoxic effect through inhibition of ubiquitin proteasome activity and/or by augmentation of reactive oxygen species (ROS)

[1,3]. The later mode of action of copper complexes is particularly important because it can exploit the metabolic difference of normal and cancer cells to achieve tumor selective chemotoxicity [5,6].

Since porphyrin and chlorin derivatives can localize preferentially in tumor [7,8], there is considerable interest to synthesize their metal complexes and explore these as multimodal agent for combined or synergistic anticancer therapeutics. For example, tetrapyrrole compounds complexed to platinum (Pt), gold (Au), and ruthenium (Ru) have been reported which exert anticancer effect via both chemo as well as phototoxicity [9–19]. Recently, we have reported a novel iodinated chlorin p_6 copper complex (IC p_6 -Cu) in which copper is attached at the periphery of the chlorin ring through coordination with the carboxylic groups. IC p_6 -Cu demonstrated pronounced photodynamic activity via free radical generation and induced potent phototoxic effect against cancer cells under both normoxic and hypoxic condition [20].

In the present study, we have evaluated the efficacy of IC p_6 -Cu to induce chemotoxicity in human oral cancer cells and non-

* Corresponding author. Laser Biomedical Applications Section, Raja Ramanna Centre for Advanced Technology, Indore 452013, India.

E-mail address: okdube@rrcat.gov.in (A. Dube).

cancerous keratinocytes. The effect of ICp_6 -Cu on cell viability, cell proliferation and cell morphology has been studied to assess its cytotoxic potential. The underlying mechanism of cytotoxic action of ICp_6 -Cu has been investigated by monitoring the changes in intracellular ROS levels and the effect of antioxidants on induced cytotoxicity. These studies revealed that ICp_6 -Cu exert potent anti-proliferative action against cancer cells through elevation of oxidative stress.

2. Materials and method

Dulbecco's Modified Eagle's Medium (DMEM), DMEM with Nutrient Mixture F-12 Ham, Tetrazolium salt 3-(4, 5-dimethylthiazol-2-yl)-2,5-diphenyltetrazolium bromide (MTT), Trypsin/EDTA and Fetal bovine serum (FBS) were obtained from Himedia, India. Alexa Fluor 488 phalloidin was procured from Thermo Fisher Scientific, USA. Acridine orange (AO), 2', 7'-Dichlorodihydrofluorescein diacetate (DCFH-DA), Hoechst 33342 (HO), Propidium iodide (PI) were purchased from Sigma, USA.

ICp_6 -Cu was synthesized from Cp_6 following the procedure described in our Indian patent application no. 4912/MUM/2015. Stock solution of concentrated ICp_6 -Cu prepared in ethanol: PEG (400): water (20:30:50) was used for experiments.

2.1. Cell culture

Human oral cancer cell lines NT8e derived from upper aerodigestive tract (pyriform fossa) and 4451 derived from recurrent tumor in the lower jaw were obtained from Advanced Centre for Treatment, Research and Education in Cancer (ACTREC), Mumbai, India and Institute of Nuclear Medicines and Allied Sciences (INMAS), Delhi, India respectively. HaCaT, a non-cancerous immortalized dermal keratinocyte cell line was obtained from National Centre For Cell Science (NCCS), Pune, India. Oral cancer cell lines and HaCaT cell line were maintained in DMEM and DMEM/

Nutrient Mixture F-12 Ham (1:1), respectively. The growth media contained antibiotics (streptomycin, nystatin, penicillin) and 10% FBS. The cells were maintained at 37 °C under 5% CO_2 + 95% air atmosphere in a humidified incubator (Galaxy R, RS Biotech). The cells after 80% confluent growth were harvested by trypsinization and seeded either in 96 well plates, 24 well plates or 35 mm petri dishes. After 18 h incubation the cells grown as monolayer were used for experiments.

2.2. Cell viability assay

The cells were seeded in 96 well plate at a density of 8×10^3 cells/well. After overnight incubation, the cells were treated with ICp_6 -Cu (10–100 μ M) for 48 h, in dark. After incubation, the cells were washed twice with DMEM (without serum) and the effect of ICp_6 -Cu on cell viability was determined by MTT assay [21]. Briefly, the cells were incubated in DMEM (without serum) containing 0.5 mg/ml MTT for 3 h at 37 °C, in dark. Then the medium was removed and 100 μ l dimethyl sulfoxide (DMSO) was added to

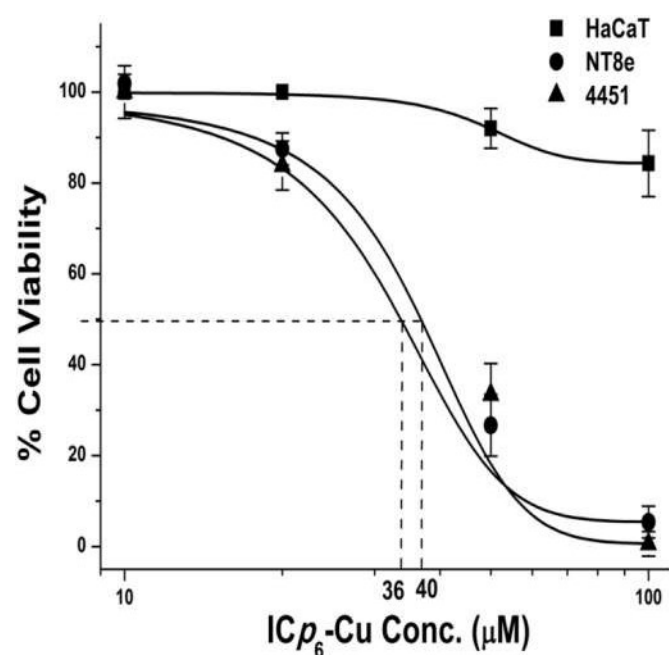


Fig. 1. Effect of ICp_6 -Cu treatment (48 h) on the viability of NT8e, 4451 and HaCaT cells. Percent cell viability was calculated with respect to control (without ICp_6 -Cu treatment). The horizontal dashed line represents 50% growth inhibition. Each data point represents mean \pm SD of three independent experiments.

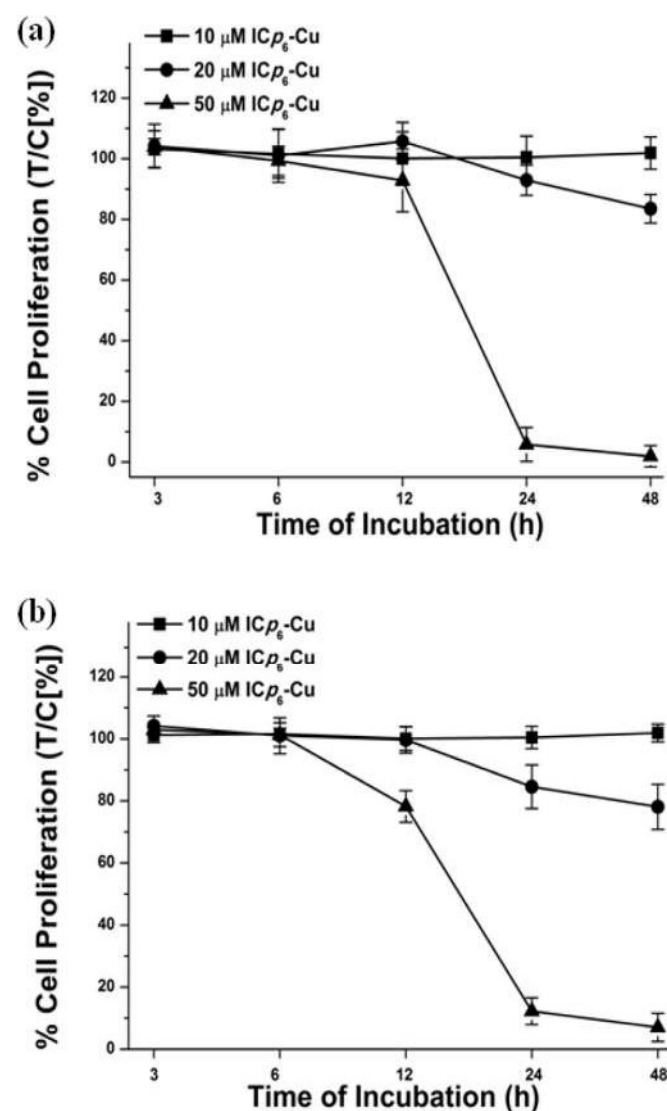


Fig. 2. Time dependent effect of ICp_6 -Cu treatment (10, 20 and 50 μ M) on the proliferation of NT8e (a) and 4451 (b) cells. The T/C values represent percent cell proliferation with respect to a control sample (without ICp_6 -Cu treatment). Each data represents mean \pm SD of three independent experiments.

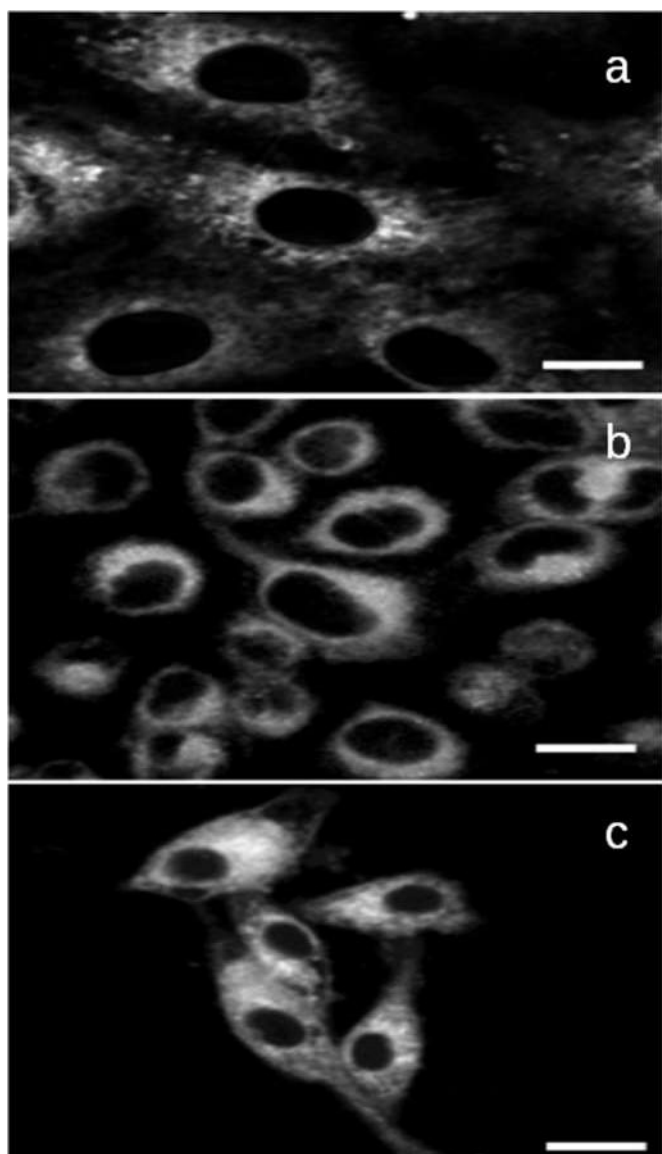


Fig. 3. Photomicrographs of HaCaT (a), NT8e (b) and 4451 (c) cells showing fluorescence of ICp₆-Cu. The cells were treated with 10 μ M ICp₆-Cu for 48 h, in dark. Experiments were repeated three times with similar results and representative images are shown. Magnification 40 \times , scale bar 20 μ m.

dissolve the formazan crystals formed within the cells. The absorbance of the samples at 570 nm with reference wavelength at 690 nm was measured on a microplate reader (Power Wave 340, Bio-tek instruments Inc., USA). The percent cell viability was determined with respect to the absorbance value of the control samples (without ICp₆-Cu treatment).

2.3. Cell proliferation assay

Effect of ICp₆-Cu treatment on proliferation of cancer cells was determined by multiple time point MTT assay [22,23]. This method allows determination of growth inhibition (antiproliferative) as well as cytotoxic activity of the test compounds [24]. A similar method developed by National Cancer Institute in which MTT is replaced with sulforhodamine B is widely used for the large scale screening of potential anticancer agents [25]. Briefly, the monolayer of cells in 96 well plate (8×10^3 cells/well) were incubated with 10,

20 and 50 μ M ICp₆-Cu in growth media for 3, 6, 12, 24 and 48 h, in dark. For each time point, a set of control without ICp₆-Cu treatment was used. At the end of incubation, MTT assay was performed for each set of control and treated cells as described above. The absorbance value obtained for control at 0 time point (C₀), ICp₆-Cu treated cells at various time points (T) and the corresponding control at each time point (C), were used to obtain percent cell proliferation using the following equation

$$\frac{T}{C} [\%] = \left[\frac{(T - C_0)}{(C - C_0)} \right] \times 100 [\%]$$

The value of T/C % denotes the effect of the compound on the cell growth where the value of 100% indicates no effect, the values between 100 and 0% indicates inhibition of cell proliferation (cytostatic effect) and the value below 0% shows cytotoxic effect [22].

2.4. Confocal microscopy

Intracellular uptake of ICp₆-Cu and changes in cellular morphology after ICp₆-Cu treatment was studied by confocal microscopy using LSM880 confocal microscope (Carl Zeiss, Germany). For this, the cells were grown on glass bottom cell culture petridishes and treated with ICp₆-Cu for 48 h in dark. The localization of ICp₆-Cu in cells was visualized by excitation with 405 nm Diode laser and imaging the fluorescence emission above 570 nm on a high sensitivity GaAsP detector.

To identify necrotic and apoptotic cells, HO and PI double staining procedure was used. PI is cell impermeable red fluorescent dye which enters the cells when membrane integrity is lost due to necrosis. HO is cell permeable DNA binding dye which gives intense blue fluorescence upon binding with condensed DNA, a hallmark of apoptosis. Briefly, the cell monolayer after treatment with ICp₆-Cu was stained with HO (10 μ g/ml) and PI (2.5 μ g/ml) for 5 min. The cells were washed twice with HBSS and the fluorescence of HO and PI was visualized using excitation laser/emission bandpass combination of 405 nm/420–480 nm and 488 nm/610–680 nm, respectively. For cell morphology, bright-field DIC images were captured using transmitted light PMT detector.

To visualize acidic lysosomal compartment, the cell monolayer after treatment with ICp₆-Cu was stained with AO (5 μ M). After washing twice with HBSS, the red fluorescence of AO in cells was imaged using excitation laser/emission bandpass combination of 488 nm/600–660 nm. For confocal imaging of cytoskeleton, the cells were stained with Alexa Fluor 488 labeled Phalloidin which binds with F-actin filaments of cytoskeleton. After counter staining with DAPI (1 μ g/ml), the fluorescence of Phalloidin and DAPI in cells was visualized using excitation laser/emission bandpass combination of 488 nm/550–660 nm and 405 nm/420–480 nm, respectively.

2.5. Determination of intracellular ROS levels

The cell monolayers were treated with ICp₆-Cu for 3, 6, 12, 24 and 48 h, in dark and the level of intracellular ROS in control and treated cells was measured by fluorescence spectroscopy using fluorescence probe DCFH-DA. The non-fluorescent DCFH-DA freely diffuses in cells and converted into another non-fluorescent product 2',7'-dichlorodihydrofluorescein (DCFH) by the enzymatic action of cellular esterases. In cells, DCFH reacts with ROS and oxidized into highly fluorescent product dichlorofluorescein (DCF) [26]. Briefly, the cell monolayers after ICp₆-Cu treatment were washed twice with ice cold PBS and incubated for 30 min at 37 $^{\circ}$ C in culture media (without serum) containing 10 μ M DCFH-DA. After

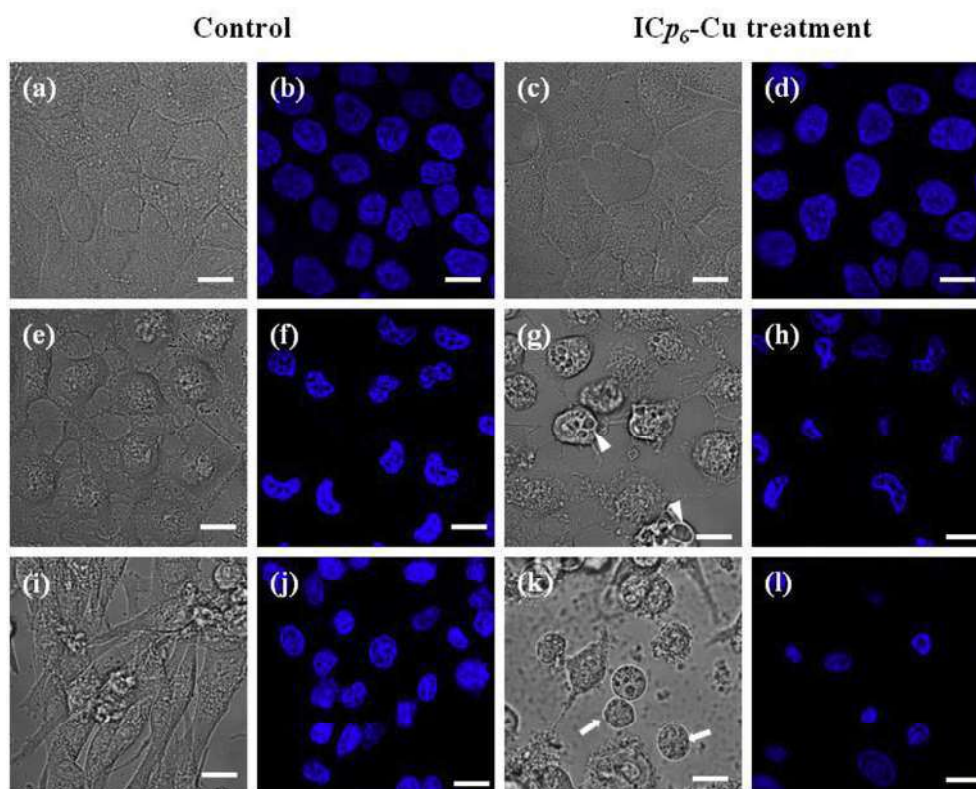


Fig. 4. Photomicrographs of control and ICp₆-Cu treated (50 μ M, 48 h) HaCaT (a–d), NT8e (e–h) and 4451 (i–l) cells. The cells were stained with PI and HO and in each case bright-field and corresponding fluorescence images are shown. Formation of vacuoles in NT8e cells and loss of cell adherence with 'rounded shape' morphology in 4451 cells are indicated by arrow heads, and arrows, respectively. Experiments were repeated three times with similar results and representative images are shown. Magnification 40 \times , scale bar 20 μ m.

incubation, the cells were released by trypsinization, re-suspended in PBS and the fluorescence of DCF in cells was measured on Fluorolog-2 spectrofluorometer (Spex, USA) using λ_{ext} at 488 nm and λ_{emm} at 525 nm with ~ 1.7 nm and ~ 3.7 nm band pass, respectively. All the procedures were done in diffused room light. The fluorescence intensity of the cell suspension was normalized with cell number and the values obtained for treated cells were plotted as fold increase in ROS levels relative to control.

2.6. Statistical analysis

All the experiments were performed in triplicate and repeated at least three times. The data represent mean \pm SD of three independent experiments. Differences between percent cell viability of ICp₆-Cu treated cells in presence and absence of antioxidants were statistically analyzed by Student's *t*-test. The value of *p* < 0.05 was considered statistically significant.

3. Results

3.1. Cytotoxicity of ICp₆-Cu

Fig. 1 shows the effect of ICp₆-Cu treatment on viability of oral cancer cells (NT8e and 4451) and non cancerous keratinocytes (HaCaT). In both cancer cells lines, treatment with ICp₆-Cu led to decrease in cell viability in concentration dependent manner whereas, no significant change was observed in the viability of HaCaT cells. The IC₅₀ value determined from the sigmoidal concentration-response curve was ~ 36 μ M and ~ 40 μ M for NT8e and 4451, respectively. The metal free Cp₆ under similar conditions

did not induce significant cytotoxicity in cancer cells as well as in HaCaT cells (data not shown).

Fig. 2 shows percent cell proliferation (T/C %) in NT8e (Fig. 2 a) and 4451 cells (Fig. 2 b) that were treated with 10, 20 and 50 μ M ICp₆-Cu for varying time periods. ICp₆-Cu at lower concentration (10 μ M) did not show any significant effect on proliferation of cancer cells. At concentration below IC₅₀ (20 μ M), $\sim 20\%$ decrease in cell proliferation was observed at 48 h. At concentration above IC₅₀ (50 μ M), the inhibition of cell proliferation occurred much earlier and was more pronounced, as indicated by decrease in the value of T/C % to $\sim 6\%$ at 24 h after treatment. At later time point (48 h) the value of T/C % did not decrease further.

3.2. Effect of ICp₆-Cu on cell morphology

Fig. 3 shows the fluorescence photomicrograph of HaCaT (Fig. 3 a), NT8e (Fig. 3 b) and 4451 (Fig. 3 c), cells that were treated with ICp₆-Cu (10 μ M) for 48 h. In all the cell types, the fluorescence of ICp₆-Cu is localized in the cytoplasm sparing the nucleus. This indicates that there is no cell line specific difference in cellular uptake and localization of ICp₆-Cu.

The confocal microscopic images of HaCaT, NT8e and 4451 cells in control and ICp₆-Cu treated (50 μ M, 48 h) monolayers are shown in Fig. 4. In control, HaCaT, NT8e and 4451 cells appear healthy indicated by intact cell morphology, absence of PI fluorescence and no DNA fragmentation or condensation (Fig. 4 a, b, e, f, i & j). After ICp₆-Cu treatment, while HaCaT cells show no change in the morphology (Fig. 4 c), both NT8e and 4451 cells displayed marked alterations as indicated by highly vacuolated cytoplasm in NT8e cells (Fig. 4 g) and 'rounded shape' morphology and loss of

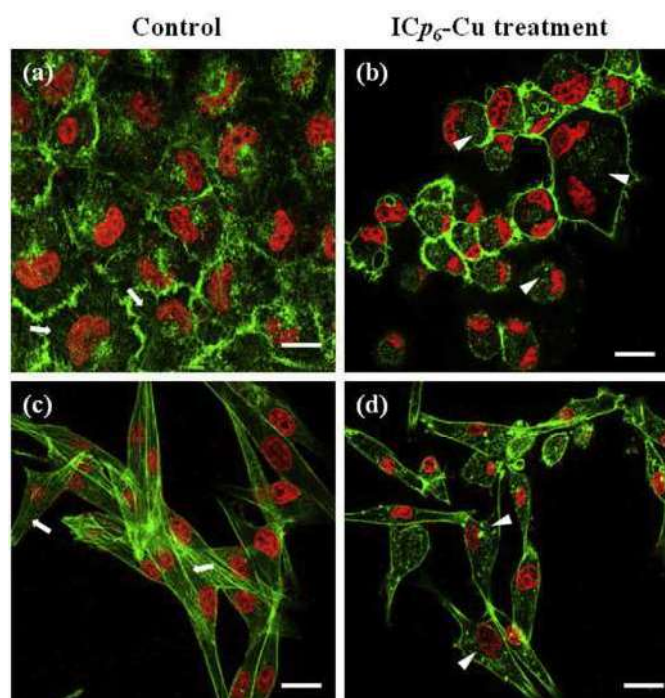


Fig. 5. Confocal fluorescence micrographs of control and ICp₆-Cu (50 μ M, 48 h) treated NT8e (a, b) and 4451 (c, d) cells showing F- actin filaments of cytoskeleton. The cells were stained with DAPI and Alexa Fluor 488 Phalloidin. Experiments were repeated three times with similar results and representative images are shown. Arrow indicates intact F- actin filaments; arrow heads indicates F- actin aggregates. Magnification 40 \times , scale bar 20 μ m.

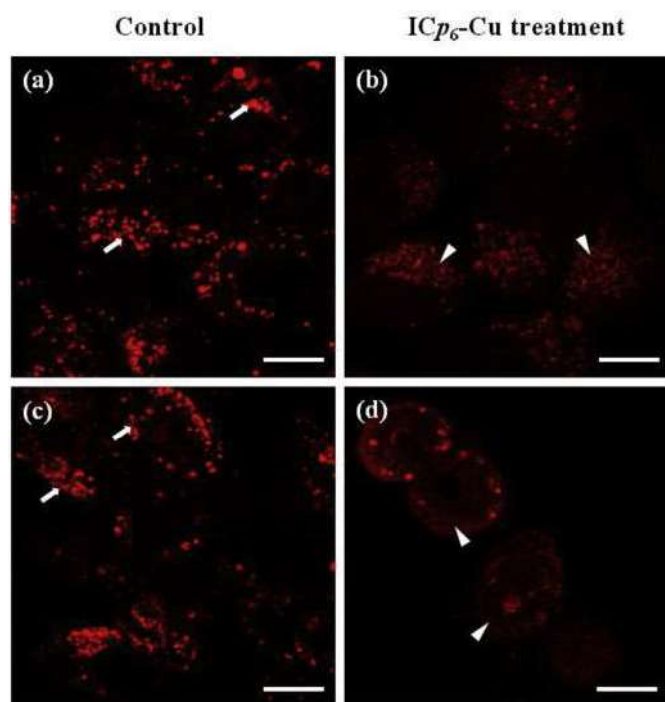


Fig. 6. Confocal fluorescence micrographs of control and ICp₆-Cu treated (50 μ M, 48 h) NT8e (a, b) and 4451 (c, d) cells showing AO stained lysosomal acidic vesicles. Experiments were repeated three times with similar results and representative images are shown. Arrows indicate intact acidic lysosome, arrow heads indicate weak diffused lysosome staining. Magnification 40 \times , scale bar 20 μ m.

adherence in 4451 cells (Fig. 4 k). The corresponding fluorescence images of NT8e and 4451 cells (Fig. 4 h & i), did not show either PI uptake and/or DNA condensation or fragmentation indicating absence of necrotic and apoptotic cell death.

To further verify that ICp₆-Cu exerted cytotoxic effect, damage to F-actin filaments of cytoskeleton and Lysosomal membrane permeabilization (LMP) which are major hallmark of non apoptotic modes of cell death were probed. Fig. 5 shows the photomicrographs of control and ICp₆-Cu treated NT8e and 4451 cells after staining with F-actin specific Phalloidin Alexa Fluor 488 and DAPI. The cells in control displayed brightly stained intact F- actin filaments (Fig. 5 a & c). In contrast, cells treated with ICp₆-Cu lack intact actin filaments and the fluorescence of Phalloidin is localized as dotted structures indicating disruption of F- actin filaments (Fig. 5 b & d).

Fig. 6 shows the photomicrographs of control and ICp₆-Cu treated NT8e and 4451 cells that were stained with AO, a fluorescence probe which accumulates in acidic vacuoles and emits red/orange fluorescence [41]. In the control cells, intact lysosomes in cytoplasm are clearly visible as discrete vesicles having bright red punctuate fluorescence (Fig. 6 a & c). In cells treated with ICp₆-Cu (Fig. 6 b & d), the red fluorescence of AO is diminished and the vesicles with punctuate red fluorescence staining are less or absent. These observations indicate that ICp₆-Cu treatment led to partial or complete permeabilization of lysosomal membrane in both NT8e and 4451 cells.

3.3. Effect of ICp₆-Cu on intracellular ROS levels

Fig. 7 shows changes in intracellular ROS levels in HaCaT and NT8e cells at different time period after the treatment with 10 μ M and 50 μ M ICp₆-Cu. In HaCaT cells, ICp₆-Cu treatment did not lead to any significant change in the level of intracellular ROS (Fig. 7 a). Whereas in cancer cells, the level of ROS was observed to increase in time dependent manner subsequent to the treatment with 50 μ M ICp₆-Cu (Fig. 7 b). As compared to control, a maximum increase of ~4 fold was seen at 24 h after the treatment. At lower concentration (10 μ M) ICp₆-Cu did not cause any change in the level of intracellular ROS. For 4451 cells, similar increase in ROS level as observed for NT8e was expected because the cytotoxic effect of ICp₆-Cu was almost same in both the cancer cell lines.

To confirm the involvement of ROS in cytotoxic action of ICp₆-Cu, the effect of antioxidants (glutathione and trolox) on ICp₆-Cu induced cytotoxicity was studied. Fig. 8 a & b shows percent cell viability of NT8e and 4451 cells subjected to ICp₆-Cu treatment (50 μ M) for 24 and 48 h, without and with GSH (1 mM) and trolox (10 μ M) pre-treatment (2 h). At 24 h, the percent cell viability in ICp₆-Cu treated cells that received antioxidant pre-treatment was significantly higher as compared to cells which received no pre-treatment. At prolonged treatment time (48 h), antioxidant pre-treatment did not led to any significant increase in cell viability. Similarly, the inhibition of cell proliferation induced by ICp₆-Cu at 24 h was also reduced significantly by pretreatment of cells with antioxidants (GSH and trolox) and the effect at prolonged time was less pronounced (Fig. 8 c & d) These results show that pre-treatment of cells with antioxidants inhibited the cytotoxic effect of ICp₆-Cu at earlier time point but the effect diminished when ICp₆-Cu treatment was prolonged.

4. Discussion

Oral squamous cell carcinoma (OSCC) is most prevalent cancer in India and other Asian countries which accounts for ~ 2% of all deaths by cancer worldwide [27]. Chemotherapy of oral cancer with clinically applied chemotherapeutic agents such as cisplatin is

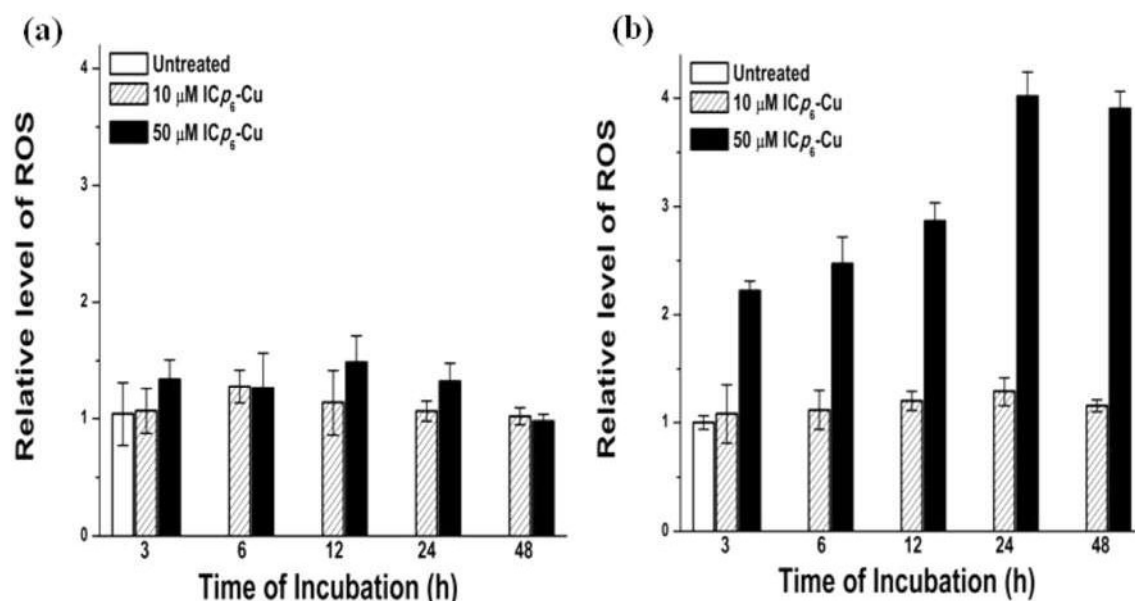


Fig. 7. Changes in the levels of intracellular ROS relative to control in HaCaT (a) and NT8e (b) cells at different time periods after treatment with 10 μ M and 50 μ M of ICp₆-Cu. Data represents mean \pm SD obtained from three independent experiments.

associated with the concern of serious side effects and emergence of resistance after prolonged treatment [28,29]. A promising approach to improve the selectivity of chemotherapy is to exploit the difference of redox environment between cancer and normal cells [30]. In this context, copper complexes due to ability to enhance the intracellular ROS levels via redox process have received considerable attention [31].

Using chlorin *p*₆, a chlorophyll derivative that showed considerable tumor localizing property in our previous studies [32], we synthesized a novel iodinated Cp₆-copper complex (ICp₆-Cu) for its potential application as multimodal anticancer agent [patent, 20]. In the present study, we examined the chemotoxic activity of ICp₆-Cu in two human oral cancer cell lines and a non-cancerous keratinocyte cells. Results demonstrate that ICp₆-Cu exhibited pronounced cytotoxic action against oral cancer cells and did not affect non-cancerous human keratinocytes. The IC₅₀ value of ICp₆-Cu (~40 μ M) is comparable to that reported for platinum complexes [33] as well as some copper based anticancer compounds such as copper (II) complexes of Schiff base, phthalate and dipyriddy [1]. Anticancer agents based on their ability to suppress the growth of cancer cells or induce cell killing have been categorized as cytostatic and cytotoxic agents, respectively [34]. Results of multiple point chemosensitivity assay revealed that ICp₆-Cu exhibited pronounced cytostatic effect in both NT8e and 4451 cells (Fig. 2). It is well known that majority of anticancer agents induces cytostatic effect and when the cytostasis is prolonged and profound it can lead to cell death [34]. Staining cells with PI/HO revealed that ICp₆-Cu did not induce either apoptosis or necrosis in both 4451 and NT8e cells (Fig. 4). Interestingly, the morphological alterations induced by ICp₆-Cu treatment, such as formation of large cytoplasmic vacuoles in NT8e cells (Fig. 4 g) and rounded shape morphology in 4451 cells (Fig. 4 k) indicated that apart from the suppression of cell proliferation, ICp₆-Cu also exerted distinct cytotoxic effect. This is further confirmed by observations on damage to F-actin filaments of cytoskeleton (Fig. 5) and lysosomal membrane permeabilization (Fig. 6) in ICp₆-Cu treated cells. Similar morphological alteration in cancer cells after treatment with anticancer agents have been reported in several studies and these were believed to be hallmarks of non-apoptotic mechanisms of cell death

such as autophagy, anoikis and lysosomal membrane permeabilization [35]. Although, further investigation is required to know the exact cell death pathway, here it is important to mention that anticancer agent, which induce non-apoptotic cell death holds considerable promise for the treatment of apoptosis resistant tumor [35]. Consistent with this, ICp₆-Cu showed almost same effectiveness against 4451 and NT8e cells, despite the fact that 4451 cell line has defective apoptotic machinery due to mutated p53 gene [36], whereas, NT8e with wild type p53 is apoptotic proficient [37].

Results on elevation of intracellular ROS levels by ICp₆-Cu (Fig. 7) and the inhibitory action of antioxidants on ICp₆-Cu induced cytotoxicity (Fig. 8) provided evidence that the antiproliferative effect of ICp₆-Cu is mediated via increase in oxidative stress. This is also consistent with changes observed in cellular morphology of treated cells (Figs. 4–6) and further supported by several reports. For example, enhanced oxidative stress has been shown to induce cytoplasmic vacuolization [38,39], disruption of actin cytoskeleton [40] and lysosomal membrane permeabilization [41,42]. Interestingly, as compared to cancer cells the non-cancerous HaCaT cells did not show increase in ROS levels after ICp₆-Cu treatment which explains the absence of its cytostatic effect in these cells. HaCaT cells have been used in several studies as normal cells to test the efficacy and selectivity of anticancer drugs [43,44]. The absence of cytotoxicity of ICp₆-Cu in HaCaT cells suggest that it is not likely to cause any cytotoxic effect in normal cells. Further, it is important to mention that keratinocytes are the major cell population of the normal oral tissue. It is well known that the cellular redox homeostasis in normal cells is well regulated through antioxidant defense mechanism. In contrast, since cancer cells exhibit dysregulated redox homeostasis, they are more susceptible to further increase in intracellular ROS levels than the normal cells [30,45]. This provides explanation for the difference in sensitivity of HaCaT and cancer cells to oxidative stress and the observed difference is in agreement with previous reports [43].

In conclusion, results of our study demonstrated that ICp₆-Cu acts as redox active anticancer agent capable of inducing pronounced chemotoxicity in oral carcinoma through elevation of intracellular ROS levels. ICp₆-Cu exhibited potent cytostatic effect

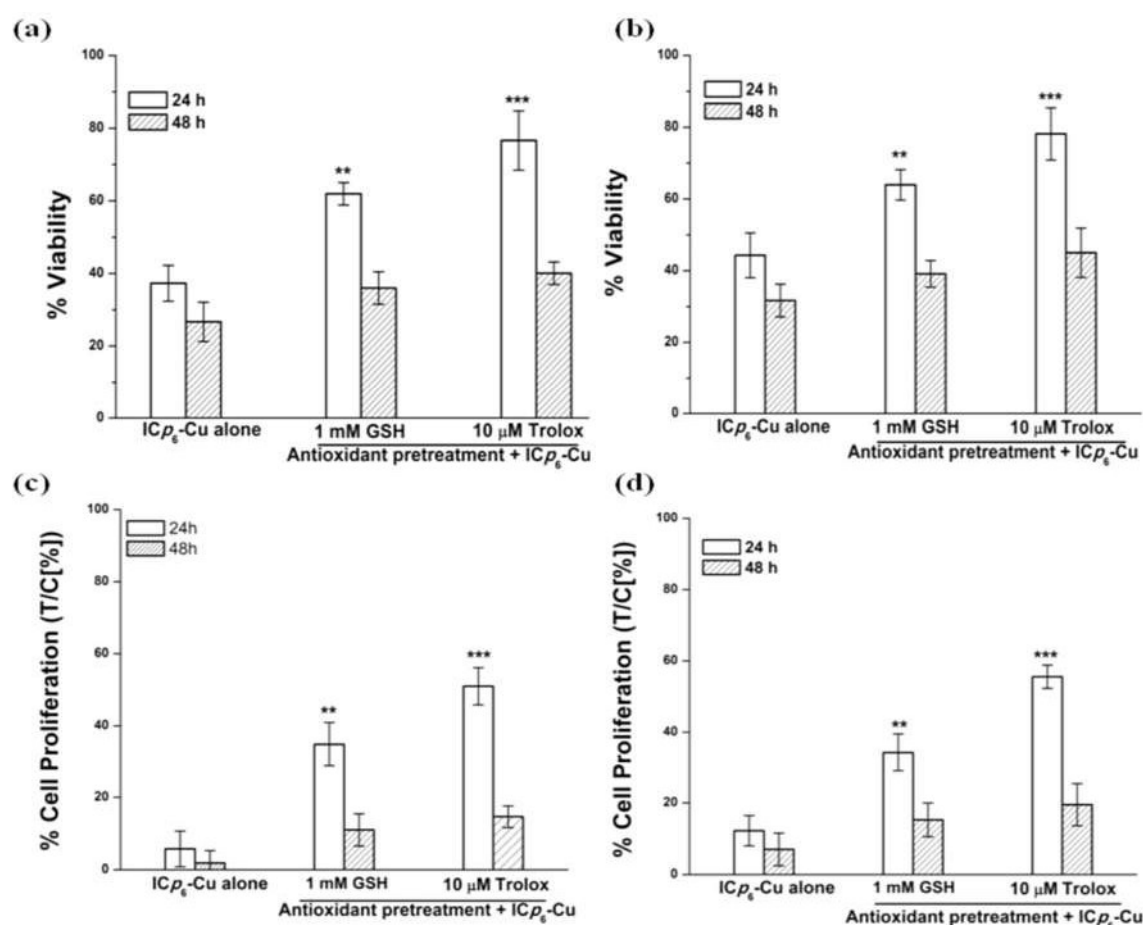


Fig. 8. Percent cell viability and cell proliferation of ICp₆-Cu treated (50 μM) NT8e (a, c) and 4451 (b, d) cells without and with GSH and Trolox pretreatment (2 h). Data represents mean ± S.D obtained from three independent experiments. * = (P < 0.05), ** = (P < 0.01), *** = (P < 0.005), indicate significant difference from untreated control (without GSH and Trolox treatment).

and prolonged cytostasis led to non-apoptotic cell death characterized by alterations in cellular morphology, cytoskeletal F-actin architecture and lysosomal membrane permeabilization. Thus, ICp₆-Cu could be a potential anticancer agent which may provide selective chemotoxic effect based on difference in susceptibility of normal and cancer cells to ROS.

Disclosure

Alok Dube, Paromita Sarbadhikary and Pradeep Kumar Gupta are named patent inventors for Indian Patent Application no. 4912/MUM/2015 titled 'A metal complex of chlorophyll derivative for magnetic resonance imaging and photodynamic therapy', filed on December 29, 2015.

Acknowledgments

We would like to thank Dr B. S. Dwarakanath, INMAS, Delhi and Dr U. M. Warawdekar, ACTREC, Mumbai for providing oral cancer cell lines. S Paromita acknowledges Homi Bhabha National Institute, Mumbai for senior research fellowship.

Transparency document

Transparency document related to this article can be found online at <http://dx.doi.org/10.1016/j.cbi.2017.09.011>.

References

- [1] C. Santini, M. Pellei, V. Gandini, M. Porchia, F. Tisato, C. Marzano, Advances in copper complexes as anticancer agents, *Chem. Rev.* 114 (2014) 815–862, <http://dx.doi.org/10.1021/cr400135x>.
- [2] D. Denoyer, S. Masaldan, S. La Fontaine, M.A. Cater, Targeting copper in cancer therapy: 'Copper that Cancer', *Metallomics* 7 (2015) 1459–1476, <http://dx.doi.org/10.1039/c5mt00149h>.
- [3] C. Marzano, M. Pellei, F. Tisato, C. Santini, Copper complexes as anticancer agents, *Anticancer Agents Med. Chem.* 9 (2009) 185–211, <http://dx.doi.org/10.2174/187152009787313837>.
- [4] C.X. Zhang, S.J. Lippard, New metal complexes as potential therapeutics, *Curr. Opin. Chem. Biol.* 7 (2003) 481–489, [http://dx.doi.org/10.1016/S1367-5931\(03\)00081-4](http://dx.doi.org/10.1016/S1367-5931(03)00081-4).
- [5] A. Ganguly, S. Basu, K. Banerjee, P. Chakraborty, A. Sarkar, M. Chatterjee, S.K. Chaudhuri, Redox active copper chelate overcomes multidrug resistance in T-lymphoblastic leukemia cell by triggering apoptosis, *Mol. Biosyst.* 7 (2011) 1701–1712, <http://dx.doi.org/10.1039/c0mb00306a>.
- [6] J. Wang, J. Yi, Cancer cell killing via ROS: to increase or decrease that is the question, *Cancer Biol. Ther.* 7 (2008) 1875–1884, <http://dx.doi.org/10.4161/cbt.7.12.7067>.
- [7] H. Abrahamse, M.R. Hamblin, New photosensitizers for photodynamic therapy, *Biochem. J.* 473 (2016) 347–364, <http://dx.doi.org/10.1042/BJ20150942>.
- [8] P. Agostinis, K. Berg, K.A. Cengel, T.H. Foster, A.W. Girotti, S.O. Gollnick, S.M. Hahn, M.R. Hamblin, A. Juzeniene, D. Kessel, M. Korbelik, J. Moan, P. Mroz, D. Nowis, J. Piette, B.C. Wilson, J. Golab, Photodynamic therapy of cancer: an update, *CA Cancer J. Clin.* 61 (2011) 250–281, <http://dx.doi.org/10.3322/caac.20114>.
- [9] G. Battogtokh, H.-B. Liu, S.-M. Bae, P.K. Chaturvedi, Y.-W. Kim, I.-W. Kim, W.S. Ahn, Synthesis of di-pyropheophorbide-a-platinum(II) complex and the in vitro cytotoxicity against TC-1 tumor cells, *J. Porphyr. Phthalocyanines* 16 (2012) 1024–1031, <http://dx.doi.org/10.1142/S1088424612500782>.
- [10] H. Brunner, M.R. Arndt, B. Treitinger, Porphyrin platinum conjugates – new aims, *Inorganica Chim. Acta* 357 (2004) 1649–1669, <http://dx.doi.org/>

- 10.1016/S0020-1693(03)00479-1.
- [11] H. Brunner, N. Gruber, Carboplatin-containing porphyrin–platinum complexes as cytotoxic and phototoxic antitumor agents, *Inorganica Chim. Acta* 357 (2004) 4423–4451, <http://dx.doi.org/10.1016/j.ica.2004.03.061>.
 - [12] C.M. Che, R.W. Sun, W.Y. Yu, C.B. Ko, N. Zhu, H. Sun, Gold(III) porphyrins as a new class of anticancer drugs: cytotoxicity, DNA binding and induction of apoptosis in human cervix epitheloid cancer cells, *Chem. Commun. (Camb)* 21 (2003) 1718–1719, <http://dx.doi.org/10.1039/B303294A>.
 - [13] T. Gianferrara, A. Bergamo, I. Bratsos, B. Milani, C. Spagnul, G. Sava, E. Alessio, Ruthenium–porphyrin conjugates with cytotoxic and phototoxic antitumor activity, *J. Med. Chem.* 53 (2010) 4678–4690, <http://dx.doi.org/10.1021/jm1002588>.
 - [14] C. Lottner, R. Knuechel, G. Bernhardt, H. Brunner, Combined chemotherapeutic and photodynamic treatment on human bladder cells by hematoporphyrin–platinum(II) conjugates, *Cancer Lett.* 203 (2004) 171–180, <http://dx.doi.org/10.1016/j.canlet.2003.09.001>.
 - [15] C.T. Lum, Z.F. Yang, H.Y. Li, Wai-Yin, R. Sun, S.T. Fan, R.T. Poon, M.C. Lin, C.M. Che, H.F. Kung, Gold(III) compound is a novel chemocytotoxic agent for hepatocellular carcinoma, *Int. J. Cancer* 118 (2006) 1527–1538, <http://dx.doi.org/10.1002/ijc.21484>.
 - [16] G. Momekov, M. Karaivanova, I. Ugrinova, E. Pasheva, G. Gencheva, D. Tsekova, S. Arpadjan, P.R. Bontchev, In vitro pharmacological study of monomeric platinum(III) hematoporphyrin IX complexes, *Invest. New Drugs* 29 (2011) 742–751, <http://dx.doi.org/10.1007/s10637-010-9412-8>.
 - [17] F. Schmitt, P. Govindaswamy, G. Süß-Fink, W.H. Ang, P.J. Dyson, L. Juillerat-Jeanneret, B. Therrien, Ruthenium porphyrin compounds for photodynamic therapy of cancer, *J. Med. Chem.* 51 (2008) 1811–1816, <http://dx.doi.org/10.1021/jm701382p>.
 - [18] S. Tu, Wai-Yin, R. Sun, M.C. Lin, Tao, J. Cui, B. Zou, Q. Gu, H.F. Kung, C.M. Che, B.C. Wong, Gold (III) porphyrin complexes induce apoptosis and cell cycle arrest and inhibit tumor growth in colon cancer, *Cancer* 115 (2009) 4459–4469, <http://dx.doi.org/10.1002/cncr.24514>.
 - [19] J.X. Zhang, J.W. Zhou, C.F. Chan, T.C. Lau, D.W. Kwong, H.L. Tam, N.K. Mak, K.L. Wong, W.K. Wong, Comparative studies of the cellular uptake, subcellular localization, and cytotoxic and phototoxic antitumor properties of ruthenium(II)–porphyrin conjugates with different linkers, *Bioconjug. Chem.* 23 (2012) 1623–1638, <http://dx.doi.org/10.1021/bc300201h>.
 - [20] P. Sarbadhikary, A. Dube, P.K. Gupta, Synthesis and characterization of photodynamic activity of an iodinated Chlorin p6 copper complex, *RSC Adv.* 6 (2016) 75782–75792, <http://dx.doi.org/10.1039/C6RA14026B>.
 - [21] T. Mosmann, Rapid colorimetric assay for cellular growth and survival: application to proliferation and cytotoxicity assays, *J. Immunol. Methods* 65 (1983) 55–63, [http://dx.doi.org/10.1016/0022-1759\(83\)90303-4](http://dx.doi.org/10.1016/0022-1759(83)90303-4).
 - [22] G. Bernhardt, H. Reile, H. Birnböck, T. Spruß, H. Schönenberger, Standardized kinetic microassay to quantify differential chemosensitivity on the basis of proliferative activity, *J. Cancer Res. Clin. Oncol.* 118 (1992) 35–43, <http://dx.doi.org/10.1007/BF01192309>.
 - [23] H. Reile, H. Birnböck, G. Bernhardt, T. Spruß, H. Schönenberger, Computerized determination of growth kinetic curves and doubling times from cells in microculture, *Anal. Biochem.* 187 (1990) 262–267, [http://dx.doi.org/10.1016/0003-2697\(90\)90454-H](http://dx.doi.org/10.1016/0003-2697(90)90454-H).
 - [24] M.L. Low, C.W. Chan, P.Y. Ng, I.H. Ooi, M.J. Maah, S.M. Chye, K.W. Tan, S.W. Ng, C.H. Ng, Ternary and binary copper (II) complexes: synthesis, characterization, ROS-inductive, proteasome inhibitory, and anticancer properties, *J. Coord. Chem.* 70 (2017) 223–241, <http://dx.doi.org/10.1080/00958972.2016.1260711>.
 - [25] R.H. Shoemaker, The NCI60 human tumour cell line anticancer drug screen, *Nat. Rev. Cancer* 6 (2006) 813–823, <http://dx.doi.org/10.1038/nrc1951>.
 - [26] W.J. Guo, S.S. Ye, N. Cao, J. Huang, J. Gao, Q.Y. Chen, ROS-mediated autophagy was involved in cancer cell death induced by novel copper(II) complex, *Exp. Toxicol. Pathol.* 62 (2010) 577–582, <http://dx.doi.org/10.1016/j.etp.2009.08.001>.
 - [27] A.K. Chaturvedi, W.F. Anderson, J. Lortet-Tieulent, M.P. Curado, J. Ferlay, S. Franceschi, P.S. Rosenberg, F. Bray, M.L. Gillison, Worldwide trends in incidence rates for oral cavity and oropharyngeal cancers, *J. Clin. Oncol.* 31 (2013) 4550–4559, <http://dx.doi.org/10.1200/JCO.2013.50.3870>.
 - [28] C. Andreadis, K. Vahtsevanos, T. Sidiras, I. Thomaidis, K. Antoniadis, D. Mouratidou, 5-Fluorouracil and cisplatin in the treatment of advanced oral cancer, *Oral Oncol.* 39 (2003) 380–385, [http://dx.doi.org/10.1016/S1368-8375\(02\)00141-0](http://dx.doi.org/10.1016/S1368-8375(02)00141-0).
 - [29] P. Ramos, M. Bentires-Alj, Mechanism-based cancer therapy: resistance to therapy, therapy for resistance, *Oncogene* 34 (2015) 3617–3626, <http://dx.doi.org/10.1038/onc.2014.314>.
 - [30] F.N. Akladios, S.D. Andrew, C.J. Parkinson, Selective induction of oxidative stress in cancer cells via synergistic combinations of agents targeting redox homeostasis, *Bioorg. Med. Chem.* 23 (2015) 3097–3104, <http://dx.doi.org/10.1016/j.bmc.2015.05.006>.
 - [31] U. Jungwirth, C.R. Kowol, B.K. Keppler, C.G. Hartinger, W. Berger, P. Heffeter, Anticancer activity of metal complexes: involvement of redox processes, *Antioxid. Redox Signal* 15 (2011) 1085–1127, <http://dx.doi.org/10.1089/ars.2010.3663>.
 - [32] A. Dube, S. Sharma, P.K. Gupta, Tumor regression induced by photodynamic treatment with chlorin p(6) in hamster cheek pouch model of oral carcinogenesis: dependence of mode of tumor cell death on the applied drug dose, *Oral Oncol.* 47 (2011) 467–471, <http://dx.doi.org/10.1016/j.joraloncology.2011.03.030>.
 - [33] K. Suntharalingam, O. Mendoza, A.A. Duarte, D.J. Mann, R. Vilar, A platinum complex that binds non-covalently to DNA and induces cell death via a different mechanism than cisplatin, *Metallomics* 5 (2013) 514–523, <http://dx.doi.org/10.1039/c3mt20252f>.
 - [34] O. Rixe, T. Fojo, Is cell death a critical end point for anticancer therapies or is cytostasis sufficient? *Clin. Cancer Res.* 13 (2007) 7280–7287, <http://dx.doi.org/10.1158/1078-0432.CCR-07-2141>.
 - [35] A. Kornienko, V. Mathieu, S.K. Rastogi, F. Lefranc, R. Kiss, Therapeutic agents triggering nonapoptotic cancer cell death, *J. Med. Chem.* 56 (2013) 4823–4839, <http://dx.doi.org/10.1021/jm400136m>.
 - [36] F. Zölzer, S. Hillebrandt, C. Streffer, Radiation induced G1-block and p53 status in six human cell lines, *Radiother. Oncol.* 37 (1995) 20–28, [http://dx.doi.org/10.1016/0167-8140\(95\)01618-Q](http://dx.doi.org/10.1016/0167-8140(95)01618-Q).
 - [37] R. Mulherkar, A.P. Goud, A.S. Wagle, K.N. Naresh, M.B. Mahimkar, S.M. Thomas, S.A. Pradhan, M.G. Deo, Establishment of a human squamous cell carcinoma cell line of the upper aero-digestive tract, *Cancer Lett.* 118 (1997) 115–121, [http://dx.doi.org/10.1016/S0304-3835\(97\)00241-3](http://dx.doi.org/10.1016/S0304-3835(97)00241-3).
 - [38] R.B. Badisa, S.S. Kumar, E. Mazzio, R.D. Haughbrook, J.R. Allen, M.W. Davidson, C.A. Fitch-Pye, C.B. Goodman, N-acetyl cysteine mitigates the acute effects of cocaine-induced toxicity in astroglia-like cells, *PLoS One* 10 (2015) e0114285, <http://dx.doi.org/10.1371/journal.pone.0114285>.
 - [39] C. Focaccetti, A. Bruno, E. Magnani, D. Bartolini, E. Principi, K. Dallaglio, E.O. Bucci, G. Finzi, F. Sessa, D.M. Noonan, A. Albini, Effects of 5-fluorouracil on morphology, cell cycle, proliferation, apoptosis, autophagy and ROS production in endothelial cells and cardiomyocytes, *PLoS One* 10 (2015) e0115686, <http://dx.doi.org/10.1371/journal.pone.0115686>.
 - [40] M.E. Farah, V. Sirotkin, B. Haarer, D. Kakhniashvili, D.C. Amberg, Diverse protective roles of the actin cytoskeleton during oxidative stress, *Cytoskeleton* 68 (2011) 340–354, <http://dx.doi.org/10.1002/cm.20516>.
 - [41] P. Boya, G. Kroemer, Lysosomal membrane permeabilization in cell death, *Oncogene* 27 (2008) 6434–6451, <http://dx.doi.org/10.1038/onc.2008.310>.
 - [42] N. Kavcic, K. Pegan, B. Turk, Lysosomes in programmed cell death pathways: from initiators to amplifiers, *Biol. Chem.* 398 (2016) 289–301, <http://dx.doi.org/10.1515/hsz-2016-0252>.
 - [43] M.S. Ahamad, S. Siddiqui, A. Jafri, S. Ahmad, M. Afzal, M. Arshad, Induction of apoptosis and antiproliferative activity of naringenin in human epidermoid carcinoma cell through ROS generation and cell cycle arrest, *PLoS One* 9 (2014) e110003, <http://dx.doi.org/10.1371/journal.pone.0110003>.
 - [44] Y.S. Wimardhani, D.F. Sunarti, H.J. Freisleben, S.I. Wanandi, N.C. Siregar, M. Ikeda, Chitosan exerts anticancer activity through induction of apoptosis and cell cycle arrest in oral cancer cells, *J. Oral Sci.* 56 (2014) 119–126, <http://dx.doi.org/10.2334/josnusd.56.119>.
 - [45] S. Galadari, A. Rahman, S. Pallichankandy, F. Thayyullathil, Reactive oxygen species and cancer paradox: to promote or to suppress? *Free Radic. Biol. Med.* 104 (2017) 144–164, <http://dx.doi.org/10.1016/j.freeradbiomed.2017.01.004>.



Enhancement of radiosensitivity of oral carcinoma cells by iodinated chlorin p_6 copper complex in combination with synchrotron X-ray radiation

Paromita Sarbadhikary^{a,b} and Alok Dube^{a,b*}

Received 23 June 2017

Accepted 5 September 2017

Edited by R. W. Strange, University of Essex, UK

Keywords: chlorophyll derivative; DNA damage; radiosensitization; reactive oxygen species; synchrotron photon activation therapy.

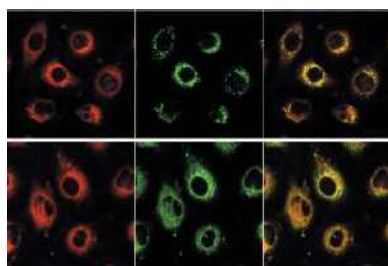
Supporting information: this article has supporting information at journals.iucr.org/s

^aLaser Biomedical Applications Section, Raja Ramanna Centre for Advanced Technology, Indore, Madhya Pradesh 452013, India, and ^bHomi Bhabha National Institute, Training School Complex, Anushakti Nagar, Mumbai 400094, India. *Correspondence e-mail: okdube@rrcat.gov.in

The combination of synchrotron X-ray radiation and metal-based radio-sensitizer is a novel form of photon activation therapy which offers the advantage of treating malignant tumors with greater efficacy and higher precision than conventional radiation therapy. In this study the anticancer cytotoxic efficacy of a new chlorophyll derivative, iodinated chlorin p_6 copper complex (ICp_6 -Cu), combined with synchrotron X-ray radiation (8–10 keV) in two human oral cancer cell lines is explored. Pre-treatment of cells with 20 μ M and 30 μ M ICp_6 -Cu for 3 h was found to enhance the X-ray-induced cytotoxicity with sensitization enhancement ratios of 1.8 and 2.8, respectively. ICp_6 -Cu localized in cytoplasm, mainly in lysosomes and endoplasmic reticulum, and did not cause any cytotoxicity alone. The radiosensitization effect of ICp_6 -Cu accompanied a significant increase in the level of reactive oxygen species, damage to lysosomes, inhibition of repair of radiation-induced DNA double-strand breaks, increase in cell death and no significant effect on cell cycle progression. These results demonstrate that ICp_6 -Cu is a potential agent for synchrotron photon activation therapy of cancer.

1. Introduction

Photon activation therapy (PAT) based on the photoactivation of a metal complex with synchrotron X-ray radiation is a promising approach for the treatment of chemo- and radio-resistant tumors (Adam *et al.*, 2008; Deman *et al.*, 2010; Gil *et al.*, 2011). Photoactivation of high-Z elements with an X-ray beam energy higher than the binding energy of the electrons leads to ionization of the atom or molecule and creation of an inner shell vacancy. Subsequently, the relaxation of the excited state results in the generation of photoelectrons and secondary electrons of very low energies (~ 20 –500 eV) via radiative and non-radiative processes known as the photoelectric effect and Auger effect, respectively. Both photoelectrons and Auger electrons can damage the nearby biomolecules directly and also cause radiolysis of water molecules resulting in the generation of cytotoxic free radicals (Kobayashi *et al.*, 2010). The sensitization effect of metal complexes results in higher dose deposition in tumor tissue and, since relatively low doses of radiation are required, damage to the normal tissue can be reduced significantly. Owing to this advantage, PAT is actively being investigated for the treatment of high-grade brain tumors with promising outcomes. For example, studies in glioma-bearing rats and mice have shown that administration of iodine or platinum compounds and their activation with X-rays results in larger tumor reduction and higher survival compared with radiation



alone (Biston *et al.*, 2004; Adam *et al.*, 2006, 2008; Rousseau *et al.*, 2009; Ricard *et al.*, 2013). Recently, Ceresa *et al.* (2014) reported that cisplatin plus irradiation with synchrotron radiation X-rays produces substantially higher cell killing compared with conventional X-ray irradiation in highly resistant glioblastoma multiforme cells. However, the use of cisplatin is associated with severe side effects which warrant development of less toxic and more effective agents to fully exploit the advantages of this therapeutic approach (Astolfi *et al.*, 2013). Some metal-nanoparticle-based radiation-dose enhancers such as gold (Hainfeld *et al.*, 2008; Su *et al.*, 2014), gadolinium (Taupin *et al.*, 2015), iron (Choi *et al.*, 2012) and tantalum oxide (Engels *et al.*, 2017) have also been investigated for PAT.

The propensity of porphyrin and chlorin derivatives to accumulate preferentially in tumor has been successfully exploited for the photodynamic therapy (PDT) of cancer (Abrahamse & Hamblin, 2016). However, due to the low penetration depth of light in tissue, PDT is not effective for deep-seated tumors. Recently, a novel therapeutic approach that utilizes X-ray radiation to activate photosensitizer (PS) directly or indirectly through absorption of X-ray energy by high-Z elements has gained considerable attention (Ishibashi *et al.*, 2013; Chen *et al.*, 2015; Kaščáková *et al.*, 2015; Wang *et al.*, 2016). One such approach requires activation of PS indirectly *via* X-ray-induced luminescence of metal nanoparticles or lanthanide atoms such as europium or terbium, placed in close vicinity of the PS (Liu *et al.*, 2008). The efficacy of this approach depends on several factors such as the effective energy transfer between PS and the scintillating material, the cellular uptake of the conjugate, and most importantly the singlet oxygen yield which in deeper tumor regions will be limited by hypoxic conditions (Chapman *et al.*, 1991; Moan & Sommer, 1985; Morgan *et al.*, 2009). Alternatively, a therapeutic approach based on the direct X-ray photoactivation of metal conjugated PS can be more suitable for the treatment of deep-seated tumors, because it acts *via* free-radical generation which is less likely to be affected by hypoxia. So far, only a few metal conjugated PSs such as gold complex of chlorin e6 (Tsuchida *et al.*, 2003) and iodinated pyropheophorbide derivative (Ishibashi *et al.*, 2013) have been investigated for the X-ray photoactivation treatment of cancer.

Recently, we have reported a novel metal complex of chlorin p_6 referred to as iodinated chlorin p_6 copper complex (IC p_6 -Cu) for potential use in PDT of cancer. IC p_6 -Cu demonstrated pronounced photodynamic activity *via* free-radical generation and induced potent phototoxic effect against cancer cells under both normoxic and hypoxic conditions (Sarbadhikary *et al.*, 2016). The presence of copper and iodine in IC p_6 -Cu makes it suitable for X-ray photoactivation using an X-ray energy of ≥ 8.9 keV or ≥ 33.2 keV, respectively. While a lower X-ray energy (~ 9 keV) due to low tissue penetration (half value layer ~ 1.0 mm) can be used for superficial tumors, higher-energy X-rays (~ 33 keV) due to better tissue penetration (half value layer ~ 2.0 cm) can be exploited for deeper tumor treatment. In the present study we explored the efficacy of IC p_6 -Cu for X-ray photoactivation-

induced cytotoxicity in two human oral cancer cell lines. The effects of synchrotron X-ray radiation (8–10 keV) without and with IC p_6 -Cu treatment on cell viability and colony forming ability of cancer cells were examined. Studies on cellular reactive oxygen species (ROS) levels, intracellular localization of IC p_6 -Cu, DNA damage and cell cycle progression were performed to understand the mode of IC p_6 -Cu-induced radiosensitization.

2. Materials and methods

2.1. Materials

IC p_6 -Cu was prepared from Cp $_6$ following the procedure described in our Indian patent application (No. 4912/MUM/2015). Stock solution of concentrated IC p_6 -Cu (molecular weight 792) was made in ethanol:PEG (400):water (20:30:50) and used in experiments.

The fluorescence organelle probes mito tracker green, lyso tracker blue, ER tracker green and Golgi tracker green were obtained from Thermo Fischer Scientific, USA. 2',7'-Dichlorodihydrofluorescein diacetate (DCFH-DA), Hoechst 33342 (HO), propidium iodide (PI), and Dulbecco's modified eagle's medium (DMEM) were purchased from Sigma, USA. Phosphate-buffered saline (PBS), tetrazolium salt 3-(4,5-dimethylthiazol-2-yl)-2,5-diphenyltetrazolium bromide (MTT), trypsin/EDTA and fetal bovine serum (FBS) were obtained from Himedia, India. All other solvents and reagents used were of analytical grade.

2.2. Cell culture

Two oral carcinoma cell lines, NT8e and 4451, obtained from ACTREC, Mumbai, India, and INMAS, Delhi, India, respectively, were maintained in DMEM containing antibiotics (streptomycin, nystatin and penicillin) and 10% FBS. Cells were grown at 37°C under 5% CO $_2$ + 95% air atmosphere in a humidified incubator (ESCO). The cells after 80% confluent growth were harvested by trypsinization and plated either in flat-bottomed 96-well plates, 24-well plates or glass-bottom petridishes. The cells were allowed to grow for 18 h and then used for the experiments.

2.3. Cellular uptake of IC p_6 -Cu

The monolayer of cells ($\sim 2 \times 10^5$ cells) grown in a 24-well plate were incubated in DMEM medium containing 10, 20 and 30 μ M IC p_6 -Cu for 3 h at 37°C, in the dark. The cells were washed twice with PBS and solubilized in 200 μ l detergent solution (0.1 M NaOH + 0.1% SDS) by scrapping and repeated pipetting. After centrifugation (10000 r.p.m., 10 min), absorption of the cell extract at 640 nm was measured on a plate reader (Power Wave 340, Bio-tek instruments Inc., USA). The protein content of each sample was determined by bicinchoninic acid protein assay (Sapan *et al.*, 1999) and a standard curve of IC p_6 -Cu prepared in NaOH/SDS solution was used to calculate the amount of IC p_6 -Cu in cells (nM μ g $^{-1}$ of protein).

2.4. Intracellular localization of ICp_6 -Cu

The distribution of ICp_6 -Cu in various cell organelles was studied by fluorescence imaging using an LSM 880 confocal microscope (Carl Zeiss, Germany). The cells grown on glass-bottom petriplates were incubated with $10\ \mu M$ ICp_6 -Cu in DMEM medium for 3 h at $37^\circ C$, in the dark. The cells were then washed twice with PBS and stained with either ER tracker green, mito tracker green, lyso tracker blue, Golgi tracker green or HO. The localization of ICp_6 -Cu in cells was imaged by excitation with a 405 nm diode laser and collection of the emitted fluorescence using a 570 nm long-pass filter on a high-sensitivity GaAsP detector. HO and lyso tracker blue were excited with the 405 nm laser and fluorescence emission from 420 nm to 480 nm was imaged on a photomultiplier tube (PMT) detector. Mito, Golgi and ER tracker probes were excited at 488 nm with argon ion laser and the emitted fluorescence emission from 490 nm to 560 nm was recorded on the PMT detector.

2.5. ICp_6 -Cu treatment and X-ray irradiation

NT8e and 4451 cells grown in 96-well plates were incubated in growth medium containing ICp_6 -Cu for 3 h, in the dark. The cell monolayers were washed twice with DMEM (without serum) and, subsequent to the addition of fresh DMEM, were exposed to X-ray radiation (8–10 keV) using beamline BL7 of the Indus-II synchrotron source at Raja Ramanna Centre for Advanced Technology, Indore, India. A photograph of the experimental setup is shown in Fig. 1(a). The X-ray energy was tuned in the range 8–10 keV (Fig. 1b) by inserting a $396\ \mu m$ -thick aluminium filter into the beam path. For irradiation, the 96-well plate was mounted vertically on a motorized stage in front of the source. The beam size was $3.5\ mm \times 70\ mm$ to allow simultaneous irradiation of six wells horizontally. The variation in photon flux of the beam in the horizontal direction was $<7.0\%$. Further, the stage was translated in the vertical

direction to ensure homogeneous exposure. Absorbed X-ray doses were determined using the xylene orange Fricke dosimetry method (Gohary *et al.*, 2015). The dose rate computed from a plot of the change in absorbance of xylene orange Fricke solution *versus* number of scans was $\sim 33.5 \pm 0.6\ cGy\ scan^{-1}$ (see Fig. S1 of the supporting information). An X-ray dose of 1–17 Gy was delivered by varying the number of scans. To take into account the ring current variation, prior to each exposure (samples in a 96-well plate) the scan translation speed of the stage was adjusted in the range from $7\ mm\ s^{-1}$ to $9\ mm\ s^{-1}$ with respect to the value of the ring current variation. Further, to minimize the day-to-day variation, the experiments were performed when the ring current was between 90 and 120 mA. For this, the time to initiate the sample preparation was adjusted accordingly. In addition, prior to each experiment, a 96-well plate containing xylene orange Fricke solution was also exposed to X-rays to ensure that the dose delivered was almost the same in different experiments.

2.6. Cell cytotoxicity assay

After X-ray irradiation, the cells were washed with DMEM (without serum) and allowed to grow for 96 h at $37^\circ C$ under $5\%\ CO_2 + 95\%$ air atmosphere. Subsequently, X-ray-induced cytotoxicity without and with ICp_6 -Cu pre-treatment was determined by MTT assay (Price & McMillan, 1990). In live cells, MTT is converted into dark blue formazan through enzymatic action of mitochondrial succinate dehydrogenase and the optical density of the color produced is used to determine the relative number of viable cells (Mosmann, 1983). To perform this assay, the growth medium from the cells was replaced with DMEM (without serum) containing $0.5\ mg\ ml^{-1}$ MTT. After incubation at $37^\circ C$ for 3 h in the dark, the medium was removed and $100\ \mu l$ DMSO was added to dissolve the formazan crystals formed within the cells. The absorbance of the samples at 570 nm with reference wavelength at 690 nm was read using a microplate reader. The percent cytotoxicity was calculated with respect to the absorbance value of the control samples.

2.7. Clonogenic survival assay

The sensitizer enhancement ratio (SER) at 7 Gy was determined by clonogenic survival assay. Cells were seeded in 24-well plates (~ 100 cells per well) and allowed to attach overnight. Then cells were treated with ICp_6 -Cu ($10, 20, 30\ \mu M$) for 3 h and then irradiated with X-rays at a fixed dose of 7 Gy which was predetermined from cytotoxicity experiments. After irradiation, the cells were washed with DMEM media (without serum) and allowed to grow for 10–14 days to form colonies.

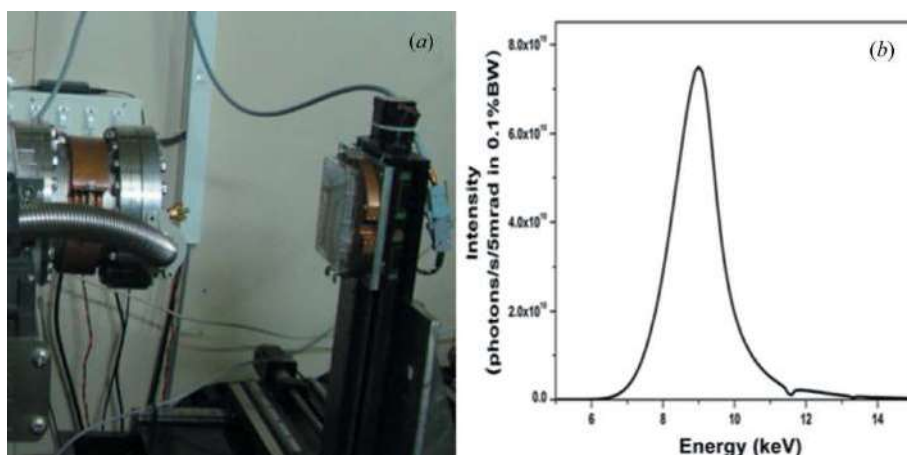


Figure 1
(a) Experimental set-up at the X-ray lithography beamline (BL7) used for X-ray irradiation of cells in a 96-well plate. The plate was mounted vertically onto a motorized stage in front of the beam (beam size of $3.5\ mm \times 70\ mm$). (b) Calculated spectrum of synchrotron X-rays in the energy range 8–10 keV.

The colonies were fixed in 4% paraformaldehyde, stained with crystal violet and then counted. The surviving fraction (SF) was calculated as

$$SF = \frac{\text{mean number of colonies formed after treatment}}{\text{number of cells seeded} \times PE}, \quad (1)$$

where PE (the plating efficiency) was determined as

$$PE = \frac{\text{mean number of colonies formed in untreated control}}{\text{number of cells seeded}} \times 100, \quad (2)$$

$$SER(7\text{ Gy}) = \frac{SF \text{ at } 7\text{ Gy of radiation alone}}{SF \text{ at } 7\text{ Gy of radiation} + IC_{p_6}\text{-Cu}}. \quad (3)$$

2.8. Detection of ROS generation

The relative level of intracellular ROS in cells was measured by fluorescence spectroscopy using the fluorescent probe DCFH-DA. The non-fluorescent DCFH-DA freely diffuses in cells and converted into a non-fluorescent product 2',7'-dichlorodihydrofluorescein (DCFH) by the enzymatic action of cellular esterases. In cells, DCFH reacts with ROS to yield a highly fluorescent product dichlorofluorescein (DCF). The fluorescence intensity of DCF in cells is directly proportional to the level of ROS (Rappole *et al.*, 2012). To perform this assay, the cells after X-ray irradiation were incubated at 37°C for 30 min in DMEM (without serum) containing 10 µM DCFH-DA. Cells were released by trypsinization, re-suspended in PBS and the fluorescence of DCF in cell suspension was measured on a spectrofluorometer (model Fluorolog-2; Spex, USA) using a 488 nm excitation wavelength and 525 nm emission wavelength with a band pass of ~1.7 nm and ~3.7 nm, respectively. The fluorescence intensity of DCF in the control and different treatment groups after normalization with the cell number was used to express the relative ROS levels.

2.9. γ-H2AX immunofluorescence

The effect of X-ray irradiation either alone or combined with IC_{p₆}-Cu treatment (30 µM, 3 h) on DNA damage and repair in oral cancer cells was determined by γ-H2AX immunofluorescence, which is a reliable and sensitive biomarker for the detection of DNA double-strand breaks (DSBs) (Mah *et al.*, 2010). For this, cells were grown on X-ray transparent Kapton film and, subsequent to X-ray exposure (~7.0 Gy), were fixed in 4% paraformaldehyde for 15 min at room temperature. The cells were washed three times with PBS, permeabilized by treatment with 0.5% Triton X-100 for 5 min. After washing three times with PBS the cells were treated with 5% BSA solution for 1 h to block non-specific binding sites. The cells were then incubated with mouse anti-human γ-H2AX antibody (Millipore, dilution 1:200) for 1.5 h, washed twice with 0.05% Tween-20 in PBS and incubated with Alexa Fluor 488 labeled rabbit anti-mouse antibody (Inv-

trogen, dilution 1:400) for 1 h. After a final wash with PBS for 10 min, cells were counterstained with DAPI (1 µg ml⁻¹) for 5 min and the fluorescence in the cells was examined on a Zeiss LSM 880 confocal microscope. Alexa Fluor was excited at 488 nm and its fluorescence was recorded in channel 1 with a bandpass of 490–560 nm. DAPI was excited at 405 nm and its fluorescence in the wavelength range 420–480 nm was recorded in channel 2. Images were captured using 40× (numerical aperture 1.3) objective and analyzed by *Image J* software to count the number of γ-H2AX foci in each cell. For each treatment and control, at least 100 cells were analyzed to obtain the value of the number of foci per cell.

2.10. Cell cycle analysis

The effect of X-ray irradiation without and with IC_{p₆}-Cu pre-treatment on cell cycle and cell death was assessed by flow cytometry. After X-ray irradiation, the cells were allowed to grow for 24 h and then the non-adherent cells in media were collected by centrifugation and the adherent cells were released by trypsinization. The adherent and non-adherent cells were mixed, washed with PBS, re-suspended in ice-cold 70% ethanol and stored at 4°C until analysis. For flow cytometry measurements, the cells were centrifuged, washed in PBS and re-suspended in 1.0 ml PBS containing 50 µg ml⁻¹ PI. The cells were kept at 4°C in the dark for ~18 h, and the DNA content in the cells was measured on a Cyflow cytometer (Partec, Germany). The percentage of cells in G₁, S and G₂/M phases of the cell cycle were analyzed from DNA histograms. The sub-G₁ hypodiploid DNA content peak in the histogram was used to determine the apoptotic population (Darzynkiewicz *et al.*, 2010).

2.11. Statistical analysis

All the experiments were performed at least three times using three replicates in each experiment. The data obtained from three independent experiments were plotted as mean ± standard deviation and a Student's t-test was applied for comparisons between different treatments. *p* < 0.05 was considered to be statistically significant.

3. Results

3.1. Intracellular uptake and localization of IC_{p₆}-Cu

As shown in Fig. 2, both NT8e and 4451 cells accumulated a significant amount of IC_{p₆}-Cu after 3 h incubation. The cellular level of IC_{p₆}-Cu was found to increase with concentration and, as compared with NT8e cells, 4451 cells showed significantly higher accumulation of IC_{p₆}-Cu at 20 µM and 30 µM. Next, we examined the intracellular distribution of IC_{p₆}-Cu in NT8e cells. In Fig. 3 the confocal microscopic image of NT8e cells showing the fluorescence of IC_{p₆}-Cu together with cell organelle probes ER and lyso tracker are presented. The red fluorescence of IC_{p₆}-Cu was observed mainly in cytoplasm [Figs. 3(a) and 3(d)]. The green fluorescence of lyso tracker as well as ER tracker is well demarcated [Figs. 3(b) and 3(e)] which overlapped considerably with the

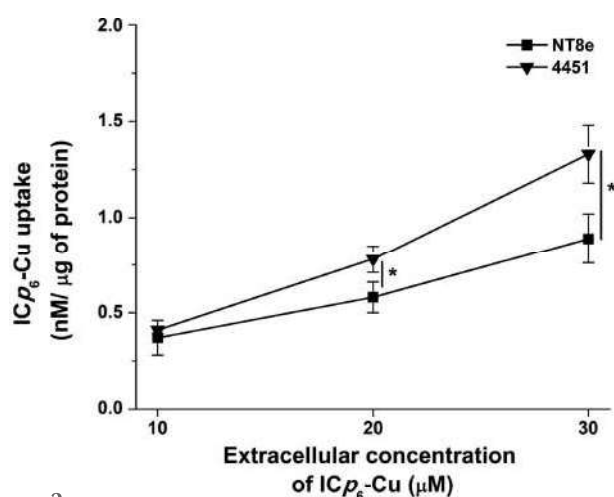


Figure 2
Intracellular uptake of ICp₆-Cu as a function of concentration in NT8e and 4451 cells. Data are mean \pm standard deviation of three independent experiments.

red fluorescence of ICp₆-Cu as indicated by yellow regions in the overlay images [Figs. 3(c) and 3(f)]. With mito and Golgi specific fluorescence probes, the fluorescence of ICp₆-Cu did not show significant overlap (data not shown). These observations showed that ICp₆-Cu localized mainly in lysosomes and ER.

3.2. ICp₆-Cu pre-treatment enhances X-ray-induced cytotoxicity

The effect of ICp₆-Cu pre-treatment on X-ray-induced cytotoxicity in NT8e and 4451 cells is shown in Fig. 4. In both of the cell lines, X-ray irradiation led to a dose-dependent decrease in cell viability wherein $\sim 50\%$ and 90% cytotoxicity was observed at ~ 10 Gy and ~ 17 Gy, respectively. In 4451 cells, pre-treatment with $10 \mu\text{M}$ ICp₆-Cu led to a significant increase in X-ray-induced cytotoxicity at X-ray doses ≥ 7.0 Gy (Fig. 4b), whereas, in NT8e cells, pre-treatment with $10 \mu\text{M}$ ICp₆-Cu did not lead to any significant increase in X-ray-induced cytotoxicity at any dose (Fig. 4a). At $20 \mu\text{M}$, ICp₆-Cu led to a significant increase in X-ray-induced cytotoxicity ($p < 0.05$) in both of the cell lines, and the magnitude of the effect was observed to increase further with increase in concentration of ICp₆-Cu. At 7 Gy X-ray dose, the loss of cell viability in 4451 cell was $\sim 38\%$ which increased to $\sim 48\%$, $\sim 64\%$ and $\sim 78\%$ in cells pre-treated with $10 \mu\text{M}$, $20 \mu\text{M}$ and $30 \mu\text{M}$ ICp₆-Cu, respectively. In NT8e cells, a similar concentration-dependent increase in X-ray-induced cytotoxicity was seen but the magnitude of the effect was significantly lower ($p < 0.05$) than that for 4451 cells (Fig. 4c). At 7 Gy X-ray dose, the loss of cell viability in NT8e cells was $\sim 42\%$ which increased to $\sim 47\%$, $\sim 56\%$ and $\sim 67\%$ in cells pre-treated with 10 , 20 and $30 \mu\text{M}$ ICp₆-Cu, respectively.

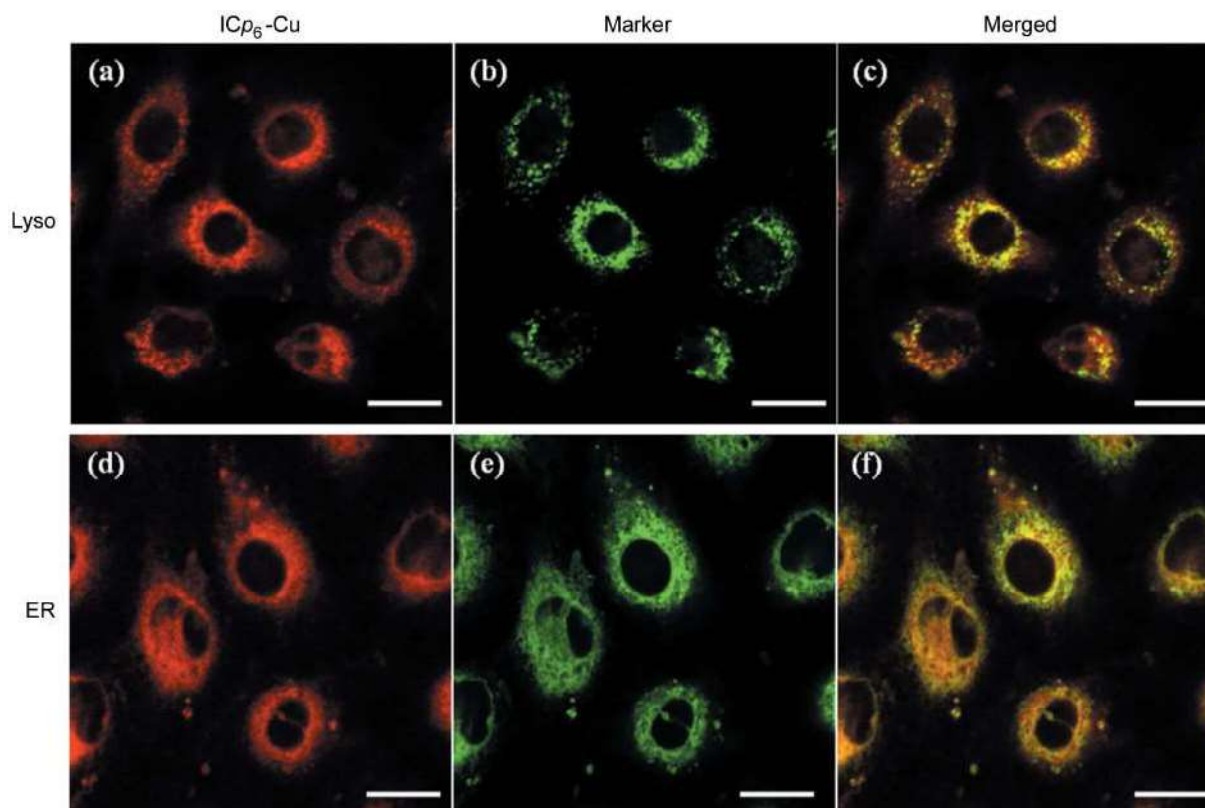


Figure 3
Localization of ICp₆-Cu in NT8e cells. Confocal fluorescence micrographs of NT8e cells showing red fluorescence of ICp₆-Cu (a, d), and green fluorescence of lysotracker (b), ER tracker (e) and the merged image of ICp₆-Cu and the organelle probes (c, f). Experiments were repeated three times with similar results and representative images are shown. Magnification $40\times$; scale bar $20 \mu\text{m}$.

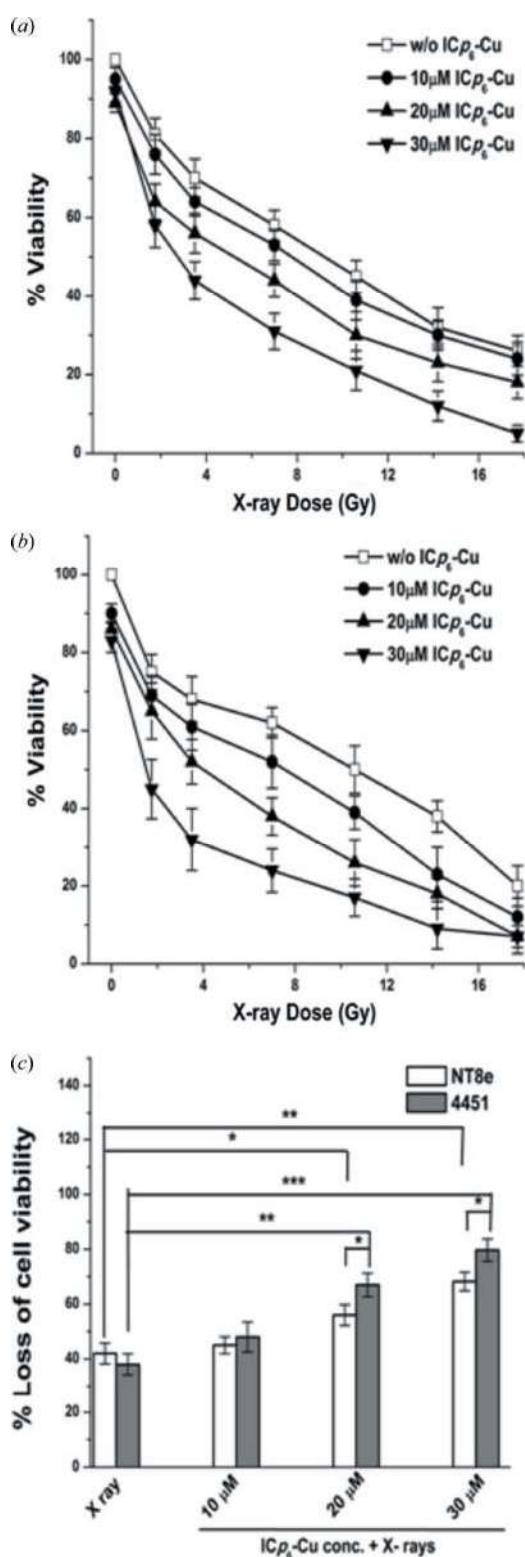


Figure 4
Cytotoxic effects of X-rays without and with ICp_6-Cu pre-treatment in oral cancer cells determined by MTT assay. Changes in percent cell viability in NT8e (a) and 4451 (b) cells as a function of X-ray dose; the cells were pre-treated with 10, 20 and 30 μM ICp_6-Cu for 3 h. Percent cell viability was calculated with respect to a control sample (without ICp_6-Cu treatment). (c) Percent loss of cell viability in NT8e and 4451 for X-rays alone and X-rays plus ICp_6-Cu at 7 Gy X-ray dose. * ($p < 0.05$), ** ($p < 0.01$), *** ($p < 0.005$) indicate significant difference. Each data point is mean \pm standard deviation of three independent experiments.

3.3. X-ray dose enhancement effect by ICp_6-Cu

The effect of X-rays alone (7 Gy) and ICp_6-Cu plus X-ray treatment on the percent cell survival of NT8e and 4451 cells is shown in Fig. 5(a). Compared with X-rays alone, ICp_6-Cu plus X-ray treated cells shows a greater decrease in the surviving fraction and the magnitude of the effect increased with an increase in the concentration of ICp_6-Cu (Fig. 5a).

The SER obtained from the cell survival data for NT8e cells was ~ 1.0 , 1.7 and 2.68 at 10 μM , 20 μM and 30 μM ICp_6-Cu , respectively (Fig. 5b). Consistent with the MTT assay, the radiosensitization effect of ICp_6-Cu was more pronounced in 4451 cells than that for NT8e cells. SER values for 4451 cells

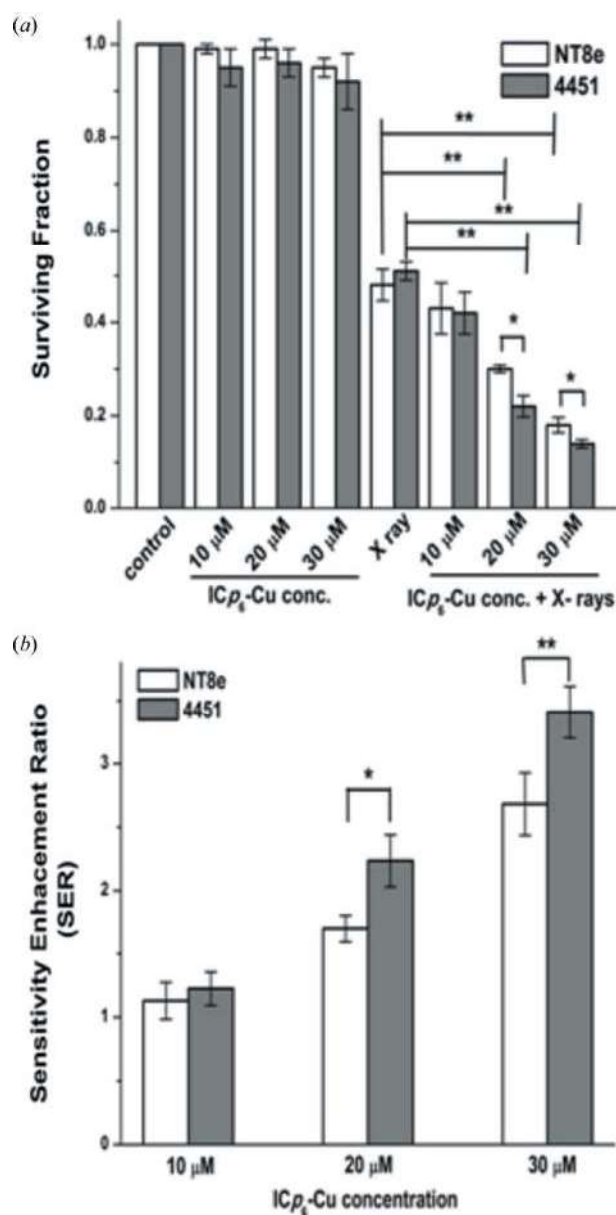


Figure 5
Radiosensitization effect of ICp_6-Cu in oral cancer cells determined by clonogenic assay. (a) Surviving fraction and (b) sensitivity enhancement ratio (SER) in NT8e and 4451. The cells were treated with ICp_6-Cu (10, 20 and 30 μM) for 3 h and then irradiated with X-rays at a fixed dose of 7.0 Gy. * ($p < 0.05$) and ** ($p < 0.01$) indicate significant difference. Data are mean \pm standard deviation of three independent experiments.

were ~ 1.0 , 2.23 and 3.4 at 10 μM , 20 μM and 30 μM $\text{ICp}_6\text{-Cu}$, respectively. At 20 and 30 μM , the values of SER for 4451 cells are significantly higher than those for NT8e cells ($p < 0.05$).

3.4. Enhancement in X-ray-induced ROS formation by $\text{ICp}_6\text{-Cu}$

The effect of X-ray irradiation on the relative level of ROS in 4451 and NT8e cells without and with $\text{ICp}_6\text{-Cu}$ pre-treatment is shown in Fig. 6. Results show that, compared with control, X-ray irradiation alone led to only a marginal increase in the intracellular level of ROS ($p < 0.05$) in both of the cell lines. The level of ROS in the combination group increased significantly relative to the X-rays alone, with a more pronounced increase in cells pre-treated with 20 μM and 30 μM $\text{ICp}_6\text{-Cu}$. These results correlated with the enhancement in X-ray-induced cytotoxicity supporting the radiosensitization efficacy of $\text{ICp}_6\text{-Cu}$.

3.5. DNA damage induction and repair

The formation of DSBs and its repair play a significant role in X-ray-induced cytotoxicity. $\gamma\text{-H2AX}$, a DNA damage-sensing protein, is a most reliable marker for radiation-induced DNA damage (Mah *et al.*, 2010). Microphotographs of 4451 and NT8e cells showing the presence of $\gamma\text{-H2AX}$ foci at 30 min, 2 h and 24 h after X-ray (7 Gy) irradiation are presented in Fig. 7. As expected, cells in control and $\text{ICp}_6\text{-Cu}$ treatment did not show $\gamma\text{-H2AX}$ foci [Figs. 7(a)-(i) and 7(a)-(ii)]. In contrast, cells irradiated with X-rays either without or with $\text{ICp}_6\text{-Cu}$ pre-treatment displayed a large number of

$\gamma\text{-H2AX}$ foci within 30 min after irradiation. At this time, the number of $\gamma\text{-H2AX}$ foci in X-rays alone and $\text{ICp}_6\text{-Cu}$ plus X-ray irradiated cells was almost equal (Fig. 7b) indicating that pre-treatment with $\text{ICp}_6\text{-Cu}$ did not affect X-ray-induced DNA damage. At 2 h and 24 h post-irradiation, the number of $\gamma\text{-H2AX}$ foci in X-ray-irradiated cells declined to $\sim 40\%$ and $\sim 15\%$, respectively, indicating repair of DSBs [Figs. 7(c)-(i) and 7(c)-(ii)], whereas in cells treated with $\text{ICp}_6\text{-Cu}$ plus X-ray irradiation the number of $\gamma\text{-H2AX}$ foci decreased to a lesser extent by $\sim 60\%$ at 2 h and thereafter no significant decrease was observed [Figs. 7(c)-(i) and 7(c)-(ii)]. These results showed that DNA repair is impaired due to combined treatment. Moreover, the number of $\gamma\text{-H2AX}$ foci at 24 h after combined treatment was higher in 4451 cells than for NT8e cells (Fig. 7c) which was consistent with the higher radiosensitivity of 4451 cells.

3.6. Radiation-induced cell organelle damage

Since $\text{ICp}_6\text{-Cu}$ localized in lysosomes and ER, the possibility of damage to these vital organelles was studied by confocal fluorescence microscopy. In Fig. 8, microphotographs of NT8e cells in control, $\text{ICp}_6\text{-Cu}$ alone, X-ray irradiated and $\text{ICp}_6\text{-Cu}$ plus X-ray irradiated cells are shown. In control, $\text{ICp}_6\text{-Cu}$ alone and X-ray irradiation, lysosomes are intact as indicated by well demarcated punctuate fluorescence [Figs. 8(a), 8(b) and 8(c)]; whereas in cells that received combined treatment the fluorescence of lysotracker was diffuse and less intense indicating disintegration of lysosomes [Fig. 8(d)]. X-ray irradiation alone or $\text{ICp}_6\text{-Cu}$ plus X-rays led to no significant

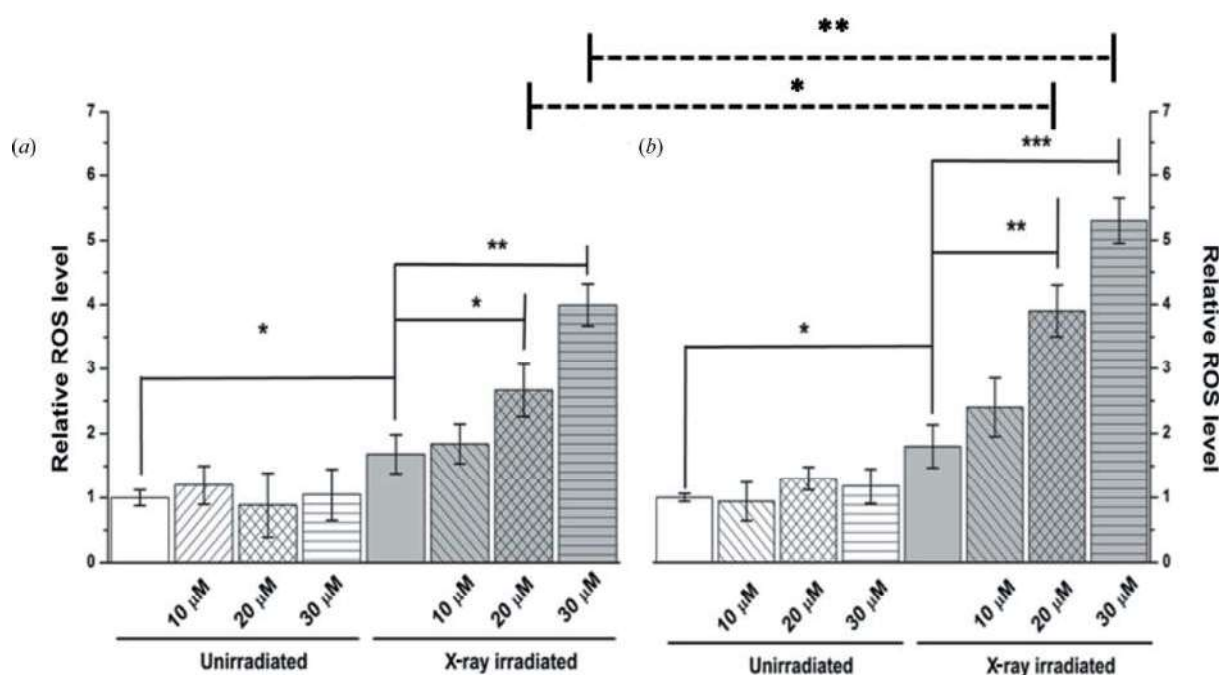


Figure 6
Effects of $\text{ICp}_6\text{-Cu}$ and X-ray irradiation on ROS formation. Relative levels of ROS after X-ray irradiation (7 Gy), in NT8e (a) and 4451 (b) without or with $\text{ICp}_6\text{-Cu}$ pre-treatment. Data are mean \pm standard deviation of three independent experiments. * ($p < 0.05$), ** ($p < 0.01$), *** ($p < 0.005$) indicate statistical significance.

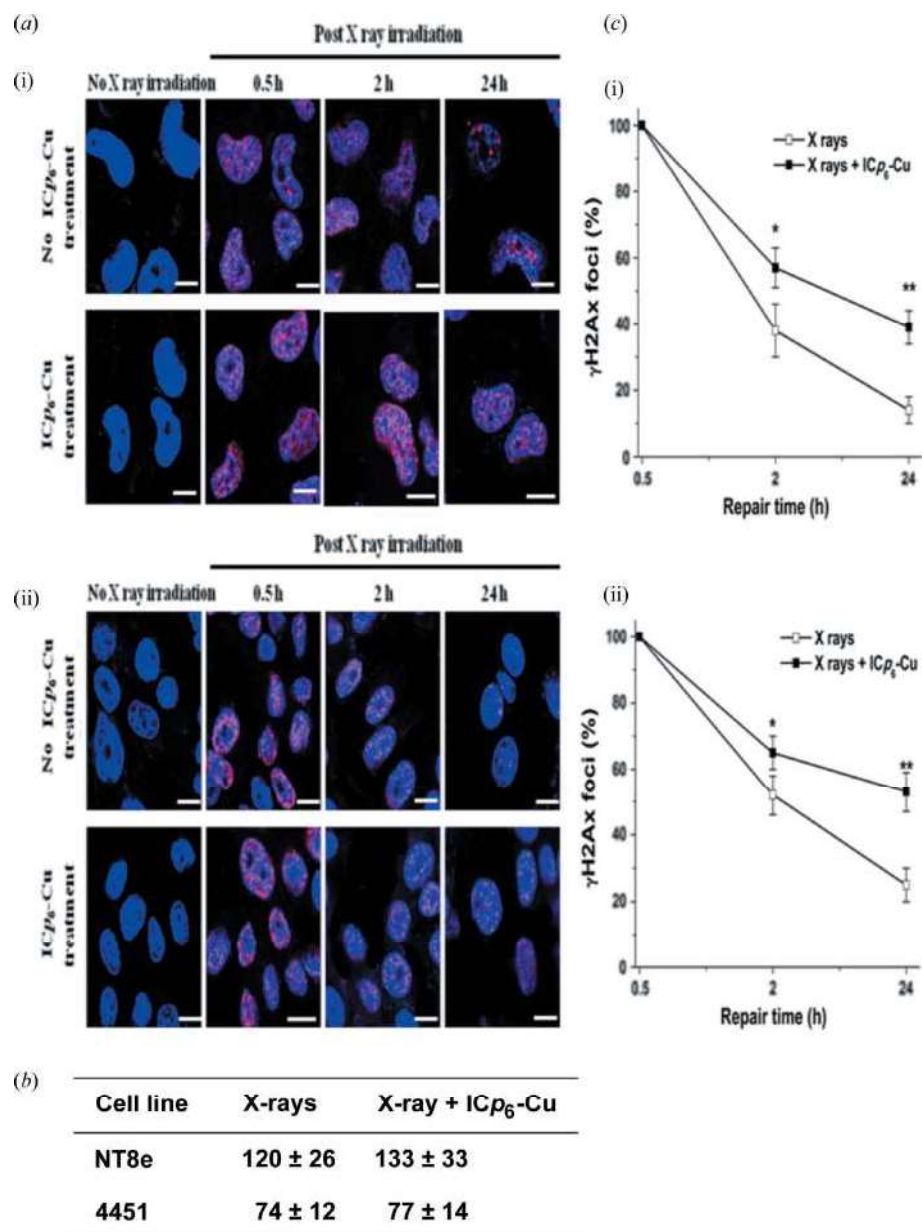


Figure 7
Effect of ICp_6 -Cu and X-ray irradiation on DNA damage determined by γ -H2AX immunostaining. (a) Representative immunofluorescence images of NT8e (i) and 4451 (ii) cells treated without (upper panel) or with (lower panel) 30 μ M ICp_6 -Cu at various time points post-irradiation (7 Gy). Images show cell nuclei in blue and γ -H2AX foci in red. (b) Number of γ -H2AX foci at 30 min post-irradiation (7 Gy) in NT8e and 4451 cells without or with ICp_6 -Cu treatment (30 μ M). (c) Changes in percentage of γ -H2AX foci in NT8e (i) and 4451 (ii) cells treated with or without 30 μ M ICp_6 -Cu at different time periods post-irradiation (7 Gy), indicating repair kinetics of DSBs. Data represent mean \pm standard deviation obtained from three independent experiments. * ($p < 0.05$), ** ($p < 0.01$) indicate statistical significance between X-rays alone and ICp_6 -Cu plus X-ray treatment.

change in ER structure (Fig. S2 of the supporting information).

3.7. Cell cycle distribution and induction of cell death

Fig. 9 shows the effect of X-ray irradiation without and with ICp_6 -Cu treatment on the cell cycle distribution in NT8e and 4451 cells. As compared with the control, ICp_6 -Cu treatment alone showed no effect on the cell cycle. X-rays alone and

X-rays in combination with ICp_6 -Cu treatment led to no change in the fraction of cells in S and G2/M which suggested that these treatments have no effect on cell cycle distribution, *i.e.* no cell cycle arrest. In addition, results also revealed that, compared with X-rays alone, the combined treatment led to a significant increase in apoptosis as indicated by the $\sim 15\%$ increase in sub-G1 population ($p < 0.05$) [Fig. 9(b)].

4. Discussion

ICp_6 -Cu is a novel chlorophyll-based PS recently reported by us for potential application in the PDT of cancer (Sarbadhikary *et al.*, 2016). The motivation to synthesize ICp_6 -Cu was to exploit the tumor-localizing property of chlorin for multi-modal cancer therapy. One such modality is X-ray photon activation therapy, which in comparison with light-based PDT offers the advantage that the tumor in a deep tissue region can also be treated. Use of metal-based porphyrin can provide an important advantage that the damage to surrounding normal tissue can be minimized due to its selective accumulation in tumor and subsequent localized dose enhancement effect of X-ray photoactivation. Thus, the combined treatment approach may possibly be employed for the treatment of oral cavity cancer where sparing normal tissue architecture and function is important. With this motivation we explored the efficacy of ICp_6 -Cu for X-ray photoactivation-induced cytotoxicity in oral cancer cells. Results of our study show that ICp_6 -Cu combined with synchrotron X-rays induced significant radiosensitization in the two oral cancer cell lines. At present, the X-ray photoactivation of ICp_6 -Cu is performed using an X-ray energy above the *K*-edge absorption of copper

(>8.9 keV). Based on the linear absorption coefficient of the soft tissue (Böke, 2014), the estimated half value layer for 9 keV is ~ 1 mm (the depth in tissue where the fluence reduces by 50%) which is suitable for only superficial small tumors. The sensitivity enhancement ratio at 20 μ M ICp_6 -Cu was >1.0 and increased further at higher concentration [Fig. 5(b)] due to an increase in cellular uptake (Fig. 2). Interestingly, the radiosensitization effect of ICp_6 -Cu was more pronounced in 4451 cells compared with NT8e cells. An important difference

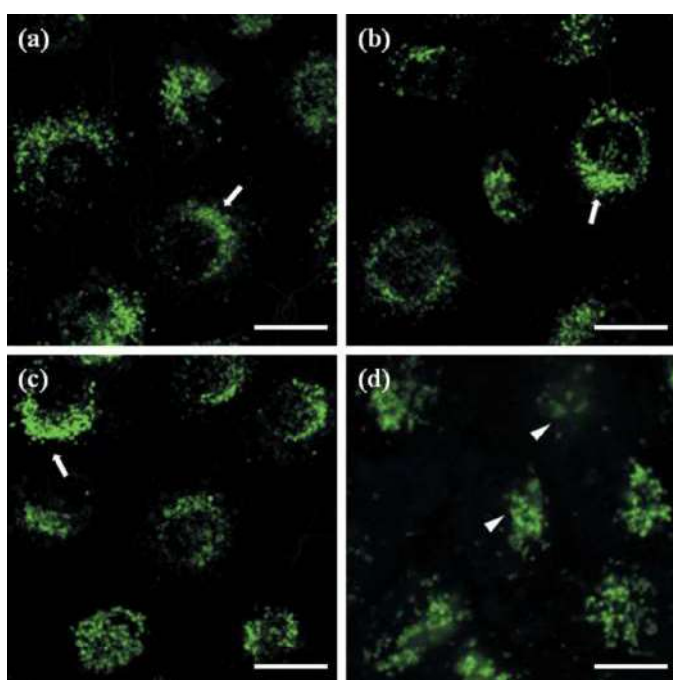


Figure 8

Confocal fluorescence micrographs of NT8e cells showing the effect of ICp_6 -Cu-induced radiosensitization on the integrity of lysosomes. Cells were stained with lysosome-specific lysoTracker probe. (a) Control, (b) ICp_6 -Cu (30 μ M) treatment alone, (c) X-ray (7 Gy) treatment alone and (d) ICp_6 -Cu (30 μ M) plus X-ray (7 Gy) treatment. Experiments were repeated three times with similar results and representative images are shown. Arrows indicate intact lysosome; arrow heads indicate weakly disintegrated lysosomes. Magnification 40 \times ; scale bar 20 μ m.

between the two cell lines is the status of the p53 gene, *i.e.* cell line 4451 has the mutated p53 gene (Zölzer *et al.*, 1995) whereas NT8e has wild-type p53 (Mulherkar *et al.*, 1997). However, the difference in their sensitivity to radiosensitization cannot be attributed to the difference in the status of p53, because the sensitivity of the two cell lines to X-rays alone was almost similar (Fig. 4). The relationship between p53 status and radiosensitivity is not well understood and there are several conflicting reports on radiosensitivity *versus* p53 gene mutation (Anderson *et al.*, 2014; Takahashi *et al.*, 2004; Zhang *et al.*, 2015). As shown in Figs. 2 and 6, the intracellular level of ICp_6 -Cu and the relative level of ROS are significantly higher in 4451 cells than for NT8e cells. These results correlated with the higher sensitivity of 4451 cells to ICp_6 -Cu-induced radiosensitization and further substantiate the role of photoactivation-induced ROS generation in the radiosensitization effect of ICp_6 -Cu. The results are also in agreement with the fact that ROS generated *via* radiolysis of water plays a major role in X-ray-induced cytotoxicity, and the presence of X-ray absorbing metal can further enhance this process (Kobayashi *et al.*, 2010). Here it is important to note that the irradiation of high-Z elements is expected to yield better radiosensitization efficacy because they can generate more secondary electrons than by irradiating lower-Z elements (Kobayashi *et al.*, 2010). In the present study, the X-ray energy used for photoactivation of ICp_6 -Cu was close to the copper *K*-edge absorption. Since ICp_6 -Cu also contains iodine, irradiation with the X-ray energy tuned to the iodine

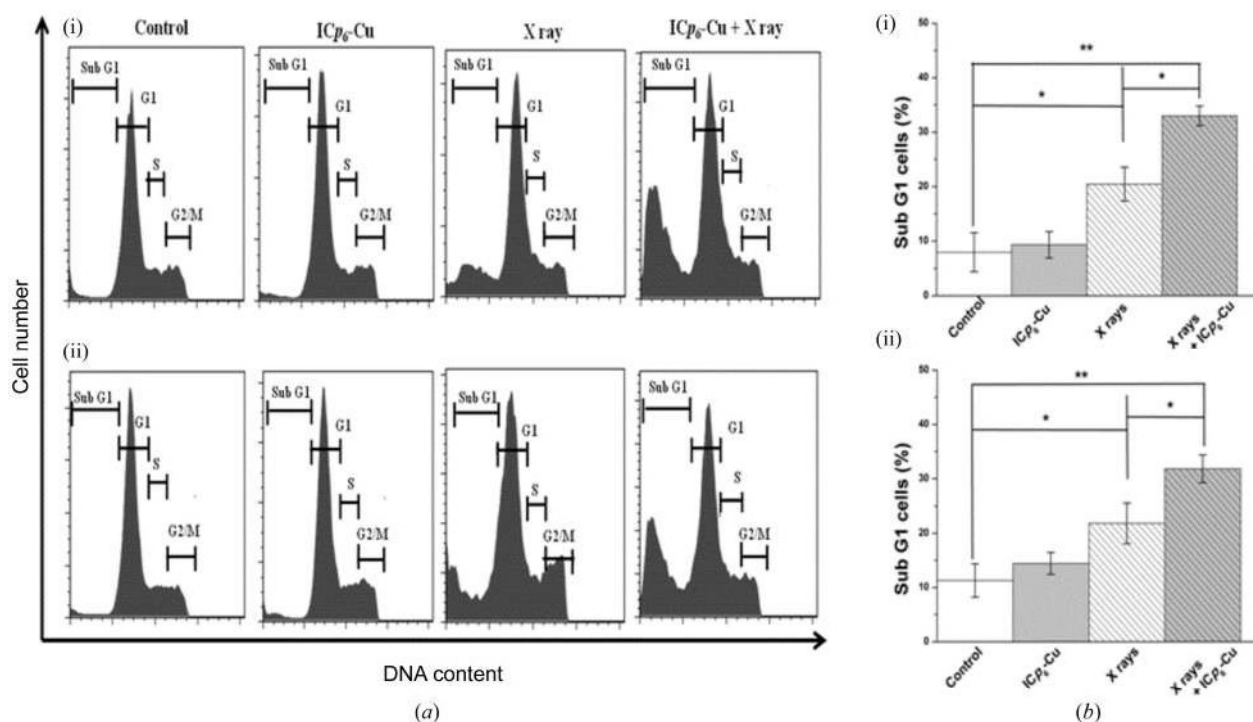


Figure 9

Effect of ICp_6 -Cu and X-ray irradiation on cell cycle distribution in NT8e and 4451 at 24 h post-irradiation. (a) Cell cycle histograms of NT8e (i) and 4451 (ii) cells. (b) Percentage of NT8e (i) and 4451 (ii) cells in sub-G1-phase, for control, ICp_6 -Cu treatment alone, X-ray irradiation alone and ICp_6 -Cu plus X-ray treatment. The cells were treated with 30 μ M ICp_6 -Cu for 3 h and then irradiated with X-rays at a fixed dose of 7 Gy. Data represent mean \pm standard deviation obtained from three independent experiments. * ($p < 0.05$), ** ($p < 0.01$) indicate statistical significance.

K_{α} edge (~ 33 keV) may produce more efficient radiosensitization against cancer cells.

An important mechanism of the radiosensitization effect of currently applied PAT drugs such as cisplatin and 5-iodo-2'-deoxyuridine is the enhancement in DNA damage and/or inhibition of DNA repair which is primarily attributed to the localization of these drugs in the cell nucleus (Turchi *et al.*, 2000; Biston *et al.*, 2009; Bayart *et al.*, 2017). As shown in Fig. 7(b), ICp₆-Cu pre-treatment did not lead to any increase in the level of X-ray-induced DSBs which is consistent with the absence of its localization in the cell nucleus (Fig. 3). Interestingly, analysis of γ -H2AX foci at 2 h and 24 h post-irradiation (Fig. 7c) revealed that the repair of DSBs is significantly inhibited in ICp₆-Cu treated cells. Previous studies have shown that platinated drugs inhibit or delay X-ray-induced DSBs due to the formation of cisplatin–DNA adducts (Turchi *et al.*, 2000). For, ICp₆-Cu the reason for the inhibition of DNA repair and accumulation of unrepaired DNA is not clear. The observations that ICp₆-Cu localized in lysosomes and combined treatment led to disintegration of lysosomes suggested that, unlike platinum drugs, the radiosensitization effect of ICp₆-Cu involved dose deposition in cytoplasm and damage to vital cell organelles. The formation of free radicals and ROS due to the photoactivation of ICp₆-Cu in lysosomes may lead to inactivation of lytic enzymes and destabilization of these organelles (Persson *et al.*, 2005; Dayal *et al.*, 2014). Lysosomes play an important role in the clearance of damaged DNA through the action of *Dnase2a*, a lysosomal endonuclease that degrades DNA to oligonucleotides and nucleotides. Recent studies have shown that the deficiency of *Dnase2a* results in elevated levels of DSBs subsequent to treatment with DNA-damaging agents (Lan *et al.*, 2014). Moreover, the persistence of unrepaired DSBs has been identified as a potentially lethal event that triggers apoptotic cell death (Roos & Kaina, 2013). Consistent with this, ICp₆-Cu plus X-ray treatment led to significant increase in sub-G1 population that mainly corresponds to apoptotic cells (Darzynkiewicz *et al.*, 2010).

5. Conclusions

Results demonstrated that ICp₆-Cu through X-ray photoactivation induced potent radiosensitization effect in oral cancer cells. The underlying mechanism of radiosensitization involved photoactivation-induced enhancement in ROS production, damage to lysosomes and subsequent impairment of the ability of cells to repair X-ray-induced DSBs. Since an X-ray energy of 9.0 keV penetrates only a few millimeters in soft tissue, it needs further investigations using X-ray energies tuned to the iodine K_{α} edge (~ 33 keV) to establish the efficacy of ICp₆-Cu for the treatment of deep-seated tumors.

Acknowledgements

We would like to thank Dr B. S. Dwarakanath, INMAS, Delhi, and Dr U. M. Warawdekar, ACTREC, Mumbai, for providing the oral cancer cell lines. We are also thankful to Dr V. P.

Dhamgaye and Shri. B. S. Thakur for their assistance in carrying out X-ray irradiation experiments at beamline BL7 of the Indus-II synchrotron source at our center. We would like to acknowledge Dr Santosh K. Sandur and Dr Deepak Sharma (BARC) for providing technical support and expert guidance in flow cytometry experiments. PS acknowledges Homi Bhabha National Institute, Mumbai, for a senior research fellowship. Disclosure statement: Alok Dube, Paromita Sarbadhikary and Pradeep Kumar Gupta are named patent inventors for Indian Patent Application No. 4912/MUM/2015 titled 'A metal complex of chlorophyll derivative for magnetic resonance imaging and photodynamic therapy', filed on 29 December 2015.

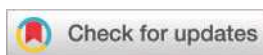
Funding information

The following funding is acknowledged: Department of Atomic Energy, Government of India, Homi Bhabha National Institute, Raja Ramanna Centre of Advanced Technology (scholarship No. Senior Research Fellowship to Paromita Sarbadhikary).

References

- Abrahamse, H. & Hamblin, M. R. (2016). *Biochem. J.* **473**, 347–364.
- Adam, J. F., Biston, M., Rousseau, J., Boudou, C., Charvet, A., Balosso, J., Estève, F. & Elleaume, H. (2008). *Phys. Med.* **24**, 92–97.
- Adam, J. F., Joubert, A., Biston, M. C., Charvet, A. M., Peoc'h, M., Le Bas, J. F., Balosso, J., Estève, F. & Elleaume, H. (2006). *Int. J. Radiat. Oncol. Biol. Phys.* **64**, 603–611.
- Anderson, D. L., Mirzayans, R., Andrais, B., Siegbahn, E. A., Fallone, B. G. & Warkentin, B. (2014). *J. Synchrotron Rad.* **21**, 801–810.
- Astolfi, L., Ghiselli, S., Guaran, V., Chicca, M., Simoni, E., Olivetto, E., Lelli, G. & Martini, A. (2013). *Oncol. Rep.* **29**, 1285–1292.
- Bayart, E., Pouzoulet, F., Calmels, L., Dadoun, J., Allot, F., Plagnard, J., Ravanat, J. L., Bridier, A., Denozière, M., Bourhis, J. & Deutsch, E. (2017). *PLoS One*, **12**, e0168395.
- Biston, M. C., Joubert, A., Adam, J. F., Elleaume, H., Bohic, S., Charvet, A. M., Estève, F., Foray, N. & Balosso, J. (2004). *Cancer Res.* **64**, 2317–2323.
- Biston, M. C., Joubert, A., Charvet, A. M., Balosso, J. & Foray, N. (2009). *Radiat. Res.* **172**, 348–358.
- Böke, A. (2014). *Radiat. Phys. Chem.* **102**, 49–59.
- Ceresa, C., Nicolini, G., Semperboni, S., Requardt, H., Le Duc, G., Santini, C., Pellei, M., Bentivegna, A., Dalprà, L., Cavaletti, G. & Bravin, A. (2014). *Anticancer Res.* **34**, 5351–5355.
- Chapman, J., Stobbe, C., Arnfield, M., Santus, R., Lee, J. & McPhee, M. (1991). *Radiat. Res.* **126**, 73–79.
- Chen, H., Wang, G. D., Chuang, Y. J., Zhen, Z., Chen, X., Biddinger, P., Hao, Z., Liu, F., Shen, B., Pan, Z. & Xie, J. (2015). *Nano Lett.* **15**, 2249–2256.
- Choi, G. H., Seo, S. J., Kim, K. H., Kim, H. T., Park, S. H., Lim, J. H. & Kim, J. K. (2012). *Radiat. Oncol.* **7**, 184.
- Darzynkiewicz, Z., Halicka, H. D. & Zhao, H. (2010). *Adv. Exp. Med. Biol.* **676**, 137–147.
- Dayal, R., Singh, A., Pandey, A. & Mishra, K. P. (2014). *J. Cancer Res. Ther.* **10**, 811–818.
- Deman, P., Edouard, M., Besse, S., Vautrin, M., Elleaume, H., Adam, J. F. & Estève, F. (2010). *Rev. Med. Interne.* **31**, 586–589.
- Engels, E., Lerch, M., Tehei, M., Konstantinov, K., Guatelli, S., Rosenfeld, A. & Corde, S. (2017). *J. Phys. Conf. Ser.* **777**, 012011.
- Gil, S., Fernández, M., Prezado, Y., Biete, A., Bravin, A. & Sabés, M. (2011). *Clin. Transl. Oncol.* **13**, 715–720.
- Gohary, M. I. El., Shabban, Y. S., Amin, E. A., Abdel Gawad, M. H. & Desouky, O. S. (2015). *Nat. Sci.* **13**, 139–143.

- Hainfeld, J. F., Dilmanian, F. A., Slatkin, D. N. & Smilowitz, H. M. (2008). *J. Pharm. Pharmacol.* **60**, 977–985.
- Ishibashi, N., Fujiwara, K., Pandey, R. K., Kataba, M., Oguni, A., Igarashi, J., Soma, M., Shizukuishi, T., Maebayashi, T. & Abe, K. (2013). *Nihon Univ. J. Med.* **72**, 212–219.
- Kašćáková, S., Giuliani, A., Lacerda, S., Pallier, A., Mercère, P., Tóth, E. & Réfrégiers, M. (2015). *Nano Res.* **8**, 2373–2379.
- Kobayashi, K., Usami, N., Porcel, E., Lacombe, S. & Le Sech, C. (2010). *Mutat. Res.* **704**, 123–131.
- Lan, Y. Y., Londoño, D., Bouley, R., Rooney, M. S. & Hacohen, N. (2014). *Cell. Rep.* **9**, 180–192.
- Liu, Y., Chen, W., Wang, S. & Joly, A. G. (2008). *Appl. Phys. Lett.* **92**, 043901.
- Mah, L., El-Osta, A. & Karagiannis, T. (2010). *Leukemia*, **24**, 679–686.
- Moan, J. & Sommer, S. (1985). *Cancer Res.* **45**, 1608–1610.
- Morgan, N. Y., Kramer-Marek, G., Smith, P. D., Camphausen, K. & Capala, J. (2009). *Radiat. Res.* **171**, 236–244.
- Mosmann, T. (1983). *J. Immunol. Methods*, **65**, 55–63.
- Mulherkar, R., Goud, A. P., Wagle, A. S., Naresh, K., Mahimkar, M. B., Thomas, S. M., Pradhan, S. & Deo, M. (1997). *Cancer Lett.* **118**, 115–121.
- Persson, H. L., Kurz, T., Eaton, J. W. & Brunk, U. T. (2005). *Biochem. J.* **389**, 877–884.
- Price, P. & McMillan, T. J. (1990). *Cancer Res.* **50**, 1392–1396.
- Rappole, C. A., Mitra, K. & Wen, H. (2012). *Opt Nanoscopy*, **1**, 5.
- Ricard, C., Fernandez, M., Requardt, H., Wion, D., Vial, J.-C., Segebarth, C. & van der Sanden, B. (2013). *J. Synchrotron Rad.* **20**, 777–784.
- Roos, W. P. & Kaina, B. (2013). *Cancer Lett.* **332**, 237–248.
- Rousseau, J., Adam, J.-F., Deman, P., Wu, T.-D., Guerquin-Kern, J.-L., Gouget, B., Barth, R. F., Estève, F. & Elleaume, H. (2009). *J. Synchrotron Rad.* **16**, 573–581.
- Sapan, C. V., Lundblad, R. L. & Price, N. C. (1999). *Biotechnol. Appl. Biochem.* **29**, 99–108.
- Sarbadhikary, P., Dube, A. & Gupta, P. K. (2016). *RSC Adv.* **6**, 75782–75792.
- Su, X. Y., Liu, P. D., Wu, H. & Gu, N. (2014). *Cancer Biol. Med.* **11**, 86–91.
- Takahashi, A., Matsumoto, H., Yuki, K., Yasumoto, J. I., Kajiwar, A., Aoki, M., Furusawa, Y., Ohnishi, K. & Ohnishi, T. (2004). *Int. J. Radiat. Oncol. Biol. Phys.* **60**, 591–597.
- Taupin, F., Flaender, M., Delorme, R., Brochard, T., Mayol, J. F., Arnaud, J., Perriat, P., Sancey, L., Lux, F., Barth, R. F., Carrière, M., Ravanat, J. L. & Elleaume, H. (2015). *Phys. Med. Biol.* **60**, 4449–4464.
- Tsuchida, T., Kato, H., Okunaka, T., Harada, M., Ichinose, S. & Hirata, T. (2003). *Lung Cancer*, **41**, S133.
- Turchi, J. J., Henkels, K. M. & Zhou, Y. (2000). *Nucleic Acids Res.* **28**, 4634–4641.
- Wang, G. D., Nguyen, H. T., Chen, H., Cox, P. B., Wang, L., Nagata, K., Hao, Z., Wang, A., Li, Z. & Xie, J. (2016). *Theranostics*, **6**, 2295–2305.
- Zhang, J., Shen, L. & Sun, L. Q. (2015). *Cancer Lett.* **363**, 108–118.
- Zölzer, F., Hillebrandt, S. & Streffer, C. (1995). *Radiother. Oncol.* **37**, 20–28.



Cite this: *Photochem. Photobiol. Sci.*, 2017, **16**, 1762

Spectroscopic investigations on the binding of an iodinated chlorin p_6 -copper complex to human serum albumin

P. Sarbadhikary^{a,b} and A. Dube  ^{a,b}

The insertion of suitable metals or high Z elements in tumour-avid tetrapyrrole compounds is a promising approach to obtain potential agents for multimodal cancer therapeutics and tumour imaging. Using chlorin p_6 , a chlorophyll derivative, we synthesized a novel iodinated chlorin p_6 -copper complex (IC p_6 -Cu) that can be applied to the photodynamic therapy and photon activation therapy of cancer. In the present study, we investigated the interaction of IC p_6 -Cu with human serum albumin (HSA) using UV-Vis absorption and fluorescence spectroscopy. The addition of HSA to IC p_6 -Cu at physiological pH led to a ~ 7 nm red shift in its Soret and Q band absorption. The binding constant (K_b) and the number of binding sites (n) of IC p_6 -Cu obtained from the quenching of the intrinsic fluorescence of HSA were $2.9 \times 10^5 \text{ M}^{-1}$ and 1.2 respectively. The distance between the Trp-214 residue and IC p_6 -Cu computed from Förster non-radiative energy transfer (FRET) theory was 3.1 nm. The emission of the IC p_6 -Cu fluorescence when excited at the protein's Trp absorption (295 nm) further substantiated the FRET between the Trp residue and IC p_6 -Cu. Synchronous spectroscopy revealed that the quenching of protein Trp fluorescence was higher than that of Tyr with no significant shift in peak position. Results suggested that HSA acts as a carrier protein for IC p_6 -Cu with a high probability that the binding of IC p_6 -Cu occurred at subdomain IIA and the binding had no effect on the conformation of HSA.

Received 30th May 2017,
Accepted 15th October 2017

DOI: 10.1039/c7pp00197e

rsc.li/pps

Introduction

Porphyrins and chlorins have been extensively investigated as potential photosensitizers (PSs) for the photodynamic therapy (PDT) of cancer.^{1,2} The suitability of a PS for PDT is primarily determined by its photophysical properties such as the absorption coefficient in the wavelength region of therapeutic interest, the lifetime as well as the yield of the excited triplet state and the efficiency to generate reactive oxygen species (ROS).^{1,2} A promising approach to improve the photophysical properties of a PS is the insertion of a heavy metal or a non-metal in the tetrapyrrole ring, which promotes Inter System Crossing and improves the triplet state quantum yield and lifetime *via* the heavy atom effect.^{3,4} Metal complexes of porphyrins,⁵ chlorins,^{6,7} and bacteriochlorins⁸ have been synthesized and characterized as potential PSs for PDT. Moreover, metallo-porphyrins have also been investigated as potential agents for combined therapeutic approaches because they can offer dual anticancer activity through the photodynamic action and che-

mototoxic action of the metal ion.^{9,10} In addition, porphyrins radiolabelled with radioisotopes of various metals such as ⁹⁹Tc, ⁶⁴Cu, ^{68/67}Ga, ¹⁰⁹Pd, ¹⁴⁰Nd and ¹⁶⁶Ho and non-metal ¹²⁴I *etc.* have also been reported for their potential application in tumour imaging and therapy.¹¹

Despite their favourable properties, promising PSs often fail to produce desirable therapeutic outcomes and/or cause side effects due to a lack of tumour selectivity and prolonged retention in normal tissues. This is due to the fact that the change in the chemical nature of the PS brought about by the insertion of a metal ion can alter its ability to bind with a drug transport protein and can influence its pharmacokinetics and its accumulation in tumours. In this context, the interaction of porphyrin and chlorin derivatives with serum albumin, a major drug transport protein, has been the subject matter of several studies and it is well accepted that the structure, charge, and hydrophobicity of the PS can greatly influence its binding affinity with serum albumin. For example, hematoporphyrin, a clinically approved anionic PS, was shown to bind strongly to serum albumin, whereas tetramethylethylenepyrrolium porphyrin (TMPP), a cationic porphyrin, had a very weak association with albumin.¹² Studies on a series of porphyrins demonstrated that the affinity to bind to serum albumin correlated with an increase in the hydrophobicity of the porphyr-

^aRaja Ramanna Centre for Advanced Technology, Indore, Madhya Pradesh, India.
E-mail: okdube@rrcat.gov.in; Tel: +91731 2488437

^bHomi Bhabha National Institute, Training School Complex, Anushakti Nagar, Mumbai 400094, India

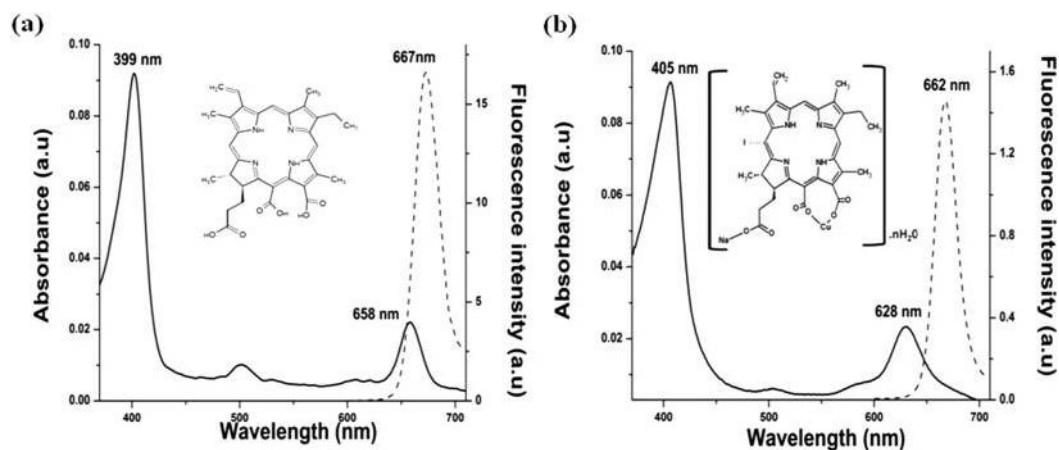


Fig. 1 Absorption and fluorescence spectra of Cp_6 (a) and ICp_6-Cu (b) in phosphate buffer (pH 7.4).

ins.¹³ However, chlorin-type PSs which differ from porphyrins with respect to the presence of a reduced pyrrole ring in the molecules showed an inverse correlation between their hydrophobicity and binding affinity to albumin.¹³

Recently we have reported a novel copper-containing iodinated chlorophyll derivative referred to as iodinated chlorin p_6 copper complex (ICp_6-Cu) as a potential PS for the PDT of cancer.¹⁴ Structurally, unlike other copper complexes of chlorophyll derivatives such as chlorophyllin, which contain copper attached to the pyrrole nitrogen, in ICp_6-Cu (Fig. 1), copper is attached *via* coordination with two adjacent side carboxylic groups at C13 and C15. The advantage of ICp_6-Cu over other PDT agents was found to be its ability to induce phototoxicity *via* free radical generation to allow the treatment of cancer cells under hypoxic conditions.¹⁴ Furthermore, ICp_6-Cu displayed selective antiproliferative activity against cancer cells through the alleviation of intracellular ROS levels in the dark.¹⁵ In the present study, we investigated the interaction of ICp_6-Cu with human serum albumin (HSA) using ultraviolet-visible (UV-Vis) and fluorescence spectroscopy. The binding constant and the number of binding sites are determined from the quenching of the intrinsic fluorescence of the protein. Förster energy transfer theory is applied to determine the distance between the tryptophan and the bound ICp_6-Cu . In addition, change in the conformation of HSA is probed by synchronous spectroscopy and the influence of such binding on the stability of the copper complex and the integrity of the protein have been discussed.

Materials and methods

Reagents and chemicals

ICp_6-Cu was synthesized as reported earlier in the Indian patent application no. 4912/MUM/2015 and was dissolved in 25 mM phosphate buffer (pH 7.4).¹⁴ A stock solution of HSA (Sigma, St Louis, USA) was prepared in phosphate buffer (pH 7.4). Millipore water was used throughout for the preparation

of the solution. All other chemicals were of analytical reagent grade and procured locally.

Spectroscopic measurements

The absorption spectra and fluorescence spectra of ICp_6-Cu (5 μ M) in the absence and in the presence of varying concentrations of HSA (0–10 μ M) were recorded using a 1.0 nm band pass on a double beam Cintra-20 spectrophotometer (GBC, Australia) and a Fluorolog-2 spectrofluorometer (Spex, USA), respectively. To assess the albumin binding affinity, the intrinsic fluorescence of HSA due to tryptophan (Trp) and tyrosine (Tyr) was excited at 280 nm and 295 nm (band pass 3.7 nm) and the emission spectra were recorded from 300–500 nm (band pass 1.7 nm). The fluorescence intensity of HSA in the presence of ICp_6-Cu was corrected for the inner filter effect using the following equation:

$$F_{\text{cor}} = F_{\text{obs}} \times e^{\frac{A_{\text{ex}} + A_{\text{em}}}{2}} \quad (1)$$

where F_{cor} and F_{obs} are the corrected and observed fluorescence intensities, respectively. A_{ex} and A_{em} are the absorptions of ICp_6-Cu at the excitation and the emission wavelengths, respectively.¹⁶ To determine the change in protein conformation, the synchronous fluorescence spectra of HSA from 220–350 nm with a difference between the excitation and emission wavelengths ($\Delta\lambda$) of 15 nm and 60 nm were recorded to resolve the intrinsic fluorescence of the Tyr and Trp residues, respectively. For fluorescence measurements, the concentration of HSA was fixed at 5 μ M, while the concentration of ICp_6-Cu was varied from 1 μ M to 10 μ M.

In FRET studies, the 280 nm and 295 nm excited fluorescence emission spectra of ICp_6-Cu were recorded on a FLS920-s spectrometer (Edinburgh Instruments Ltd, UK). The excitation and emission bandpasses were 2 nm and 3 nm, respectively and to eliminate the higher order excitation, a 330 nm short wavelength cut-off filter was placed before the emission monochromator.

Fluorescence lifetime measurements

The experiment setup used to determine the fluorescence lifetime of ICp_6 -Cu and Cp_6 consisted of a time-correlated single photon counting (TCSPC) system 'Lifespec-Red' (Edinburgh Instruments, UK) equipped with a Hamamatsu MCP-PMT. The system has an instrument response function (IRF) of ~ 40 ps. The chlorins were excited by vertically polarized light at 400 nm using a Coherent Mira 900F femtosecond laser system, the output of which was pulse picked (Coherent 9200 pulse picker) at a rate of 3.8 MHz and then the frequency doubled in an ultrafast harmonic generation system (Inrad 5-050). The excitation light was eliminated using an appropriate filter and emission was detected at the magic angle over the entire band. The fluorescence traces after deconvolution by the iterative reconvolution method were fitted to a single- or multiexponential function using FAST software of the TCSPC system.

Statistical analysis

Each experiment was repeated at least three times and the data shown in Fig. 3 and 5 represents values as the average \pm standard deviation.

Results and discussion

Interaction and binding of ICp_6 -Cu with HSA

The characterization of the property of potential anticancer drugs to bind with serum albumin is considered important in terms of understanding their mode of transport and accumulation in tumours. It is also believed that the macromolecular PS-protein complex can accumulate preferentially in tumours through the enhanced permeability and retention (EPR) effect.¹⁷ Using Cp_6 , an amphiphilic chlorophyll derivative, we have recently synthesized a novel metal complex ICp_6 -Cu (Fig. 1b) which can be exploited for multimodal cancer therapy and tumour imaging. In the present study, the interaction and binding of ICp_6 -Cu with HSA were characterized by absorption and fluorescence spectroscopy. The UV-Vis spectra and fluorescence of both ICp_6 -Cu and metal free chlorin p_6 (Cp_6) are shown in Fig. 1. As compared to Cp_6 , the Q band of ICp_6 -Cu is ~ 20 nm blue shifted and the fluorescence yield is ~ 10 times reduced. The large blue shift of the Q band is characteristic of the insertion of Cu in chlorin.¹⁴ The changes in the absorption spectra of 5 μ M ICp_6 -Cu in phosphate buffer (pH 7.4) alone and upon addition of increasing concentrations of HSA are shown in Fig. 2. The Soret band at 405 nm and the major Q band at 628 nm of ICp_6 -Cu showed a gradual red shift upon addition of HSA. The maximum red shift of 7.0 nm occurred with 4 μ M HSA and these changes were accompanied by a slight decrease in the absorbance of the Soret band and an increase in the absorbance of the Q band. Beyond 4 μ M HSA, the absorption spectrum of ICp_6 -Cu did not change both with respect to the intensity and position of the Soret and Q bands indicating that the interaction of ICp_6 -Cu with HSA completed at a ratio of 5 : 4 (Table 1). The red shift of the Soret and

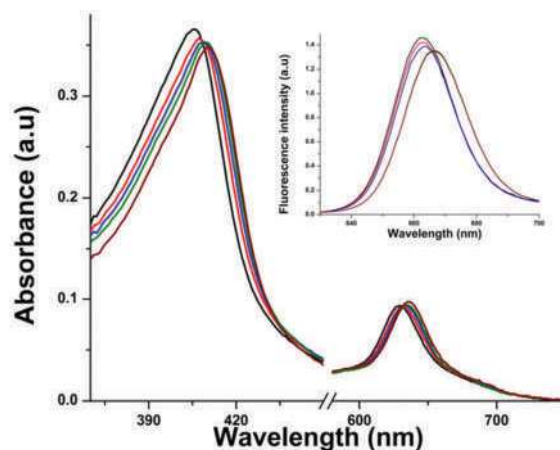


Fig. 2 Absorption and fluorescence spectra (inset) of ICp_6 -Cu (5 μ M) alone (black) and in the presence of 1.0 μ M (red), 2.0 μ M (blue), 4.0 μ M (green) and 10.0 μ M (brown) HSA in phosphate buffer (pH 7.4).

Table 1 Absorption characteristics of ICp_6 -Cu (5 μ M) with various concentrations of HSA

Concentration of HSA (μ M)	Soret band		Q band	
	λ_{\max} (nm)	FWHM (nm)	λ_{\max} (nm)	FWHM (nm)
0	405	47	628	32
1	407	47	630	32
2	409	47	632	32
3	410	47	633	32
4	411	47	635	32
10	411	47	635	32

Q bands indicates a decrease in energy of the π to π^* transitions, which can occur when the chlorin ring interacts with aromatic ligands in proteins *via* electrostatic or hydrophobic interactions.¹⁸ In a previous study on the interaction of Cp_6 with HSA, the Soret band absorbance of Cp_6 was observed to decrease initially at lower concentrations of HSA and when the HSA concentration was increased it led to the hyperchromism and red shift of the Soret band.¹⁹ These spectral changes were attributed to the aggregation of Cp_6 at a low HSA:PS ratio (0.25) followed by its disaggregation and then formation of ground-state complex between monomeric Cp_6 and HSA.¹⁹ While ICp_6 -Cu also showed a decrease in the Soret band absorption upon addition of HSA, there was one major difference: the increase in concentration of HSA did not lead to the hyperchromism of the Soret band (Fig. 2). Moreover, ICp_6 -Cu showed a large red shift of the Soret and Q bands initially at lower concentrations of HSA, which is similar to the red shift of the Soret and Q bands of Cp_6 when it forms a monomeric complex with HSA.¹⁹ The aggregation and disaggregation of Cp_6 upon addition of HSA were also reflected in its fluorescence spectrum as a decrease in fluorescence intensity at lower HSA concentrations, then as an increase with a red shift of the fluorescence band upon further increase in the HSA concentration.¹⁹ The fluorescence spectra of ICp_6 -Cu in the

absence and presence of HSA are shown in Fig. 2 (inset). The addition of 1–4 μM HSA to $\text{ICp}_6\text{-Cu}$ led to only a small decrease in its fluorescence intensity with a red shift in peak position. However, unlike Cp_6 , further increases in the concentration of HSA did not lead to an increase in the fluorescence intensity of $\text{ICp}_6\text{-Cu}$ again. In addition, the FWHM (full width at half maximum) of the Soret band and the Q band did not increase upon the addition of HSA (Table 1). This trend in absorption and fluorescence was otherwise expected if $\text{ICp}_6\text{-Cu}$ also aggregates and then disaggregates upon a gradual increase in the concentration of HSA. These results suggest that the aggregation of $\text{ICp}_6\text{-Cu}$ did not occur upon interaction with HSA. To confirm this, the fluorescence lifetimes of both Cp_6 and $\text{ICp}_6\text{-Cu}$ in the absence and presence of HSA were compared (Table 2). It can be seen that the fluorescence lifetime of Cp_6 is increased upon addition of HSA, which is due to its disaggregation as reported previously.¹⁹ In contrast, there is no change in the fluorescence lifetime of $\text{ICp}_6\text{-Cu}$ upon addition of HSA which confirmed that there is no aggregation of $\text{ICp}_6\text{-Cu}$. Cp_6 contains three ionizable carboxylic groups and hence its interaction with HSA at physiological pH is mainly governed by electrostatic interactions.¹⁹ Whereas, in $\text{ICp}_6\text{-Cu}$, the two adjacent carboxylic groups are coordinated with Cu^{2+} and hence the net negative charge on the molecule is reduced. Despite this, the aqueous solubility of $\text{ICp}_6\text{-Cu}$ is not reduced and its aggregation did not take place. This is mainly because of the presence of water molecules in the coordination sphere of Cu^{2+} , which increase the interaction of $\text{ICp}_6\text{-Cu}$ with solvent molecules through hydrogen bonding and thus prevent the stacking of chlorin molecules.²⁰

Fluorescence quenching of HSA by $\text{ICp}_6\text{-Cu}$

Upon absorption of ultraviolet light HSA shows intrinsic fluorescence emission from aromatic amino acid residues such as phenylalanine, Trp and Tyr. HSA is a 585 amino acid long monomer protein, structurally organized into three homologous helical domains (I–III) and each domain contains two subdomains denoted as A and B.²¹ Trp-214 and Tyr-263 are located close to the drug binding site at subdomain IIA.^{22,23} HSA contains 18 Tyr residues but it is mainly Tyr-263 that is responsible for HSA fluorescence because the remaining Tyr residues in HSA are completely buried inside the protein and suffer fluorescence quenching.²³ The quenching of protein fluorescence by drug molecules is widely used as a sensitive assay to probe the interaction of HSA with drugs and to deter-

mine binding parameters, such as the binding constant, number of binding sites and binding distance.

Fig. 3a shows the fluorescence spectra of HSA ($\lambda_{\text{ext}} = 280 \text{ nm}$) in the absence and presence of varying concentrations of $\text{ICp}_6\text{-Cu}$. With an increase in the concentration of $\text{ICp}_6\text{-Cu}$, there is a decrease in fluorescence intensity of the HSA (330 nm) along with a gradual blue shift of the emission peak. To ascertain whether the fluorescence quenching involves a collisional or static mechanism, the value of the quenching rate constant was determined by analyzing the fluorescence quenching data according to the following Stern–Volmer equation:

$$\frac{F_0}{F} = 1 + K_{\text{SV}}[Q] = 1 + K_q\tau_0[Q] \quad (2)$$

where F_0 and F are the fluorescence intensities of HSA in the absence and presence of the quencher, respectively, τ_0 is the average lifetime of the HSA Trp residue in the absence of the quencher ($\tau_0 = 10^{-8} \text{ s}$),²⁴ $[Q]$ is the concentration of the quencher, K_q is the biomolecular quenching rate constant and K_{SV} is the Stern–Volmer quenching constant.²⁵ The value of the slope ($1.2 \pm 0.1 \times 10^6$) is obtained from the linear fit of the plot of F_0/F vs. $[Q]$ (Fig. 3b), which represents K_{SV} .

The value of K_q given by the K_{SV}/τ_0 ratio for $\text{ICp}_6\text{-Cu}$ was in the order of $10^{13} \text{ M}^{-1} \text{ s}^{-1}$ which is greater than the maximum scatter collision quenching constant of quenchers with albumin ($K_{\text{dif}} = 2.0 \times 10^{10} \text{ M}^{-1} \text{ s}^{-1}$).^{26,27} These results suggest that quenching of HSA fluorescence is dominated by static quenching arising due to the specific interaction between HSA and $\text{ICp}_6\text{-Cu}$.

Binding constant and number of binding sites

When the binding of a ligand to HSA involves the static quenching of Trp fluorescence, the binding constant and number of binding sites can be calculated from the following equation:

$$\log \left[\frac{F_0 - F}{F} \right] = \log K + n \log [Q] \quad (3)$$

where F_0 and F are the fluorescence intensities in the absence and presence of the quencher and $[Q]$ is the quencher concentration.²⁵ In the plot of $\log[(F_0 - F)/F]$ vs. $\log[Q]$ (Fig. 3c), the values of the y-intercept and slope represent the binding constant (K_b) and the number of binding sites (n), which were $2.9 \pm 0.2 \times 10^6 \text{ M}^{-1}$ and 1.2 ± 0.1 , respectively. The similar values of K_{SV} and K_b further confirmed that the quenching of fluorescence was static in nature. The values of K_b and n suggest that HSA has one high affinity binding site for $\text{ICp}_6\text{-Cu}$. In comparison, the number of binding sites for Cp_6 was more than 1 which is in agreement with previous studies by Datta *et al.*²⁵ Based on site marker competition experiments they have identified the binding sites for Cp_6 as Sudlow site I and II.^{25,28} Although in a previous study, the possibility of dicarboxylic porphyrins or chlorins binding to HSA at the high affinity heme binding site *i.e.* at subdomain IB has also been reported.²⁹ It was hypothesized that the side carboxylic

Table 2 Average fluorescence lifetime (τ_{avg}) of $\text{ICp}_6\text{-Cu}$ and Cp_6 in the presence and absence of HSA (5 μM). The value of χ^2 is given in parentheses

Concentration of PS (μM)	τ_{avg} of Cp_6 (ns)		τ_{avg} of $\text{ICp}_6\text{-Cu}$ (ns)	
	Without HSA	With HSA	Without HSA	With HSA
1	3.06(1.05)	4.01(1.07)	3.26(1.08)	3.30(1.01)
5	3.04(1.03)	4.07(1.05)	3.26(1.04)	3.07(1.05)
10	3.20(1.08)	3.90(1.03)	3.00(1.00)	3.16(1.07)

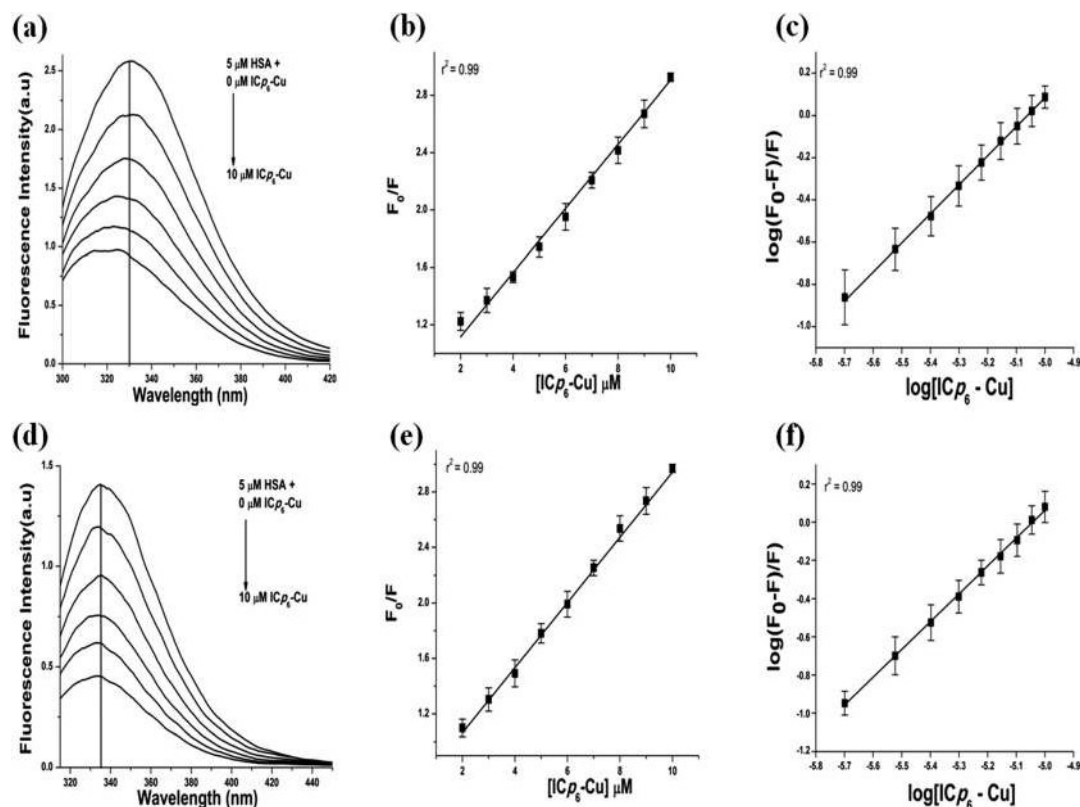


Fig. 3 Changes in the fluorescence emission spectra of HSA (5.0 μM) upon addition of different concentrations of $\text{ICp}_6\text{-Cu}$ (0–10 μM) in phosphate buffer (pH 7.4) excited at 280 nm (a) and 295 nm (d). Stern–Volmer plots of protein fluorescence quenching (F_0/F) vs. the concentration of $\text{ICp}_6\text{-Cu}$ for the HSA fluorescence excited at 280 nm (b) and 295 nm (e). Double reciprocal plots of $\log(F_0 - F)/F$ vs. $\log[\text{ICp}_6\text{-Cu}]$ for HSA fluorescence excited at 280 nm (c) and 295 nm (f).

groups of tetrapyrrole compounds play an important role in binding through the formation of salt bridges with basic residues (Lys, Arg, His) at the entrance of subdomain IB.²⁹ As compared to Cp_6 , the two adjacent carboxylic groups in $\text{ICp}_6\text{-Cu}$ at the C13 and C15 positions are occupied by Cu^{2+} , which could explain the decrease in the number of binding sites of $\text{ICp}_6\text{-Cu}$.

While the intrinsic protein Trp fluorescence excited at 280 nm has been widely applied in protein research including studies on drug binding properties of serum albumin,^{30,31} it is important to mention that the fluorescence of HSA excited at 280 nm also contains a significant contribution from the Tyr-263 residue. Hence to avoid uncertainty in the interpretation of the binding properties of drugs/ligands with HSA, it is often preferred to probe the protein fluorescence using 295 nm excitation, which eliminates the fluorescence of the Tyr-263 residue to a large extent.³¹ In Fig. 3d, we show the results of the fluorescence quenching of protein Trp by $\text{ICp}_6\text{-Cu}$, when excited at 295 nm. The values of K_{SV} ($1.5 \pm 0.2 \times 10^6$), K_b ($3.4 \pm 0.3 \times 10^6 \text{ M}^{-1}$) and n (1.3 ± 0.1) obtained from the Stern–Volmer plot (Fig. 3e) and the double reciprocal plot (Fig. 3f), respectively, are similar to the values obtained with excitation at 280 nm suggesting that $\text{ICp}_6\text{-Cu}$ interacts specifically with the Trp-214 residue in HSA.

Proximity of $\text{ICp}_6\text{-Cu}$ to tryptophan in HSA

The proximity of the bound ligand to the Trp in albumin can be confirmed from fluorescence quenching occurring due to the Förster non-radiative energy transfer (FRET) between the donor (Trp) and the acceptor (ligand).²⁵ The possibility of FRET is likely when (1) there is overlap between the fluorescence emission and the absorbance spectrum of the donor and acceptor, respectively and (2) the distance between the two is less than 8 nm. As can be seen in Fig. 4a, there is considerable overlap between the absorption spectrum of $\text{ICp}_6\text{-Cu}$ (acceptor) and the fluorescence spectrum of HSA (donor) obtained at either 280 nm or 295 nm excitation wavelengths. Therefore, the efficiency of energy transfer, E , between the two was computed according to the Förster non-radiative energy transfer theory using the equation:

$$E = \frac{R_0^6}{(R_0^6 + r^6)} = \frac{(F_0 - F)}{F_0} \quad (4)$$

where F and F_0 are the fluorescence intensities of HSA in the presence and absence of PS and r is the distance between the acceptor and donor.²⁵ R_0 is the critical distance when the

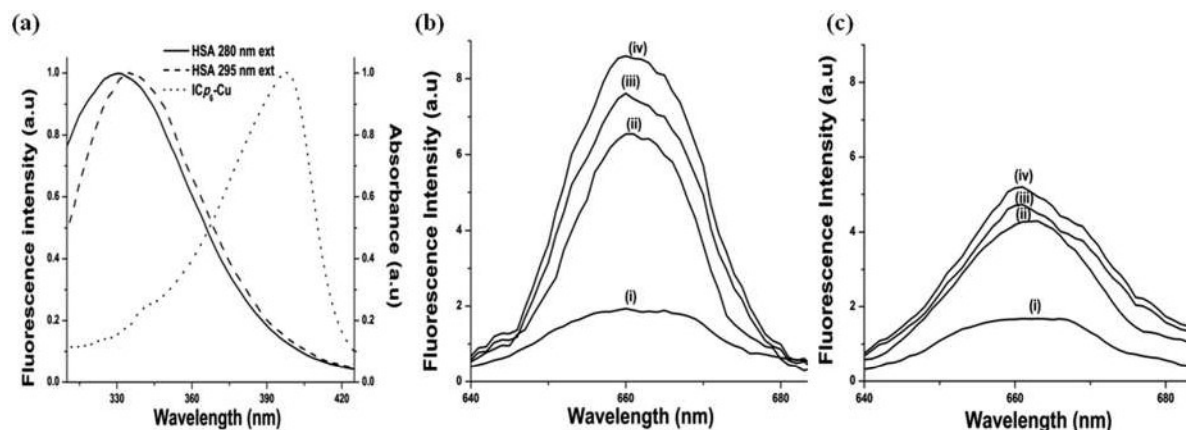


Fig. 4 (a) Normalized spectral overlap of the fluorescence of 5.0 μM HSA (λ_{ex} 280 nm and 295 nm) and the absorption of 5.0 μM ICp₆-Cu in phosphate buffer (pH 7.4). 280 nm (b) and 295 nm (c) excited fluorescence spectra of 5.0 μM ICp₆-Cu alone (i) and in the presence of 1.0 μM (ii), 2.0 μM (iii) and 3.0 μM (iv) HSA in phosphate buffer (pH 7.4).

transfer efficiency is 50%, which is given by the following equation:

$$R_0^6 = 8.8 \times 10^{-25} k^2 N^{-4} \Phi J \quad (5)$$

where k^2 is the spatial orientation factor between the emission dipole of the donor and the absorption dipole of the acceptor, N is the refractive index of the medium and Φ is the fluorescence quantum yield of the donor. For the experimental conditions used, the values of k^2 , N , and Φ were taken as 0.66, 1.336 and 0.188, respectively.²⁵ J is the overlap integral of the fluorescence emission spectrum of the donor and the absorption spectrum of the acceptor and is calculated from the equation:

$$J = \frac{(\sum F(\lambda) \epsilon(\lambda) \lambda^4 \Delta\lambda)}{(\sum F(\lambda) \Delta\lambda)} \quad (6)$$

where $F(\lambda)$ is the corrected fluorescence intensity of the donor at wavelength λ and $\epsilon(\lambda)$ is the molar absorption coefficient of the acceptor at wavelength λ .

With respect to the 280 nm excited fluorescence spectrum of HSA, the values of J , R_0 , E and r were $2.8 \times 10^{-14} \text{ M}^{-1} \text{ cm}^3$, 2.9 nm, 0.40 and 3.1 nm, respectively and those with respect to the 295 nm excited fluorescence spectrum of HSA were $3.1 \times 10^{-14} \text{ M}^{-1} \text{ cm}^3$, 3.1 nm, 0.43 and 3.2 nm, respectively. In both cases, the distance between ICp₆-Cu and Trp in HSA is <8 nm, which further fulfills the $0.5R_0 < r < 1.5R_0$ criterion for a high probability of energy transfer from a donor to acceptor. These results together strengthen the probability of binding of ICp₆-Cu close to Sudlow Site I where the Trp-214 residue is located. This is also in agreement with previously reported FRET distances for Cp₆ that binds to Sudlow Site I.²⁵ Here it is important to mention that in most of the studies on tetrapyrrole compounds including Cp₆, the FRET distance is generally calculated using a value of k^2 of 0.667 (2/3) considering that the motion of both Trp-214 and the bound chlorin is not very restricted.²⁵ Considering an extreme value of k^2 of 4.0,¹⁶ which

applies when the motions of the donor and acceptor are restricted (rigid orientation) the FRET distance for ICp₆-Cu was 4.2 nm, which is well within the high probability of energy transfer from a donor to acceptor. To confirm the possibility of FRET, the fluorescence spectra of ICp₆-Cu (5 μM) were recorded in the absence and in the presence of HSA (1–3 μM) using λ_{ext} at 280 nm and 295 nm. As shown in Fig. 4b and c, the addition of 1 μM HSA led to a ~3 fold increase in the fluorescence intensity of ICp₆-Cu. The magnitude of the effect increased further with an increase in the concentration of HSA. These results suggested an energetic interaction between the excited Trp residue of HSA and the unexcited ICp₆-Cu. These results thus provide evidence that the electronic excitation energy of HSA was transferred to the bound ICp₆-Cu.

Here it is important to mention that the calculation of the FRET efficiency and the donor–acceptor distance from the quenching of the steady state fluorescence of HSA suffer from the drawback of large variation particularly due to artefacts of the inner filter effect and the uncertainty of donor–acceptor configurations that determine the value of the orientation factor (k^2). As reported by Van de Weert *et al.*, calculations of the FRET efficiency from the fluorescence lifetime of HSA provide a better approach because it does not include the same possibility of artefacts and uncertainty of the donor–acceptor configuration.³²

Effect of ICp₆-Cu on protein conformation

The binding of drugs or xenobiotics on HSA can often lead to changes in the conformation of proteins.^{33,34} Any change in the conformation of a protein generally leads to a red shift in fluorescence of the Trp and Tyr residues as the environment around these residues becomes more polar. Results on the quenching of protein fluorescence by ICp₆-Cu showed that there is a blue shift in the fluorescence spectrum indicating the possibility of a change in the conformation of the protein. However, since both Trp and Tyr contribute to the fluorescence of a protein with a 280 nm excitation, to verify any change in

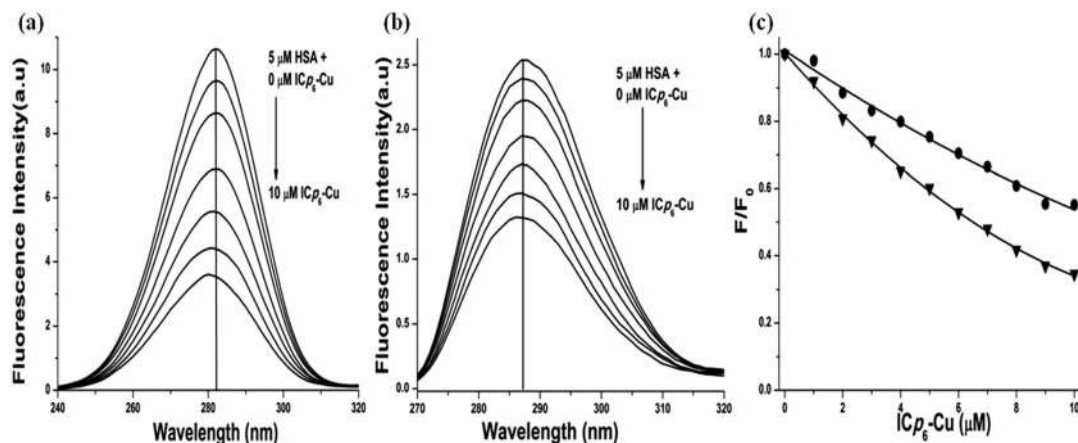


Fig. 5 Synchronous fluorescence spectra of HSA (5.0 μM) alone and in the presence of different concentrations of $\text{ICp}_6\text{-Cu}$ (0–10 μM) recorded at $\Delta\lambda = 60$ nm and $\Delta\lambda = 15$ nm to resolve the fluorescence of the Trp (a) and Tyr (b) residues, respectively. (c) Fluorescence quenching (F_0/F) of Trp (triangles) and Tyr (circles) residues vs. the concentration of $\text{ICp}_6\text{-Cu}$.

the conformation of HSA, the individual contribution of these residues to the protein's fluorescence was resolved by synchronous fluorescence spectroscopy. In Fig. 5, we show the synchronous fluorescence spectra of Trp and Tyr residues after the addition of various concentrations of $\text{ICp}_6\text{-Cu}$ in HSA. With an increase in the concentration of $\text{ICp}_6\text{-Cu}$, the fluorescence of both Tyr and Trp is gradually quenched but there is no change of the peak position in the spectrum. In the plot of F/F_0 versus $[\text{ICp}_6\text{-Cu}]$ (Fig. 5c), the slope of the curve obtained for $\Delta\lambda = 60$ nm was higher than the slope of the curve for $\Delta\lambda = 15$ nm indicating that the quenching of Trp fluorescence is higher than that of Tyr upon binding of $\text{ICp}_6\text{-Cu}$ to HSA. These results suggest that $\text{ICp}_6\text{-Cu}$ binds close to the Trp residue and that binding did not affect the conformation of the protein.

Effect of HSA on the stability of $\text{ICp}_6\text{-Cu}$

HSA possesses specific binding sites for transition metal ions at the N-terminal site, which comprises the first three amino acid sequence (Asp-Ala-His) and the sulfhydryl groups. A secondary weaker binding site (site A) for metal ions has also been reported, which comprises the side chain carbonyl of Asn99 of domain I, the imidazole of His247 and the carboxylate of Asp249, both of domain II.³⁵ HSA can compete with the ligand for metal ions and consequently can result in *trans*-complexation of metal ions from the ligand to the albumin under normal physiological conditions.^{36–39} In addition, such interaction can affect the stability of the metal complex under physiological conditions or lead to structural modifications and oxidation of HSA.^{36,38} The UV-Vis spectra of $\text{ICp}_6\text{-Cu}$ is very distinct from that of Cp_6 (Fig. 1). If Cu^{2+} dissociated from chlorin, it would result in a decrease in the Q band intensity concomitantly with a reappearance of the band at 658 nm. Fig. 6 shows the absorption spectra of $\text{ICp}_6\text{-Cu}$ at various time intervals after incubation with HSA in the dark. There was no change in the absorption spectra of $\text{ICp}_6\text{-Cu}$ (in both the intensity and position of the Soret band and the Q band) even after

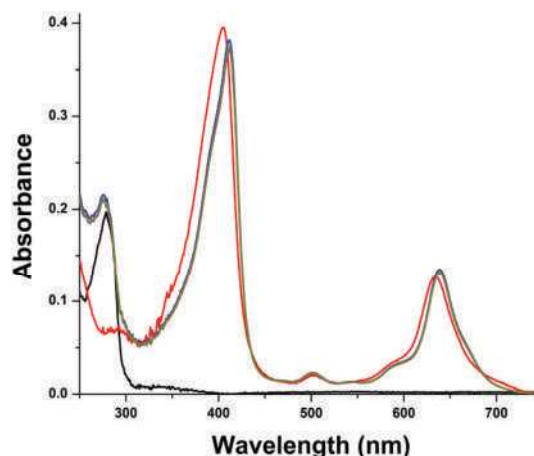


Fig. 6 Absorption spectra of 5.0 μM $\text{ICp}_6\text{-Cu}$ (red) in the presence of 5 μM HSA (black) after 0 h (blue), 12 h (dark cyan), 24 h (magenta) and 48 h (dark yellow) of incubation in the dark.

prolonged incubation with HSA. This suggested that the interaction did not destabilize the metal from $\text{ICp}_6\text{-Cu}$.

Conclusions

In conclusion, the results of this study show that $\text{ICp}_6\text{-Cu}$ binds strongly with HSA and the binding did not affect the conformation of the protein or destabilize the metal from $\text{ICp}_6\text{-Cu}$. The pronounced quenching of Trp-214 fluorescence and the value of the Förster distances (r) between Trp-214 and $\text{ICp}_6\text{-Cu}$ suggest that the probable binding site is the same as that of Cp_6 , *i.e.* Sudlow site I at subdomain IIA. Thus strong binding of $\text{ICp}_6\text{-Cu}$ with HSA could play an important role in its biodistribution, bioavailability and accumulation in tumours.

Disclosure

Alok Dube, Paromita Sarbadhikary and Pradeep Kumar Gupta are named patent inventors for the Indian Patent Application no. 4912/MUM/2015 titled 'A metal complex of chlorophyll derivative for magnetic resonance imaging and photodynamic therapy', filed on December 29, 2015.

Conflicts of interest

The authors declare that there are no conflicts of interest.

Acknowledgements

We are thankful to Dr K. Das for helping with fluorescence lifetime measurements. P. Sarbadhikary thankfully acknowledges Homi Bhabha National Institute, Mumbai for the senior research fellowship.

References

- 1 H. Abrahamse and M. R. Hamblin, New photosensitizers for photodynamic therapy, *Biochem. J.*, 2016, **473**, 347–364.
- 2 P. Agostinis, K. Berg, K. A. Cengel, T. H. Foster, A. W. Girotti, S. O. Gollnick, S. M. Hahn, M. R. Hamblin, A. Juzeniene, D. Kessel, M. Korbelik, J. Moan, P. Mroz, D. Nowis, J. Piette, B. C. Wilson and J. Golab, Photodynamic therapy of cancer: an update, *CA-Cancer J. Clin.*, 2011, **61**, 250–281.
- 3 L. B. Josefsen and R. W. Boyle, Photodynamic therapy and the development of metal-based photosensitisers, *Met.-Based Drugs*, 2008, **2008**, 276109.
- 4 J. M. Dąbrowski, B. Pucelika, A. Regiel-Futyraa, M. Brindella, O. Mazuryka, A. Kyzioła, G. Stochela, W. Macyka and L. G. Arnaut, Engineering of relevant photodynamic processes through structural modifications of metallotetrapyrrolic photosensitizers, *Coord. Chem. Rev.*, 2016, **325**, 67–101.
- 5 Q. Huang, Z. Pan, P. Wang, Z. Chen, X. Zhang and H. Xu, Zinc(II) and copper(II) complexes of β -substituted hydroxyl-porphyrins as tumor photosensitizers, *Bioorg. Med. Chem. Lett.*, 2006, **16**, 3030–3033.
- 6 V. A. Ol'shevskaya, R. G. Nikitina, A. N. Savchenko, M. V. Malshakova, A. M. Vinogradov, G. V. Golovina, D. V. Belykh, A. V. Kutchin, M. A. Kaplan, V. N. Kalinin, V. A. Kuzmin and A. A. Shtil, Novel boronated chlorin e6-based photosensitizers: Synthesis, binding to albumin and antitumour efficacy, *Bioorg. Med. Chem. Lett.*, 2009, **17**, 1297–1306.
- 7 M. Obata, S. Hirohara, R. Tanaka, I. Kinoshita, K. Ohkubo, S. Fukuzumi, M. Tanihara and S. Yano, In Vitro Heavy-Atom Effect of Palladium(II) and Platinum(II) Complexes of Pyrrolidine-Fused Chlorin in Photodynamic Therapy, *J. Med. Chem.*, 2009, **52**, 2747–2753.
- 8 S. Fukuzumi, K. Ohkubo, X. Zheng, Y. Chen, R. K. Pandey, R. Zhan and K. M. Kadish, Metal Bacteriochlorins Which Act as Dual Singlet Oxygen and Superoxide Generators, *J. Phys. Chem. B*, 2008, **112**, 2738–2746.
- 9 G. Momekov, M. Karaivanova, I. Ugrinova, E. Pasheva, G. Gencheva, D. Tsekova, S. Arpadjan and P. R. Bontchev, In vitro pharmacological study of monomeric platinum(III) hematoporphyrin IX complexes, *Invest. New Drugs*, 2011, **29**, 742–751.
- 10 T. Gianferrara, A. Bergamo, I. Bratsos, B. Milani, C. Spagnul, G. Sava and E. Alessio, Ruthenium-Porphyrin Conjugates with Cytotoxic and Phototoxic Antitumor Activity, *J. Med. Chem.*, 2010, **53**, 4678–4690.
- 11 P. A. Waghorn, Radiolabelled porphyrins in nuclear medicine, *J. Labelled Compd. Radiopharm.*, 2014, **57**, 304–309.
- 12 J. A. Silvester, G. S. Timmins and M. J. Davies, Photodynamically generated bovine serum albumin radicals: evidence for damage transfer and oxidation at cysteine and tryptophan residues, *Free Radical Biol. Med.*, 1998, **24**, 754–766.
- 13 S. B. Dror, I. Bronshtein, H. Weitman, K. M. Smith, W. G. O'Neal, P. A. Jacobi and B. Ehrenberg, The binding of analogs of porphyrins and chlorins with elongated side chains to albumin, *Eur. Biophys. J.*, 2009, **38**, 847–855.
- 14 P. Sarbadhikary, A. Dube and P. K. Gupta, Synthesis and characterization of photodynamic activity of an iodinated Chlorin p_6 copper complex, *RSC Adv.*, 2016, **6**, 75782–75792.
- 15 P. Sarbadhikary and A. Dube, Iodinated chlorin p_6 copper complex induces anti-proliferative effect in oral cancer cells through elevation of intracellular reactive oxygen species, *Chem.-Biol. Interact.*, 2017, **277**, 137–144.
- 16 J. R. Lakowicz, *Principles of Fluorescence Spectroscopy*, Springer, New York, USA, 1st edn, 1983.
- 17 F. Yuan, M. Dellian, D. Fukumura, M. Leunig, D. A. Berk, V. P. Torchilin and R. K. Jain, Vascular permeability in a human tumor xenograft: molecular size dependence and cutoff size, *Cancer Res.*, 1995, **55**, 3752–3756.
- 18 H.-M. Ma, X. Chen, N. Zhang, Y. Y. Han, D. Wu, B. Du and Q. Wei, Spectroscopic studies on the interaction of a water-soluble cationic porphyrin with proteins, *Spectrochim. Acta, Part A*, 2009, **72**, 465–469.
- 19 P. P. Mishra, S. Patel and A. Datta, Effect of Increased Hydrophobicity on the Binding of Two Model Amphiphilic Chlorin Drugs for Photodynamic Therapy with Blood Plasma and Its Components, *J. Phys. Chem. B*, 2006, **110**, 21238–21244.
- 20 W. I. White, in *The Porphyrins physical chemistry part C*, D. Dolphin, Academic Press, inc., London, UK, 1978, ch. 7, pp. 303–339.
- 21 A. M. Merlot, D. S. Kalinowski and D. R. Richardson, Unraveling the mysteries of serum albumin—more than just a serum protein, *Front. Physiol.*, 2014, **5**, 299.
- 22 K. Yamasaki, V. T. G. Chuang, T. Maruyama and M. Otagiri, Albumin–drug interaction and its clinical implication, *Biochim. Biophys. Acta*, 2013, **1830**, 5435–5443.

- 23 O. K. Abou-Zied and O. I. Al-Shihi, Characterization of Subdomain IIA Binding Site of Human Serum Albumin in its Native, Unfolded, and Refolded States Using Small Molecular Probes, *J. Am. Chem. Soc.*, 2008, **130**, 10793–10801.
- 24 J. R. Lakowicz and G. Weber, Quenching of fluorescence by oxygen. A probe for structural fluctuations in macromolecules, *Biochemistry*, 1973, **12**, 4161–4170.
- 25 S. Patel and A. Datta, Steady State and Time-resolved Fluorescence Investigation of the Specific Binding of Two Chlorin Derivatives with Human Serum Albumin, *J. Phys. Chem. B*, 2007, **111**, 10557–10562.
- 26 R. Yousefi, A. Taheri-Kafrani, S. M. Nabavizadeh, Z. Pouryasini, M. B. Shahsavani, K. Khoshaman and M. Rashidi, The binding assessment with human serum albumin of novel six-coordinate Pt(IV) complexes, containing bidentate nitrogen donor/methyl ligands, *Mol. Biol. Res. Commun.*, 2015, **4**, 167–179.
- 27 N. Shahabadi and M. Maghsudi, Binding studies of a new copper(II) complex containing mixed aliphatic and aromatic dinitrogen ligands with bovine serum albumin using different instrumental methods, *J. Mol. Struct.*, 2009, **929**, 193–199.
- 28 S. Patel, K. K. Sharma and A. Datta, Competitive binding of Chlorin *p*₆ and Dansyl-L-Proline to Sudlow's site II of human serum albumin, *Spectrochim. Acta, Part A*, 2015, **138**, 925–931.
- 29 H. Mojzisoova, S. Bonneau, C. Vever-Bizet and D. Brault, The pH-dependent distribution of the photosensitizer chlorin *e*₆ among plasma proteins and membranes: A physico-chemical approach, *Biochim. Biophys. Acta*, 2007, **1768**, 366–374.
- 30 A. B. Ghisaidoobe and S. J. Chung, Intrinsic Tryptophan Fluorescence in the Detection and Analysis of Proteins: A Focus on Förster Resonance Energy Transfer Techniques, *Int. J. Mol. Sci.*, 2014, **15**, 22518–22538.
- 31 O. K. Abou-Zied, Understanding the physical and chemical nature of the warfarin drug binding site in human serum albumin: experimental and theoretical studies, *Curr. Pharm. Des.*, 2015, **21**, 1800–1816.
- 32 M. Van de Weert and L. Stella, Fluorescence quenching and ligand binding: a critical discussion of a popular methodology, *J. Mol. Struct.*, 2011, **998**, 144–150.
- 33 M. Fasano, S. Curry, E. Terreno, M. Galliano, G. Fanali, P. Narciso, S. Notari and P. Ascenzi, The extraordinary ligand binding properties of human serum albumin, *IUBMB Life*, 2005, **57**, 787–796.
- 34 A. Ahmed-Ouameur, S. Diamantoglou, M. R. Sedaghat-Herati, Sh. Nafisi, R. Carpentier and H. A. Tajmir-Riahi, The effects of drug complexation on the stability and conformation of human serum albumin, *Cell Biochem. Biophys.*, 2006, **45**, 203–213.
- 35 W. Bal, M. Sokołowska, E. Kurowska and P. Faller, Binding of transition metal ions to albumin: Sites, affinities and rates, *Biochim. Biophys. Acta*, 2013, **1830**, 5444–5455.
- 36 M. K. Moi, S. J. DeNardo and C. F. Meares, Stable bifunctional chelates of metals used in radiotherapy, *Cancer Res.*, 1990, **50**(Suppl. 3), 789s–793s.
- 37 V. C. da Silveira, G. F. Caramori, M. P. Abbott, M. B. Gonçalves, H. M. Petrilli and A. M. da Costa Ferreira, Oxindole-Schiff base copper(II) complexes interactions with human serum albumin: Spectroscopic, oxidative damage, and computational studies, *J. Inorg. Biochem.*, 2009, **103**, 1331–1341.
- 38 M. A. A. Azzellini, M. P. Abbott, A. Machado, M. T. M. Miranda, L. C. Garcia, G. F. Caramori, M. B. Gonçalves, H. M. Petrilli and A. M. C. Ferreira, Interactions of di-Imine Copper(II) Complexes with Albumin: Competitive Equilibria, Promoted Oxidative Damage and DFT Studies, *J. Braz. Chem. Soc.*, 2010, **21**, 1303–1317.
- 39 S. Tabassum, W. M. Al-Asbahy, M. Afzal and F. Arjmand, Synthesis, characterization and interaction studies of copper based drug with Human Serum Albumin (HSA): Spectroscopic and molecular docking investigations, *J. Photochem. Photobiol., B*, 2012, **114**, 132–139.

(12) PATENT APPLICATION PUBLICATION

(21) Application No.4912/MUM/2015 A

(19) INDIA

(22) Date of filing of Application :29/12/2015

(43) Publication Date : 12/02/2016

(54) Title of the invention : A METAL COMPLEX OF CHLOROPHYLL DERIVATIVE FOR MAGNETIC RESONANCE IMAGING AND PHOTODYNAMIC THERAPY.

(51) International classification	:C07D 487/22	(71)Name of Applicant :
(31) Priority Document No	:NA	1)THE SECRETARY, DEPARTMENT OF ATOMIC ENERGY
(32) Priority Date	:NA	Address of Applicant :Govt. of India, Anushakti Bhavan,
(33) Name of priority country	:NA	Chatrapati Shivaji Maharaj Marg, Mumbai -400001, Maharashtra,
(86) International Application No	:NA	India. Maharashtra India
Filing Date	:NA	(72)Name of Inventor :
(87) International Publication No	: NA	1)DUBE, Alok
(61) Patent of Addition to Application Number	:NA	2)SARBADHIKARY, Paromita
Filing Date	:NA	3)GUPTA, Pradeep Kumar
(62) Divisional to Application Number	:NA	
Filing Date	:NA	

(57) Abstract :

ABSTRACT TITLE : A METAL COMPLEX OF CHLOROPHYLL DERIVATIVE FOR MAGNETIC RESONANCE IMAGING AND PHOTODYNAMIC THERAPY. The invention provides a water soluble halogenated metal complex of chlorophyll derivative and process for its preparation. Advantageously, the metal complex of chlorophyll derivative contains paramagnetic metal cation and is capable of generating singlet oxygen and other Reactive Oxygen Species (ROS) when activated by red wavelength region of visible light and thus would have application in simultaneous Photodynamic Therapy (PDT) and Magnetic Resonance Imaging (MRI) of tumours. Advantageously such compounds would be useful for other PDT applications, such as inactivation of viruses and bacteria in vivo and ex-vivo. Further, the said metal complex of chlorophyll derivative would have application in tumor imaging using techniques such as computed tomography (CT), positron emission tomography (PET), single, photon emission computed tomography (SPECT) as well as therapy using photon activation therapy and radiotherapy.

No. of Pages : 33 No. of Claims : 16